Thermochemical conversion of biomass in a Swirling Fluidized Bed: A design procedure and numerical simulation

A Master's Thesis
by

Daniel Armando Pinilla Fernández

July 22, 2022

Thesis tutors:
Assist. Prof. Dr. Arturo González Quiroga
Prof. Dr. Antonio José Bula Silvera

Universidad del Norte
Engineering Division
Department of Mechanical Engineering

Acknowledgements

I would like to express my sincere gratitude to my research tutors, Prof. Arturo González Quiroga and Prof. Antonio Bula Silvera, for giving me the opportunity to do research with UREMA Research Group and providing the tools to grow as a scientist. Their commitment, contribution, and guidance during the development of all the research were crucial to successfully accomplish this work. I will keep in my mind how they always supported me with a smile in their faces, even when I was in a stressful moment. I consider them more than my tutors; they are my colleagues and friends. Additionally, I would like to thank to Prof. Victor Pugliese for its patience and dedication teaching me how to properly use the Computational Fluid Dynamics simulation software. And I would like to thank Prof. Virginia Paredes and Prof. Mauricio Carmona for all their support from the Mechanical Engineer Coordination of Postgraduates.

Funding support of this project was obtained by Fundación para la Promoción de la Investigación y la Tecnología (FPIT) under the project "Desarrollo de una metodología de diseño para reactores de lecho toroidal con enfoque en la transformación termoquímica de biomasa y residuos plásticos" with contract number UN-OJ-2021-51879.

During the path through the postgraduate studies, I met other researchers who gave me their point of view to improve my work and made this process funnier. I would like to especially mention to my friends from the 'Lab', where we shared very especial moments during our free time: Lily, Eliecer, Orlando, Omar, Wilson, Marielena, Jonathan, Shardaine and Andrés. Also, I would like to mention Rafael and Alberto, friends who made contributions to the development of this work.

Lastly, I thank my family who always supported and encouraged me to construct my path and trust in my abilities. I appreciate the support of my siblings, Adriana and Jesus, and my father, Armando. I am especially grateful to my mom, Gertrudis, who gave me her blind confidence since the very first moment I decided to follow this path. She is the corner stone of my life and I would not be here today as the person who I am without her teachings.

Contents

Contents i
Nomenclature vi
List of Figures xi
List of Tables xv
Summary xviii
Glossary xx
1. Introduction and Outline 1
1.1. Introduction 1
1.2. Objectives 3
1.2.1. General objective 3
1.2.2. Specific objectives 3
1.3. Outline 3
1.4. References 4
2. The Past, Present, and Potential for Swirling Bed Technology in Gas-Solid Fluidization 7
Abstract 7
2.1. Introduction 8
2.2. Methods 9
2.2.1. Systematic literature review 9
2.2.1.1. Identification 10
2.2.1.2. Screening 10
2.2.1.3. Eligibility and inclusion 10
2.2.2. Descriptive characteristics of the sample 10
2.2.3. Content-based analysis 11
2.3. Results & discussion 13
2.3.1. A systematic review of the literature 13
2.3.2. Characteristics of the swirling fluidized bed reactor 18
2.3.2.1. A brief history of the swirling fluidized bed 18
2.3.2.2. Fabrication and design 21
2.3.2.2.1. Gas distributor 22

2.3.2.2.2. Bed reactor column 22
2.3.2.3. Flow regimes and minimum fluidization velocity 26
2.3.2.4. Effect of input or design parameters on SFB reactor operation 27
2.3.2.5. Swirling fluidized bed reactor performance in different applications 33
2.3.2.6. New designs and modifications of the SFB reactor 36
2.3.3. Relevance of computational fluid dynamics in swirling fluidized bed design 39
2.4. Outlook 39
2.4.1. Operating and design modeling 40
2.4.2. Experimentation route 40
2.4.3. CFD analysis 40
2.5. Conclusion 40
2.6. References 41
3. Computational Fluid Dynamics Model-Based Analysis of Flow Patterns in a Gas-Solid Swirling Fluidized Bed Reactor 49
Abstract 49
3.1. Introduction 50
3.2. Methods 51
3.2.1. Experimental Setup 51
3.2.2. Computational procedure 52
3.2.2.1. Governing equations 52
3.2.2.2. Simulation settings 54
3.2.2.3. Simulation procedure 56
3.2.3. Computational grid 57
3.2.4. Model validation 60
3.3. Results and discussion 60
3.3.1. Grid independence 60
3.3.2. Model validation 62
3.3.3. Hydrodynamics 63
3.3.3.1. Azimuthal-radial plane analysis 63
3.3.3.1.1. Solids volume fraction 64
3.3.3.1.2. Solids azimuthal velocity 65

3.3.3.1.3. Solids radial velocity 66
3.3.3.1.4. Air azimuthal velocity 66
3.3.3.1.5. Air radial velocity 67
3.3.3.1.6. Solids centrifugal acceleration 67
3.3.3.2. Axial-radial plane analysis 68
3.3.3.2.1. Solids hydrodynamics 68
3.3.3.2.2. Air hydrodynamics 70
3.4. Conclusion 71
3.5. References 72
4. Design of a Swirling Fluidized Bed Reactor demonstration unit for biomass conversion 75
Abstract 75
4.1. Introduction 76
4.2. Swirling fluidized bed operational setting 77
4.2.1. Operating conditions and input requirements of biomass treatments 78
4.2.1.1. Combustion 79
4.2.1.2. Gasification 82
4.2.1.3. Pyrolysis 85
4.2.1.4. Torrefaction 87
4.3. Design procedure of the swirling fluidized bed reactor 89
4.3.1. Minimum fluidization velocity and actual gas velocity 89
4.3.2. Dimensioning of the swirling fluidized bed reactor 92
4.3.2.1. Housing 92
4.3.2.2. Single row blades type distributor 93
4.3.3. Load and stress analysis 95
4.3.3.1. Single row blades type distributor 95
4.3.3.1.1. External forces and moments and free body diagram 95
4.3.3.1.2. Internal forces and moments 100
4.3.3.1.3. Statically indeterminate analysis 101
4.3.3.1.4. Resultant stresses and failure theory 102
4.3.3.2. Thin-walled vessel under internal pressure 103
4.3.3.2.1. Cylindrical shell wall 103

4.3.3.2.2. Heads and closures 104
4.3.3.2.3. Conical section 105
4.3.3.2.4. Compression stress due to weight loads 105
4.3.3.2.5. Design of vessel subject to combined loads 106
4.3.4. Corrosion 107
4.3.5. Minimum wall thickness 108
4.3.6. Requirements list of design specifications 108
4.3.7. Materials selection 108
4.3.8. Instrumentation 111
4.3.9. Pressure-drops and gas driving system selection 111
4.3.9.1. Pressure-drop across the distributor 111
4.3.9.2. Pressure-drop across the bed 112
4.3.9.3. Pressure-drop across the flowmeter 112
4.3.9.4. Pressure-drop across the cyclones 112
4.3.9.5. Major pressure-drop and driving system 112
4.3.10. Particles feeder selection 113
4.4. Design of a swirling fluidized bed reactor demonstration unit for rice husk combustion 113
4.4.1. Experimental setup 113
4.4.2. Equilibrium and thermodynamics of the rice husk combustion 114
4.4.3. Minimum fluidization velocity 116
4.4.4. Dimensions of the swirling fluidized bed reactor for rice husk combustion 116
4.4.4.1. Global dimensions 116
4.4.4.2. Single row blades distributor 117
4.4.5. Load and stress subject to the swirling fluidized bed reactor during rice husk combustion 117
4.4.5.1. Single row blade distributor 117
4.4.5.1.1. External forces and moments 117
4.4.5.1.2. Allowable stresses in the blades 119
4.4.5.2. Vessel under internal pressure 119
4.4.6. Requirements list of the swirling fluidized bed reactor for rice husk combustion .. 119
4.4.7. Constructive material of the swirling fluidized bed reactor 122

4.4.8. Pressure-drop and blower selection 123
4.4.8.1. Major pressure drops 123
4.4.8.2. Blower selection 123
4.4.9. Design drawings 125
4.5. Conclusion 125
4.6. References 126
5. Conclusions and perspectives 131
5.1. Conclusions 131
5.2. Future perspectives 133
A. Systematic Literature Review 134
A.1. Articles in the ‘Only-mention’ category 134
A.2. Articles in the ‘Related records’ category 134
A.3. Database of the content-based analysis of the selected records 134
B. Calculation and dimensioning of the gas-solid Swirling Fluidized Bed reactor 135
B.1. Shomate equation constants to estimate the enthalpy of the ideal gas at temperature $\boldsymbol{T}$. 135
B.2. Minimum inner radius of the distributor to avoid interference 136
B.3. List of design specifications 137
B.4. Determination of the drag coefficient in the openings between blades 138
B.5. Pressure-drop through the turbine flowmeter 139
B.6. Pressure-drop across the cyclone 139
B.7. Blower selection from performance curves 140
B.8. Design drawings of the SFB reactor for rice husk combustion 141
References 146

Nomenclature

Roman

%op	Percentage area of opening, %
a_c	Solids centrifugal acceleration, m s^{-2}
A	Area
A_{rh}	Pre-exponential factor of the Arrhenius Equation, s^{-1}
Ar	Archimedes number
c_p	Specific heat, J kg^{-1}
C_D	Standard drag coefficient
CR	Convergence ratio, -
d_s	Particle size, m
e	Restitution coefficient, -
E	Modulus of elasticity, Pa
E_a	Activation energy, kJ $kmol^{-1}$
Er	Relative error, -
F	Distributed force or force, N, N m^{-1} or N m^{-2}
F_S	Safety factor, -
g	Earth's gravitational acceleration
g_0	Radial distribution function, -
G	Dimensionless solids centrifugal acceleration, -
h	Mass specific enthalpy, J kg^{-1}
$\bar{h}$	Molar specific enthalpy, J $kmol^{-1}$
H	Enthalpy or energy, W Height, m
H	Height, m
I	Turbulence intensity at inlet boundary condition
I_u	Uniformity Index
$I(x)$	Moment of inertia, m^4
J_s	Change of granular energy due momentum exchange, kg m^{-1} s^{-3}
k	Turbulence kinetic energy, m^2 s^{-2}
K_c	Fracture toughness, Pa $m^{-1/2}$
K_d	Interfacial drag coefficient, kg m^3 s^{-1}
K_e	Equilibrium constant
L	Length, m
m	Mass, kg
$\dot{m}$	Mass flow rate, kg s^{-1}
$M(x)$	Internal bending moment, N m
M_R	Reacting moment, N m
MY_{daf}	Desired mass yield as dry ash-free, -

N	Number of moles, -
N_{blades}	Number of blades, -
N_{cells}	Number of cells in the grid
p_k	Production of turbulence kinectic energy, kg m^{-1} s^{-3}
p	Order of accuracy for grid refinement study, -
P	Pressure, Pa
P_r	Prandtl number, -
$\dot{Q}$	Heat flow, W
r	Radius or radial position, m
r_{grid}	Grid refinement ratio, -
R	Reacting Force, N
Re	Reynolds number, -
S_y	Yield strength, Pa
t	Thickness, m
T	Temperature, °C or K
u	Velocity
U	Solids Velocity or Velocity, m s^{-1}
V	Volume, m^3
V	Gas Velocity, m s^{-1}
$\dot{V}$	Volumetric flow rate, m^3 s^{-1}
$V(\text{x})$	Internal shearing force, N
w	Weight, N or N m^{-1}
W	Distributed eight, N m^{-2}
$\bar{\text{x}}$	Centroid, m
x	Mass fraction, kg per kg of fuel
X	Conversion rate of the biomass into bio-oil, -
y	Mole fraction, -
y	Width between blades, m
z	Axial position, m

Greek

A	Angle between blades, °
α	Phase volumen fraction, -
β	Free length angle, °
B	External heating rate, s^{-1}
γ	Overlapping length angle, °
γ_s	Collisional energy dissipation rate, kg m^{-1} s^{-3}
δ	Error estimator of the grid refinement study, -

ΔP	Pressure drop, Pa
$\Delta(x, y, z)$	Grid spacing, m
ε	Absolute error of the grid refinement study
ϵ	Turbulence energy dissipation rate, $m^2\ s^{-3}$
η	Efficiency, %
θ	Horizontal blade inclination angle, °
Θ	Granular temperature, $m^2\ s^{-2}$
λ	Bulk viscosity, kg $m^{-1}\ s^{-1}$
κ	Solid conductivity of fluctuating energy, kg $m^{-1}\ s^{-1}$
μ	Dynamic viscosity, kg $m^{-1}\ s^{-1}$
ρ	Density, kg m^{-3}
σ	Normal stress, Pa
τ	Shearing stress, Pa
$\bar{\bar{\tau}}$	Stress-strain tensor, Pa
υ	Deflection displacement, m
φ	Half cone apex angle
φ_s	Specularity coefficient
ϕ	Blade overall angle, °
ω	Absolute humidity, kg of H_2O per kg of dry air
$d°\mathcal{V}$	Elemental volumes

Abbreviations

AF	Air-fuel ratio, -
CFD	Computational Fluid Dynamics
EA	Excess Air ratio
ER	Equivalence ratio, -
FB	Fluidized bed
GCI	Grid Convergence Index, %
GSV	Gas-Solid Vortex
HHV	Higher Heating Value, J kg^{-1} or J m^{-3}
IC	Corrosion resistance Index
KTGF	Kinetic Theory of Granular Flow
LHV	Lower Heating Value
MR	Moisture ratio
MW	Molecular Weight, kg $kmol^{-1}$
PI	Process Intensification
PISO	Pressure Implicit Split Operator
PIV	Particle Image Velocimetry
OPF	Oil Palm Frond

PRISMA	Preferred Reporting Items for Systematic Reviews and meta-Analyses
ROI	Return of Investment
SFB	Swirling Fluidized Bed
SIMPLE	Semi-Implicit Method for Pressure-Linked Equations
STL	Stereolithography
TORBED	Toroidal Bed
VOF	Volume Of Fluid

Subscripts

a	Air
act	Actual
b	Biomass
bed	Bed
col	Collisional
comb	Combustion
cw	Conical wall
da	Dry air
daf	Dry ash free
distr	Distributor
eff	Effective
ew	End wall
exp	Experimental
fr	Frictional
flow	Flow
g	Gas phase
gasif	Gasification
h	High, circumferential
i	Inner
in	Inlet
inj	Injection
kin	Kinetic
l	Low
L	Longitudinal
loss	Loss
m	Molecular
moist	Humid
mf	Minimum fluidization
mff	Minimum of full fluidization
msf	Minimum swirling fluidization

o	Outer
oil	Bio-oil
op	Opening
out	Outlet
Press	Pressure
prod	Products
pw	Piper wall
pyr	Pyrolysis
r	Hoop or radial
react	Reactive
res	Resultant
s	Solid phase
sim	Simulated
sup	Superficial
st	Stoichiometry
sw	Shell wall
t	Turbulent
torr	Torrefaction
total	Total
θ	Azimuthal
vap	Vaporization
w	Weight
wall	Wall boundary
z	Axial, longitudinal

List of Figures

Figure 2-1 Flow diagram of the systematic review process according to the Preferred Reporting Items for Systematic Reviews and meta-Analyses (PRISMA) guidelines. Source: Figure created by author. 9
Figure 2-2 Time distribution of records concerning the swirling fluidized bed reactor. (Last updated: January 2022). Source: Figure created by author. 11
Figure 2-3 Geographical distribution of the contributions per country related to the SFB reactor. The color scheme denotes the number of contributions per country. The Asia Oceania region has pursued the most extensive research about the SFB reactor. Source: Figure created by author. 11
Figure 2-4 Distribution of documents per objectives. The chart includes repeated documents, i.e., with one or more objectives. Source: Figure created by author. 13
Figure 2-5 Distribution of documents per methodology. The chart includes repeated documents, i.e., with one or more methodologies employed. Source: Figure created by author. 14
Figure 2-6 Relations of objectives and methodologies. Source: Figure created by author. 15
Figure 2-7 Distribution of documents per application. Source: Figure created by author. 16
Figure 2-8 Relations of type of reactor and applications. Source: Figure created by author. 16
Figure 2-9 Distribution of documents per (a) type of bed material, and (b) 1g-Geldart's group of fluidized particles. Source: Figure created by author. 17
Figure 2-10 Swirling fluidized bed reactor state of the art. Source: Figure created by author. 18
Figure 2-11 SFB reactor embodiment and composition. The reactor consists of (1) a gas/product outlet, (2) a cylindrical housing, (3) particulated solids inlet, (4) annular gas distributor, (5) central structure (optional solids outlet), (6) gas inlet. Source: Figure created by author. 21
Figure 2-12 Schemes of the four types of annular gas distributors in Table 2-3. The left side corresponds to the isometric view of each distributor, and right side to the top view. The includes distributors are (a) the inclined holes, (b) the gill plate, (c) the single row blades, and (d) the three row blades. Source: Figure created by author. 24
Figure 2-13 Hybrid mesh-inclined blades distributor. Source: Figure created by author. 25
Figure 2-14 SFB (a) compact and (b) expanded schemes. Source: Figure created by author. 25
Figure 2-15 Typical pressure drop across the bed vs. Superficial velocity diagram. It presents the different flow regimes of the SFB operation. Source: Figure created by author. 27
Figure 2-16 Multi-stage SFB reactor scheme. Source: Figure created by author. 39
Figure 3-1 SFB reactor composition. The reactor comprises (1) the gas/product outlet, (2) the cylindrical outer wall column, (3) the solids inlet, (4) the annular single-row blade gas distributor, (5) the central support structure, and (6) the fluidizing gas inlet. Source: Figure created by author. 50
Figure 3-2 Schematic of the SFB reactor of the simulation. Dimensions are in mm. Source: Adapted from [19]. Source: Figure created by author. 52
Figure 3-3 Computational domain composed of hexahedral mesh with a level 0 size of 0.01m. The mesh is finer near the inlet, outlet, and walls. The computational domain is enclosed by (1) the cone wall, (2) two cyclic boundaries, (3) an outlet path, (4) inlet blades walls (grey), (5) inlet openings (red), and (6) the cylindrical outer wall. Source: Figure created by author. 57

Figure 3-4 Corresponding meshes for the GCI-based grid refinement process generated using the snappyHexMesh utility. The grids are (a) the coarse, (b) the medium, and (c) the fine. Source: Figure created by author. 58
Figure 3-5 Pressure-drop across the bed vs. Normalized grid spacing results obtained from the simulations of the three meshes for the GCI-based refinement process (red dots) and the Richardson Extrapolation solution for the zero grid spacing (blue diamond). Source: Figure created by author. 62
Figure 3-6 Simulated solid volume fraction $\boldsymbol{\alpha s}$ distribution in the SFB reactor at the view from (a) the outer wall and (b) the inner cone wall. The bed height at the outer wall view is almost uniform, while there is a formation of dunes in the inner wall. Source: Figure created by author. 64
Figure 3-7 Solids volume fraction $\boldsymbol{\alpha s}$ in a quarter of the SFB reactor for the air superficial velocity 2.23 m s^{-1} and particle density 1312 kg m^{-3}. Volume fraction fields correspond to three axial positions $\boldsymbol{z}$: (a) 10%$\boldsymbol{Hbed}$ = 6.8 mm, (b) 50%$\boldsymbol{Hbed}$ = 34 mm, and (c) 90%$\boldsymbol{Hbed}$ = 61.2 mm. Dashed lines represent the middle line of the annular region for each height. Source: Figure created by author.. 65
Figure 3-8 Solids azimuthal velocities $\boldsymbol{U\theta}$ in a quarter of the SFB reactor for the air superficial velocity 2.23 m s^{-1} and particle density 1312 kg m^{-3}. Velocity fields correspond to three axial positions $\boldsymbol{z}$: (a) 10%$\boldsymbol{Hbed}$ = 6.8 mm, (b) 50%$\boldsymbol{Hbed}$ = 34 mm, and (c) 90%$\boldsymbol{Hbed}$ = 61.2 mm. Dashed lines represent the middle line of the annular region for each height. Source: Figure created by author.. 65
Figure 3-9 Solids radial velocities $\boldsymbol{Ur}$ in a quarter of the SFB reactor for the air superficial velocity 2.23 m s^{-1} and particle density 1312 kg m^{-3}. Velocity fields correspond to three axial positions $\boldsymbol{z}$: (a) 10%$\boldsymbol{Hbed}$ = 6.8 mm, (b) 50%$\boldsymbol{Hbed}$ = 34 mm, and (c) 90%$\boldsymbol{Hbed}$ = 61.2 mm. Dashed lines represent the middle line of the annular region for each height. Source: Figure created by author. 66
Figure 3-10 Air azimuthal velocities $\boldsymbol{V\theta}$ in a quarter of the SFB reactor for the air superficial velocity 2.23 m s^{-1} and particle density 1312 kg m^{-3}. Velocity fields correspond to three axial positions $\boldsymbol{z}$: (a) 10%$\boldsymbol{Hbed}$ = 6.8 mm, (b) 50%$\boldsymbol{Hbed}$ = 34 mm, and (c) 90%$\boldsymbol{Hbed}$ = 61.2 mm. Dashed lines represent the middle line of the annular region for each height. Source: Figure created by author. 67
Figure 3-11 Air radial velocities $\boldsymbol{Vr}$ in a quarter of the SFB reactor for the air superficial velocity 2.23 m s^{-1} and particle density 1312 kg m^{-3}. Velocity fields correspond to three axial positions $\boldsymbol{z}$: (a) 10%$\boldsymbol{Hbed}$ = 6.8 mm, (b) 50%$\boldsymbol{Hbed}$ = 34 mm, and (c) 90%$\boldsymbol{Hbed}$ = 61.2 mm. Dashed lines represent the middle line of the annular region for each height. Source: Figure created by author. 67
Figure 3-12 Dimensionless solids centrifugal acceleration ($\boldsymbol{G}$) in a quarter of the SFB reactor for the air superficial velocity 2.23 m s^{-1} and particle density 1312 kg m^{-3}. Centrifugal acceleration fields correspond to three axial positions $\boldsymbol{z}$: (a) 10%$\boldsymbol{Hbed}$ = 6.8 mm, (b) 50%$\boldsymbol{Hbed}$ = 34 mm, and (c) 90%$\boldsymbol{Hbed}$ = 61.2 mm. Dashed lines represent the middle line of the annular region for each height. Source: Figure created by author. 68
Figure 3-13 Solids hydrodynamics profiles on the axial-radial plane of the SFB reactor. (a) Solids volume fraction $\boldsymbol{\alpha s}$, and (b) azimuthal $\boldsymbol{U\theta}$, (c) radial $\boldsymbol{Ur}$, and (d) axial $\boldsymbol{Uz}$ solids velocity components. Source: Figure created by author. 69
Figure 3-14 Air hydrodynamics profiles on the axial-radial plane of the SFB reactor. (a) Azimuthal $\boldsymbol{V\theta}$, (b) radial $\boldsymbol{Vr}$, and (c) axial $\boldsymbol{Vz}$ solids velocity components. Source: Figure created by author. 70

Figure 4-1 SFB reactor operational schematic diagram. (a)-(d) illustrate the steps of the SFB reactor operation. The color of the elements in the diagram represents the process streams: red represents the fluidizing gas, blue the solids, and black the products. Source: Figure created by author..... 78
Figure 4-2 Schematic of gas flow passing through the openings of the distributor. $\boldsymbol{Vsup}$ is the superficial gas velocity before the distributor, and $\boldsymbol{Vinj}$ the injection gas velocity after passing the distributor. $\boldsymbol{Vinj,z}$ and $\boldsymbol{Vinj,\theta}$ are axial and azimuthal components of the injection gas velocity in the cylindrical coordinates. Source: Figure created by author. 89
Figure 4-3 Global dimensions of the (a) compact and (b) expanded SFB reactors. Source: Figure created by author. 92
Figure 4-4 Schematic of a single row blade distributor. Source: Figure created by author. 93
Figure 4-5 Geometrical specifications of the blades' arrangement. The top view of one blade (a) illustrates the main angles and lengths. The top (b) and front (c) views show the separation and overlapping dimensions in the distributor. Source: Adapted from [42]. 94
Figure 4-6 Annular single row blades distributor scheme. $\boldsymbol{Wbed}$ is the bed weight and $\boldsymbol{Fflow}$ the force acting on the blades due to gas flow. Source: Figure created by author. 95
Figure 4-7 Free body diagram of the control volume CV, comprising the gas flow passing through the opening between two adjacent blades, and the net applied force on a fixed inclined blade due to gas flow $\boldsymbol{Fblade}$. Source: Figure created by author. 96
Figure 4-8 Vector diagram for solving the linear momentum change and the net force on the blade. Source: Figure created by author. 97
Figure 4-9 (a) Acting forces on one blade due to bed weight $\boldsymbol{Wbed}$ and the effect of gas flow $\boldsymbol{Fblade}$, and (b) rotation of coordinate axis $\boldsymbol{xy'z'}$ with the conversion of bed weight to the new rectangular components $\boldsymbol{Wbed,z'}$ and $\boldsymbol{Wbed,y'}$. Source: Figure created by author. 98
Figure 4-10 3D Free body diagram of one blade comprising: bed weight $\boldsymbol{Wbed,y'}$ and $\boldsymbol{Wbed,z'}$, the effect of the gas flow on the blade $\boldsymbol{Fblade,y'}$ and $\boldsymbol{Fblade,z'}$, and the support reacting forces $\boldsymbol{R1,x}$, $\boldsymbol{R1,y'}$, $\boldsymbol{R1,z'}$, $\boldsymbol{R2,x}$, $\boldsymbol{R2,y'}$, $\boldsymbol{R2,z'}$ and reacting moments $\boldsymbol{MR1}$, $\boldsymbol{MR2}$. (a) Upper view, and (b) bottom view. Source: Figure created by author. 99
Figure 4-11 2D free body diagram of one blade. The blade is assumed as a beam supported at both ends. Source: Figure created by author. 100
Figure 4-12 Free body diagram of a section of the blade. Source: Figure created by author. 100
Figure 4-13 Elastic curve of one blade and its boundary conditions. The displacement and deflection are zero at both ends due to fixed supports. Source: Figure created by author. 102
Figure 4-14 Flat ends considered in this procedure. (a) Flanged plate, (b) and (c) welded plates, and (d) and (e) bolted cover. Adapted from [68]. 104
Figure 4-15 Domed ends considered in this procedure. (a) Hemispherical, (b) ellipsoidal, and (c) torispherical. Adapted from [68]. 104
Figure 4-16 Transition of conical-cylindrical sections. Source: Adapted from [68]..... 106
Figure 4-17 Yield strength $\boldsymbol{Sy}$ vs. maximum service temperature $\boldsymbol{Tmax}$ for metallic materials. Source: Chart extracted from CES Edupack [77]. 110
Figure 4-18 Process and Instrumentation diagram of a SFB reactor. Source: Figure created by author. 111

Figure 4-19 Experimental setup of the SFB reactor used for rice husk combustion. Figure extracted study from [39]. 114
Figure 4-20 Yield strength $\boldsymbol{Sy}$ vs. maximum service temperature $\boldsymbol{Tmax}$ after the first screening step using the constraints $\boldsymbol{Sy}$ ≥200 MPa and $\boldsymbol{Tmax}$ ≥970°C. Source: Chart extracted from CES Edupack [77]. 122
Figure 4-21 Yield before break vs Corrosion resistance index (a) with the reference levels of the indexes to optimize the objectives, and (b) the surviving materials after filtering the indexes. Source: Chart extracted from CES Edupack [77]. 123
Figure 4-22 Embodied energy for primary production vs. price per unit volume of the materials obtained after screening the constraints and the objectives of the material selection methodology. Source: Chart extracted from CES Edupack [77]. 124
Figure B-1 ISA flow nozzle chart for estimating the discharge coefficient value. Source: Extracted and adapted from [2]. 138
Figure B-2 Tokico turbine flowmeter model GS-F2011E-02 pressure drop characteristic curves extracted from [3]. The vertical red line is the actual operating point with 404.86 m3 h-1. The horizontal red line represents the pressure drop of the operating point for the Connection Size 20 (according to the manufacture is equal to a connection of 200 mm-diameter). The resultant pressure drop across the turbine flowmeter is about 6 kPa. 139
Figure B-3 Performance curves of the Gardner Denver side blower channel with frequency converter model G-BH1 2BH1 900 extracted from [6]. The operating point at the total pressure difference of 140 mbar and frequency 60 Hz. The suction capacity of the blower is around 1050 m^3 h^{-1} and the power consumption 9.1 kW at the operating point. 140
Figure B-4 Design drawing of the blade for the single row blades distributor. Source: Figure created by author. 141
Figure B-5 Design drawing of the tapered section of the pressure vessel. Source: Figure created by author. 142
Figure B-6 Design drawing of the cylindrical section of the pressure vessel. Source: Figure created by author. 143
Figure B-7 Design drawing of the head flat bolted end. Source: Figure created by author. 144
Figure B-8 Design drawing of the SFB reactor with global dimensions. Source: Figure created by author. 145

List of Tables

Table 2-1 Content-based analysis structure..... 12
Table 2-2 Current operating facilities using SFB reactors. 20
Table 2-3 Classification of the annular gas distributors for SFBs, design, and fabrication 23
Table 2-4 Description of the SFB compact and expanded bed reactors. Information based on [12], [13], [15], [78], [79] 26
Table 2-5 Matrix of correlations of the effects of design or input parameters on the operating variables. Arrows direction denotes the relationship between variables. Upward (↗) are directly related, downward (↘) inversely relateded, horizontal line (−) no significantly related, NA relationships does not apply. 29
Table 2-6 Summary of models used or developed in the reviewed documents from four main topics: design, heat transfer, hydrodynamics, and drying. The models include analytical and experimental estimations validated or not..... 32
Table 2-7 Summary of drying experiments and operating conditions 34
Table 2-8 Summary of combustion experiments and operating conditions 35
Table 2-9 Summary of potential and individual uses reported of the SFB reactor 37
Table 3-1 Constitutive equations required for solving the SFB reactor model. 54
Table 3-2 Operating conditions of phase properties and boundary and initial conditions for the numerical simulation. 55
Table 3-3 Overview of simulation settings 56
Table 3-4 Mesh characteristics for the three refinement grids. Number of cells (N_{cells}) in the mesh at level 0 grid spacings. 58
Table 3-5 Johnson-Jackson boundary condition combinations of parameters. Combinations of specularity coefficients used to determine the validated SFB reactor computational model. 60
Table 3-6 Simulation results for the three meshes to perform the GCI-based grid refinement study. Number of cells (N_{cells}) in the mesh at level 1 grid spacings, i.e., after using snappyHexMesh utility. 61
Table 3-7 Relative errors between the simulated $\boldsymbol{U\theta,sim}$ and experimental $\boldsymbol{U\theta,exp}$ [19] data of averaged solids azimuthal velocities at different specularity coefficient combinations. The selected combination is $\boldsymbol{\varphi s,p}$ = 0.125 and $\boldsymbol{\varphi s,c}$ = 0.05. 63
Table 3-8 Comparison of experimental $\boldsymbol{U\theta,exp}$ [19] and the simulated $\boldsymbol{U\theta,sim}$ average solids azimuthal velocities. 63
Table 4-1 Operating conditions of biomass treating processes considered for the design of the SFB reactor [12]. 78
Table 4-2 pre-exponential factor of the Arrhenius Equation $\boldsymbol{A}$ and the activation energy $\boldsymbol{Ea}$ for different wood biomass [63]. 87
Table 4-3 Compact and expanded SFB reactor operating constraints for selection purposes. 92
Table 4-4 Flat ends types and models to estimate the $\boldsymbol{C}$ value for each type [68]. 105
Table 4-5 Typical alloys reported as construction material for biomass processing reactors. 107

Table 4-6 Minimum wall thickness required to ensure the stiffness of the SFB reactor structure to support its own weight and incidental load [68]. 108
Table 4-7 Design requirements for selecting the material for building a SFB reactor for biomass thermochemical conversion..... 109
Table 4-8 Selected indexed to optimize the objectives of the materials required to build a SFB reactor for biomass thermochemical conversion. 109
Table 4-9 Index values of the typical contruction material for reactors in biomass processing applications reported in the literature. The data is extracted from [77]. 110
Table 4-10 Primary operating characteristics of four type of converyors for particles feeding in the SFB reactor..... 113
Table 4-11 Ultimate analysis of a sample of rice husk used in this case study. Data extracted from [39]. 114
Table 4-12 Stoichiometric constants obtained from the molar balances of each component from the stoichiometric formula. 115
Table 4-13 Results of the stoichiometric air-fuel ratio and inlet flow rate due to combustion of 80 kg h^{-1} of rice husk. 115
Table 4-14 Stoichiometric constants obtained from the molar balances of each component at actual conditions of operations of combustion of 80 kg h^{-1} of rice husk. 115
Table 4-15 Results of actual air-fuel ratio, air and hot product gas flow rates, and composition of the hot product gas due to combustion of 80 kg h^{-1} of rice husk..... 115
Table 4-16 Higher and lower heating values, and enthalpy of formation of the rice husk. 116
Table 4-17 Results of the heat of combustion, the heat of vaporization, the heat loss, the power output of the SFB reactor, the enthalpy of the products, and the enthalpy of reactive due to combustion of 80 kg h^{-1} of rice husk at 935°C. 116
Table 4-18 Results of air superficial and injection velocities for minimum fluidization, minimum swirling fluidization, and at actual conditions to achieve combustion of 80 kg h^{-1} of rice husk. ... 117
Table 4-19 Global dimension of the SFB reactor for combustion of 80 kg h^{-1} of rice husk. 117
Table 4-20 Dimensions of the single row blades distributor for combustion of 80 kg h^{-1} of rice husk. 118
Table 4-21 Results of external forces on the blade assumed as a statically indeterminate beam due to combustion of 80 kg h^{-1} of rice husk. 118
Table 4-22 Change of internal shear force and bending moment in the blade at different positions. 119
Table 4-23 Change of stress values in the blade at different positions. The allowable stress of the construction material of the blade should be at least 90 MPa. 119
Table 4-24 Stress components and thickness values of the components of the vessel subjected to internal pressure. The thickness value of 3 mm is adequate to construct all the components of the vessel. The minimum allowable yield strength of the construction material of the vessel should be at least 186 MPa. 120
Table 4-25 List of design specifications of the SFB reactor for combustion of 80 kg h^{-1} of rice husk. 121

Table 4-26 Design requirement for selecting the construction material of the SFB reactor for combustion of 80 kg h^{-1} of rice husk. 122
Table 4-27 Suggested construction materials based on the best technical performance classified according to their material group. 123
Table 4-28 Suggested construction materials with the lowest energy consumption and cost. 124
Table 4-29 Results of major pressure-drops by contributor in the SFB reactor for combustion of 80 kg h^{-1} of rice husk. 124
Table 4-30 Required specifications of the blower to drive the SFB reactor for combustion of 80 kg h^{-1} of rice husk. 124
Table 4-31 Operating point conditions of the selected blower Gardner Denver G-BH1 2BH1 900 [87] for combustion of 80 kg h^{-1} of rice husk. 125
Table B-1 Shomate equation constants for the formed compounds during biomass combustion [1]. 135
Table B-2 Minimum inner radius $\boldsymbol{ri}$ values for different combinations of $\boldsymbol{t}$ and $\boldsymbol{\theta}$ with 60 blades to avoid interference between the blades. 136
Table B-3 Template of a list of designs specifications of a SFB reactor for biomass thermochemical conversion. 137

Summary

Process intensification (PI) of biomass conversion as a route to a low-carbon manufacturing industry pursues novel solutions able to achieve safe, cost-efficient, energy-efficient, and environment-friendly processes. Implementation of PI in gas-solid operations enhances mass, heat, and momentum transfer rates, while develops multifunctional equipment to increase production capacity per size of installation. Gas-solid processes are typically performed in conventional Fluidized Beds (FB), i.e., gravitational beds, in different industrial applications for a variety of processes, such as heating, drying, separation, or reactions. In particular, the present work encompasses the Swirling Fluidized Bed (SFB) reactor, which is a gas-solid contacting device that replaces the Earth's gravitational field with a centrifugal field generating a centrifugal bed that achieves more uniform beds, higher transfer rates, and shorter processing times than conventional FBs. The study of the SFB reactor comprises three stages: a systematic literature review, a numerical simulation of the reactor, and the development of the design procedure.

The literature review provides an in-depth description of the SFB reactor showing the advancements of studies about the operation of the device in different applications. The SFB reactor is capable of fluidize a wide range of particle sizes and densities due to the use of a centrifugal field. This has increased the research interest on the device for biomass processing from experimental and theoretical approach, which include analysis of the hydrodynamics and thermal behaviors of the SFB. However, the review denotes a gap of research in two points: binary-phase numerical simulation to study both gas and solid hydrodynamics, and the constructive design of the SFB reactor related to expected operating conditions.

Therefore, a cold-flow gas-solid simulation is carried out in the open-source Computational Fluid Dynamics (CFD) software OpenFOAM®. A comparison between the simulated and experimental data obtains differences lower than 5% validating the computational model. The CFD results shows that both the dissipation of axial kinetic energy and the change of direction of the gas radial velocity when moving upwardly promotes the swirling motion of the bed. The simulation gives insight of the SFB reactor operation useful for the decision making during early stages of design. Then, the design procedure of the SFB reactor is developed including four biomass conversion routes: combustion, gasification, pyrolysis, and torrefaction. Thermochemical and mechanical design models together with technical procedures are used for dimensioning and selecting components and materials of the SFB reactor. A case study of design compares the design procedure results with an operational SFB reactor used for experiments about rice husk combustion. The proposed design of the SFB reactor for combustion shows good agreement with the operational reactor.

Future works should include CFD-based simulations for conducting parametric studies that identify possible optimum operating conditions of the SFB reactor which would improve the selection of factors and levels for experiments before manufacturing and acquiring equipment. This would lead to the development of additional semi-experimental models that could be useful for the design procedure. The analysis of heat transfer across the SFB reactor walls would lead to the design of a

thermal insulation system. The improvement of the design procedure to obtain a complete setup for biomass processing should include the design of other subsystems, such as the solids feeder, the separators, and supplementary heating systems.

Glossary

Annular gas distributor	Device that reduces the area of gas flow using a set of inclined openings, slots or orifices that increase gas flow velocity and change its direction; and includes a central body at the top to form a doughnut-shaped region.
Computational fluid dynamics	Branch of fluid mechanics that solves and analyzes fluid flow problems using numerical methods and algorithms.
Flow regime	Recognizable pattern of the motion of a substance. In a fluidized bed, it depends on the gas-solid slip velocity.
Gas axial velocity	Gas velocity in the axial direction z, denoted as V_z
Gas azimuthal velocity	Gas velocity in the azimuthal direction θ, denoted as V_θ
Gas radial velocity	Gas velocity in the radial direction r, denoted as V_r
List of design requirements	Consolidated of functions, constraints, and characteristics that a product must or should fulfill after finishing its fabrication.
Minimum fluidization velocity	Velocity that counteracts solids weight to start the solids motion in a fluidized bed.
Paris conference of parties	Agreement within the United Nations Framework Convention on Climate Change, dealing with reduction, adaptation, and finance of greenhouse-gas-emissions.
Preferred reporting items for systematic reviews and meta-analyses guidelines	Guided process to create a comprehensive review that consists of searching literature, screening records, and applying eligibility criteria that results in an improved quality of the selected articles.
Process intensification	Development of novel solutions to improve industrial processes increasing production capacity while reducing plant size, energy consumption, or waste production
Reynolds-averaged Navier-Stokes	Set of equations of motion of fluid flow resulting from Reynolds decomposition and time averaged solutions to the Navier-Stokes equations.
Solids axial velocity	Solids velocity in the axial direction z, denoted as U_z
Solids azimuthal velocity	Solids velocity in the azimuthal direction θ, denoted as U_θ
Solids centrifugal acceleration	Radially outward acceleration acting upon the solids, defined as $a_c = \frac{U_\theta^2}{r}$

Solids radial velocity	Solids velocity in the radial direction r, denoted as U_r
Swirling flow	Flow with a predominant azimuthal velocity component.
Terminal velocity	Constant velocity of a particle falling in a stationary fluid at the equilibrium condition.

1. Introduction and Outline

1.1. Introduction

Reliable and affordable energy access is crucial for developing human society with a continuous economic growth. However, the maintenance and improvement of living standards for a growing population could scarce the available natural resources [1], [2], aggravating the climate change risks and its effects. By 2040, the economic growth involves a potential raise of global energy demand in 20% compared to 2017, with an increase of CO_2 emissions about 5% above the level of 2017 [1]. The latter value lies within the range proposed in the Paris Conference of Parties agreement due to the implementation of cleaner energy sources, increasing electrification, and reducing of fossil fuels shares to the energy mix [1], [3]. Also, the transformation of the energy market to low-carbon energy sources will decline the hydrocarbons share to global primary energy to 20-60% in 2050, instead of 80% in 2019. Therefore, the transition to a more sustainable energy system requires the integration of alternative energy sources and cost-effective technologies [3].

Process Intensification (PI) offers strategies to develop alternative technologies for contributing to the transition to a more sustainable energy market, e.g., remote installation and lower costs compared to conventional solutions [4]. In this context, PI purpose is to improve the chemical production developing novel methods and equipment. PI aims to the design of processes with lower orders of magnitudes in size while increasing production capacity, decreasing energy consumption, and reducing waste generation [5], [6]. Implementation of PI strategies enhances mixing, heat, and mass transport rates, and improves process control in solids handling applications, e.g., precipitation, drying, and thermal treatments. The higher heat and mass transfer rates provides benefits in biological processing, such as biomass, considering the inherent low reaction rates of this type of material [6]. In other words, the use of PI to develop technology for chemicals processing, but not limited to this, results in more energy efficient, smaller, cleaner and safer operation [7]. Prevention of particles agglomeration and fouling is important when designing equipment for solids handling using PI approach [6].

In Colombia, both solids agricultural biomass and plastic residues are significant. In 2020, around 97% of the 32500 tons per day of municipal solid wastes were disposed in landfill sites. At the end of 2020, the useful life of about 15% of the 281 final disposal sites expired or would expire within 0 to 3 years [8]. A previous study showed that the energy potential of the total available biomass in Colombia could cover 39-45% of the primary energy consumption in 2017, which agricultural residues contribute with 53% of the total energy potential [9]. Subsequent study indicated that the biomass share in the energy mix can increase up to 15–28% for heat and electricity production using combined heat and power systems, including 27–53% of the electricity produced in 2018 [10]. Modern bioenergy is gaining interest in the power sector because it provides low-carbon alternatives to fossil fuels, e.g., biofuels and solid biomass [3]. Some industries (e.g., cement, energy, and

chemical precursors) have studied the possibility of biomass and residues conversion to value-added products [11]–[13]. Application of policies about the progressive land use for bioenergy crops in Colombia could result in a cumulative energy potential of up to 610 TWh by 2050 [14]. This opens the possibility for developing technologies to use biomass and its by-products as raw materials for further chemical processes and alternatives energy sources in Colombia.

In biomass conversion processes, gas-solid operation handles biomass in form of solid particles. Gas-solid processes typically occur in conventional fluidized beds, i.e., gravitational beds, where a particulate material interacts with a gas flow. The operation presents relatively high heat and mass transfer rates and order-of-second residence times. The interaction between the particulate solid and the gas flow produces a drag force that counteracts the particle's effective weight, which generates the fluidization of the bed. The operation in conventional fluidized beds has inherent limitations. First, Earth’s gravitational field limits the gas-solid slip velocity to the terminal velocity of the particles. The width-to-height ratio of the bed of particles must be small enough to mitigate the formation of large-scale non-uniformities, e.g., channeling and slugging, which hinder interfacial heat and mass exchange. Large and dense particles, i.e., 1g-Geldart’s group D, are prone to spouting instead of fluidizing. On the other hand, light cohesive particles, i.e., 1g-Geldart’s groups A and C, are challenging to fluidize because of the inter-particle forces that surpass the drag and gravitational forces [6], [15]–[17].

Using a centrifugal field to replace the gravitational field achieves denser beds and higher gas-solid slip velocities. Processing biomass in a centrifugal field reduces equipment size to production yield ratio and increases the range of particles sizes and shapes, enhancing the heat and mass transfer rates. The centrifugal fluidized beds largely suppress the non-uniformities of the conventional fluidized beds. Also, the range of particle sizes and shapes is wider in a centrifugal bed, including fine and cohesive materials as well as coarse and spouting ones. Summing up, gas-solid contact in centrifugal beds enables PI in the thermochemical transformation of biomass [6], [17].

Generation of a centrifugal field requires the change of direction of the gas flow which occurs after passing through the inclined slots of the distributor, or a second gas injection in the direction of rotation. The Swirling Fluidized Bed (SFB) reactor uses an annular distributor with an inclined blades arrangement to induce the centrifugal field and the angular momentum change of the bed of particles to fluidize. This reactor requires smaller space per production yield compared to the conventional fluidized bed reactor. The SFB have been largely used in different industries for drying, separation, thermochemical conversion, or the integration of all these processes, treating materials within a wide range of particle sizes, densities, and shapes. These features place the SFB reactor in the field of spatial and functional PI [6], [18].

Several studies about the SFB reactor carried out the analysis of hydrodynamics, e.g., [18], [19], and thermal [20], [21] bed behaviors. Hydrodynamics studies developed experiments to analyze operation of the reactor, e.g., [22], derived hemi-empirical models to describe relationships between variables [23], and performed Computational Fluid Dynamics (CFD) simulations to gain insights in the operation of the SFB reactor [24]. Thermal studies in the SFB reactor have focused on experiments

to analyze the temperature profiles of the bed [25], and the heat transfer coefficient [26]. There are no studies about the process and mechanical design consideration of the SFB reactor, as it is the case for biomass thermochemical conversion routes in this MSc thesis.

1.2. Objectives

1.2.1. General objective

Develop a design procedure of Swirling Fluidized Bed reactors for thermochemical conversion of biomass to energy, fuels, chemical precursors, and high-value molecules.

1.2.2. Specific objectives

- Conduct a technology roadmap of SFB reactors based on scientific literature, patents, and secondary information sources to identify the parameters, mathematical models, and technical procedures for the design of the device.
- Execute a CFD-based simulation in a gas-solid SFB reactor validated with experimental data from the literature to evaluate its potential for the design of the equipment.
- Construct the design procedure of a SFB reactor demonstration unit for thermochemical conversion of biomass.

1.3. Outline

The objective of this MSc thesis is to develop a design procedure of SFB reactors for thermochemical conversion of biomass. The literature review, cold flow CFD testing, and a design case study are presented and discussed. The PI potential of the SFB reactor for biomass processing in gas-solid operations is demonstrated in various industries and experimentation but the works do not include the constructive design of the reactor. SFB reactor design for biomass conversion including thermochemical and mechanical analysis is carried out for the first time, which opens perspectives for further studies about the reactor performance. The thesis comprises manuscripts to submit for publication in journals in the near future. Every chapter includes an introduction to describe the pertinent context.

Chapter 2 conducts a systematic literature review about the development of the SFB reactor including actual and potential applications. The Preference Reporting Items for Systematic Reviews and Meta-Analysis (PRISMA) methodology guides the systematic literature review. The eligibility of the records follows a screening step process to filter the scientific and technical literature. The review uses a content-based analysis to classify the selected records about the use of the SFB reactor by objectives and methodologies studied, applications addressed, and type of particles fluidized. The current research areas and future trends related to the development of the SFB reactor technology are identified with the gathered information. Although there are some reviews using the concept of the SFB technology, the focus of their research is not exclusively about the SFB reactor. The systematic literature review fills a research gap of a document gathering the studies and development to date, and potential research areas and applications related to the SFB reactor.

Chapter 3 presents a gas-solid cold flow CFD-based model of the SFB reactor to gain insights into the flow properties. The open-source CFD-software OpenFOAM® is the selected tool to solve the gas-solid model in the SFB reactor from the Euler-Euler approach. The two-phase fluid flow

simulation assumes that the two phases are insoluble, i.e., follows the volume of fluid method. Comparison between the simulated and experimental data validates the computational model. CFD simulation gives the flow patterns used to analyze solids distribution in the bed and flow regimes, azimuthal and radial velocities fields of both solids and gas phases, and solids centrifugal acceleration. The results are promising for further development of CFD-based model simulations of gas-solid SFB reactor, e.g., heat transfer analysis.

Chapter 4 establishes the design procedure of the SFB reactor for thermochemical conversion of biomass comprising chemical, thermodynamics, and mechanical models. Operating conditions and assumptions support the employed models. Four biomass thermochemical conversion routes are considered in the procedure: combustion, gasification, pyrolysis, and torrefaction. Then, the analysis of the flow passing through the distributor gives the minimum fluidization velocity and constraints for dimensioning the SFB reactor. The minimum allowable yield strength is obtained from a loads and stress analysis on the main components, i.e., the distributor and the pressure vessel. The Ashby's approach guides the selection of the construction materials of the SFB reactor. An analysis of the major pressure-drop across the SFB reactor gives the input data to select a gas flow driving system depending on the selected biomass treating process. The solution of a case study shows the potential of the design procedure for appropriate process and equipment dimensioning.

Finally, Chapter 5 presents the general conclusions and perspectives for future research.

1.4. References

[1] Exxon Mobil, "2019 Outlook for Energy: A Perspective to 2040", 2019. [Online]. Available: https://corporate.exxonmobil.com/-/media/Global/Files/outlook-for-energy/2019-Outlook-for-Energy_v4.pdf

[2] F. J. Lozano *et al.*, "New perspectives for green and sustainable chemistry and engineering: Approaches from sustainable resource and energy use, management, and transformation", *J. Clean. Prod.*, vol. 172, pp. 227–232, 2018, doi: https://doi.org/10.1016/j.jclepro.2017.10.145.

[3] BP, "BP Energy Outlook 2022 edition", 2022.

[4] D. Fernandez Rivas *et al.*, "Process intensification education contributes to sustainable development goals. Part 2", *Educ. Chem. Eng.*, vol. 32, pp. 15–24, 2020, doi: https://doi.org/10.1016/j.ece.2020.05.001.

[5] A. I. Stankiewicz and J. A. Moulijn, "Process intensification: transforming chemical engineering", *Chem. Eng. Prog.*, vol. 96, no. 1, pp. 22–34, 2000.

[6] H. Wang *et al.*, "A review of process intensification applied to solids handling", *Chem. Eng. Process. Process Intensif.*, vol. 118, pp. 78–107, 2017, doi: https://doi.org/10.1016/j.cep.2017.04.007.

[7] R. Law, C. Ramshaw, and D. Reay, "Process intensification – Overcoming impediments to heat and mass transfer enhancement when solids are present, via the IbD project", *Therm. Sci. Eng. Prog.*, vol. 1, pp. 53–58, 2017, doi: https://doi.org/10.1016/j.tsep.2017.02.004.

[8] Superintendencia de Servicio Públicos Domiciliarios, "Informe de Disposición Final de Residuos Sólidos -2020", 2021. [Online]. Available: https://www.superservicios.gov.co/sites/default/archivos/Publicaciones/Publicaciones/2021/Jun/informe_df_2019_final_22-12-2020.pdf

[9] M. A. Gonzalez-Salazar *et al.*, "Methodology for estimating biomass energy potential and its application to Colombia", *Appl. Energy*, vol. 136, pp. 781–796, 2014, doi: https://doi.org/10.1016/j.apenergy.2014.07.004.

[10] A. Sagastume Gutiérrez, J. J. Cabello Eras, L. Hens, and C. Vandecasteele, "The energy potential of agriculture, agroindustrial, livestock, and slaughterhouse biomass wastes through direct combustion and anaerobic digestion. The case of Colombia", *J. Clean. Prod.*, vol. 269, p. 122317, 2020, doi: https://doi.org/10.1016/j.jclepro.2020.122317.
[11] M. Nehdi, J. Duquette, and A. El Damatty, "Performance of rice husk ash produced using a new technology as a mineral admixture in concrete", *Cem. Concr. Res.*, vol. 33, no. 8, pp. 1203–1210, 2003, doi: https://doi.org/10.1016/S0008-8846(03)00038-3.
[12] F. Janssen and A. Konings, "Method and installation for recovering energy from biomass and waste". Google Patents, Jan. 24, 2002.
[13] P. C. Albert Bergman, "Method and device for treating biomass", US20130298457A1, 2013
[14] A. Younis, Y. Trujillo, R. Benders, and A. Faaij, "Regionalized cost supply potential of bioenergy crops and residues in Colombia: A hybrid statistical balance and land suitability allocation scenario analysis", *Biomass and Bioenergy*, vol. 150, p. 106096, 2021, doi: https://doi.org/10.1016/j.biombioe.2021.106096.
[15] F. Scala, *Fluidized Bed Technologies for near-Zero Emission Combustion and Gasification*. Cambridge, UNITED KINGDOM: Elsevier Science & Technology, 2013. [Online]. Available: http://ebookcentral.proquest.com/lib/unorte-ebooks/detail.action?docID=1581395
[16] L. Theodore and D. C. Cortinhas, *Chemical Reactor Analysis and Applications for the Practicing Engineer*. New York, UNITED STATES: John Wiley & Sons, Incorporated, 2012. [Online]. Available: http://ebookcentral.proquest.com/lib/unorte-ebooks/detail.action?docID=818494
[17] V. V Kumar, V. R. Raghavan, V. Vinod Kumar, and V. R. Raghavan, "Developments in fluidized bed technology — A review", in *2011 National Postgraduate Conference*, 2011, pp. 1–10. doi: 10.1109/NatPC.2011.6136395.
[18] B. Sreenivasan and V. R. Raghavan, "Hydrodynamics of a swirling fluidised bed", *Chem. Eng. Process. Process Intensif.*, vol. 41, no. 2, pp. 99–106, 2002, doi: https://doi.org/10.1016/S0255-2701(00)00155-0.
[19] C. S. Miin, S. A. Sulaiman, V. R. Raghavan, M. R. Heikal, and M. Y. Naz, "Hydrodynamics of multi-sized particles in stable regime of a swirling bed", *Korean J. Chem. Eng.*, vol. 32, no. 11, pp. 2361–2367, 2015, doi: 10.1007/s11814-015-0151-6.
[20] M. H. M. Tawfik, M. Refaat Diab, and H. Mohmed Abdelmotalib, "An experimental investigation of wall-bed heat transfer and flow characteristics in a swirling fluidized bed reactor", *Appl. Therm. Eng.*, vol. 155, no. April, pp. 501–507, 2019, doi: 10.1016/j.applthermaleng.2019.04.022.
[21] M. F. Mohideen, B. Sreenivasan, S. A. Sulaiman, and V. R. Raghavan, "Heat transfer in a swirling fluidized bed with geldart type-D particles", *Korean J. Chem. Eng.*, vol. 29, no. 7, pp. 862–867, 2012, doi: 10.1007/s11814-011-0255-6.
[22] M. Y. Naz, S. A. Sulaiman, and M. A. Bou-Rabee, "Particle tracking velocimetry investigations on density dependent velocity vector profiles of a swirling fluidized bed", *Dry. Technol.*, vol. 35, no. 2, pp. 193–202, Jan. 2017, doi: 10.1080/07373937.2016.1166124.
[23] R. Kaewklum, V. I. Kuprianov, and P. L. Douglas, "Hydrodynamics of air-sand flow in a conical swirling fluidized bed: A comparative study between tangential and axial air entries", *Energy Convers. Manag.*, vol. 50, no. 12, pp. 2999–3006, 2009, doi: 10.1016/j.enconman.2009.07.019.
[24] K. Sirisomboon and P. Arromdee, "A computational fluid dynamics study of gas–solid distribution of Geldart Group B particles in a swirling fluidized bed", *Powder Technol.*, vol. 393, pp. 734–750, 2021, doi: 10.1016/j.powtec.2021.08.020.
[25] V. I. Kuprianov, R. Kaewklum, and S. Chakritthakul, "Effects of operating conditions and fuel properties on emission performance and combustion efficiency of a swirling fluidized-bed combustor fired with a biomass fuel", *Energy*, vol. 36, no. 4, pp. 2038–2048, 2011, doi: 10.1016/j.energy.2010.05.026.

[26] K. Sirisomboon and P. Laowthong, "Experimental investigation and prediction of heat transfer in a swirling fluidized-bed combustor", *Appl. Therm. Eng.*, vol. 147, no. August 2018, pp. 718–727, 2019, doi: https://doi.org/10.1016/j.applthermaleng.2018.10.097.

2. The Past, Present, and Potential for Swirling Bed Technology in Gas-Solid Fluidization

Abstract

The Swirling Fluidized Bed (SFB) reactor is a centrifugal gas-solid contactor with proven capabilities to process particles with wide distribution under enhanced heat and mass transfer rates. Many studies relate to the operation and feasibility of SFB devices, but none offer a comprehensive overview of their development. This systematic review provides an in-depth description of the SFB reactor, its operation variables, design parameters, current and potential applications, and new designs and modifications. Here we assess 96 records from literature published between 1995 and 2021. The study classifies and evaluates the records according to their objectives, methodologies, type of reactor, and applications. The analysis led to identifying research avenues and knowledge gaps for further studies. Future research about the SFB reactor should concentrate on more accurate Computational Fluid Dynamic models, including heat and mass transfer, dedicated experiments for model validation, distributor design procedures, and scale-up.

2.1. Introduction

Humanity faces a dual challenge of dealing with climate change and its effect, while supporting economic growth. In the Paris Agreement of 2015, the governments agreed to maintain the global average temperature below 15.6 °C, i.e., 2 °C above pre-industrial levels, and to conduct efforts to restrict to 1.5 °C the temperature increase [1]. This objective entails the implementation of cost-effective and environment-friendly technologies supported by government policies and consumption habits. The industrial challenge is supplying goods and services to a growing population while pursuing the reduction of environmental impact, including risks of climate change and the potential scarcity of vital natural resources [2]. In this context, process intensification (PI) aims to improve chemical processes and equipment, leading to cheaper, safer, and sustainable technologies. PI could enable lower orders of magnitude in size, enhance mixing, heat, and mass transport rates, improve process control, decrease energy requirements, and reduce waste streams. Solids handling applications have used PI to improve its performance for precipitation, drying, and thermal treatments in gas-solid operations [3]–[5].

Gas-solid processes typically occur in conventional fluidized beds, i.e., gravitational beds, where a particulate material interacts with a gas flow. The operation presents relatively high heat and mass transfer rates and order-of-second residence times. The interaction between the particulate solid and the gas flow produces a drag force that counteracts the particle's effective weight, which generates the fluidization of the bed. The operation in conventional fluidized beds has inherent limitations. First, Earth’s gravitational field limits the gas-solid slip velocity to the terminal velocity of the particles. The width-to-height ratio of the bed of particles must be small enough to mitigate the formation of large-scale non-uniformities, e.g., channeling and slugging, which hinder interfacial heat and mass exchange. Large and dense particles, i.e., 1g-Geldart’s group D, are prone to spouting instead of fluidizing. On the other hand, light cohesive particles, i.e., 1g-Geldart’s groups A and C, are challenging to fluidize because of the inter-particle forces that surpass the drag and gravitational forces [4], [6]–[8].

Centrifugal accelerations exceeding multiple times Earth’s gravity induce a centrifugal field which replace the gravitational field. The centrifugal field results in a denser bed of particles and higher gas-solid slip velocities, enhancing the heat and mass transfer rates. The centrifugal fluidized beds largely suppress the non-uniformities of the conventional fluidized beds. Also, the range of particle sizes and shapes is wider in a centrifugal bed, including fine and cohesive materials as well as coarse and spouting ones. Gas-solid operation in centrifugal beds represents an attractive PI path to achieve more compact, sustainable, safer, and energy-efficient processes [4], [8].

The Swirling Fluidized Bed (SFB) reactor is a novel gas-solid contacting device for processing particulate material in an annular or toroidal-shaped centrifugal fluidized bed. The device is gaining interest for processing particles in different industries, e.g., mineral processing, food, and energy [9], [10]. The swirling fluidized bed concept introduced different designs with similar bed behaviors. Dodson from Torftech Ltd obtained the first patent of a SFB-type in 1984 [11] and named it the TORoidal BED reactor or TORBED. Later, this type of SFB reactor was classified into two designs depending on the process needs: compact SFB and expanded SFB [12]. The main differences between these SFBs are the particles to fluidize and the reactor geometry. The compact SFB reactor operates with a shallow bed capable of fluidizing coarse

particles (e.g. 1g-Geldart's group D and B) [13], [14]. On the other hand, the expanded SFB reactor fluidizes smaller particle sizes (1g-Geldart's groups A and C) in a diffused bed of particles [14], [15].

The research about the SFB reactor has delivered methodologies for understanding and improving its operation. The most common topics studied about the SFB reactor are hydrodynamics, e.g., [16], [17]; and thermal [18], [19] bed behaviors. Other studies aim to analyze the SFB performance under varying operating conditions in different applications such as combustion [20], [21], and drying [22], [23]. Some studies evaluate the feasibility of the SFB reactor in uncommon reported applications, e.g., carbon capture [24] and flash roasting of sulfide concentrates [25]. The patent development has advanced with innovative methods and devices from the same assignee as the original patent [26], [27], and other assignees [28]–[30]. To date, some reviews briefly mention the SFB reactor for applications such as torrefaction [31], [32], gasification [33], [34], and other biomass conversion techniques [35], [36]; or comparing fluidized bed technologies [8].

Selecting suitable records follows the Preferred Reporting Items for Systematic Reviews and meta-Analyses (PRISMA) guidelines [37]. The bibliometric analysis comprises the annual distribution of the published records and the geographical distribution of articles. The content-based analysis focuses on the selected articles by assessing their objective and methodology, SFB reactor type, and applications. Finally, this paper offers an outlook of the SFB reactor research trends for future works.

2.2. Methods

2.2.1. Systematic literature review

We conducted the literature review following the PRISMA guidelines [37]. Figure 2-1 shows the PRISMA guidelines, which comprise a four-step process to ensure the quality of the results.

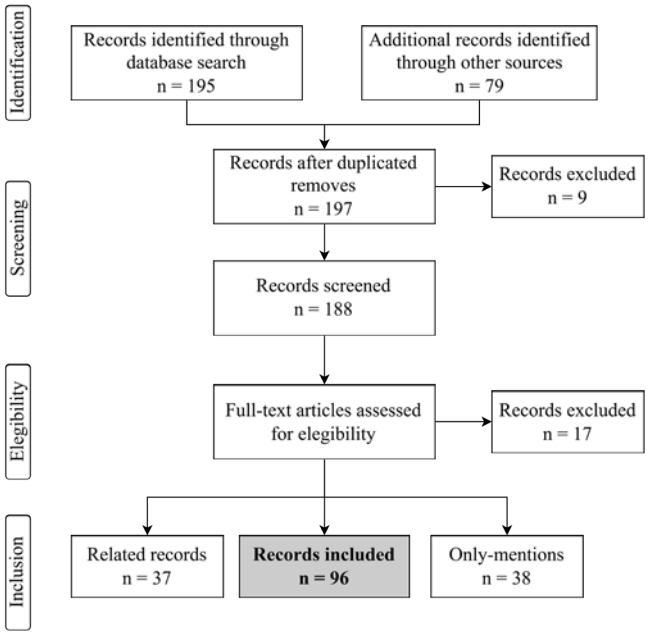

Figure 2-1 Flow diagram of the systematic review process according to the Preferred Reporting Items for Systematic Reviews and meta-Analyses (PRISMA) guidelines. Source: Figure created by author.

2.2.1.1. Identification

The keywords used to identify relevant studies were: toroidal bed reactor; SFB; swirling fluidized bed; annular blade distributor; and twin cyclonic fluidized bed. The literature search yielded 81 publications from Web of Science and 114 from Scopus. Additionally, publications from other sources added 79 documents, including thesis, conference papers, and case studies.

2.2.1.2. Screening

A total of 197 articles remained after removing duplicates. The screening step excluded nine records after assessing the article title and abstract.

2.2.1.3. Eligibility and inclusion

Records eligible for inclusion met at least one of the following criteria: (i.) assess SFB operating concept; (ii.) characterize the hydrodynamic or heat and mass transfer; (iii.) evaluate the feasibility of existing and potential applications; and (iv.) propose innovative designs and methodologies. In addition, some publications were classified as 'related records' and 'only-mention records'. 'Related records' report similar technologies, but they did not fulfill the characteristics of a SFB reactor. 'Only-mention' records mention the SFB technology, but they did not study the reactor operation or concept. Appendix A.1 and A.2 complement the literature review with the consolidated of articles in the 'related records' and 'only-mention records'.

2.2.2. Descriptive characteristics of the sample

In 1984, Dodson from Torftech Ltd [11] received a patent for a SFB-type reactor called the TORBED reactor. The license of the patent could limit early studies, leaving six related publications from 1995 to 2000. Figure 2-2 exhibits the annual distribution of the selected publications from 2001 to date. Though the original patent license expired in 2002, the increase in publications per year started only after 2008. The expiration of the original patents [38], [39] and some pioneering studies [16], [40] could encourage further research. Another patent for a variant of the SFB reactor expired in 2018 [41]. Twelve documents from the selected works are not in Figure 2-2 because they do not report the publication date. These documents correspond to case studies and manufacturer catalogs. Figure 2-2 shows an annual growth of records in the last 20 years, accompanied by two research peaks, suggesting a constant development and deployment of the SFB technology. Consequently, this review is relevant to understanding the current state of the art, the barriers, and future research topics.

Figure 2-3 shows the distribution of selected articles per country. Some Asian countries and Australia have most of the contributions. Though the original invention is from England, Europe and the Americas report fewer publications. The countries with the higher number of contributions are Malaysia (37), Thailand (14), Pakistan (8), and the United Kingdom (7). The 15 countries studying the SFB reactor are part of the Paris Agreement [1].

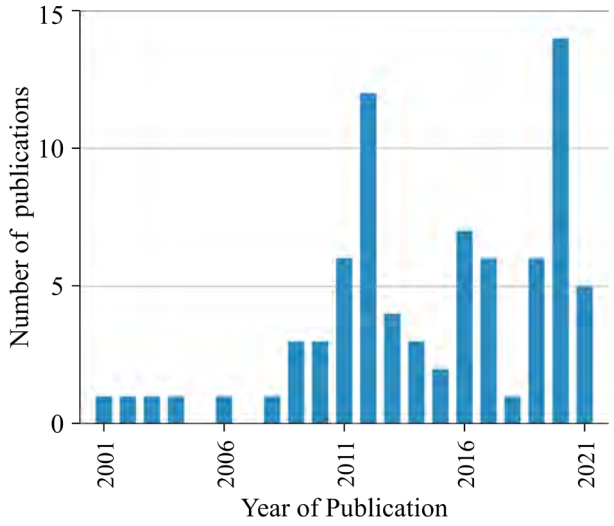

Figure 2-2 Time distribution of records concerning the swirling fluidized bed reactor. (Last updated: January 2022). Source: Figure created by author.

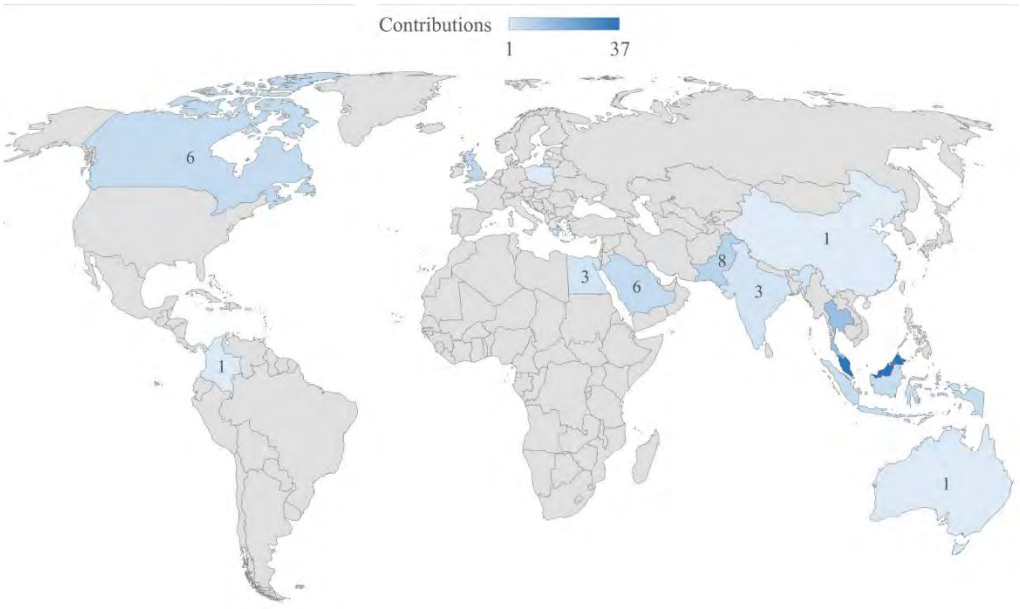

Figure 2-3 Geographical distribution of the contributions per country related to the SFB reactor. The color scheme denotes the number of contributions per country. The Asia Oceania region has pursued the most extensive research about the SFB reactor. Source: Figure created by author.

2.2.3. Content-based analysis

The content-based analysis consists of a set of investigated aspects and their respective categories. The investigated aspects studied in this work are objectives, methodologies, reactor types, and applications. Categories are different items within each investigated aspect. Table 2-1 summarizes the investigated aspects and categories covered in this study. Appendix A.3 is a database with a coding process, which relates the classification of the selected records based on the Content-bases analysis structure.

Table 2-1 Content-based analysis structure.

Investigated aspect	Relevance to SFB reactor literature	Categories	Category definition
Objective	what previous literature has done	Propose novelty solutions	Propose or develop designs, methodologies, indicators, or models (e.g. development of new gas distributor designs).
		Analyze relationships and determinants	Analyze stated relationships, hypotheses, or determinants between operating and design variables.
		Explore feasibility of applications	Explore the technical feasibility of the SFB use in known or new applications (e.g. treating flue gases in carbon capture).
Methodology	how the objective has been achieved and how the methodologies have been applied	Analytical model	Develop an analytical model for estimating variables or properties.
		Simulation	Develop a computational simulation to evaluate variables and gain insights.
		Experiment	Conduct experiments with laboratory or industrial equipment
		Commercial	Describe one or multiple applications or configurations of the SFB reactor from a technical-commercial perspective.
		Measure and case study	Collect data from one or several existing devices or takes measures using a case study.
Application	how the SFB reactor has been used and what the results have shown	Drying	Address the use of the SFB reactor in a drying process.
		Combustion	Address the use of the SFB reactor in a combustion process.
		Gasification/Pyrolysis	Address the use of the SFB reactor in a gasification or pyrolysis process.
		Mineral processing	Address the use of the SFB reactor in mineral processing, e.g., ore roasting, calcination, and vermiculite exfoliation.
		Only experimental purposes	Address the use of the SFB reactor only for experimental purposes, i.e., characterization of the reactor during cold- or hot-state without any specific process.
		Other uses	Address the use of the SFB reactor in potential uses with a smaller number of studies.
		Various processes	Mention the SFB reactor employed in multiple applications.
1g-Geldart's group of particles	what type of particle has been fluidized in the SFB based on the 1g-Geldart's classification	A	Study the SFB reactor using particles from the 1g-Geldart's A group.
		B	Study the SFB reactor using particles from the 1g-Geldart's B group.
		C	Study the SFB reactor using particles from the 1g-Geldart's C group.
		D	Study the SFB reactor using particles from the 1g-Geldart's D group.
		None	Study the operation of the SFB reactor using the fluidizing gas only.
		Not specified	Mention the use of solids without enough information to identify the 1g-Geldart's group

2.3. Results & discussion

In this section, the classification of the articles is presented according to the content-based analysis structure.

2.3.1. A systematic review of the literature

Figure 2-4 shows that most publications analyze the relationship between variables (62%), followed by the proposals of new designs, methodologies, or indicators related to the SFB reactor (38%). Articles exploring the feasibility of applications represent 33% of the selected works. The results indicate a high interest in an improved understanding of the SFB reactor operation under different conditions. The interest in developing innovative solutions and exploring the feasibility of potential and new applications of the SFB reactor are almost equal. Only 28 out of 96 works focused on more than one objective; 20 of these combined the proposal of novelty solutions and the relationship between variables.

Figure 2-5 shows that experimental studies (65%) prevail over the mathematical modeling, simulation, and qualitative methodology. The second methodology reported is the analytical model approach, representing 30% of the selected works. The least used method is the measure and case study, with 8% of the selected works including the data of operating devices. Simulation methods (14%) consist of CFD simulations to obtain solutions for the SFB reactor design and operation. Records that use more than one methodology sum up to 27 documents. Validation or development of an analytical model based on experiments is the most common combination of methodologies with 20 records.

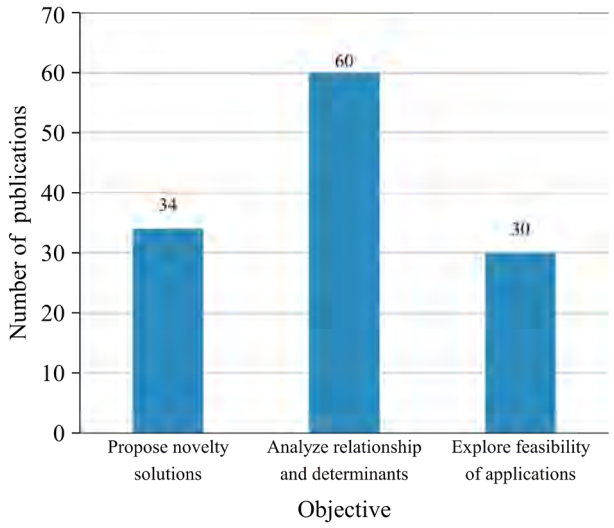

Figure 2-4 Distribution of documents per objectives. The chart includes repeated documents, i.e., with one or more objectives. Source: Figure created by author.

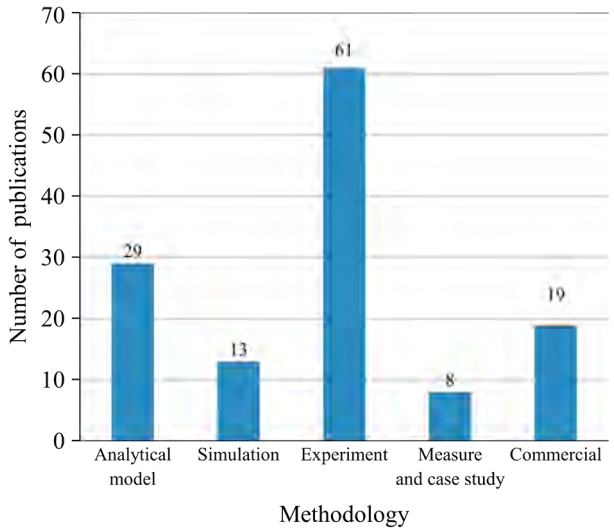

Figure 2-5 Distribution of documents per methodology. The chart includes repeated documents, i.e., with one or more methodologies employed. Source: Figure created by author.

Figure 2-6 illustrates the relationship between the objective and the employed methodology for the 96 selected works. The predominant one was selected for this analysis if a publication aims at two or more objectives or follows more than one methodology. As the main result, 50% of the publications analyze relationships between variables. Most of these works concern an experiment, followed by simulation and analytical models. Around 24% of the documents focus on exploring the feasibility of applications, where most implement promotional approaches, the second-place experimentation, measure and case study, and simulation. Finally, the selected works proposing novelty solutions represent 26%. Most works adopt the experiment or promotional methodologies to pursue this objective; a smaller amount adopts the simulation or analytical model approach. Figure 2-6 confirms some expected linkages, such as the prevailing use of experiments to analyze the relationship between variables. On the other hand, there are some overlooked or unexplored matches. A few works use the analytical model methodology. Some develop hydrodynamic models such as angular momentum change, pressure drops, and particles velocity; and thermal, e.g., Nusselt number and heat convection coefficient.

Figure 2-7 shows the practical application of the SFB reactor in the selected works. 45% of the works reported that the SFB reactor was used only for experimental purposes, such as hydrodynamics and interfacial heat and mass transfer studies. The greatest number of experimental studies suggests that the SFB reactor is currently under development for a more in-depth understanding of its functioning and scale-up. Regular uses correspond to the most reported applications of the SFB reactor in the selected works and comprise drying, torrefaction, pyrolysis, gasification, combustion, and mineral processing. The reviewed documents concerning combustion processes (21%) for generating energy showed that the SFB reactor mainly uses lignocellulosic biomass as feedstock. The drying application of the SFB reactor represents 12% of the works, which study drying residence times and heat transfer characteristics for different materials. Mineral processing represents 5% of the selected publications. It is essential to point out the low amount of research (1%) concerning the transformation of biomass into biofuels and chemical precursors through gasification, pyrolysis, and other chemical processes, using the SFB reactor. Potential and other uses (8%)

encompass the studies of the SFB reactor operation in particular applications or individual contributions, including metallurgical, food, and carbon capture technologies. Various processes category (8%) relates to promotional documents comprising a conceptual approach of the technology developed by manufacturers and case studies. These documents describe a series of applications for the SFB reactor, such as biomass treatment, coating, granulation, and drying, among others.

Figure 2-8 illustrates the relationship between the type of SFB reactor and its applications. The selected documents report that the compact SFB reactor is the most used for drying and experimental purposes, while the expanded version is used for combustion. Other potential uses and applications show a fair distribution of compact and expanded reactors studies. “Various processes” mainly includes works with both SFB reactor types. The works about mineral processing report the use of a compact SFB reactor, though some promotional documents describe both types of SFB reactor. The only work related to biomass treatment applications (i.e., gasification or pyrolysis) reports using both types of SFB reactors. The lack of research using the compact or expanded SFB reactor for gasification or pyrolysis reveals a research gap related to biomass treatment in this equipment. The study of the SFB reactor for gasification or pyrolysis is essential to explore its potential to produce bio-oil, syngas, or other high-value chemicals.

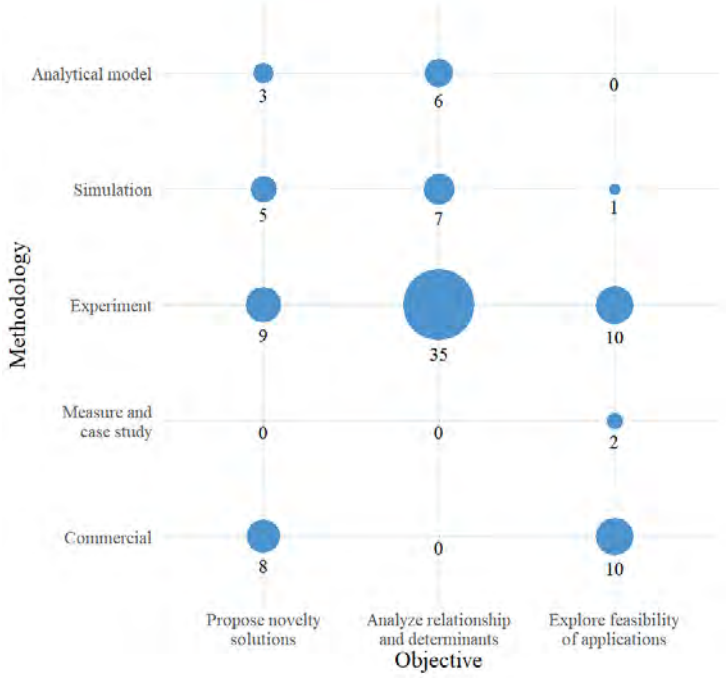

Figure 2-6 Relations of objectives and methodologies. Source: Figure created by author.

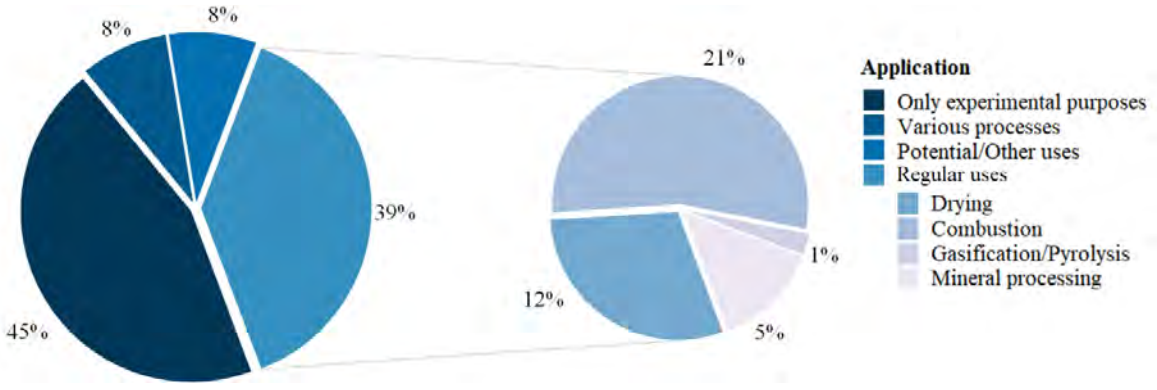

Figure 2-7 Distribution of documents per application. Source: Figure created by author.

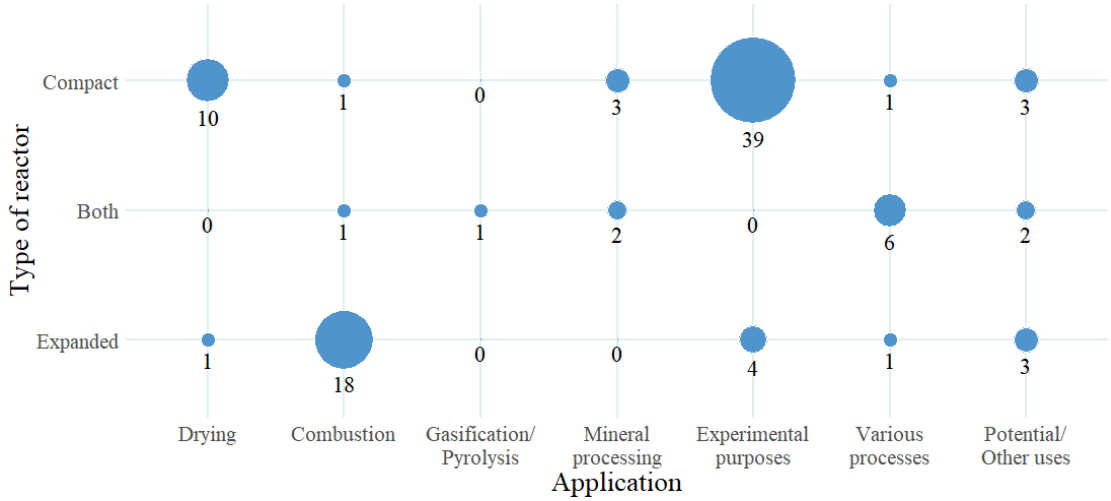

Figure 2-8 Relations of type of reactor and applications. Source: Figure created by author.

Figure 2-9a shows the bed materials reported in the selected works. The most common bed material found in the selected works is inert (38%). The use of inert material in the SFB reactor prevails in experimental studies about the behavior of hydrodynamics and heat transfer operational variables. Secondly, biomass or residues sums up 26% of the reported bed material in the SFB reactor. This bed material is known for its irregular shapes, variable densities, and wide particle-size distribution, highlighting the SFB reactor's capability to treat non-uniform particles. These documents correspond to proposals of new designs or explorative studies which do not extend the application to the type of particles to fluidize. 14% of the selected works do not use any particles as bed material, mainly for two reasons. First, a part of these focuses on studying air hydrodynamics, and the other comprises conceptual works such as case studies or catalogs from the manufacturer. The type of bed material was not specified in 5% of the publications. Despite its good performance, 4% of the selected works study fossil fuel processing with the SFB reactor. The category ‘other’ corresponds to individual works which use specific materials such as salts, food, and active pharmaceutical ingredients.

Figure 2-9b illustrates the distribution of 1g-Geldart’s group particles reported in the reviewed documents. Counting of documents repeats if they reported the use of more than one particulate material during the

study. 1g-Geldart's group D is the most common material used for studying the SFB reactor operation (56%), i.e., particles with bigger sizes and higher densities such as plastics to analyze operating variables and biomass as fuel in combustion studies. The 1g-Geldart's group B corresponds to 32% of the used particles. The use of sand quartz or glass beads as stabilization materials in different studies (e.g. drying or combustion) influenced the high amount of reported studies about these particles. The 1g-Geldart's groups C and A are reported in 11 and 9% of the reviewed documents. Some works about fine powders or minerals processing relate to particles of low density and small sizes. As stated in Figure 2-9a, some of the selected works (13%) do not use particles since the study focuses on the aerodynamics within the SFB reactor. Finally, 16% of the reviewed documents excluded the details about the density or size of the fluidized particles.

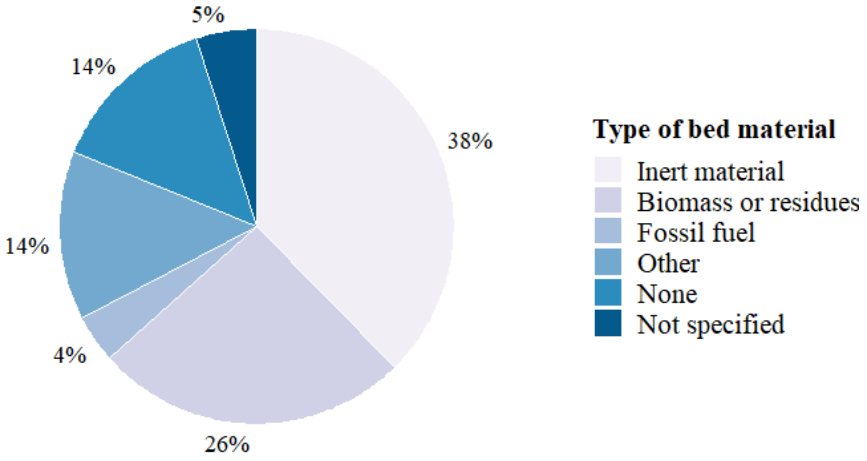

(a)

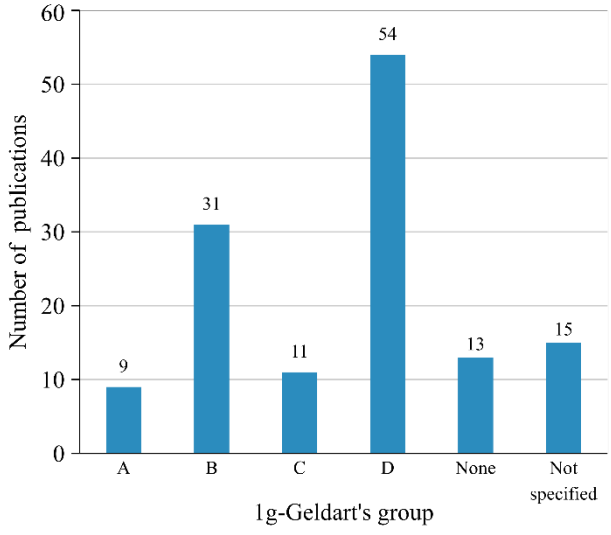

(b)

Figure 2-9 Distribution of documents per (a) type of bed material, and (b) 1g-Geldart's group of fluidized particles. Source: Figure created by author.

2.3.2. Characteristics of the swirling fluidized bed reactor

2.3.2.1. A brief history of the swirling fluidized bed

Figure 2-10 illustrates a brief history timeline of the swirling fluidized bed development. Torftech Limited developed a SFB design in 1981 for the exfoliation of perlite and vermiculite [14]. They named this design the TORBED reactor due to its capacity to generate a doughnut-shaped TORoidal fluidized BED of particles. This characteristic improves the gas-solid interphase transfer properties and achieves denser beds of particles in compact operations [9]. Dodson published the patent of the SFB reactor in 1987, assigned to Torftech Limited [11]. Due to the patent, the public domain literature regarding the SFB and TORBED reactors was quasi-scientific marketing orientated material. Torftech Limited installed the first commercial prototypes of the TORBED reactor in 1986 [12]. Simultaneously, Ouyang & Levenspiel published a study on a novel spiral distributor for fluidized beds, with a design closely resembling the SFB distributor, although their development appears to be independent [42]. In 1990, Huttlin published a patent for a SFB for granulation processes with characteristics similar to the TORBED from Torftech [43]. The technical publications from Torftech Limited highlighted the advantages of using the SFB reactor for gas-solid operations, promoting its use in other industries, such as food production, mineral processing, and waste management [12], [44]–[46].

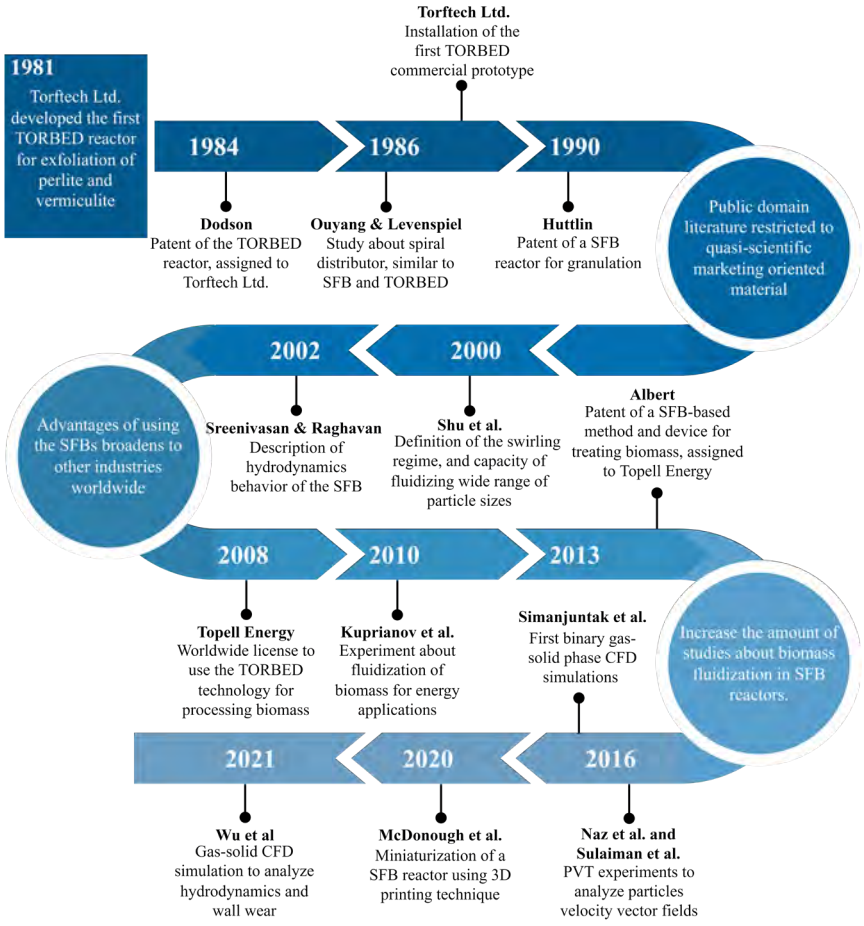

Figure 2-10 Swirling fluidized bed reactor state of the art. Source: Figure created by author.

Shu et al. [40] and Sreenivasan & Raghavan [16] were the first authors that publish a peer-reviewed scientific paper about SFB hydrodynamics. In 2000, Shu et al. analyzed the flow regimes of the particles bed and defined the SFB/Swirling regime for the first time. Also, they demonstrated the capacity of the SFB to fluidize particles from all of the 1g-Geldart's groups classification. Sreenivasan & Raghavan published an experimental study about the SFB in 2002. In this paper, they described the hydrodynamics of the SFB and developed semi-empirical models to estimate the pressure drop and the rotational velocity of the bed. Later in 2008, Torftech Limited granted Topell Energy of the Netherlands a worldwide license to use the SFB Technology for torrefaction of biomass and converting it into 'biocoal' pellets [47]. Albert [48] published a patent related to the previous application assigned to Topell Energy in 2013. Although Torftech Limited referred to biomass processing in SFB for energy applications in technical literature [49], Kuprianov et al. [50] were the first authors that publish a peer-reviewed paper about the topic in 2010. This publication promoted the experimentation with biomass in SFBs for thermochemical transformation [21], [51]–[53].

Faizal et al. [54], [55] introduced single-phase CFD simulations for SFB design in 2012. However, experiments of gas-solid operations within the SFBs restrict the analysis to global variables of the process, e.g. pressure drops [56] and average temperatures [51]. In 2016, the implementation of two novel techniques improved the analysis of SFB-based systems to gain insights into the hydrodynamics behavior of the SFBs, particle image velocimetry (PIV) experiments, and binary-phase CFD simulations. Naz et al. [57] and Sulaiman et al. [58] developed PIV experiments with an inert material to identify the velocity vector fields of the particles in the SFB. Meanwhile, Simanjuntak et al. [59] carried out gas-solid CFD simulations for drying applications. In addition, McDonough et al. [24] miniaturized a SFB reactor to a 50 mm diameter scale using 3D printing in 2020. This novel manufacturing process enables good tolerances at this scale in a practical and cost-effective timeframe. Later in 2021, Wu et al. [60] simulated gas-solid flow via CFD to analyze hydrodynamics and wall wear.

The advancement of the SFB technology shows excellent potential for diverse applications. For example, in developing countries, such as Colombia, the implementation of this device in power generation and waste management applications contributes to the implementation of more efficient and cleaner processes. In 2020, Díaz [61] proposed using the SFB technology for power generation through rice husk burning in Colombia. He estimated the potential of 10 MWe of power generation capacity and the production of silica ash, waste of combustion, as a by-product for selling.

Torftech Limited reports current SFB reactor facilities in different sectors, e.g., energy, mineral processing, and waste management. Table 2-2 summarizes the principal information of the facilities using SFB technologies, e.g., application, capacity, throughput, and year of installation. Though the first development of the SFB was a TORBED reactor in 1981 [14] and the commercial prototype was installed in 1986 [12], the first reported industrial installation was in 1989 for waste management applications. The technology used in The SFB reactor shows processing capacities up to 20 t h^{-1} of particulate material. In addition, the reported SFB reactors generated up to 6.3 MW of thermal power through gasification or direct combustion of biomass and torrefaction of biomass to produce biofuels.

Table 2-2 Current operating facilities using SFB reactors.

Sector	Ref	Application	Plant size	Feedstock	Capacity	Throughput	Location	Year of installation
Energy	[9]	Thermal dissociation of cyanide in Spent potlining		Spent potlining	1.1 t h^{-1}		Australia	1994
		Combustion	2 units	Wood waste		$5MW_{th}$	Netherlands	1999
	[45]	Combustion	1 unit 1.5m diameter	Wood waste		$3MW_{th}$	Holland	
		Combustion		Papermill sludge	6 t h^{-1}			
		Gasification		Wood waste	1 t h^{-1}			
		Torrefaction	4 units	Wood waste	9.1 t h^{-1}		Netherlands	2011
	[62]	Gasification		Wood waste Straw	1.6 t h^{-1}	$5MW_{th}$	Poland	2013
		Gasification		Wood waste	5.1 t h^{-1}	$6.3MW_{th}$	UK	2014
Mineral processing	[9]	Calcination		Vermiculite	1-5 t h^{-1}		Europe and Japan	
		Calcination	1 unit 1m diameter	Industrial minerals				1998
		Flash processing		Fine powders	0.3 t h^{-1}			1998
Wastes management	[9]	Removal of volatiles from solids		Oil-contaminated solids	0.15 t h^{-1}		UK	1993
		Removal of volatiles from solids		Swarf containing oil and water	3 t h^{-1}			1989
		Devolatilization	1 unit of 1.8m diameter reactor	Old asphalt coated road stone	20 t h^{-1}			2000
Contaminants control	[9]	Gas pollutants adsorption	14 units 6m diameter	Aluminum smelting fumes	200000 Nm^3 h^{-1} per unit		New Zealand	1996
		Gas pollutants adsorption	6 units 6m diameter	Aluminum smelting fumes	200000 Nm^3 h^{-1} per unit		Australia	1997
Food	[9]	Frying			0.05-0.5 t h^{-1}		Worldwide	
		Pasteurization		Spices	0.3-0.4 t h^{-1}			
	[45]	Puffing	1 unit 1m diameter	Rice	0.5 t h^{-1}		New Zealand	

2.3.2.2. Fabrication and design

The Swirling Fluidized Bed or SFB reactor technologies are novel gas-solid contactors developed to improve the processing of particulate materials in different fields [9]. In 1984, Dodson [11] reported the invention of a device for treating particulate material in a fluidized bed that circulates about the vertical axis of an annular process chamber. In the reactor, a gas flow passes upwards through a distributor to produce an inclined gas flow (with vertical and horizontal velocity components) [26], [27], [29], [30], [38]. A change of angular momentum of the flow of gas passing through the bed fluidizes the particles generating centrifugal force, which, combined with the gravitational effect, causes a swirling movement (circumferential and helical) to the particles [41], [43], [63]. The particles are in continuous motion in the fluid flow as it moves along an annular path. The use of the SFB reactor provides the rapid formation of a circulating mass of particles with a uniform distribution in the flow path. This enhances the heat transfer between the particles and fluid flow, improving temperature control in the processing chamber [64]–[67].

Figure 2-11 shows the SFB reactor scheme, which comprises a cylindrical housing, a central structure, a gas distributor, an annular chamber, a gas inlet, a gas/product outlet, and a chute for injecting particulate material [11]. The central structure supports the gas distributor, consisting of a central body, preferably conical, on a stationary disc with an array of inclined openings. The space above the distributor and between the central body and the housing wall is the annular processing chamber [65]–[68]. Implementing the central body improves the uniformity of the distribution of the particles across the bed and avoids the formation of a dead zone. The gas inlet supplies air, an inert gas, or a gas mixture that flows upwardly until it faces and passes through the openings of the gas distributor. The area reduction in the inclined blades increases the gas velocity and changes its direction [14], [16], [63]. This results in a highly turbulent swirling flow in the processing chamber that influences the mass of particles injected through the chute to form a toroidal bed. After processing, the exhaust or product fluid leaves the reactor through the gas outlet located in the upper region of the chamber [11], [27]. Some designs include a solids outlet at the center of the gas distributor where the solids fall through the central structure and exit at the bottom of the reactor [41].

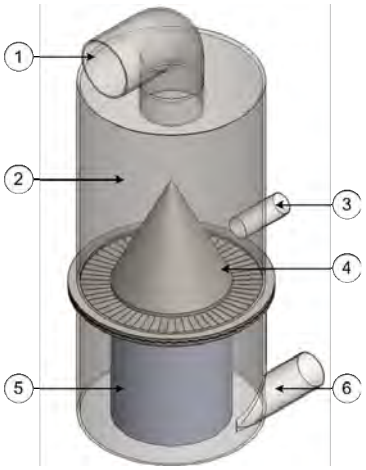

Figure 2-11 SFB reactor embodiment and composition. The reactor consists of (1) a gas/product outlet, (2) a cylindrical housing, (3) particulated solids inlet, (4) annular gas distributor, (5) central structure (optional solids outlet), (6) gas inlet. Source: Figure created by author.

Different SFBs have been reported with various bed column and gas distributor designs but similar fluidizing characteristics. The SFB reactor considered in this work must fulfill some operating and constructing features. Injection of the main fluidization gas is through the end wall of the reactor. The gas distributor is static with inclined orifices formed by slots, vanes, or holes. The distributor has a cylindrical or conical central body to ensure the toroidal (annular or doughnut-shaped) bed formation and avoid a dead zone in the center of the bed. The distributor changes the fluidization gas direction, transferring angular momentum to the static bed of particles, thus producing the rotation of the bed about the central axis and the helical motion of particles. The processing zone of particulate material locates in the annular chamber above the distributor and between the outer wall and the central body. The particulate material feeding point is above the distributor. Exhaust gas moves away through the upper region of the processing zone. In most configurations, the particles are entrained with the exhaust gas, though some have a particle outlet at the bed bottom. This description will correspond to the SFB reactor definition.

2.3.2.2.1. Gas distributor

The objective of the gas distributor in a SFB is to generate a turbulent swirling gas flow at the exit to change the angular momentum of the bed of particles. This momentum change causes the rotation of the bed about both the central vertical axis of the reactor and the axis of the doughnut-shaped bed. The gas flow must pass through inclined openings radially arranged. Variations of the gas distributor affect the pressure drop across the distributor, so the energy consumption to maintain the operation running. Table 2-3 summarizes the design and fabrication of four types of gas distributors reported in the literature: inclined holes, gill plates, single row blades, and three-row blades. Figure 2-12 shows the schematics of the four types of annular gas distributors.

Some works developed innovative designs to improve the SFB reactor performance. For example, Figure 2-13 shows the idea from some PIV studies of a distributor hybrid design, including a mesh above the inclined inlets to prevent the smaller particles from falling through the distributor openings [72]–[77]. The effect of the additional mesh on hydrodynamics is insignificant and prevents obstruction with fine particles in the distributor orifices.

The cold-work use of the SFB reactor is common in experimental studies and prototypes. Based on this, the use of plastic as the material of the components eases manufacturing, reduces costs, and decreases weight. McDonough et al. explored the option of 3D printing a miniaturized SFB reactor (50 mm of outer diameter) and analyzed its hydrodynamic behavior [24]. The experimental results showed that the miniaturized SFB reactor achieved the desired flow pattern with high gas flow rates.

2.3.2.2.2. Bed reactor column

The selection of cylindrical or tapered bed columns with different diameters affects the fluidization performance and the 1g-Geldart's group of particles. Figure 2-14 shows the two types of SFB reactor defined by Torftech Limited: compact and expanded beds. These reactors possess inherent advantages depending on the solids to fluidize and processes to perform. Table 2-4 compares the physical and operational characteristics of the two SFB types.

Table 2-3 Classification of the annular gas distributors for SFBs, design, and fabrication

Type of distributor	**Design**	**Fabrication**	**Ref**
Inclined holes (Figure 2-12a)	Disk plate with inclined holes Circular openings Hole size and radial and circular pitches define the number of holes Circumferential and tangential arranged	Drilled holes at the desired inclination in a plate disk	[69]–[71]
Gill plate (Figure 2-12b)	Flat plate with arrays of channeling holes or 'gills' Gills arranged on a series of concentric circles Rectangular openings	The channeling holes or 'gills' are mechanically punched	[14]
Single row blades (Figure 2-12c)	One row of overlapping inclined blades Blades shape is a truncated sector of a circle Trapezoidal openings between blades Circumferentially arranged Opening width and blade inclination angle determine the number of blades	Two rings of different diameters made from a steel plate (inner and outer) hold the blades with cut grooves The blades are made per design using a steel plate	[69]
Three-row blades (Figure 2-12d)	Three rows of overlapping inclined blades Blades shape is a truncated sector of a circle Trapezoidal openings between blades Circumferentially arranged Opening width and blade inclination angle determine the number of blades	Three rings of different diameters made from a steel plate (inner and outer) hold the blades with cut grooves The blades are made per design using a steel plate	[69]

The compact SFB reactor retains a shallow packed bed of particles for fast processing with high precision, and properties across the bed are almost uniform during operation. After passing the distributor, the blades impart a strong horizontal component to the resultant gas velocity vector, while the vertical component is only a fraction of it. These conditions generate a high slip velocity, which leads to higher heat and mass transfer rates per unit volume with low-pressure drops, enabling smaller reactor size with rapid start-up and controlled operation. This has similar superficial velocity restrictions as a bubbling fluidized bed to minimize elutriation but fewer particle shape and size distribution restrictions. The typical feedstocks particle size ranges from 25 mm to a few microns. The void fraction of larger particles causes the solid to fluidize in a shallow vertical band, avoiding expansion over a significant height. Because of the shallow bed, the solid phase residence time is short, within the range of 0.1-120 s [12]–[14], [79].

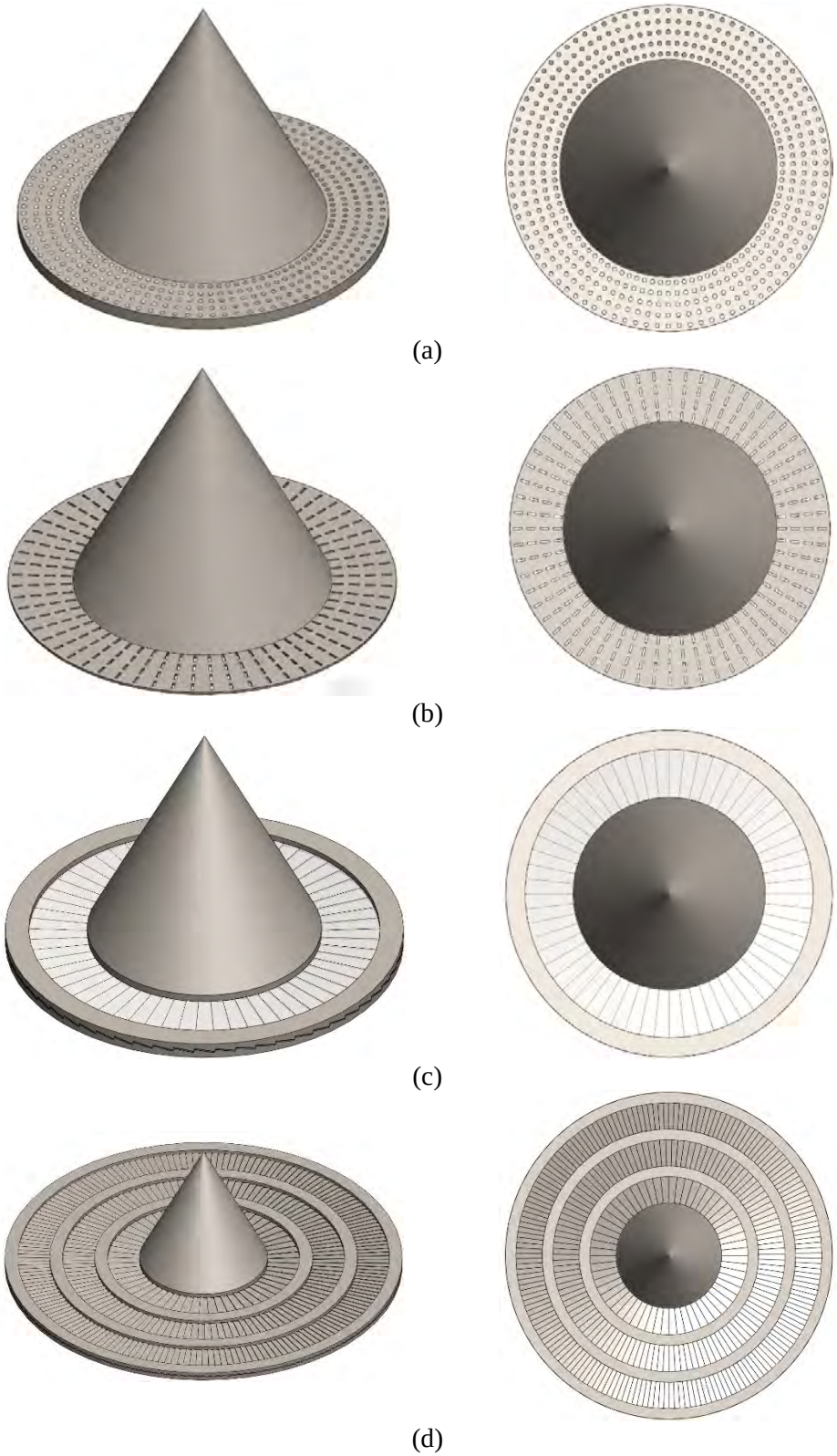

Figure 2-12 Schemes of the four types of annular gas distributors in Table 2-3. The left side corresponds to the isometric view of each distributor, and right side to the top view. The includes distributors are (a) the inclined holes, (b) the gill plate, (c) the single row blades, and (d) the three row blades. Source: Figure created by author.

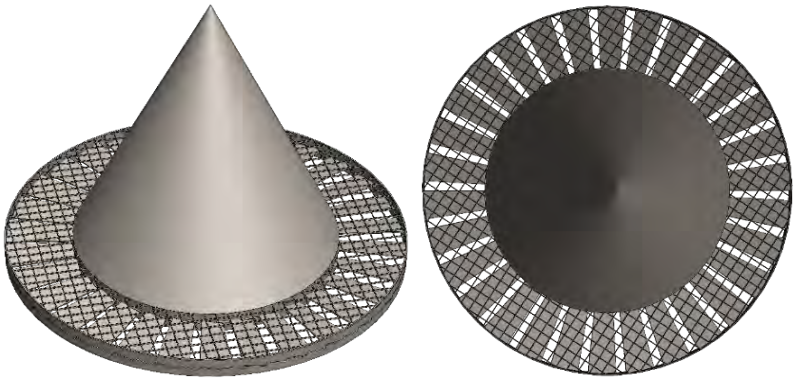

Figure 2-13 Hybrid mesh-inclined blades distributor. Source: Figure created by author.

The expanded SFB reactor retains an expanded diffused bed of particles, which provides a quick and efficient gas-solid contact, as in circulating fluidized beds. However, it uses higher gas flow rates with a lower pressure drop in a shorter reactor vessel. The blade's orientation is vertical instead of horizontal, so the vertical component of the resultant gas velocity vector extends the bed height. The horizontal component of the motion provides a longer contact path and allows uniformity of the process conditions and the bed particles. The resultant velocity and the conical section of the housing at the bottom generate the cyclone effect in the expanded bed. The cyclone effect enables particle separation, and direct recirculation in the SFB expanded reactor without internal or external cyclones. This effect spins out coarse particles to the walls close to the bottom of the reactor while finer particles travel with the gas in a toroidal path. Turbulent conditions in the reactor ensure high slip velocity and rate of attrition, so the surfaces of the particles are always exposed to the process environment, enhancing heat and mass transfer rates. The preferred feedstocks are particles from 1g-Geldart's groups A, B, and C, with diameters between 5-150 μm. The typical solids residence time ranges between 5 to 10 min [12], [14], [15], [78], [79].

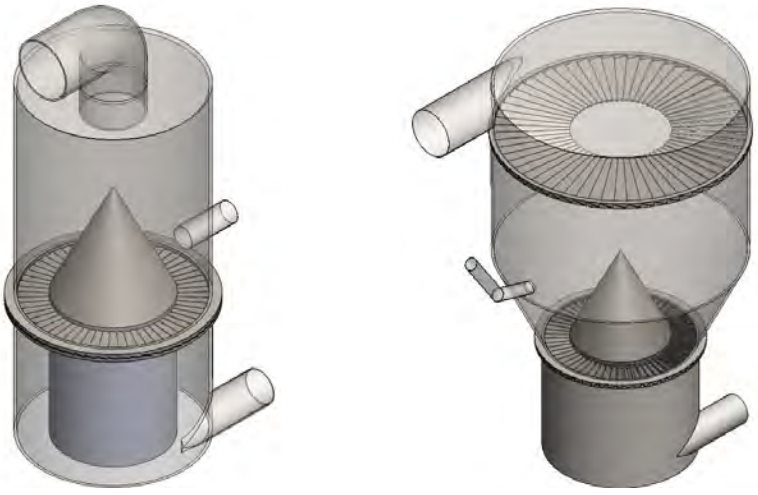

(a) (b)

Figure 2-14 SFB (a) compact and (b) expanded schemes. Source: Figure created by author.

Table 2-4 Description of the SFB compact and expanded bed reactors. Information based on [12], [13], [15], [78], [79]

Characteristic	Compact	Expanded
Column geometry	One cylindrical section	Two sections: tapered and cylindrical
Preferred operation	Continuous or batch	Continuous
Applications	Minerals	Ashes handling
	Metallurgical	Combustion
	Chemicals	Solid fuels gasification
	Foods	Roasting
		Calcination
		Gas scrubbing
		Classification
Bed characteristics	Shallow packed bed	Expanded diffuse bed
Dominant vector velocity component	Horizontal	Vertical
Feedstock characteristics	1g-Geldat's D group particles	1g-Geldart's A, B, and C groups of particles
	Size from 25 mm to a few microns	Size from 150 to 5 μm
	Spherical, cylindrical, plate-like, shredded, or other shapes	Spherical, cylindrical, plate-like, shredded, or other shapes
Typical solid's residence time	0.1-120 s	5-10 min
Cyclone	Optional	Unnecessary

2.3.2.3. Flow regimes and minimum fluidization velocity

The SFB reactor presents different flow regimes with increasing the gas flow rate during its operation. The regimes slightly differ between shallow and deep beds. In shallow beds, low static bed heights, the fluidization of particles develop four main flow regimes: packed-bed regime, bubbling regime, wavy regime, and swirling/TORBED regime [16], [40], [52], [56], [80]–[82]. The different regimes exhibit hydrodynamic characteristics mainly explained using the pressure drop across the bed (ΔP_{bed}) and the superficial velocity of the gas (u_{sup}). Figure 2-15 shows a typical $\Delta P_{\mathrm{bed}} - u_{\mathrm{sup}}$ diagram that illustrates the flow regimes behavior in the SFB reactor.

Packed-bed regime: The superficial velocity is not high enough to produce fluidization in the packed bed region. While the gas fluids across the bed of particles, the bed pressure drop increases almost exponentially with the superficial velocity until it reaches a maximum (ΔP_{mf}) [16], [52].

Bubbling regime: It starts when the vertical velocity component of the gas jets leaving the blades corresponds to the minimum fluidization (u_{mf}). The bed fluidization starts with the minor formation of random bubbles that agitate the particles [16], [56].

Wavy regime: The superficial velocity value reaches the minimum velocity of full fluidization (u_{mff}) and the bed enters the wavy regime. Swirling and static zones differentiate because of the formation of dunes along the bed, and particles constantly move from one zone to another. Reduction of the bed pressure drop occurs and stays at a nearly constant value (ΔP_{mff}) with superficial velocity increase during this regime [80]–[82].

Swirling regime: Further increase of the superficial velocity extends the swirling region until the dunes disappear, which represents the fully swirling or 'TORBED' regime [16], [40], which occurs at the minimum velocity of full swirling fluidization (u_{msf}). Bed pressure drop increases with the superficial velocity at a lower rate than in the packed regime. The interaction between gas and particles is optimal, and heat and mass transfer rates reach their highest values in this operation regime. The swirling regime in deep beds, i.e., high mass bed loading, presents a two-layer condition under a two-layer minimum velocity operation: the lower layer flows under a thin, continuously swirling regime and the top layer under a bubbling regime [80], [81].

Entrainment regime: Some authors refer to the entrained condition as the final regime in SFB operation [24], [80], [81]. In this condition, superficial velocity is sufficiently high that particles entrain progressively, causing the drop in bed pressure to decrease until all the particles blow out from the vessel.

The development of the SFB reactor contributes to the continuous improvement of particulate matter processing in gas-solid contact applications. The swirling flow in the processing zone contributes to the uniformity of the fluidization of particles in the bed. The high gas-solid slip velocities operation enhances the heat and mass transfer rates. SFB compact and expanded reactors ease the use of the equipment according to the operation's needs. The reported applications in different industries demonstrate its capability to process various particles. The following section will show the results of experimental and analytical studies to define the operative behavior of the SFB reactor because of changes in the design and input parameters.

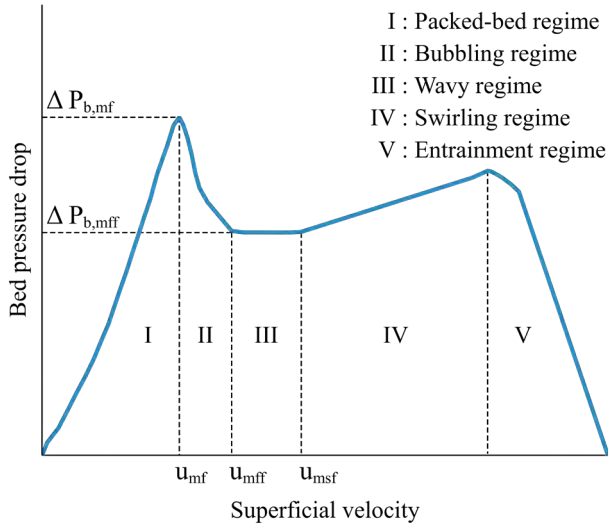

Figure 2-15 Typical pressure drop across the bed vs. Superficial velocity diagram. It presents the different flow regimes of the SFB operation. Source: Figure created by author.

2.3.2.4. Effect of input or design parameters on SFB reactor operation

Different authors developed studies for analyzing the operating variables of the SFB reactor under diverse conditions, mainly using lab-scale equipment in experiments, solving analytical models, or developing simulations. The most studied field was the hydrodynamics behavior of the reactor, which includes the analysis of the flow regimes of the bed, e.g., [40], [56]; pressure drops across the bed and the distributor

[14], [80]; bed height [83]; minimum fluidization velocity [70]; particles velocity [17]; and particles residence time [84], [85]. Other works focused on studying thermal parameters of the reactor, such as the radial and axial distributions of both bed temperature and heat transfer coefficient [18], [19].

The reviewed articles studied the relations between the operating variables and the input or design parameters of the SFB reactor. Table 2-5 gathers the reported results from these articles in the form of a correlation matrix about the effect of changing the input or design parameters (independent variables) on the operating variables (dependent variables) of the SFB reactor. The independent variables comprise operation parameters, such as superficial velocity, static bed height, and bed weight; particles size, shape, and density; design parameters such as cone height, depth of plenum chamber, number of blades, blade length, blade overlap angle, blade horizontal inclination angle, blade radial inclination angle, blade twist angle, and number of gas inlets; and bed radial and axial locations. The variables with the most number of relationships with the input and design parameters are the pressure drops across the bed [16], [22], [52], [55]–[57], [60], [69]–[72], [75]–[77], [80], [81], [83], [85]–[97] and the distributor [14], [18], [22], [54], [69], [72], [75], [81]–[83], [89], [93], [97]–[104], bed particles velocity [17], [57], [58], [71]–[77], [96], [105], minimum fluidization [18], [40], [56], [69], [70], [72], [75]–[77], [82], [87]–[92], and convective heat transfer coefficient of the bed [18], [19], [93], [94], [106]. Pressure drop is one of the key variables in the operation of any fluid system because of its relationship with energy consumption. In the case of fluidized beds, pressure drops across the distributor and the bed represent the most significant pressure losses in the system. The total pressure drop of the SFB reactor is lower than the conventional fluidized bed reactor. The distributor pressure drop is the predominant pressure loss of the SFB reactor. The reduction of area and inclination of inlets cause a high turbulence zone in the entrance of the distributor, increasing the pressure drop. On the other hand, the lower bed heights in the SFB reactor than in conventional fluidized beds decrease the bed pressure drop.

The study of individual particle motion is important to understanding fluidization quality [57]. The velocity profile of particles in the SFB regime is useful for improving the design and operation of the fluidization system [17] [58]. For this purpose, particle image velocimetry (PIV) experiments showed the bed particle velocity magnitude and vector profiles under different operating conditions [17], [57], [58], [71]–[77], [105]. The results showed good fluidization of particle sizes from 3-6 mm under different operating conditions. At lower superficial velocities, the velocity profile of the particles forms a Gaussian distribution along the radial line, with the highest value at the centerline of the annular bed. In contrast, particles move slower at the bed boundaries. At higher superficial velocities, the particles near the central cone boundary acquire almost the same velocities as in the middle of the bed, while the particles near the outer bed boundary maintain low velocities. An analytical model predicted the behavior of the average velocity of particles [96] and showed good agreement with experimental results.

Table 2-5 Matrix of correlations of the effects of design or input parameters on the operating variables. Arrows direction denotes the relationship between variables. Upward (↗) are directly related, downward (↘) inversely relateded, horizontal line (–) no significantly related, NA relationships does not apply.

Operating variable	**Distributor pressure drop**	**Bed pressure drop**	**Particle velocity**	**Minimum fluidization**	**Residence time**	**Convective heat transfer**	**Bed temperature**
Design/input parameter							
Operation parameter							
Superficial velocity	↗	↗	↗	NA		↗	↘
Static bed height	NA	↗	↘	↗		↘	
Bed weight	NA	↗	↘***	↗	↗		
Particles parameter							
Particle size	NA	*	–	↗	↗	↘	
Particle shape**	NA	↘	↗	↗			
Particle density	NA		↘	↗		↗	
Design parameter							
Cone height	–	↗					
Depth of plenum chamber	–	↘				↘	
Number of blades	↗	↘		↘		↗	
Blade length		↘					
Blade overlap angle	↗	↗	↘	↗	–		
Blade horizontal inclination angle	↗	↘	↘	↘		↘	
Blade radial inclination angle	↘						
Blade twist angle	↘						
Number of gas inlets	↗						
Bed location							
Radial	NA	NA	****	NA	NA	*****	–
Axial	NA	NA	↘	NA	NA	↘	↘******

The particle size effect in the bed pressure drop depends on the flow regime. For the packed-bed regime, larger particles induce less resistance to the gas flow than smaller ones. The transition to different flow regimes causes an inverse relation of the pressure drop with particle size [56], [97].

****Evaluation of particle shape corresponds to the effective drag area of the particles (A_{drag}). $A_{drag,cylindrical} > A_{drag,elliptical} > A_{drag,spherical}$.***

*****The bed weight has an inverse relation with the particle's velocity. However, a continuous increase in the bed weight reduces the effect of the change on the particle velocity. This condition also affects the superficial velocity influence on particle velocity. Particle velocity is more sensitive to the variation of superficial velocity in light-weight beds than in heavier beds. A larger number of particles in the heavier beds results in higher interparticle friction and greater friction between particles and the wall, requiring higher momentum to swirl particles, i.e., higher superficial velocities [17], [58].***

*******At lower superficial velocities, the particle velocity presents a higher value at the centerline of the annular bed while particles move slower at the bed boundaries. The velocity vectors form a Gaussian distribution along the radial line. At higher superficial velocities, the particles near the central cone boundary acquire almost the same velocities as in the middle of the bed. On the other hand, the particles near the outer bed boundary maintain low velocities [57], [71], [72], [74], [105].***

******** The heat transfer coefficient radial profiles present the maximum values at the center of the bed and near the reactor walls [93], [106]. Although, one study reports that good elutriation of the particles in the bed makes the radial location effect on the heat transfer coefficient insignificant [18].***

********* The relationship between temperature and axial location is mainly inverse [108], [109]. However, during combustion in shallow beds, the axial temperature profile is relatively uniform, indicating good gas-solid mixing [92].***

Minimum fluidization is of high interest due to its relationship with the minimum swirling velocity, and the swirling regime is the desired operation regime in the SFB reactor. Also, the gas velocity relationship with the gas volume flow rate determines the energy consumption to achieve an adequate fluidization regime [40]. As in previous models of minimum fluidization, particle size, shape, and density are significant for the minimum fluidization [18], [40], [56], [82]. The static bed height imposes a higher resistance to the gas flow, increasing its requirement for fluidization related to the implicit increase of the bed weight [56], [90], [92]. The number of blades and blade design is related to the free opening annular area and the angle of gas injection. These variables determine the axial velocity of the gas leaving the distributor and generate the fluidization of the bed [69], [70], [72], [75]–[77], [82], [90].

Heat transfer studies [18], [19], [93], [94], [106] agree that the annular bed presents a uniform temperature behavior in the radial direction. This feature facilitates the temperature control of the processes inside the SFB reactor. As expected, the increase of superficial velocity enhances the convective heat transfer coefficient across the bed. A higher number of particles improved the heat transfer coefficient in the axial direction due to decreasing the area available for air flow. This increases the swirl effect on solid particles, i.e., improves the mixing and strengthening of the particle's motion, enhancing the heat transfer coefficient [94]. The increase of specific surface area, so the heat transfer surface, during fine particles fluidization resulted in higher heat transfer than in larger particles. Some combustion applications use secondary and tertiary air injections at ambient temperature, hindering the heat transfer coefficient. The addition of the air injection reduces the temperature of bed particles and decreases the heat transfer coefficient.

The less related variables are the residence time of the particles[40], [85] and bed temperature 13 [18], [20], [21], [50]–[53], [92], [94], [107]–[110]. The residence time of the particles is important to maintain the solid enough time in the toroidal path and achieve adequate product quality. Further understanding of this variable improves process performance and reduces material recirculation due to incomplete reaction. The bed temperature distribution was similar to the heat transfer coefficient; it showed radial uniformity and decreased with the height above the distributor. The central body avoids the formation of the dead zone and enhances the swirling behavior of the bed, which improves the bed temperature uniformity. However, the absence of a dead zone in the center of the reactor decreases the temperature in the vicinity of the central body. The dead zone would increase the particle concentration in the central region, hence the conduction heat transfer and bed temperature.

The study of various materials covered the fluidization testing in the SFB reactor of particles from all the 1g-Geldart's classification groups. Visual observations confirmed the SFB reactor capacity of good quality fluidization for processing a wider range of particle sizes over a broader range of superficial velocities. Relatively coarse particles (1g-Geldart particles B and D) could be effectively retained in the bed until a fragmentation process occurs. In the case of group C particles, the retention time was the lowest. The particle only rotates one time around the central body. Due to kinetic limitations, limited conversions could sometimes occur with the toroidal fluidized bed reactor for the coarse particles. Enhanced reaction conditions or multiple passes might be required in those cases to achieve the reaction conversion requirements [40] [88].

Though the equipment has some advantages over other fluidization technologies, its novelty opens the possibilities of designing several experiments to increase the knowledge about its operation. Thus, it facilitates the development of mathematical models to improve the SFB reactor performance from the design stage.

Table 2-6 summarizes the mathematical models used and developed in the selected documents. Some authors developed analytic geometry models for designing the annular blade distributor [58], [82]. The hydrodynamics models are the most developed. Some of the velocity and pressure drop prediction models have good correspondence with experimental results [56], [70], [75]. An analytical model from the momentum balance equation facilitated a good prediction of the angular velocity of the bed [16]. Drying models predicted drying rates of the process, moisture content of the treated material, and convection mass transfer equation [59], [111], [112]. Heat transfer models pursue the prediction of thermal resistance of the materials, Nusselt number and heat transfer coefficient in the bed, and heat transfer rate [19], [94], [106].

Other variables less studied are wear of air distributor, wall and central body [60], solid hold-up [95], uniformity index [24], and air velocity distribution [115]. The wear problem of a SFB is crucial because it contributes to the erosion of the walls and components of the reactor. The centrifugal force of the rotating bed moves the particles outwardly, causing the outer wall wear to be more severe than the wear of the central body. Some strategies to weak the walls wear in the SFB reactor are reducing the central body height, gas superficial velocity, and residence time of the particles [60].

The solid hold-up measures the local volume fraction of the solid phase in the SFB reactor. An experiment determined the solid hold-up radial and axial distributions in a SFB combustor with varying operating parameters [95]. The solid hold-up tends to decrease with the radial and axial positions, with a peak at the center of the combustor. The bed particle size presents an inverse relationship with the solid hold-up. The larger bed particle size ranges have lower voidage causing higher interparticle friction and decreasing the transfer of momentum from the fluidizing agent when lifting the bed. On the other hand, the solid hold-up increases with the percentage of excess air (EA) since the higher gas flow rate has more energy available to fluidize the bed of particles.

Table 2-6 Summary of models used or developed in the reviewed documents from four main topics: design, heat transfer, hydrodynamics, and drying. The models include analytical and experimental estimations validated or not.

Topic	Ref	Models	Type	Validation
Design	[58], [69], [82]	Geometry of the distributor	Analytical	Yes
Heat transfer	[19]	The instantaneous bed-wall thermal resistance	Analytical	Yes
	[19], [106]	Heat transfer equation	Analytical/ Experimental	Yes
	[19], [106]	Nusselt number	Analytical/ Experimental	Yes
	[94]	The local bed-wall heat transfer coefficient	Analytical/ Experimental	Yes
Hydrodynamics	[14]	Pressure drop across the distributor	Analytical/ Experimental	Yes
	[16], [56], [96]	Pressure drop across the bed	Analytical/ Experimental	Yes
	[16]	Angular velocity	Analytical	Yes
	[16]	Mass conservation	Analytical	Yes
	[16]	Rate of change of angular momentum of gas	Analytical	Yes
	[40]	Minimum swirling velocity	Analytical	Yes
	[40]	Particle motion estimation model. Inverse relaxation time F	Analytical	Yes
	[56], [57], [70], [96]	Minimum fluidization	Analytical/ Experimental	Yes
	[58], [82]	Superficial velocity	Analytical	Yes
	[60]	Oka wear model	Analytical/ Experimental	Yes
	[70]	Axial mixing in bubbling fluidized bed model	Analytical/ Experimental	Yes
	[84]	Residence time distribution model	Analytical	No
Drying	[111]	Convection mass transfer rate	Analytical/ Experimental	Yes
	[111]	Drying rate	Analytical/ Experimental	Yes
	[112]	Linear-plus-exponential drying model	Analytical/ Experimental	Yes
	[113]	Verma et al. drying model	Analytical/ Experimental	Yes
	[114]	Zero-Dimensional calculation drying model	Analytical/ Experimental	Yes

The uniformity index (I_u) measures the adequate bed formations in a uniformly packed state. This index depends on the ratio between the standard deviation of the velocity distribution of the particles and the mean particle velocity. Because of this, the values of $I_u > 0.3$ indicates better uniformity of the bed. The experiment was carried out in a SFB reactor with an outer diameter of 50 mm. The bed weight and gas flow rate had the most significant influence on the uniformity index. The desirable uniformly packed state occurred at bed weight ≥ 1.2 kg and gas flow rates ≥ 0.0355 m3 min^{-1} [24].

Air velocity distribution affects the motion of the particles in bed to obtain the desired flow regime. A uniform distribution contributes to improving the mixing and processing of particles simultaneously. A high number of blades and low values of blade twist angles enhance the uniformity of airflow distribution and increase the tangential velocity [115].

2.3.2.5. Swirling fluidized bed reactor performance in different applications

The performance of the SFB reactor varies from one application to another. Table 2-7 summarizes the processing conditions of the drying performance of the SFB reactor. The studies include different particles such as inert material, biomass and wastes, solid fuels, and food. The batch mode is the preferred operation for drying in the SFB reactor with 0.1-3.0 kg bed loadings. The SFB reactor achieves the objective moisture content (14-20%) or completely dries (0%) the media within 10-90 min of drying time and temperatures ranging from 35 to 100 °C, depending on the dried material and bed loading. The drying rates were up to 30 g of H2O min-1 and decreased with time. The calculated mass transfer coefficient ranges from 0.043 to 0.058 m s-1 [111], ten times higher than conventional fluidized beds for coal [116] and four to five times for biomass [117]. The experiments that did not reach the desired moisture were those with lower temperatures (45-60°C°) using oil palm frond (OPF) leaves and petiole [23].

Table 2-8 presents the combustion performance of the SFB reactor for different processing conditions. The feedstock material reported in this application was pure or blended biomass. The continuous mode of operation is preferred during combustion in the SFB reactor, with mass flow rates of biomass ranging from 25 to 80 kg h^{-1}. During combustion, EA was tested in the range of 16-80% to control the process temperature at temperatures between 700 and 1100°C. As a result, the combustion in the SFB reactor achieves efficiency values from 84 to 99.9%. The high performance of the combustion in the SFB is connected to the high heat and mass transfer rates caused by the high level of elutriation of the toroidal bed. The feedstock moisture content did not significatively affect the combustion performance.

Rice husk is the most frequent biomass material studied for combustion in the SFB reactor. The process produces energy after burning out the rice husk, and the remaining ash has a 90% concentration of amorphous silica. This by-product presents surface areas above 15 m^2 g^{-1} and loss on ignition below 6%. In addition, the amorphous silica makes the ash attractive for blending into concrete as a cement replacement [79], [122]. A manufacturer proposes some SFB designs for combustion of up to 7 t h^{-1} of rice husk, producing up to 35 t h^{-1} of steam at 4 MPa or up to 7 MWhe on a condensing steam turbine [123]. A study analyzed the feasibility of installing a facility for simultaneous production of electric power and amorphous silica through rice husk combustion. The power plant would produce 1 MWe/ton of rice husk and 0.2 t/h of rice husk ash, with an ROI of 11% after ten years [61].

Table 2-7 Summary of drying experiments and operating conditions

Ref	**Feedstock material**	**Bed loading, kg**	**Temperature, °C**	**Drying time, min**	**Feedstock**			**Air velocity, m s^{-1}**
					Initial moisture, %	Desired final moisture, %	Final moisture, %	
[118]	OPF leaves	0.1-0.14	60	90	57 wet basis	15 wet basis	5 wet basis	1.25
	OPF petiole		45		70 wet basis		20-27 wet basis	2
[23]	OPF leaves	0.1-0.14	50-80	90	57 wet basis	15 wet basis	2-35 wet basis	1.25
	OPF stems				70 wet basis		2-35 wet basis	2
[119]	Sponge media	1.7-2.3	80-100	20	32-37 dry basis		0	>6.9
[22]	Sponge media	1.7-2.3	80-100	20	30-40		0	>2.52
[59]	Coal	0.6	55	10	25.17 wet basis		0	
[111]	Coal	0.6	55	5	25.17 wet basis		9.5-13.8	
[113]	Sponge media	0.5-1	80-100	20			0	
[91]	Pepper	1-1.8	90	50			<0.1	
[114]	Lignite	2.5	35-80	40	39-63 wet basis	20	8	
[112]	Paddy	1.0-3.0	55	45	31.23 dry basis	14.21	0.05 MR	16.2

Table 2-8 Summary of combustion experiments and operating conditions

Ref	Feedstock material	LHV, MJ kg^{-1}	Feedstock moisture, wt%	Feed rate, kg h^{-1}	EA, %	Temperature, °C	Combustion efficiency, %
[110]	Rice husk	10.6-14.6	8.40-30 "as-fired" basis	80	20-80	850-980	97.22-99.73
[56]	Rice husk	11.5-14.6	8.40-25 "as-fired" basis	80	20-80	850-980	97.22-99.73
[51]	Sunflower shell	17.2	9.1 as received basis	60, 45	20-80	750-980	94.2-99.1
[52]	Rice husk	14.6	8.4 as received basis	80	20-80	800-1000	97.2-99.5
[53]	Eucalyptus bark Rubberwood sawdust	13.6-17.1	6.6-23 "as-fired" basis	60	20-80	800-960	96.7-99.9
[21]	Rice husk	9.7-14.6	8.4-35 as received basis	80	20-80	850-980	97.6-99.1
[20]	Sunflower shell	17.2	9.1 as received basis	60, 45	20-80	850-980	92.8-99.5
[120]	Rice husk			26.5		700-950	
[108]	Empty fruit bunch pellets	18.8		30	20-80	800-1100	99.99
[109]	Empty fruit bunch pellets	18.8	8.5	54.26	16-36	800-1100	97.84-99.11
	Oil palm shell	19.4	10.58	48.91			99.37-99.67
[92]	Rice husk	13.3	10.46	27,	30-60	720-870	98-99.3
	Sugarcane bagasse	4.7	72.29	35 (23+12)			
[121]	Leucaena (lam.)	15.6	12.15	45	40-80	1000	99.86-99.89
	Palmyra palm shell	16.6	9.65				99.4-99.61
	water hyacinth	9.7	9.24				84.67-96.36

Gasification in the SFB reactor produces syngas and a high-quality char through partial biomass combustion. Production of 160 kg of carbon char per MWh from biomass such as straw, oil palm fruit bunches, and bagasse. The SFB processes biomass with moisture content between 10 and 65%. The actual runs of gasification produce 1.0-2.8 kg s^{-1} of syngas and 0.07-0.09 kg s^{-1} of bio-char operating in the range of 650-850 °C [62].

Mineral processing is challenging because of fine particle fluidization, less than 100 microns. The reduced size particles make it difficult to keep the material enough time for a complete reaction in conventional equipment. The swirling motion of the particles in the SFB reactor overcomes the retention time issue [124]. The SFB reaches temperatures above 1000°C to process particles feed rate between 0.3-5.0 t h^{-1}, depending on the SFB size and type of particles, in short residence times thanks to high mass and heat transfer rates. The application comprises limestone and other minerals calcination, reduction of metal ores, flash processing of powders, vermiculite exfoliation and expansion, sintering of clay prills, and zeolite regeneration [44], [124]–[127]. The option of direct fuel injection in the SFB undergoes spontaneous combustion, resulting in a flame covering the entire bed leading to temperatures above 1500°C [125]. This technique decreases specific energy consumption, enhances the heat and mass transfer rates in a small chamber, and enables oxygen and temperature control, allowing the flash processing of particles.

Table 2-9 summarizes the reviewed documents that include uncommon reported applications of the SFB reactor. Industries developing the SFB reactor include carbon capture, food processing, catalyst production, radiation heat transfer, recycling, contaminant control, and sulfides processing. These industries find attractive the capacity of the SFB to process a wide range of particle sizes and shapes, energy-efficient, process control, high heat and mass transfer rates, and short residence times. However, the lack of experimental data about the use of the SFB in these applications opens the possibility for further developing and improving the related processes.

2.3.2.6. New designs and modifications of the SFB reactor

Some studies proposed a multi-stage SFB reactor design with the idea of improving the residence time of the particles [85], [133], [134]. The one-stage SFB reactor provides regular air movement around the bed and a uniform formation of the fluidized bed. However, when the air velocity is unexpectedly raised, the airflow appears to be non-uniform. It can cause a bubble inside the beds due to this condition and may result in a fluidization system where energy consumption is inadequate. Figure 2-16 shows a schematic of the multi-stage system in a SFB reactor. This novel design improved the uniformity of gas distribution, decreasing energy consumption to achieve the same level of fluidization of the bed.

A miniaturized model of the SFB reactor was designed and 3D-printed [24]. The 3D-printing method made possible the fabrication of this scale SFB in a practical, cost-effective timeframe compared to conventional manufacturing methods. The prototype had an outer diameter of 50 mm, compared to the 300 mm of a typical laboratory-scale SFB and up to 6 m of an industrial scale. The study showed good fluidization uniformity besides the size reduction.

Table 2-9 Summary of potential and individual uses reported of the SFB reactor

Industry	Ref	Process	Type of work	Objective	Feedstock	Advantages	Challenges/Opportunities
CO_2-Carbon capture	[128]	Adsorption	Theoretical research	Determine the feasibility of a SFB reactor prototype for adsorption, specifically the treatment of industrial heat and CO_2 sources.	Stack gas or power plant stack	High specific throughputs, lower power consumption, real-time temperature control, integration of adsorption, and cyclonic separation of the particles.	Likely to see enhanced attrition of the adsorbent particles and a continuing move away from fossil fuel combustion as an energy source.
	[24]		Experimental study	Study bed formations of activated carbon pellets to guide the selection of appropriate operating conditions of a miniaturized 3D-printed SFB reactor for CO_2 capture applications.	Activated carbon	Decoupling of gas velocity and gas flow rate, i.e., using either a low velocity-high gas flow rate stream and vice versa.	Short gas residence time complicates the measuring of meaningful kinetic.
						Intensifies heat and mass transfer rates.	Lack of adsorption tests and CO2 capture analysis.
						Uniform packing of the bed of particles	Using narrower slots achieve lower gas volumetric flow rates to produce the desired uniform packed state.
Food	[129]	Food processing	Experimental study	Determine viability of high-temperature potato puffing in a SFB reactor	Potato	Successful puffing process at 200°C for a wide range of moisture content	Experiments to determine the effect of bed loading and process duration in puffing performance.
	[130]		Technology description	Describe the SFB technology principle of operation in different food processing operations	Bulk food	High heat transfer rates. Energy and ecologically efficient. Controllable processing. Compact size.	Lack of experiments and technical data about operation
Recycling	[12]	Pyrometallurgical recycling	Theoretical research	Describe SFB technology and its application in recycling processes	Metallurgical wastes	Treating fine powder potentially eliminates briquetting and pelletization stages.	Wear due to fluidization of treated material.
						Compact size, higher specific throughput, and quick start-up and shut down.	Limitation for longer retention times.

	[131]	Calcination	Experimental study	Describe the improvement of a calcination process of spent potlining using the SFB technology	Spent potlining	Successful improvement of a plant for 10000 TPa commercial level, reducing the environmental impact of wastes. Increased specific unit capacity without diminishing process performance	Cheaper sources of calcium may also be used, such as gypsum.
Contaminants control	[46]	Dry gas scrubbing	Application description	Describe the use of SFB technology in dry gas scrubbing processes.	Exhaust gases from combustion	The geometry and gas flow patterns of the SFB reactor maintain the material in the scrubber until the gas flow drags the particles due to size reduction. Extend the bag filter life to its full expectancy and reduce the usage of reagents in the scrubber. Short residence times.	Develop experiments to evaluate the effect of operating conditions on performance.
Mineral processing	[25]	Flash roasting	Theoretical research	Propose the use of SFB technology for the flash roasting of sulfides	Zinc sulfide	Very fine particle processing capability, lower cost, smaller roasters, waste minimization, improved leaching efficiency, and overall process simplification. Avoid ferrite formation, which reduces the use of hot strong acid leaching to break down ferrites.	Timely evaluation of the SFB reactor to roast zinc sulfide concentrates requires close temperature control to minimize ferrite formation and avoid molten eutectics.
	[132]	Flash roasting	Experimental study	Evaluate the flash roasting of zinc sulfide concentrates on providing some insight into the morphology of the resulting calcines.	Zinc sulfide	The reactor can provide rapid, precisely controlled, and economical small-scale operation, and these features could solve a wide range of industrial problems.	Roasting at high temperatures appears to promote uneven roasting of the zinc concentrate, i.e., extensive oxidation or partial reactions. Evaluate residence times and the possibility of further comminution.

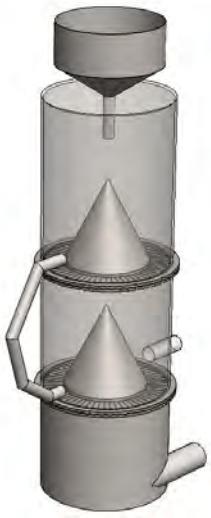

Figure 2-16 Multi-stage SFB reactor scheme. Source: Figure created by author.

2.3.3. Relevance of computational fluid dynamics in swirling fluidized bed design

Some of the selected articles developed CFD simulation models for the SFB reactor. The advantage of using CFD is the obtention of local properties, instead of global obtained in experimental studies, and the ease of testing the reactor with low economic cost. Most of the articles evaluate the behavior of the SFB reactor in a single-phase CFD simulation [54], [98], [100]–[104], [115], [133]. These studies evaluate the impact of design and operating parameters on the pressure drop across the distributor, the gas distribution, the tangential velocity of the air leaving the distributor, and the magnitude of the resultant velocity of the air. The two-phase CFD simulation performs more intensive computing tasks to numerically solve the drag models in the gas-solid interphase. Only 30% of the related articles develop two-phase models in the SFB reactor [59], [60], [90], [95]. The studies analyze flow regimes of the SFB reactor and the effect of design and operating parameters on the pressure drop across the bed, solid hold up distribution, pressure drop across the bed, and particle velocity profiles. The two-phase simulation allowed the study of drying rates and moisture content of the dried matter in drying processes [59], and the distributor, wall, and central body wear caused by the impact of particles with the boundaries [60].

2.4. Outlook

A deeper analysis of the systematic review of the SFB reactor technology, accompanied by the CFD model results, identified the trends for constructing a research agenda for advancing the investigation of the SFB reactor development. A first direction is establishing an experimentation route to determine critical operational variables and parameters in less studied applications, e.g., biomass gasification and pyrolysis. Another essential point is further studying the bed behavior to create analytical and semi-empirical models that predict SFB flow behavior under different operating conditions. Finally, another direction includes heat transfer and reacting models to the two-phase CFD models to obtain an insight into the reactor's bed behavior under these modes of operation.

2.4.1. Operating and design modeling

The experimental and simulation studies showed the influence of input and design parameters on the hydrodynamics and thermal performance of the SFB reactor. However, Table 2-5 depicts some unanalyzed relationships for future studies to develop models or identify patterns. This may simplify the decision-making during process design. For example, studies about the wall wear caused by the bed of particles in the SFB [60] and some geometry models to estimate the size of distributor components are the nearest to mechanical design [69], [82]. However, the gathered information did not show any study about the mechanical or thermal stresses due to the operation of the SFB in the walls and the distributor. Estimating stresses through analytical models in the components would enhance the SFB reactor design to obtain a device suitable for any specific application.

2.4.2. Experimentation route

The SFB reactor state-of-the-art showed its adaptability to process particulate material from different industries [9]. However, most studies about specific applications, e.g., mineral processing and biomass valorization routes different from combustion, address case studies or promotional approaches. The execution of experiments in these applications enables the analysis of relationships between operating variables, input parameters, and recognition patterns. This facilitates to study of the variation of process performance and product yield and quality with the operating conditions, as in the case of experimental combustion studies [21], [56], [108]. Furthermore, these works are the basis of prediction models for process design purposes.

2.4.3. CFD analysis

The advantages of these studies are that the equipment acquisition is unnecessary, and the control of input parameters is easier than in a laboratory prototype. However, the continuous development of these tools for the gas-solid SFB is still growing. In addition, most CFD studies report single-phase simulations which opens the possibility of further research in the two-phase simulations of SFB. These studies analyze the hydrodynamics of the bed, excluding heat and mass transfer and reacting phenomena. The inclusion of these phenomena provides insights into the complete operation of the SFB reactor, improving the design of the SFB reactor.

2.5. Conclusion

This paper developed a systematic review of the SFB reactor advancement using the PRISMA guidelines. The process resulted in a collection of 96 articles published from 1984 until 2021, classified according to the content-based analysis such as objectives, methodology, type of reactor, and application. The most common application of the SFB reactor was only for experimental purposes, which shows the interest in identifying relationships between operating variables and input or design parameters. While studying the SFB reactor with case studies approach is the less used methodology, showing low available information about actual SFB reactor installations.

The design and fabrication techniques of the SFB reactor vary according to the needs of the operation. The research results reported four different types of annular gas distributors: inclined holes, gill plate, single row blades, and three-row blades. The SFB reactor is classified as a compact and expanded bed depending on the form of the bed column. The compact bed reactor has a cylindrical column preferred to process

denser and bigger particles (1g-Geldart's D group) in shallow packed beds. On the other hand, the expanded bed reactor has a two sections column: tapered followed by cylindrical, where 1g-Geldart's A, B and C groups of particles, i.e., smaller particles, fluidize in a diffuse bed. The development of the SFB reactor is of high interest in various industries due to its capacity to process a wide range of particle from all the groups of the 1g-Geldart's classification, e.g., biomass whose size and shape varies from one type of biomass to other, and the preprocessing.

The SFB reactor reaches high gas-solid slip velocities, enhancing the process heat and mass transfer rates in small size devices. The early age of the SFB reactor has promoted an increased number of studies about the effect of the input and operating parameters on the bed behavior. The most related variables are the pressure drops across the bed and the distributor because of their strong relationship with the energy consumption required for the gas flow. These studies derived analytical and semi-empirical models for supporting the decision-making about the SFB reactor design.

Of other topics related to the SFB reactor applications, the most studied were combustion and drying in laboratory-scale reactors. The combustion in the SFB reactor showed good performance in controlling temperature and yielded efficiencies up to 99%. On the other hand, drying processes in the SFB reactor enhanced residence times and mass transfer rates compared to the conventional fluidized beds.

The use of CFD models for studying the SFB behavior has shown to be a relevant tool for obtaining local data on hydrodynamics. CFD studies predicted gas and particle velocity distribution and gained insight into flow regimes of the bed of particles using single and multiphase models. The advantage is the lower economic cost due to unnecessary equipment acquisition and easier change of operating and design conditions of the SFB reactor model.

Based on the systematic review, future research should focus on the analysis of relationships between less studied variables, simplified modeling of the operation and design of the reactor, and integration of heat and mass transfer phenomena to CFD studies. Further analytical works for studying the effect of input parameters in other variables (e.g., bed temperature and particle residence times) to derive simplified models for predicting the bed behavior. Also, we propose to develop design models that include mechanical and thermal stresses caused by operating conditions on the SFB components. Finally, studies using CFD simulation have two approaches: analyzing gas and solid velocity and acceleration fields to gain insights into the hydrodynamic of the SFB reactor, and integrating heat and mass transfer phenomena would improve model results related to heating and reacting applications.

2.6. References

[1] UNFCCC, "Adoption of the Paris Agreement", 2015. https://unfccc.int/resource/docs/2015/cop21/eng/l09r01.pdf

[2] Exxon Mobil, "2019 Outlook for Energy: A Perspective to 2040", 2019. [Online]. Available: https://corporate.exxonmobil.com/-/media/Global/Files/outlook-for-energy/2019-Outlook-for-Energy_v4.pdf

[3] A. I. Stankiewicz and J. A. Moulijn, "Process intensification: transforming chemical engineering", Chem. Eng. Prog., vol. 96, no. 1, pp. 22–34, 2000.

[4] H. Wang et al., "A review of process intensification applied to solids handling", Chem. Eng. Process. Process Intensif., vol. 118, pp. 78–107, 2017, doi: https://doi.org/10.1016/j.cep.2017.04.007.

[5] R. Law, C. Ramshaw, and D. Reay, "Process intensification – Overcoming impediments to heat and mass transfer enhancement when solids are present, via the IbD project", Therm. Sci. Eng. Prog., vol. 1, pp. 53–58, 2017, doi: https://doi.org/10.1016/j.tsep.2017.02.004.
[6] F. Scala, Fluidized Bed Technologies for near-Zero Emission Combustion and Gasification. Cambridge, UNITED KINGDOM: Elsevier Science & Technology, 2013. [Online]. Available: http://ebookcentral.proquest.com/lib/unorte-ebooks/detail.action?docID=1581395
[7] L. Theodore and D. C. Cortinhas, Chemical Reactor Analysis and Applications for the Practicing Engineer. New York, UNITED STATES: John Wiley & Sons, Incorporated, 2012. [Online]. Available: http://ebookcentral.proquest.com/lib/unorte-ebooks/detail.action?docID=818494
[8] V. V Kumar, V. R. Raghavan, V. Vinod Kumar, and V. R. Raghavan, "Developments in fluidized bed technology — A review", in 2011 National Postgraduate Conference, 2011, pp. 1–10. doi: 10.1109/NatPC.2011.6136395.
[9] Torftech Group, "An executive summary". Torftech Group.
[10] Torftech Group, "Torftech Pilot Plant Facilities". Torftech Group. [Online]. Available: http://www.torftech.com/
[11] C. E. Dodson, "Apparatus for processing matter in a turbulent mass of particulate material", US4479920, 1984
[12] C. E. Dodson and V. I. Lakshmanan, "An innovative gas-solid torbed reactor for the recycling industries", JOM, vol. 50, no. 7, pp. 29–31, 1998, doi: 10.1007/s11837-998-0189-6.
[13] Torftech Group, "TORBED Compact Bed Reactor ('CBR')". Torftech Group. [Online]. Available: http://www.torftech.com/
[14] G. A. Wellwood, "Hydrodynamic behaviour of the Torbed® reactor operating in fine particle mode", University of Queensland, 2000.
[15] Torftech Group, "TORBED Expanded Bed Reactor ("EBR")". Torftech Group. [Online]. Available: http://www.torftech.com/
[16] B. Sreenivasan and V. R. Raghavan, "Hydrodynamics of a swirling fluidised bed", Chem. Eng. Process. Process Intensif., vol. 41, no. 2, pp. 99–106, 2002, doi: https://doi.org/10.1016/S0255-2701(00)00155-0.
[17] C. S. Miin, S. A. Sulaiman, V. R. Raghavan, M. R. Heikal, and M. Y. Naz, "Hydrodynamics of multi-sized particles in stable regime of a swirling bed", Korean J. Chem. Eng., vol. 32, no. 11, pp. 2361–2367, 2015, doi: 10.1007/s11814-015-0151-6.
[18] M. H. M. Tawfik, M. Refaat Diab, and H. Mohmed Abdelmotalib, "An experimental investigation of wall-bed heat transfer and flow characteristics in a swirling fluidized bed reactor", Appl. Therm. Eng., vol. 155, no. April, pp. 501–507, 2019, doi: 10.1016/j.applthermaleng.2019.04.022.
[19] M. F. Mohideen, B. Sreenivasan, S. A. Sulaiman, and V. R. Raghavan, "Heat transfer in a swirling fluidized bed with geldart type-D particles", Korean J. Chem. Eng., vol. 29, no. 7, pp. 862–867, 2012, doi: 10.1007/s11814-011-0255-6.
[20] P. Arromdee and V. I. Kuprianov, "A comparative study on combustion of sunflower shells in bubbling and swirling fluidized-bed combustors with a cone-shaped bed", Chem. Eng. Process. Process Intensif., vol. 62, pp. 26–38, 2012, doi: 10.1016/j.cep.2012.10.002.
[21] V. I. Kuprianov, R. Kaewklum, and S. Chakritthakul, "Effects of operating conditions and fuel properties on emission performance and combustion efficiency of a swirling fluidized-bed combustor fired with a biomass fuel", Energy, vol. 36, no. 4, pp. 2038–2048, 2011, doi: 10.1016/j.energy.2010.05.026.
[22] J. H. Zakaria, M. H. H. M. Zaid, M. F. M. Batcha, and N. Asmuin, "Feasibility study on pliant media drying using fluidized bed dryer", IOP Conf. Ser. Mater. Sci. Eng., vol. 88, no. 1, 2015, doi: 10.1088/1757-899X/88/1/012071.
[23] M. Hamdan, S. Sabudin, M. Faizal, and V. R. Raghavan, "Experimental studies on oil palm frond drying using swirling fluidized bed dryer", AIP Conf. Proc., vol. 1440, no. Imat 2011, pp. 1212–1219, 2012, doi: 10.1063/1.4704339.

[24] J. R. McDonough, R. Law, D. A. Reay, D. Groszek, and V. Zivkovic, "Miniaturisation of the toroidal fluidisation concept using 3D printing", Chem. Eng. Res. Des., vol. 160, pp. 129–140, 2020, doi: 10.1016/j.cherd.2020.04.031.
[25] C. Dodson, V. Lakshmanan, R. Laughlin, and R. Sridhar, "Flash roasting of sulphide concentrates and leach residues using a TORBED reactor", EPD Congr. 1999, pp. 1–5, 1999, [Online]. Available: http://scholar.google.com/scholar?hl=en&btnG=Search&q=intitle:FLASH+ROASTING+OF+SULPHIDE+CONCENTRATES+AND+LEACH+RESIDUES+USING+A+TORBED+*+REACTOR#0
[26] C. E. Dodson, "Particle Treatment in an Expanded Toroidal Bed Reactor", US2008286164A1, 2009
[27] C. E. Dodson and G. A. Wellwood, "Process and Apparatus for Treating Particulate Matter", CA2305260A1, 1999
[28] T. Werner and M. Gross, "Bottom Element for a Device for Treating Particulate Material", US6705025B2, 2004
[29] V. Mirabelli and T. Nigris, "Fluid bed apparatus for the treatment of solid particles and fluidizing gas distributor disk for this apparatus", ITMI20111125A1, 2012
[30] H. Hüttlin, "Fluidized Bed Apparatus for Treating Particulate Materials", US5282321A, 1994
[31] M. Cremers et al., Status overview of torrefaction technologies, no. December. 2015.
[32] S. Negi, G. Jaswal, K. Dass, K. Mazumder, S. Elumalai, and J. K. Roy, "Torrefaction: a sustainable method for transforming of agri-wastes to high energy density solids (biocoal)", Rev. Environ. Sci. Biotechnol., vol. 19, no. 2, pp. 463–488, 2020, doi: 10.1007/s11157-020-09532-2.
[33] P. Costa, F. Pinto, R. N. André, and P. Marques, "Integration of gasification and solid oxide fuel cells (SOFCs) for combined heat and power (CHP)", Processes, vol. 9, no. 2, pp. 1–26, 2021, doi: 10.3390/pr9020254.
[34] R. Thomson, P. Kwong, E. Ahmad, and K. D. P. Nigam, "Clean syngas from small commercial biomass gasifiers; a review of gasifier development, recent advances and performance evaluation", Int. J. Hydrogen Energy, vol. 45, no. 41, pp. 21087–21111, 2020, doi: 10.1016/j.ijhydene.2020.05.160.
[35] W. M. Lewandowski, M. Ryms, and W. Kosakowski, "Thermal biomass conversion: A review", Processes, vol. 8, no. 5, 2020, doi: 10.3390/PR8050516.
[36] O. S. Stamenković et al., "Production of biofuels from sorghum", Renew. Sustain. Energy Rev., vol. 124, no. June 2019, 2020, doi: 10.1016/j.rser.2020.109769.
[37] D. Moher, A. Liberati, J. Tetzlaff, and D. G. Altman, "Preferred reporting items for systematic reviews and meta-analyses: the PRISMA statement", BMJ, vol. 339, p. b2535, Jul. 2009, doi: 10.1136/bmj.b2535.
[38] C. E. Dodson, "Processes in which matter is subjected to fluid flow", GB2211597B, 1991
[39] C. E. Dodson, "Heating matter", GB2219521B, 1991
[40] J. Shu, V. I. Lakshmanan, and C. E. Dodson, "Hydrodynamic study of a toroidal fluidized bed reactor", Chem. Eng. Process. Process Intensif., vol. 39, no. 6, pp. 499–506, 2000, doi: 10.1016/S0255-2701(00)00097-0.
[41] C. E. Dodson, "Particle treatment in a toroidal bed reactor", US6108935A, 2000
[42] F. Ouyang and O. Levenspiel, "Spiral Distributor for Fluidized Beds", Ind. Eng. Chem. Process Des. Dev., vol. 25, no. 2, pp. 504–507, 1986, doi: https://doi.org/10.1021/i200033a026.
[43] H. Hüttlin, "Fluidized Bed Apparatus for the Production and/or Further Treatment of Granulate Material", US4970804, 1990
[44] Torftech Group, "Industrial and Commercial Mineral & Chemical Processing". Torftech Group. [Online]. Available: http://www.torftech.com/
[45] Torftech Group, "Energy products from wood waste". Torftech Group, 2009. [Online]. Available: http://www.tappi.org/content/events/09epe/papers/49.2.pdf
[46] Torftech Group, "Dry Gas Scrubbing". Torftech Group. [Online]. Available: http://www.torftech.com/
[47] Torftech Group, "Topell Energy of Netherlands to construct 60,000 tonne/annum biomass torrefaction plant using TORBED Energy Technologies", 2010. http://torftech.blogspot.com/2010/01/topell-energy-of-netherlands-to.html (accessed Jan. 01, 2022).
[48] P. C. Albert Bergman, "Method and device for treating biomass", US20130298457A1, 2013

[49] Torftech Group, "Energy Production from Biomass and Wastes". Torftech Group. [Online]. Available: http://www.torftech.com/
[50] V. I. Kuprianov, R. Kaewklum, K. Sirisomboon, P. Arromdee, and S. Chakritthakul, "Combustion and emission characteristics of a swirling fluidized-bed combustor burning moisturized rice husk", Appl. Energy, vol. 87, no. 9, pp. 2899–2906, 2010, doi: https://doi.org/10.1016/j.apenergy.2009.09.009.
[51] P. Arromdee, V. I. Kuprianov, R. Kaewklum, and K. Sirisomboon, "Experimental study on combustion of sunflower shells in a pilot swirling fluidized-bed combustor", Energy and Fuels, vol. 24, no. 7, pp. 3850–3859, 2010, doi: 10.1021/ef100119c.
[52] R. Kaewklum and V. I. Kuprianov, "Experimental studies on a novel swirling fluidized-bed combustor using an annular spiral air distributor", Fuel, vol. 89, no. 1, pp. 43–52, 2010, doi: https://doi.org/10.1016/j.fuel.2009.07.027.
[53] S. Chakritthakul and V. I. Kuprianov, "Co-firing of eucalyptus bark and rubberwood sawdust in a swirling fluidized-bed combustor using an axial flow swirler", Bioresour. Technol., vol. 102, no. 17, pp. 8268–8278, 2011, doi: 10.1016/j.biortech.2011.06.056.
[54] M. Faizal, M. S. Suzairin, M. Al-Hafiz, and V. R. Raghavan, "CFD Studies on Velocity Distribution of Air in a Swirling Fluidized Bed", Adv. Mater. Res., vol. 468–471, pp. 25–29, 2012, doi: 10.4028/www.scientific.net/AMR.468-471.25.
[55] M. F. Mohideen, S. Md Seri, and V. R. Raghavan, "Fluidization of Geldart Type-D particles in a swirling fluidized bed", Appl. Mech. Mater., vol. 110–116, pp. 3720–3727, 2012, doi: 10.4028/www.scientific.net/AMM.110-116.3720.
[56] R. Kaewklum, V. I. Kuprianov, and P. L. Douglas, "Hydrodynamics of air-sand flow in a conical swirling fluidized bed: A comparative study between tangential and axial air entries", Energy Convers. Manag., vol. 50, no. 12, pp. 2999–3006, 2009, doi: 10.1016/j.enconman.2009.07.019.
[57] M. Y. Naz and S. A. Sulaiman, "PTV profiling of particles motion from the top and side of a swirling fluidized bed", J. Instrum., vol. 11, no. 05, pp. P05019–P05019, 2016, doi: 10.1088/1748-0221/11/05/P05019.
[58] S. A. Sulaiman, C. S. Miin, M. Y. Naz, and V. R. Raghavan, "Particle Image Velocimetry of a Swirling Fluidized Bed at Different Blade Angles", Chem. Eng. Technol., vol. 39, no. 6, pp. 1151–1160, Jun. 2016, doi: 10.1002/ceat.201500074.
[59] M. E. Simanjuntak, P. Prabowo, D. Ichsani, and W. A. Widodo, "Transient 3D modeling of swirl fluidized bed coal drying: The effect of different angles of guide vane", JP J. Heat Mass Transf., vol. 13, no. 4, pp. 497–510, Nov. 2016, doi: 10.17654/HM013040497.
[60] Q. Wu, S. Wang, K. Zhang, Y. Zhao, and Y. He, "Numerical studies of gas-solid flow behaviors and wall wear in a swirling fluidized bed", Powder Technol., vol. 388, pp. 233–240, 2021, doi: 10.1016/j.powtec.2021.04.083.
[61] D. Díaz Tovar, "Transformación tecnológica sustentable de cascarilla de arroz producida en los principales molinos del Departamento de Casanare. Tesis maestría.", no. June, pp. 1–163, 2020, doi: 10.13140/RG.2.2.34608.99845.
[62] Torftech Group, "Biomass Gasification Technology Presentation", no. May. Torftech Group, p. 48, 2020. [Online]. Available: https://making.com/wp-content/uploads/2021/06/20-05-21-Biomass-Gasification-Technology-Presentation.pdf
[63] M. F. Mohideen Batcha, "Swirling Fluidized Bed", MY164018A, 2017
[64] J. A. Kostuch and C. E. Dodson, "Furnace having Toroidal Fluid Flow Heating Zone", 2000
[65] C. Dodson, "Material processing system and method", GB2574569A, 2019
[66] C. E. Dodson, "Process for Treating a Material in a Toroidal Fluidized-Bed with Electromagnetic Radiations", WO2019145735A1, 2019
[67] C. Dodson, "Toroidal Bed Reactor", GB2558162A, 2018
[68] C. Dodson, "Toroidal Bed Reactor", US10245573B2, 2019
[69] M. Paulose, "Hydrodynamic Study of Swirling Fluidized Bed and the Role of Distributor", COCHIN UNIVERSITY OF SCIENCE AND TECHNOLOGY, 2006.

[70] A. Bakhurji, X. Bi, and J. R. Grace, "Hydrodynamics and solids mixing in fluidized beds with inclined-hole distributors", Particuology, vol. 43, pp. 19–28, 2019, doi: 10.1016/j.partic.2018.01.011.
[71] M. Y. Naz, S. A. Sulaiman, S. Shukrullah, A. Ghaffar, Y. Khan, and I. Ahmad, "PIV investigations on particle velocity distribution in uniform swirling regime of fluidization", Granul. Matter, vol. 19, no. 2, 2017, doi: 10.1007/s10035-017-0727-4.
[72] M. A. Javed, S. Shukrullah, M. Y. Naz, and R. A. Sarfraz, "Image velocimetry and statistical analysis of a mesh-coupled axial blade distributor for mass transfer in a swirling bed", J. Theor. Appl. Mech., vol. 58, no. 3, pp. 779–790, 2020, doi: 10.15632/JTAM-PL/120806.
[73] M. Y. Naz, S. A. Sulaiman, Y. Khan, A. Ghaffar, Y. Jamil, and I. Ahmad, "Study of particle dynamics in a swirling fluidized bed by using a mesh-type air distributor", J. Porous Media, vol. 21, no. 11, pp. 1059–1068, 2018, doi: 10.1615/JPorMedia.2018021481.
[74] M. Y. Naz, S. Shukrullah, S. A. Sulaiman, Y. Khan, M. A. S. Alkanhal, and A. Ghaffar, "Particle image velocimetry analysis of a swirling bed operation by using a mesh-coupled annular air distributor", J. Brazilian Soc. Mech. Sci. Eng., vol. 41, no. 9, pp. 1–8, 2019, doi: 10.1007/s40430-019-1857-x.
[75] S. Shukrullah, M. A. Javed, M. Y. Naz, Y. Khan, M. A. S. S. Alkanhal, and H. Anwar, "PIV and Statistical Analysis of a Swirling Bed Process Carried out Using a Hybrid Model of Axial Blade Distributor", Process. , vol. 7, no. 10, 2019, doi: 10.3390/pr7100697.
[76] S. Shukrullah, M. Y. Naz, A. Ghaffar, Y. Khan, A. A. Al-Arainy, and R. Meer, "Experimental and statistical validation of data on mesh-coupled annular distributor design for swirling fluidized beds", Processes, vol. 8, no. 5, 2020, doi: 10.3390/PR8050632.
[77] S. Shukrullah, M. A. Javed, M. Y. Naz, N. M. AbdEl-Salam, K. A. Ibrahim, and A. Ghaffar, "Velocimetry and response surface regression analysis of a swirling bed tested with mesh-coupled axial blade distributor", Rev. Sci. Instrum., vol. 91, no. 4, p. 45106, Apr. 2020, doi: 10.1063/1.5132312.
[78] C. E. Dodson and R. G. W. Laughlin, "Novel Thermal Treatment Capability of the TORBED ® Process Reactor Technologies", Ontario, 1998.
[79] M. T. Mcqueen, "Energy and High Surface Area Siliceous Ash From the Combustion of Rice Hulls", in Proceedings of 17th FBC: 17TH International Fluidized Bed Combustion Conference, May 2003, pp. 721–728. doi: 10.1115/FBC2003-018.
[80] G. J. Jun, V. R. Raghavan, and C. Y. Sing, "Experimental study on the hydrodynamics of swirling fluidized bed", Appl. Mech. Mater., vol. 229–231, pp. 756–760, 2012, doi: 10.4028/www.scientific.net/AMM.229-231.756.
[81] G. J. Jun, "Characterization of Swirling Fluidized Bed", Universiti Teknologi Petronas, 2012.
[82] V. K. Venkiteswaran, "Study of Hydrodynamic Properties of Swirling Fluidized Bed", Universiti Teknologi PETRONAS, 2014. [Online]. Available: http://utpedia.utp.edu.my/15439/
[83] K. V. Vinod, M. F. Batcha, and V. R. Raghavan, "Study of the Fluid Dynamic Performance of Distributor Type in Torbed Type Reactors", Eng. e-Transaction, vol. 6, no. 1, pp. 70–75, 2011.
[84] A. S. M. Yudin, V. R. Raghavan, and M. Narahari, "A mathematical model for residence time distribution analysis in swirling fluidized bed", 2011 Natl. Postgrad. Conf. - Energy Sustain. Explor. Innov. Minds, NPC 2011, no. Figure 2, pp. 1–5, 2011, doi: 10.1109/NatPC.2011.6136392.
[85] S. Fauzan Ashri, "The Effectiveness of Multi-Staged Swirling Fluidized Bed", Universiti Teknologi Petronas, 2012.
[86] V. K. Venkiteswaran, G. J. Jun, C. Y. Sing, S. A. Sulaiman, and V. R. Raghavan, "Variation of Bed Pressure Drop with Particle Shapes in a Swirling Fluidized Bed", J. Appl. Sci., vol. 12, no. 24, pp. 2598–2603, 2012, doi: 10.3923/jas.2012.2598.2603.
[87] M. F. Mohideen Batcha, S. A. Sulaiman, and V. R. Raghavan, "Hydrodynamics of oil palm frond in a swirling fluidized bed dryer", Appl. Mech. Mater., vol. 117–119, pp. 1829–1833, 2012, doi: 10.4028/www.scientific.net/AMM.117-119.1829.
[88] D. V. Venkiteswaran, S. Sulaiman, and V. Raghavan, "Comparative Study of the Hydrodynamic Performance of Shorter and Longer Blades in a Swirling Fluidized Bed", Adv. Mater. Res., vol. 772, pp. 560–565, Sep. 2013, doi: 10.4028/www.scientific.net/AMR.772.560.

[89] S. Sabudin, W. S. I. W. Salim, and M. F. M. Batcha, "Cold flow behaviour of a swirling fluidized bed incinerator", ARPN J. Eng. Appl. Sci., vol. 11, no. 18, pp. 11129–11134, 2016.
[90] P. Arromdee and K. Sirisomboon, "Effects of Air Distributor Systems on Flow Behaviors in a Twin-Cyclonic", vol. 3, no. 1, pp. 23–27, 2017.
[91] N. S. Haron, J. H. Zakaria, and M. F. M. Batcha, "Hydrodynamics study on drying of pepper in swirling fluidized bed dryer (SFBD)", IOP Conf. Ser. Mater. Sci. Eng., vol. 226, no. 1, 2017, doi: 10.1088/1757-899X/226/1/012053.
[92] P. Ninduangdee, P. Arromdee, C. Se, and V. I. Kuprianov, "Effects of (Co-)Combustion Techniques and Operating Conditions on the Performance and NO Emission Reduction in a Biomass-Fueled Twin-Cyclone Fluidized-Bed Combustor", Waste and Biomass Valorization, vol. 11, no. 10, pp. 5375–5391, 2020, doi: 10.1007/s12649-020-01124-z.
[93] M. H. M. Tawfik, M. R. Diab, and H. M. Abdelmotalib, "Heat transfer and bed dynamics study on a swirling fluidized bed under various inlet configurations", Int. J. Therm. Sci., vol. 158, no. February, p. 106523, 2020, doi: 10.1016/j.ijthermalsci.2020.106523.
[94] M. H. M. Tawfik, M. R. Diab, and H. M. Abdelmotalib, "Heat transfer and hydrodynamics of particles mixture in swirling fluidized bed", Int. J. Therm. Sci., vol. 147, no. October 2019, p. 106134, 2020, doi: 10.1016/j.ijthermalsci.2019.106134.
[95] K. Sirisomboon and P. Arromdee, "A computational fluid dynamics study of gas–solid distribution of Geldart Group B particles in a swirling fluidized bed", Powder Technol., vol. 393, pp. 734–750, 2021, doi: 10.1016/j.powtec.2021.08.020.
[96] T. C. Sheng, S. A. Sulaiman, and V. Kumar, "One-dimensional modeling of hydrodynamics in a swirling fluidized bed", Int. J. Mech. Mechatronics Eng., vol. 12, no. 6, pp. 13–22, 2012.
[97] M. F. Mohideen, S. M. Seri, V. Kumar, and V. R. Raghavan, "Experimental studies on a swirling fluidized bed with annular distributor", J. Appl. Sci., vol. 11, no. 11, pp. 1980–1986, 2011, doi: 10.3923/jas.2011.1980.1986.
[98] M. Faizal, S. M. Seri, S. Ezamuddin, and V. R. Raghavan, "Numerical investigation of air flow distribution in a swirling fluidized bed", Adv. Mater. Res., vol. 499, no. 2012, pp. 132–137, 2012, doi: 10.4028/www.scientific.net/AMR.499.132.
[99] S. Sabudin, "Flow Visualization in a Swirling Fluidized Bed", Anal. Woven Nat. Fiber Fabr. Prep. Using Self-Designed Handloom, no. July, pp. 1–3, 2013.
[100] M. A. Hafiz, M. F. M. Batcha, and N. Asmuin, "Effect of plenum chamber depth in a swirling fluidized bed", IOP Conf. Ser. Mater. Sci. Eng., vol. 50, no. 1, 2013, doi: 10.1088/1757-899X/50/1/012021.
[101] H. Hussein, M. A. M. Nawi, M. H. M. Hazwan, D. L. J. Feng, K. M. Y. K. Ibrahim, and M. L. A. Latif, "Effect of plenum chamber design on discharge coefficient in swirling fluidized bed", AIP Conf. Proc., vol. 2291, no. November, 2020, doi: 10.1063/5.0022910.
[102] H. Hussein, M. A. M. Nawi, M. H. M. Hazwan, M. L. A. Latif, and K. M. Y. K. Ibrahim, "Design of experiment (DOE) analysis in optimizing of annular blade distributor depth in fluidization system", AIP Conf. Proc., pp. 020049-1-020049–8, 2020, doi: 10.1063/5.0022909.
[103] M. F. M. Batcha, M. A. H. M. Nawi, S. A. Sulaiman, and V. R. Raghavan, "Numerical investigation of airflow in a swirling fluidized bed", Asian J. Sci. Res., vol. 6, no. 2, pp. 157–166, 2013, doi: 10.3923/ajsr.2013.157.166.
[104] R. M. Zulkifli et al., "Influence of Twisted Blades Distributor Towards Low Pressure Drop in Fluidization Systems BT - Intelligent Manufacturing and Mechatronics", 2021, pp. 703–711.
[105] M. Y. Naz, S. A. Sulaiman, and M. A. Bou-Rabee, "Particle tracking velocimetry investigations on density dependent velocity vector profiles of a swirling fluidized bed", Dry. Technol., vol. 35, no. 2, pp. 193–202, Jan. 2017, doi: 10.1080/07373937.2016.1166124.
[106] K. Sirisomboon and P. Laowthong, "Experimental investigation and prediction of heat transfer in a swirling fluidized-bed combustor", Appl. Therm. Eng., vol. 147, no. August 2018, pp. 718–727, 2019, doi: https://doi.org/10.1016/j.applthermaleng.2018.10.097.
[107] V. I. Kuprianov, R. Kaewklum, K. Sirisomboon, P. Arromdee, and S. Chakritthakul, "Improvement of combustion efficiency and minimizing CO and NO emissions of a swirling fluidized-bed combustor

firing rice husk", 2009 Int. Conf. Clean Electr. Power, ICCEP 2009, pp. 9–16, 2009, doi: 10.1109/ICCEP.2009.5212089.
[108] M. F. Othaman, S. Sabudin, and M. F. M. Batcha, "Emission studies from combustion of empty fruit bunch pellets in a fluidized bed combustor", IOP Conf. Ser. Mater. Sci. Eng., vol. 226, no. 1, p. 12003, 2017, doi: 10.1088/1757-899x/226/1/012003.
[109] M. F. Mohideen Batcha, M. F. Othaman, S. Sabudin, A. N. Mohammed, M. K. Abdullah, and M. F. M. Ali, "Combustion and emission of pelletized empty fruit bunch and oil palm shell in a swirling fluidized bed combustor", Biomass Convers. Biorefinery, vol. 10, no. 3, pp. 755–763, 2020, doi: 10.1007/s13399-020-00903-x.
[110] V. I. Kuprianov, R. Kaewklum, and K. Janvijitsakul, "A Study of Firing Rice Husk in a Swirling Fluidized-Bed Combustor Using Annular Spiral Air Distributor", pp. 26–31, 2008.
[111] M. E. Simanjuntak, Prabowo, D. Ichsani, and W. A. Widodo, "Experimental study on the effect of temperature and fluidization velocity on coal swirl fluidized bed drying with 100 angle of blade inclination", ARPN J. Eng. Appl. Sci., vol. 11, no. 21, pp. 12499–12505, 2016.
[112] A. Sitorus, Novrinaldi, S. A. Putra, I. S. Cebro, and R. Bulan, "Modelling drying kinetics of paddy in swirling fluidized bed dryer", Case Stud. Therm. Eng., no. April, p. 101572, 2021, doi: 10.1016/j.csite.2021.101572.
[113] J. H. Zakaria, M. F. M. Batcha, and N. Asmuin, "Thin layer models for sponge media drying", ARPN J. Eng. Appl. Sci., vol. 11, no. 18, pp. 11209–11214, 2016.
[114] H. Pawlak–Kruczek et al., "Drying of Lignite of Various Origins in a Pilot Scale Toroidal Fluidized Bed Dryer using Low Quality Heat", Energies, vol. 12, no. 7, 2019, doi: 10.3390/en12071191.
[115] M. A. M. Nawi et al., "Effect of twist blade distributor on velocity distribution in a swirling fluidized bed", IOP Conf. Ser. Mater. Sci. Eng., vol. 932, no. 1, 2020, doi: 10.1088/1757-899X/932/1/012113.
[116] Y. Yan, B. Qi, W. Zhang, X. Wang, and Q. Mo, "Investigations into the drying kinetics of biomass in a fluidized bed dryer using electrostatic sensing and digital imaging techniques", Fuel, vol. 308, p. 122000, 2022, doi: https://doi.org/10.1016/j.fuel.2021.122000.
[117] R. M. Moreno, G. Antolín, and A. E. Reyes, "Mass transfer during forest biomass particles drying in a fluidised bed", Biosyst. Eng., vol. 198, pp. 163–171, 2020, doi: https://doi.org/10.1016/j.biosystemseng.2020.08.003.
[118] M. F. Mohideen, M. Faiz, H. Salleh, H. Zakaria, and V. R. Raghavan, "Drying of oil palm frond via swirling fluidization technique", in Proceedings of the World Congress on Engineering 2011, WCE 2011, 2011, vol. 3, pp. 2375–2380.
[119] J. H. Zakaria, M. H. H. Md Zaid, M. F. Mohideen Batcha, and N. Asmuin, "Drying of sponge media using swirling fluidized bed dryer", Appl. Mech. Mater., vol. 660, pp. 644–648, 2014, doi: 10.4028/www.scientific.net/AMM.660.644.
[120] R. Blissett, R. Sommerville, N. Rowson, J. Jones, and B. Laughlin, "Valorisation of rice husks using a TORBED® combustion process", Fuel Process. Technol., vol. 159, pp. 247–255, 2017, doi: https://doi.org/10.1016/j.fuproc.2017.01.046.
[121] J. Udomsup and P. Choomjaihan, "The effects of operating conditions and the biomass component on combustion efficiency and emission performance of a swirling fluidized-bed combustor fired using", Agric. Eng. Int. CIGR J., vol. 23, no. 2, pp. 195–202, 2021.
[122] C. Dodson, "Building on rice", Process Eng., vol. 85, no. 6, pp. 25–27, 2004.
[123] Torftech Group, "Energy & Amorphous Silica Production from Rice Husk". Torftech Group. [Online]. Available: http://www.torftech.com/
[124] Torftech Group, "Fine Powder Processing". Torftech Group. [Online]. Available: http://www.torftech.com/
[125] Torftech Group, "Fuel Injection". Torftech Group. [Online]. Available: http://www.torftech.com/
[126] Torftech Group, "Catalyst & Zeolite Processing". Torftech Group. [Online]. Available: http://www.torftech.com/
[127] Torftech Group, "Toroidal Fluidised Bed Reactor for Mineral Processing". Torftech Group.

[128] J. R. McDonough, R. Law, D. A. Reay, and V. Zivkovic, "Intensified carbon capture using adsorption: Heat transfer challenges and potential solutions", Therm. Sci. Eng. Prog., vol. 8, no. February, pp. 17–30, 2018, doi: 10.1016/j.tsep.2018.07.012.
[129] A. I. Varnalis, J. G. Brennan, and D. B. MacDougall, "Proposed mechanism of high-temperature puffing of potato. Part I. The influence of blanching and drying conditions on the volume of puffed cubes", J. Food Eng., vol. 48, no. 4, pp. 361–367, 2001, doi: 10.1016/S0260-8774(00)00197-7.
[130] Planet Dryers Ltd Food Machinery Suppliers, "Torbed Hot Air Processors". Planet Dryers Ltd, 2014. [Online]. Available: www.planetdryers.co.uk
[131] T. Hopkins and P. Merline, "Comtor Process for Treatment of Spent Potlining", Miner. Process. Extr. Metall. Rev., vol. 15, no. 1–4, pp. 247–255, 1995, doi: 10.1080/08827509508914203.
[132] T. T. Chen and J. E. Dutrizac, "Characterization of the calcines produced by the roasting of zinc sulphide concentrates in a torbed reactor", Can. Metall. Q., vol. 42, no. 1, pp. 1–16, 2003, doi: 10.1179/cmq.2003.42.1.1.
[133] M. A. M. Nawi et al., "The effect of multi-staged swirling fluidized bed on air flow distribution", IOP Conf. Ser. Mater. Sci. Eng., vol. 864, no. 1, 2020, doi: 10.1088/1757-899X/864/1/012194.
[134] M. S. Muhamad Silmie et al., "A Short Review on Multi-stage Application in Fluidization Systems BT - Intelligent Manufacturing and Mechatronics", 2021, pp. 713–720.

3. Computational Fluid Dynamics Model-Based Analysis of Flow Patterns in a Gas-Solid Swirling Fluidized Bed Reactor

Abstract

The Swirling Fluidized Bed reactor or SFB is a gas-solid rotating fluidized bed that is gaining interest for biomass processing. In contrast with conventional fluidized beds, the SFB reactor reaches higher gas-solid slip velocities, achieving denser beds with a more uniform particles distribution. The SFB reactor enhances the gas-solid transfer of momentum, heat, and mass while expands the range of particle sizes and shapes able to fluidize. The study of complex fluid phenomena with numerical simulation techniques, such as Computational Fluid Dynamics (CFD), has shown good agreement with experimental data when modeling gas-solid fluidized beds. Advantages of CFD simulation include lower cost compared to experimental studies because of removing the need of acquiring equipment for testing. This work develops a CFD-based simulation of a gas-solid SFB reactor in the open-source software OpenFOAM®. Comparison between simulated and experimental data enables the validation of the CFD model. The bed hydrodynamics study includes the solids volume fraction, the solids and gas velocities, and solids centrifugal acceleration. The analysis gives insight into the rotational and swirling motions in the SFB reactor. Air jet velocity of 67 m s^{-1} promotes the rotation of the bed generating a maximum solids azimuthal velocity of 1.37 m s^{-1} at the bottom of the bed. Axial kinetic energy dissipation together with the gas radial velocity changing its direction from outward to inward of the reactor when moving upwardly across the bed contributes to the swirling motion the bed. The rotation of the bed is subjected to an average centrifugal acceleration of 0.07-0.48 times the Earth's gravitational field. Further works should focus on parametric studies to identify optimum operating conditions and analyze the interparticle and particle-wall heat transfer behavior of the SFB reactor.

3.1. Introduction

The Swirling Fluidized Bed (SFB) reactor is a gas-solid contacting device for processing particulate material in an annular or toroidal-shaped centrifugal fluidized bed. Compared to a conventional fluidized bed, operating in SFB reactor results in denser beds of particles and higher gas-solid slip velocities, thus enhancing the interfacial transfer of momentum, heat, and mass [1], [2]. As a result, the device is gaining high interest for processing particles in different industries, e.g., mineral processing, food, and energy [3], [4]. Figure 3-1 shows a schematic of the SFB reactor. The annular gas distributor of the SFB reactor consists of a central body (a cone or a cylinder) on a disc and an array of stationary overlapping inclined blades at the periphery of the disc [5]. The central body enhances the distribution of the particles across the bed and avoids the formation of a dead zone. The reduced area and the inclined blades increase the gas velocity and steer its direction [6], [7]. The turbulent swirling flow formed above the distributor induces the change of angular momentum of the solid phase to generate a swirling fluidized bed of particles [8].

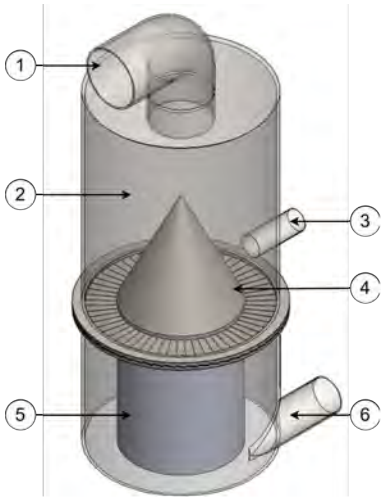

Figure 3-1 SFB reactor composition. The reactor comprises (1) the gas/product outlet, (2) the cylindrical outer wall column, (3) the solids inlet, (4) the annular single-row blade gas distributor, (5) the central support structure, and (6) the fluidizing gas inlet. Source: Figure created by author.

Previous studies about the SFB reactor focused on the hydrodynamics behavior [7], [9], using experimental and analytical model approaches. These studies showed the effect of gas superficial velocity, bed weight, and particle size on the pressure drop across the bed and angular velocity of the solids. Other studies focused on the thermal performance of the bed from an experimental side [10], [11]. The studies included the analysis of the effect of bed location, gas superficial velocity, particle size, and gas distributor design on the local heat transfer coefficient and the axial and radial temperature distribution.

Advancements in programming and numerical solutions enabled the solution of complex flow problems using computational fluid dynamics (CFD) simulations. Hence, a deeper understanding of gas-solid interactions in the SFB reactor is essential to improve and take further advantage of its unique features. Some authors studied the SFB reactor using a CFD simulation approach with single-

phase [12]–[14] and two-phase models [15], [16]. They studied the impact of operating parameters on the pressure drop across the distributor and the bed, the gas flow distribution, and particle velocity profiles. In addition, two-phase simulations allowed the analysis of solids distribution in the annular bed region, the formation of fluidizing bed regimes, and wall wear.

CFD studies about the SFB reactor showed good agreement with experimental results and great potential to gain insights into the operation of the SFB reactor. Previous works about a rotating fluidized bed reactor unit, i.e., a gas-solid vortex (GSV) reactor [17], [18], demonstrated that an experimental-supported CFD model extracts hydrodynamics details in flow patterns and profiles. This work describes the development of a gas-solid CFD simulation of the SFB reactor with the Eulerian-Eulerian approach in the open-source software OpenFOAM® v2106. In addition, the model is validated with experimental data. The simulation results include the analysis of azimuthal and radial velocities of gas and solids and the centrifugal acceleration of solids.

3.2. Methods

3.2.1. Experimental Setup

Figure 3-2 shows a schematic of the SFB reactor used in the simulation and based on the experimental study of Naz et al. [19]. The cylindrical outer wall of the SFB reactor is an acrylic glass cylinder with a diameter of 30 cm and a height of 60 cm. The distributor comprises a circumferential arrangement of sixty metal blades inclined 10° regarding a horizontal plane and a central hollow metal cone of 20 cm diameter. The annular region at the base of the cone has inner and outer diameters of 20 cm and 30 cm, respectively. Compressed air at different flow rates enters the reactor and flows upwardly. The transversal area in the space between blades determines the magnitude of the air injection velocity, while the inclination of blades determines the radial and tangential components. The SFB reactor operates in batch mode with 1.2 kg of spherical plastic beads of 6 mm diameter and 1312 kg m^{-3} density. The angular momentum transfer from the air to the particles during gas-solid contact causes the rotation of the bed. The net change of angular momentum of the gas passing through the solids bed equilibrates the torque of the azimuthal wall forces.

Naz et al. [19] developed a particle image velocimetry (PIV) study using a high-speed camera. They assumed uniform circular motion along the bed of particles to study only a quarter of the bed and repeated the experiment for six different air mass flow rates. The details of the PIV setup, accuracy, and image processing of the experiment are available in [19]. After filtering and interpolating data, they obtained the velocity vector fields of the particles in the bed.

There is not enough information about the central cone and the blade design required to calculate the geometrical parameters for generating the mesh. Then, the central cone height equals the diameter, i.e., 20 cm, and the distributor blade's thickness is 1 mm.

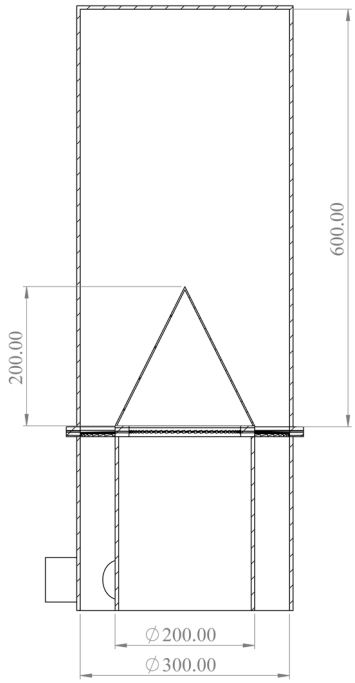

Figure 3-2 Schematic of the SFB reactor of the simulation. Dimensions are in mm. Source: Adapted from [19]. Source: Figure created by author.

3.2.2. Computational procedure

3.2.2.1. Governing equations

The model of the two-phase system uses the conservation equation from the Euler-Euler approach, with phases assumed as interpenetrating continua [20]. Equation (3-1) describes the average continuity equation of phase i (g or s).

$$\frac{\partial \alpha_i \rho_i}{\partial t} + \vec{\nabla} \cdot (\alpha_i \rho_i \vec{U}_i) = 0 \tag{3-1}$$

Equation (3-2) corresponds to the momentum equation for both phases

$$\frac{\partial \alpha_\mathrm{g} \rho_\mathrm{g} \vec{V}}{\partial t} + \vec{\nabla} \cdot (\alpha_\mathrm{g} \rho_\mathrm{g} \vec{V}\, \vec{V}) = -\alpha_\mathrm{g} \vec{\nabla} p + \vec{\nabla} \cdot \alpha_\mathrm{g} \bar{\bar{\tau}}_\mathrm{g} + \alpha_\mathrm{g} \rho_\mathrm{g} \vec{\mathrm{g}} + K_\mathrm{d}(\vec{V} - \vec{U}) \tag{3-2a}$$

$$\frac{\partial \alpha_\mathrm{s} \rho_\mathrm{s} \vec{U}}{\partial t} + \vec{\nabla} \cdot (\alpha_\mathrm{s} \rho_\mathrm{s} \vec{U}\, \vec{U}) = -\alpha_\mathrm{s} \vec{\nabla} p - \vec{\nabla} p_\mathrm{s} + \vec{\nabla} \cdot \bar{\bar{\tau}}_\mathrm{s} + \alpha_\mathrm{s} \rho_\mathrm{s} \vec{\mathrm{g}} - K_\mathrm{d}(\vec{V} - \vec{U}) \tag{3-2b}$$

And Equation (3-3) gives $\bar{\bar{\tau}}_i$, the ith phase stress-strain tensor:

$$\bar{\bar{\tau}}_i = \mu_{\mathrm{eff},i} \left(\vec{\nabla} \vec{U}_i + \vec{\nabla} \vec{U}_i^{\,T} \right) + \left(\lambda_i - \frac{2}{3} \mu_{\mathrm{eff},i} \right) (\vec{\nabla} \cdot \vec{U}_i) \bar{\bar{I}} \tag{3-3}$$

where λ_i is the bulk viscosity, and $\mu_{\mathrm{eff,i}}$ the effective dynamic viscosity. In the gas phase, the bulk viscosity λ_g is neglected, and $\mu_{\mathrm{eff,g}}$ is the sum of molecular viscosity $\mu_{\mathrm{m,g}}$ and turbulent viscosity $\mu_{\mathrm{t,g}}$, obtained from the $k-\epsilon$ turbulence model [21]. The kinetic theory of granular flow (KTGF) estimates simultaneously the bulk viscosity λ_s and the dynamic viscosity $\mu_{\mathrm{eff,s}}$ to solve the solid

phase. Equation (3-4) is the balance of granular energy required to calculate the shear viscosity, the bulk viscosity, and the solids pressure as a function of the granular temperature, equivalent to a dense gas thermodynamic temperature [20].

$$\frac{3}{2}\left[\frac{\partial}{\partial t}(\alpha_s\rho_s\Theta_s)+\vec{\nabla}\cdot(\alpha_s\rho_s\Theta_s\vec{U})\right]=(-\nabla p_s\bar{\bar{I}}+\bar{\bar{\tau}}_s):\vec{\nabla}\vec{U}+\vec{\nabla}\cdot(\kappa_s\vec{\nabla}\Theta_s)-\gamma_s-J_s \qquad (3\text{-}4)$$

The terms on the right side of Equation (3-4) are the creation of granular fluctuating energy due to shear in the solid phase, the diffusion of granular energy along the gradients in Θ_s, γ_s the dissipation due to inelastic interparticle collisions, and J_s the dissipation or creation of granular energy resulting from the fluctuating force exerted by the gas [20].

The analysis of three-dimensional turbulent shear flow equations combined with continuity and momentum equations form the $k-\epsilon$ turbulence model [22]. Equations (3-5) and (3-6) compute the turbulence kinetic energy k and the turbulence energy dissipation rate ϵ.

$$\frac{\partial}{\partial t}(\rho_g k)+\vec{\nabla}\cdot(\rho_g\vec{V}k)=\vec{\nabla}\cdot(\mu_{\text{eff},k}\nabla k)+p_k-\rho_g\epsilon \qquad (3\text{-}5)$$

$$\frac{\partial}{\partial t}(\rho_g\epsilon)+\vec{\nabla}\cdot(\rho_g\vec{V}\epsilon)=\vec{\nabla}\cdot(\mu_{\text{eff},\epsilon}\nabla\epsilon)+C_{\epsilon1}\frac{\epsilon}{k}p_k-C_{\epsilon2}\rho_g\frac{\epsilon^2}{k} \qquad (3\text{-}6)$$

Where the effective viscosity for turbulent kinetic energy $\mu_{\text{eff},k}$ and energy dissipation rate $\mu_{\text{eff},\epsilon}$ depends on molecular viscosity $\mu_{m,g}$ and turbulent viscosity $\mu_{t,g}$ as in Equation (3-7)

$$\mu_{\text{eff},k}=\mu_{m,g}+\frac{\mu_{t,g}}{\sigma_k} \qquad \mu_{\text{eff},\epsilon}=\mu_{m,g}+\frac{\mu_{t,g}}{\sigma_\epsilon} \qquad (3\text{-}7a,\ b)$$

$$\mu_{t,g}=\rho_g C_\mu\frac{k^2}{\epsilon} \qquad (3\text{-}7c)$$

With the turbulent Prandtl number P_{r_t} = 0.9, and other model constant values are $C_{\epsilon1}$ = 1.44, $C_{\epsilon2}$ = 1.92, C_μ = 0.09, σ_k = 1.0, and σ_ϵ = 1.9. Table 3-1 gives an overview of all constitutive equations used to estimate intermediate variables in the present work for solving the model.

The interphase drags force term couples both gas and solid momentum equations. Equation (3-8) gives the drag coefficient K_d estimated with Gidaspow's correlation combines the Ergun equation for solid-phase volume fractions $\alpha_s \geq 0.2$, with the correlation of Wen and Yu for $\alpha_s < 0.2$ [21].

$$\alpha_s<0.2:\ K_d=\frac{3}{4}C_D\frac{\alpha_s\alpha_g\rho_g|\vec{U}-\vec{V}|}{d_s}\alpha_g^{-2.65} \quad \text{with } C_D=\frac{24}{\alpha_g Re_s}\left[1+0.15(\alpha_g Re_s)^{0.687}\right] \qquad (3\text{-}8a)$$

$$\alpha_s\geq0.2:\ K_d=150\frac{\alpha_s(1-\alpha_g)\mu_g}{\alpha_g d_s}+1.75\frac{\alpha_s\rho_g|\vec{U}-\vec{V}|}{d_s} \qquad (3\text{-}8b)$$

Table 3-1 Constitutive equations required for solving the SFB reactor model.

Variable	Model	Eq.	Ref.
Solids total pressure	$p_s = p_{KTGF} + p_{fr}$	(T3-1.1)	[20]
Solids effective dynamic viscosity	$\mu_{eff,s} = \mu_{KTGF} + \mu_{fr}$	(T3-1.2)	[20]
KTGF pressure	$p_{KTGF} = \rho_s \alpha_s \Theta_s [1 + 2(1+e) g_0 \alpha_s]$	(T3-1.3)	[23]
KTGF dynamic viscosity	$\mu_{KTGF} = \mu_{kin,s} + \mu_{col,s}$	(T3-1.4)	[23]
Solids kinetic shear viscosity	$\mu_{kin,s} = \frac{10}{96}\frac{\rho_s d_s (\Theta_s \pi)^{1/2}}{(1+e) g_0}\left[1 + \frac{4}{5} g_0 \alpha_s (1+e)\right]^2$	(T3-1.5)	[21]
Solids collisional shear viscosity	$\mu_{col,s} = \frac{4}{5}\rho_s \alpha_s d_s g_0 (1+e)\left(\frac{\Theta_s}{\pi}\right)^{1/2}$	(T3-1.6)	[21]
Solids bulk viscosity	$\lambda_s = \frac{4}{3}\alpha_s^2 \rho_s d_s g_0 (1+e)\left(\frac{\Theta_s}{\pi}\right)^{1/2}$	(T3-1.7)	[23]
Radial distribution function	$g_0 = \frac{1}{1 - (\alpha_s/\alpha_{s,max})^{1/3}}$	(T3-1.8)	[24]
Collisional energy dissipation rate	$\gamma_s = 12(1-e^2)\frac{\alpha_s^2 \rho_s g_0}{d_s}\left(\frac{\Theta_s^3}{\pi}\right)^{1/2}$	(T3-1.9)	[23]
Granular energy source due to momentum exchange	$J_s = 3K_d \Theta_s - \frac{81 \alpha_s \mu_g^2 \left\|\vec{V} - \vec{U}\right\|^2}{\rho_s g_0 d_s^3 (\pi \Theta_s)^{1/2}}$	(T3-1.10)	[25]
Solids conductivity of fluctuating energy	$\kappa_s = \frac{75}{192}\frac{\rho_s d_s (\Theta_s \pi)^{1/2}}{(1+e) g_0}\left[1 + \frac{6}{5}(1+e) g_0 \alpha_s\right]^2 + 2\alpha_s^2 \rho_s d_s g_0 (1+e)\left(\frac{\Theta_s}{\pi}\right)^{1/2}$	(T3-1.11)	[21]
Turbulence intensity at inlet boundary condition	$I = 0.16 \mathrm{Re}_{d_s}^{-1/8}$	(T3-1.12)	[26]
Turbulence kinetic energy at inlet boundary condition	$k = \frac{3}{2}(V_{mean} I)^2$	(T3-1.13)	[22]
Turbulence dissipation rate at inlet boundary condition	$\epsilon = C_\mu \frac{k^{3/2}}{l}$ Where l is the turbulent length scale, approximated to length of cells	(T3-1.14)	[22]
Frictional pressure	$p_{fr} = Fr \frac{(\max(\alpha_s - \alpha_{s,min}, 0))^{c_p}}{(\alpha_{s,max} - \alpha_s)^{c_n}}$ With $Fr = 0.05\ Nm^{-2}$, $c_p = 2$, $c_n = 5$	(T3-1.15)	[27]
Frictional viscosity	$\mu_{fr} = p_{fr} \sin\phi$	(T3-1.16)	[27]

The Reynolds-Averaged Navier-Stokes (RANS) model includes the turbulence effect. In the RANS model, a mean velocity $\bar{V}$ and a fluctuating component V' are the decomposition of the instantaneous fluid velocities. Using the time-averaged Eulerian solution gives the mean part directly, whereas stochastic modeling [28] solves the fluctuating part.

3.2.2.2. Simulation settings

Table 3-2 summarizes the phase properties, and the boundary and initial conditions for the numerical simulation. The gas flow rate value is constant at the inlet of the SFB reactor, while the outlet boundary condition is a fixed pressure. The gas phase presents no-slip boundary conditions at the side walls. The solid phase is a granular flow, i.e., particles behave between two conditions: stick to the walls and slide freely on the wall [29]. Equations (3-9) and (3-10) are the Johnson-Jackson boundary conditions for solving the granular flow behavior for solid velocity and granular temperature [30].

$$\nabla_\perp \vec{U}_{wall} = \frac{\pi \varphi_s \rho_s \alpha_s g_0}{2\mu_s \alpha_{s,max}}\left(\frac{\Theta_{s,wall}}{3}\right)^{1/2} U_{wall} \tag{3-9}$$

$$\nabla_\perp \Theta_{s,wall} = \frac{\pi \varphi_s \rho_s \alpha_s g_0}{2\kappa_s \alpha_{s,max}}\left(\frac{\Theta_{s,wall}}{3}\right)^{1/2} U_{wall}^2 - \frac{\pi \rho_s \alpha_s g_0 (1 - e_w^2)}{4\kappa_s \alpha_{s,max}}\left(3\Theta_{s,wall}^3\right)^{1/2} \tag{3-10}$$

Table 3-2 Operating conditions of phase properties and boundary and initial conditions for the numerical simulation.

Phase	**Gas**	**Solid**
Properties		
Composition	Air	Plastic beads
Diameter		6×10^{-3} m
Density	Ideal gas equation	1312 kg m^{-3}
Viscosity	1.84×10^{-5} kg m^{-1} s^{-1}	
Turbulence properties	k-epsilon model	Kinetic theory
Maximum packing		0.62
Restitution coefficient		0.5
Maximum frictional packing		0.5
Angle of internal friction		28.5
Initial conditions		
For region	$0<z<3.7\times10^{-2}$ m	
Phase volume fraction	0.45	0.55
Velocity field	0 m s^{-1}	0 m s^{-1}
At inlet		
Turbulence kinetic energy	8.9×10^{-2} m^2 s^{-2}	
Turbulence dissipation rate	0.27 m^2 s^{-3}	
Boundary conditions		
At inlet		
Phase volume fraction	$\alpha_g = 1$	$\alpha_s = 0$
Velocity	Fixed V_z and V_θ	$\vec{U} = 0$ m s^{-1}
Pressure	$\frac{\partial P}{\partial x} = 0$	
At outlet		
Phase volume fraction	$\frac{\partial \alpha_g}{\partial x} = 0$	$\frac{\partial \alpha_s}{\partial x} = 0$
Velocity	$\frac{\partial \vec{V}}{\partial x} = 0$	$\frac{\partial \vec{U}}{\partial x} = 0$
Pressure	Atmospheric pressure	
At outer wall	No-slip	Johnson-Jackson
At inner wall (cone)	No-slip	Johnson-Jackson

Where μ_s is the solids viscosity, κ_s the solids conductivity, φ_s the specularity coefficient, and e_{wall} the particle-wall coefficient of restitution. When modeling gas-solid fluidized beds with the Eulerian-Eulerian approach, the specularity coefficient significantly affects the predicted hydrodynamics in the Johnson and Jackson boundary condition [30], [31]. Then, the two materials of the boundary walls require the definition of two specularity coefficients for each boundary, i.e., acrylic pipe $\varphi_{s,p}$, and metallic cone $\varphi_{s,c}$. Equation (3-11) approximates e_w to the particle-particle coefficient of restitution e [32],

$$e_{wall} \cong e$$
$$\frac{H_{bed}}{d_s} = \frac{\ln(1-e)/4}{\ln(1+e)/2} \tag{3-11}$$

where H_{bed} denotes the static bed height and d_s the particle size. According to this, the coefficient of restitution is set to 0.5.

3.2.2.3. Simulation procedure

Open-source CFD software OpenFOAM® v2106 solves the governing equations. A combination of the Pressure Implicit Split Operator (PISO) algorithm and the Semi-Implicit Method for Pressure-Linked Equations (SIMPLE) method couples the velocity-pressure solution [33]. This approach calculates the momentum equation coefficients and solves a predicted velocity field with the last calculated pressure. Table 3-3 summarizes the simulation settings for solving the SFB reactor model. The actual CPU time depends on the velocity field because of the restriction imposed by the global Courant number [34]. Therefore, the maximum allowable Courant number was set to 5. The two-phase fluid flow simulation follows the volume of fluid method (VOF) [35]. The VOF approach assumes that the two phases are insoluble. The sum of the volume fractions of both phases is the unity in each control volume of the computational domain. Both phases share the flow field for all variables and properties, representing volume-averaged values.

Table 3-3 Overview of simulation settings

Simulation settings	
Drag model	Gidaspow
Solution settings	
Maximum Courant number	5
Spatial discretization	Gauss, second-order
Temporal discretization	Euler, first order
Time step order	1×10^{-5} s

The simulation consists of a batch operation of the SFB reactor. First, the gas enters the annular zone at a constant rate while the bed of particles remains static on the distributor. The simulation continues until it reaches a pseudo steady regime. Finally, a time-averaging of all flow characteristics is performed.

3.2.3. Computational grid

The computational domain consists of a simplified quarter section (pie-shaped geometry) of the SFB reactor assuming uniform circular motion along the bed of particles. The simplified geometry reduces the computing power to solve the SFB reactor model. Figure 3-3 displays the mesh composed of an array of hexahedral cells. It comprises the gas inlet and the blade walls at the bottom, the gas outlet at the top, the outer cylindrical wall, and the inner conical wall. The outer wall material differs from inner and bottom walls, which requires different specularity coefficients when using the Johnson-Jackson boundary condition. The azimuthal boundaries of the computational domain are coupled using cyclic (periodic)- boundary conditions. The OpenFOAM® v2106 mesh generator function, named blockMesh, assisted the creation of a level 0 prism-shaped grid. Then, the utility snappyHexMesh read the final geometry from CAD drawings in Stereolithography (STL) format to generate the quarter pie-shaped mesh of the SFB reactor. The surfaces of the generated mesh were refined near the inlet, outlet, and wall boundaries, while cyclic boundaries remained with a level 0 grid [36].

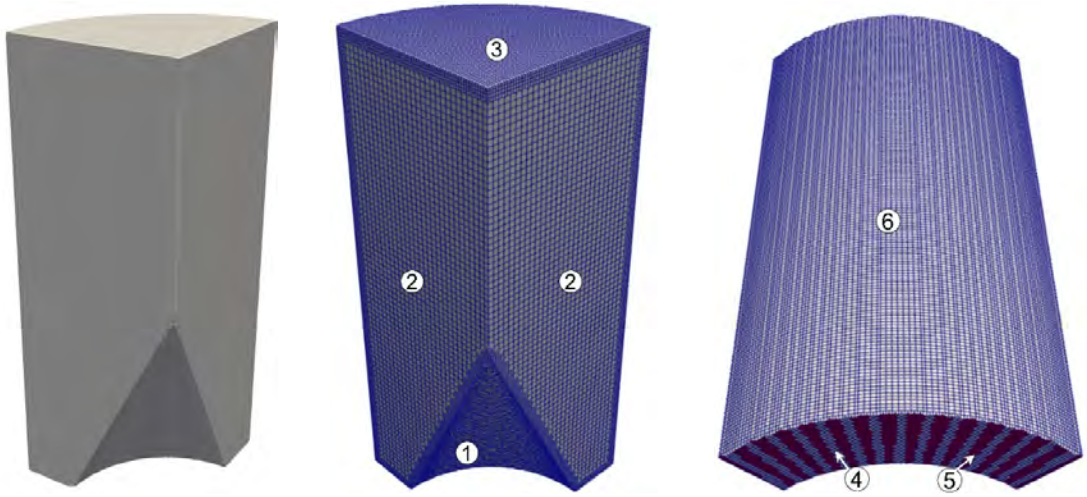

(a) (b) (c)

Figure 3-3 Computational domain composed of hexahedral mesh with a level 0 size of 0.01m. The mesh is finer near the inlet, outlet, and walls. The computational domain is enclosed by (1) the cone wall, (2) two cyclic boundaries, (3) an outlet path, (4) inlet blades walls (grey), (5) inlet openings (red), and (6) the cylindrical outer wall. Source: Figure created by author.

The Grid Convergence Index (GCI) accounts for the uncertainty of the solution in a grid refinement study using the Richardson-based error. CGI measures how much the refinement of the grid changes the solution of the simulation, i.e., the expected CGI value should be lower than 10%. The grid refinement study with Richardson extrapolation requires three different meshes varying their refinement levels [37]. Equation (3-12) estimates the grid refinement ratio r_{grid} as a function of the grid spacing in the fine Δx_1, medium Δx_2, and coarse Δx_3 meshes. The suggested grid refinement ratio is $r_{\text{grid}} \geq 1.1$ to distinguish the discretization error from other error sources (e.g., iterative convergence errors and computer round-off) [38].

$$r_{grid} = \frac{\Delta x_2}{\Delta x_1} = \frac{\Delta x_3}{\Delta x_2} \tag{3-12}$$

The refinement study consists of the following steps. First, three prismatic meshes are generated of 250 mm length, 250 mm width, and 500 mm height with different grid spacing. Table 3-4 shows the level 0 grid spacings for the three meshes with a 3D refinement ratio of $r_{\text{grid}} \cong 1.4$. Then, the snappyHexMesh utility creates the final meshes for the simulation [36]. Figure 3-4 shows the three meshes for the GCI-based grid refinement process obtained with the snappyHexMesh utility

Table 3-4 Mesh characteristics for the three refinement grids. Number of cells (N_{cells}) in the mesh at level 0 grid spacings.

Mesh No.	Grid	Δ*x*, mm	Δy, mm	Δz, mm	N_{cells}	Normalized grid spacing
3	Coarse	7.10	14.3	7.10	42875	2.0
2	Medium	5.00	10.0	0.50	125000	1.4
1	Fine	3.60	7.10	3.60	343000	1.0

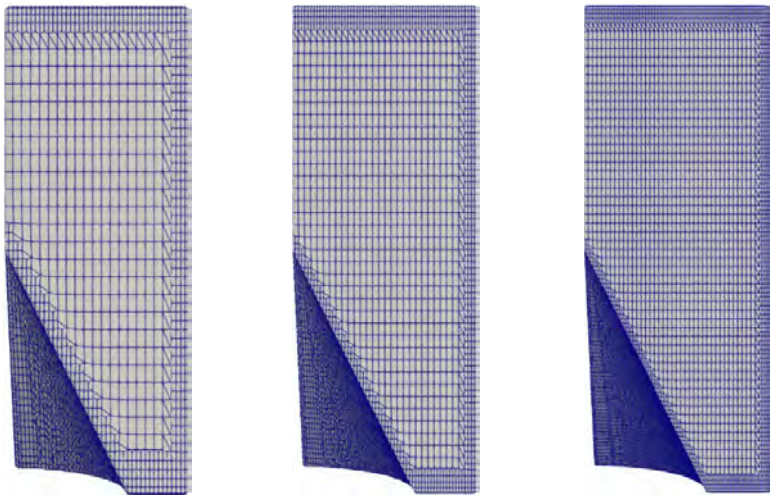

(a) (b) (c)

Figure 3-4 Corresponding meshes for the GCI-based grid refinement process generated using the snappyHexMesh utility. The grids are (a) the coarse, (b) the medium, and (c) the fine. Source: Figure created by author.

Later, the three meshes are simulated in OpenFOAM v2106. After finishing, a variable of interest is extracted from the simulation results, and GCI is calculated [37]. A stable variable is preferred to do the refinement study because of the turbulence inherent to the swirling motion of the bed. The average pressure drop across the bed (ΔP_{bed}) is the extracted variable from the solution of the three meshes. Equation (3-13) estimates the absolute error ε for medium-fine (12) and coarse-medium (23) depending on the extracted solutions from the fine, medium, and coarse grids, i.e., $\Delta P_{\text{bed},1}$, $\Delta P_{\text{bed},2}$, and $\Delta P_{\text{bed},3}$, respectively.

$$\varepsilon_{12} = \Delta P_{\text{bed},1} - \Delta P_{\text{bed},2} \tag{3-13a}$$

$$\varepsilon_{23} = \Delta P_{\text{bed},2} - \Delta P_{\text{bed},3} \tag{3-13b}$$

Equation (3-14) gives the convergence ratio CR which denotes the monotonic convergence of the solutions. If $0 < CR < 1$ the Richardson extrapolation method is adequate to calculate the order of accuracy p using Equation (3-15) and the error estimator δ for coarse-medium and medium-fine using Equations (3-16a) and (3-16b), respectively [37].

$$CR = \frac{\varepsilon_{12}}{\varepsilon_{23}} \tag{3-14}$$

$$p = \frac{\ln(\varepsilon_{23}/\varepsilon_{12})}{\ln(r_{\text{grid}})} \tag{3-15}$$

$$\delta_{23} = \frac{\frac{\Delta P_{\text{bed},2} - \Delta P_{\text{bed},3}}{\Delta P_{\text{bed},2}}}{r_{\text{grid}}^{p} - 1} \tag{3-16a}$$

$$\delta_{12} = \frac{\frac{\Delta P_{\text{bed},1} - \Delta P_{\text{bed},2}}{\Delta P_{\text{bed},1}}}{r_{\text{grid}}^{p} - 1} \tag{3-16b}$$

Then, Equation (3-17) denotes a Richardson extrapolation of the pressure-drop across the bed to solve the pressure-drop at a grid with zero spacing. The value $\Delta P_{\text{bed},\infty}$ is an estimate of the solution from the CFD-based model, i.e., ΔP_{bed}. Therefore, the difference between $\Delta P_{\text{bed},\infty}$ and $\Delta P_{\text{bed},1}$ is expected to be lower than 10% [39].

$$\Delta P_{\text{bed},\infty} = \Delta P_{\text{bed},1} + \frac{\Delta P_{\text{bed},1} - \Delta P_{\text{bed},2}}{r_{\text{grid}}^{p} - 1} \tag{3-17}$$

Roache [40] suggested that the estimation of the GCI incorporates a safety factor because the GCI represents an error band instead of an error estimator. F_S = 1 gives an error band analogous to 50% on experimental data. The recommended safety factor for a three-grid refinement study is F_S = 1.25. Then, Equation (3-18a) calculates the GCI values for the coarse-medium and medium-fine refinement.

$$\text{GCI}_{23} = F_S|\delta_{23}| \tag{3-18a}$$

$$\text{GCI}_{12} = F_S|\delta_{12}| \tag{3-18b}$$

The GCI ratio is a parameter useful to verify that the solutions of each grid level are in the asymptotic range of convergence. Equation (3-19) denotes that the GCI ratio should approximate to 1 [38].

$$r_{\text{grid}}^{p}\frac{\text{GCI}_{12}}{\text{GCI}_{23}} \cong 1 \tag{3-19}$$

The simulation settings for the grid refinement study are listed in Table 3-2. The coefficients used for the grid refinement study are restitution e_{w} = 0.5, and specularity for pipe wall $\varphi_{\text{s,cyl}}$ = 0.1 and cone wall $\varphi_{\text{s,cone}}$ = 0.05 in the Johnson-Jackson boundary conditions. Using the results of the coarser mesh as initial conditions for the finer meshes reduces the simulation time. These values are closer to the

steady-state than the best initial conditions guess. The mapFields utility in OpenFOAM interpolates the results from coarser mesh as input values into the finer meshes [36].

3.2.4. Model validation

Naz et al. [19] developed experiments to study the solids velocity profile using PIV measurements of the fluidized particles in a SFB reactor. They averaged the particle velocity profile over the radial position at a fixed angle for six different air superficial velocities. The simulation results used to validate the computational model depend on the setting of the Johnson-Jackson boundary condition coefficients. The materials used for the inner (metallic cone and blades) and outer (acrylic cylinder) walls require two values of the specularity coefficient, one for each wall. Four values of specularity coefficients are suggested for each wall material, i.e., 16 combinations, to fit a numerical model that replicates experimental results from [19]. This optimal value is valid only for a certain range of flow rates and particle properties. Table 3-5 shows the set of values of the restitution and specularity coefficients combined to obtain the validated computational model.

Table 3-5 Johnson-Jackson boundary condition combinations of parameters. Combinations of specularity coefficients used to determine the validated SFB reactor computational model.

Parameter	**Value**
Wall-particle restitution coefficient, e_{wall}	0.5
Pipe wall-particle specularity coefficient $\varphi_{\text{s,p}}$	0.05 – 0.075 – 0.1 – 0.125
Cone wall-particle specularity coefficient $\varphi_{\text{s,c}}$	0.05 – 0.075 – 0.1 – 0.125

After obtaining the simulation results, averaged particle velocities over the radial position are calculated at 90 tangential positions, i.e., separated by 1°, using the trapezoidal rule of numerical integration. Likewise, an azimuthal averaged particle velocity is calculated with the radial averaged velocities. Equation (3-20) denotes the relative error E used to compare average particle velocity from the simulation results and the experimental data from [19]. The lowest E value obtained from this analysis gives the validated simulation with the optimal specularity coefficient values. The 16 simulations of the SFB reactor are tested in batches of four combinations of specularity coefficients until obtaining a simulation with a difference lower than 5%.

$$Er = \frac{\left|\bar{U}_{\theta,\text{sim}} - \bar{U}_{\theta,\text{exp}}\right|}{U_{\theta,\text{exp}}} \times 100 \tag{3-20}$$

3.3. Results and discussion

3.3.1. Grid independence

Table 3-6 shows the extracted average pressure drop across the bed ΔP_{bed} from the three meshes after finishing the simulation.

Table 3-6 Simulation results for the three meshes to perform the GCI-based grid refinement study. Number of cells (N_{cells}) in the mesh at level 1 grid spacings, i.e., after using snappyHexMesh utility.

Mesh No.	Grid	N_{cells}	ΔP_{bed}, kPa
3	Coarse	23583	1.58
2	Medium	53900	1.91
1	Fine	125291	2.04

The absolute error ε are obtained using the information in Table 3-6 and Equation (3-13)

$$\varepsilon_{12} = 2.04 - 1.91 = 0.13$$
$$\varepsilon_{23} = 1.91 - 1.58 = 0.33$$

Then, the convergence ratio, CR = 0.37, confirms a monotonic convergence of the solutions, adequate for the grid refinement study. The next step is to calculate the order of accuracy p and the error estimators δ using Equations from (3-14) to (3-17) with a refinement ratio r_{grid}=1.4.

$$p = \frac{\ln\left(\frac{0.13}{0.33}\right)}{\ln(1.4)} = 2.93$$

$$\delta_{23} = \frac{\left(\frac{1.91 - 1.58}{1.91}\right)}{(1.4^{2.93}) - 1} = 1.04 \times 10^{-1}$$

$$\delta_{12} = \frac{\left(\frac{2.04 - 1.91}{2.04}\right)}{(1.4^{2.93}) - 1} = 3.64 \times 10^{-2}$$

The solution of the Richardson extrapolation gives the value of $\Delta P_{\text{bed},\infty}$ = 2.11 kPa for the zero grid spacing.

$$\Delta P_{\text{bed},\infty} = 2.04 + \frac{2.04 - 1.91}{(1.4^{2.93}) - 1} = 2.11 \text{ kPa}$$

The error with respect to the pressure-drop across the bed of the fine grid is $\frac{\Delta P_{\text{bed},\infty} - \Delta P_{\text{bed},1}}{\Delta P_{\text{bed},1}} \times 100$ = 4%.

The corresponding GCI values of the grid refinement study are

$$\text{GCI}_{23} = (100\%)(1.25)|1.04 \times 10^{-1}| = 13\%$$

$$\text{GCI}_{12} = (100\%)(1.25)|3.64 \times 10^{-2}| = 4.5\%$$

Finally, the GCI ratio is verified with Equation (3-19), showing that the solutions from the grid refinment study are in the asymptotic range.

$$r_{\text{grid}}^{p} \frac{\text{GCI}_{12}}{\text{GCI}_{23}} = (1.4^{2.93}) \frac{4.5}{13} = 0.94 \cong 1$$

The GCI for the medium grid of 4.5% denotes that the medium grid is sufficient for the validation study and extracting quantitative data from the simulation. Figure 3-5 illustrates how the results of the simulations of the three meshes used in the GCI-based refinement process converge to the solution of the Richardson Extrapolation for the zero grid spacing.

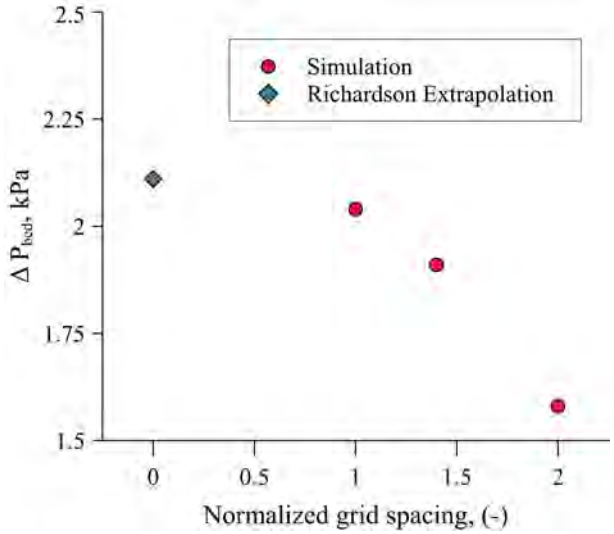

Figure 3-5 Pressure-drop across the bed vs. Normalized grid spacing results obtained from the simulations of the three meshes for the GCI-based refinement process (red dots) and the Richardson Extrapolation solution for the zero grid spacing (blue diamond). Source: Figure created by author.

An improvement opportunity for future CFD-based models of a gas-solid SFB reactor is constructing a structured grid along the azimuthal position using specialized mesh generation softwares, such as in the grid study of [18]. The snappyHexMesh utility of OpenFOAM® resulted in high skewness values and cell irregularities after the mesh generation, such as concave angles between faces. After improving the mesh generation, the GCI-based grid refinement process of the SFB reactor model would require a smaller number of cells and shorter simulation times to obtain a good grid for the validation study.

3.3.2. Model validation

Table 3-7 shows the performance of each tested set of specularity coefficients in terms of the averaged azimuthal particle velocity. The averaged solids azimuthal velocities feature error values lower than 20%, showing a good agreement with the experiments. The results show that $\overline{U}_{\theta,sim}$ is inversely related to $\varphi_{s,p}$ and $\varphi_{s,c}$ when $\varphi_{s,c} \leq 0.075$, while the relationship is direct when $\varphi_{s,c} = 0.1$. Changing the value of $\varphi_{s,p}$ by 0.025 varies the value of $\overline{U}_{\theta,sim}$ from 3 to 8%. In the case of $\varphi_{s,c}$ variations by 0.025 decreases $\overline{U}_{\theta,sim}$ from 1 to 15%. The selected combination $\varphi_{s,p} = 0.125$ on the pipe wall and $\varphi_{s,c} = 0.05$ on the cone wall shows the best performance after comparing with the experimental data, $E = 0.2\%$, for 2.23 m s^{-1} of air superficial velocity.

The convergence algorithm did not find a solution of the model for the missing combinations from Table 3-5.

Table 3-8 summarizes the comparison between experiments and simulation results for the average azimuthal velocity of the bed at different air superficial velocities. The average velocity of the particles revealed an increasing trend with air superficial velocity as in Naz et al. [19]. A relative error lower than 5% reveals that the CFD model is adequate for studying the reactor under the experimental conditions.

Table 3-7 Relative errors between the simulated $\bar{U}_{\theta,sim}$ and experimental $\bar{U}_{\theta,exp}$ [19] data of averaged solids azimuthal velocities at different specularity coefficient combinations. The selected combination is $\varphi_{s,p}$ = 0.125 and $\varphi_{s,c}$ = 0.05.

$\bar{U}_{\theta,exp}$, m s^{-1}	$\varphi_{s,p}$	$\varphi_{s,c}$	$\bar{U}_{\theta,sim}$, m s^{-1}	Er, %
0.586	0.050	0.05	0.688	17.4
	0.075		0.636	8.6
	0.100		0.608	3.7
	0.125		0.587	0.2
	0.050	0.075	0.616	5.2
	0.075		0.583	0.5
	0.100		0.554	5.4
	0.125		0.542	7.5
	0.050	0.100	0.522	10.9
	0.075		0.545	7.0
	0.100		0.577	1.6

Table 3-8 Comparison of experimental $\bar{U}_{\theta,exp}$ [19] and the simulated $\bar{U}_{\theta,sim}$ average solids azimuthal velocities.

U_{sup}, m s^{-1}	$\bar{U}_{\theta,exp,}$, m s^{-1}	$\bar{U}_{\theta,sim,}$, m s^{-1}	Er, %
1.99	0.499	0.476	4.61
2.13	0.524	0.547	4.39
2.23	0.586	0.587	0.21

3.3.3. Hydrodynamics

The validated CFD model enables insights into some hydrodynamic characteristics of the SFB reactor. This section presents the flow patterns for plastic beads and air in the SFB reactor obtained in the simulation using a superficial velocity of 2.23 m s^{-1}.

3.3.3.1. Azimuthal-radial plane analysis

The azimuthal-radial plane of the bed is plotted at three axial positions above the distributor (z). The bed height (H_{bed}) corresponds to the region of the computational volume where the solids volume fraction is larger than 5% [18]. Thus, the H_{bed} of the actual CFD model is approximately 68 mm. The

selected axial positions to analyze the flow patterns are at the proximity of the distributor, the center of the bed, and nearby the free area of the bed. The corresponding z positions are $10\%H_{bed}$ = 6.8 mm, $50\%H_{bed}$ = 34 mm, and $90\%H_{bed}$ = 61.2 mm.

First, the solids volume fraction distribution is analyzed. The fields of solids azimuthal and radial velocities are then presented. Next, the solids centrifugal acceleration is addressed. Finally, the gas azimuthal and radial velocities are analyzed.

3.3.3.1.1. Solids volume fraction

The average solids volume fraction in the SFB is 0.28. However, it is non-uniform, with solid accumulation at the bottom of the bed just upstream of the openings between blades. Figure 3-6a depicts the swirling regime occurring in the SFB reactor, whose centrifugation generates a higher bed height at the outer wall than in the inner cone wall. Other studies reported a similar behavior for the solids volume fraction trend towards the outer wall [7], [16]. Meanwhile, Figure 3-6b shows that the solids volume fraction nearby the inner wall forms peaks or dunes, i.e., a wavy bed regime. The wave motion occurs because the momentum of the fluid is not enough to carry the particle the whole circumferential distance of the SFB reactor. Then, part of the bed swirling zone, while the remaining bed is static [7]. The particles move from the swirling zone to the boundary of the static zone, where they deposit and form a dune. The dune grows continuously until a maximum and then starts decaying near the swirling zone boundary. The transition from the swirling to the static zone with the formation of dunes in the wavy bed regime is known as a single slug-wave cycle [41].

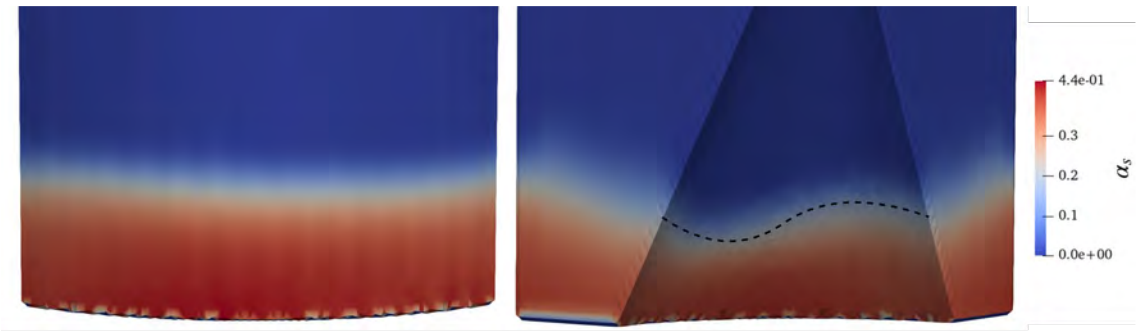

Figure 3-6 Simulated solid volume fraction α_s distribution in the SFB reactor at the view from (a) the outer wall and (b) the inner cone wall. The bed height at the outer wall view is almost uniform, while there is a formation of dunes in the inner wall. Source: Figure created by author.

Figure 3-7 shows the solid volume fraction in the SFB reactor at three axial positions (a) 6.8, (b) 34, and (c) 61.2 mm. At all the levels, the solids are entrained towards the outer wall, indicating a significant influence of the centrifugal acceleration of the bed. Figure 3-7a shows that the solids volume fraction at $r \approx$123 mm follows a periodic behavior related to forming a swirling region at the bottom of the bed. Figure 3-7b depicts that the solids distribution is uniform at the central radius at the center of the bed. Moving inwardly on the radial position reveals a variation of the solids volume fraction with the azimuthal position, i.e., the wavy bed regime. Figure 3-7c illustrates the behavior at the higher level, where both momentum transfer of the fluid to the bed and the increasing cross-

sectional area reduce the intensity of the swirling flow. The observed patterns present similar behavior to the obtained results from [15]. Naz et al. [19] obtained a wavy bed regime of the SFB reactor at the actual operating conditions, such as the results from the simulated model.

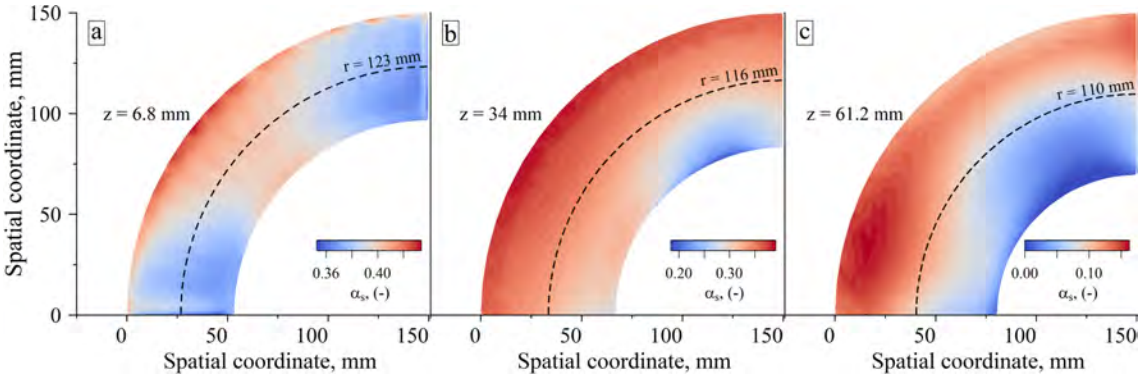

Figure 3-7 Solids volume fraction α_s in a quarter of the SFB reactor for the air superficial velocity 2.23 m s^{-1} and particle density 1312 kg m^{-3}. Volume fraction fields correspond to three axial positions z: (a) 10%H_{bed} = 6.8 mm, (b) 50%H_{bed} = 34 mm, and (c) 90%H_{bed} = 61.2 mm. Dashed lines represent the middle line of the annular region for each height. Source: Figure created by author.

3.3.3.1.2. Solids azimuthal velocity

At all the levels, Figure 3-8 shows the fields of U_θ exhibiting a slow decrease from the middle line of the bed to the walls. Both particle-wall collisions and frictional forces cause the decreasing gradient of U_θ as the radial position is closer to the walls [19], [42]. The dissipation of momentum due to inter-particle and particle-wall interactions decreases, but the centrifugal force keeps moving the particles near the outer wall [43], [44]. The interaction with the wall decreases both gas and solids velocity closer to the boundaries. Nonintrusive measurement techniques make it difficult for experimental data gathering because they only allow optical access at the top free area of the SFB [18]. The maximum value of U_θ = 1.37 m s^{-1} occurs at the center radio and just above the exit of the gas distributor. U_θ is inversely related to z because air moves faster at the exit of the air distributor, which induces a higher gas-to-solid momentum transfer rate.

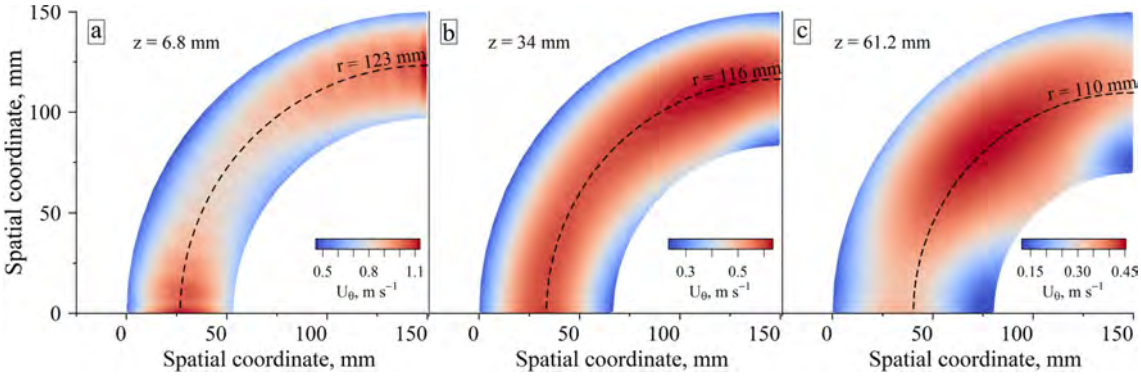

Figure 3-8 Solids azimuthal velocities U_θ in a quarter of the SFB reactor for the air superficial velocity 2.23 m s^{-1} and particle density 1312 kg m^{-3}. Velocity fields correspond to three axial positions z: (a) 10%H_{bed} = 6.8 mm, (b) 50%H_{bed} = 34 mm, and (c) 90%H_{bed} = 61.2 mm. Dashed lines represent the middle line of the annular region for each height. Source: Figure created by author.

Figure 3-6 and Figure 3-7 depict that U_θ is inversely related to α_s. Figure 3-8a illustrates a periodic change of U_θ that is strongly related to the swirling motion near the distributor exits. Moving upwardly on the axial position, U_θ at the central cone wall approximates the middle line values, such as in the experiment from Naz et al. [19]. The wavy regime at the top of the bed influences the variation of U_θ near the cone wall. U_θ is as low as the dune height is higher due to the requirement of momentum of the fluid to push the particle. The decrease in the dune height gives an impression of increasing U_θ because α_s is lower, which requires less momentum transfer. Higher overall bed height increases flow resistance, decreasing the tendency to dune formation [41].

3.3.3.1.3. Solids radial velocity

Figure 3-9 shows that U_r varies with radial and axial position, fluctuating around zero such as in another rotating fluidized beds [17], [45]. At the lowest levels, the bed predominantly moves outwardly. U_r changes its direction at the mid-level of the bed, where particles' motion prevails radially inward. The change of direction of U_r along the axial position of the bed illustrates the particles' swirling movement about the center of the annular region. This movement of the bed enhances radial mixing. At the highest levels, U_r is closest to zero because of the increase in cross-sectional area of the annular region and the lack of momentum transfer from the air. Also, particles move radially outward near the central wall because they free fall on the cone surface.

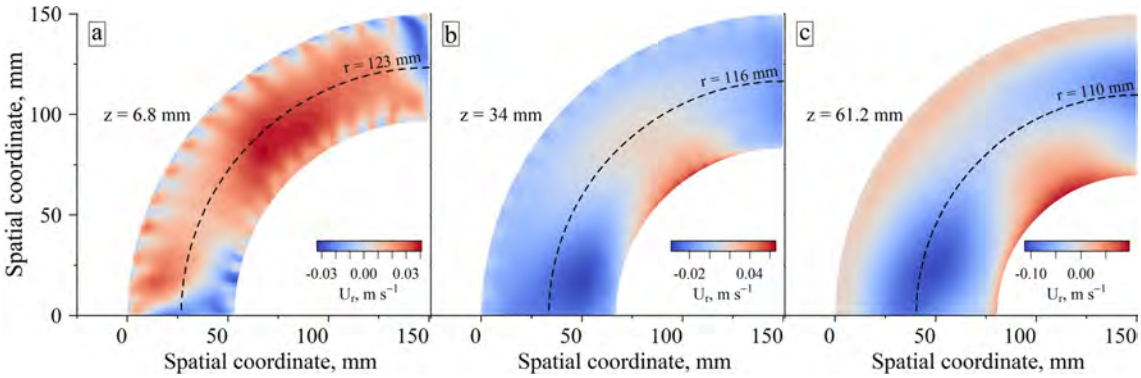

Figure 3-9 Solids radial velocities U_r in a quarter of the SFB reactor for the air superficial velocity 2.23 m s^{-1} and particle density 1312 kg m^{-3}. Velocity fields correspond to three axial positions z: (a) 10%H_{bed} = 6.8 mm, (b) 50%H_{bed} = 34 mm, and (c) 90%H_{bed} = 61.2 mm. Dashed lines represent the middle line of the annular region for each height. Source: Figure created by author.

3.3.3.1.4. Air azimuthal velocity

Figure 3-10 shows that V_θ decreases with the increase of axial position in the SFB reactor. As soon as the air exits the distributor, it loses around 90% of its kinetic energy due to the momentum transfer for fluidizing and rotating the bed [18]. Also, the increasing cross-sectional area moving upwardly in the axial position affects V_θ. At all the levels, V_θ is zero at the wall due to the no slip condition with the boundaries. V_θ varies with the radial position at the lowest levels because the air injection through the trapezoidal area between blades affects the velocity uniformity to preserve the air mass flow. At the mid-level, V_θ presents a maximum value near the middle line and periodically fluctuates with the azimuthal position. The azimuthal fluctuation of V_θ is attributed to the momentum transfer to the

particles since it agrees with the variation of U_θ in the same direction. At the highest levels, the momentum change of the particles reduces the kinetic energy of the air, which disperses the air movement on the freeboard of the bed and reduces V_θ values.

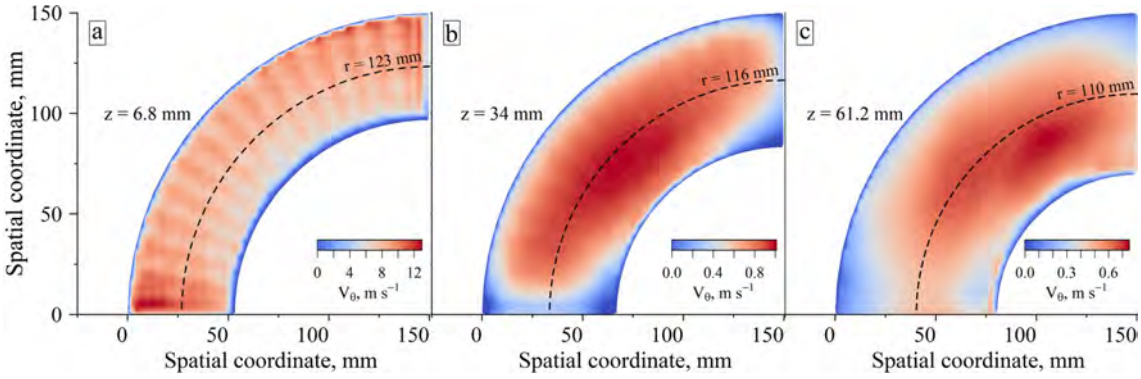

Figure 3-10 Air azimuthal velocities V_θ in a quarter of the SFB reactor for the air superficial velocity 2.23 m s^{-1} and particle density 1312 kg m^{-3}. Velocity fields correspond to three axial positions z: (a) 10%H_{bed} = 6.8 mm, (b) 50%H_{bed} = 34 mm, and (c) 90%H_{bed} = 61.2 mm. Dashed lines represent the middle line of the annular region for each height. Source: Figure created by author.

3.3.3.1.5. Air radial velocity

Figure 3-11 shows that the magnitude of V_r is inversely related to the level above the air distributor. Above the exit of the distributor, V_r is almost uniform along the radial and azimuthal positions due to the predominant effect of V_θ. At mid-level, V_r increases with the radial position, and the central cone inclination leads the air to the center of the SFB reactor, causing V_r to be more negative in the inner wall vicinity. This generates a radially inward drag force to the bed of particles which balances the centrifugal force [13]. The field of V_r at the freeboard bed levels is more dispersed, exhibiting the disengagement of the air and the bed of particles.

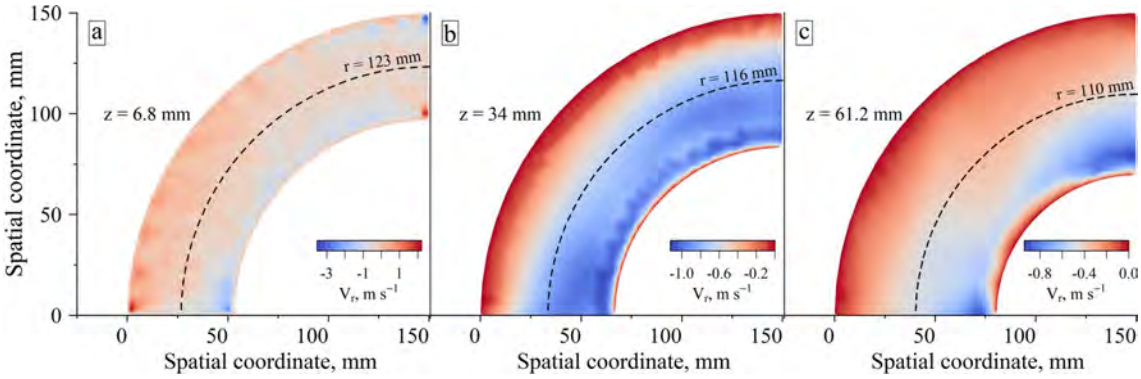

Figure 3-11 Air radial velocities V_r in a quarter of the SFB reactor for the air superficial velocity 2.23 m s^{-1} and particle density 1312 kg m^{-3}. Velocity fields correspond to three axial positions z: (a) 10%H_{bed} = 6.8 mm, (b) 50%H_{bed} = 34 mm, and (c) 90%H_{bed} = 61.2 mm. Dashed lines represent the middle line of the annular region for each height. Source: Figure created by author.

3.3.3.1.6. Solids centrifugal acceleration

The solids centrifugal acceleration (a_c) acting on the solids is given by Equation (3-21):

$$a_c = \frac{U_\theta^2}{r} \tag{3-21}$$

Figure 3-12 shows that the bed of particles is under the effect of an average G below the Earth's gravitational field, i.e., 0.24. Dissipation of the energy of the particles along the axial position reduces the average value of G from 0.48 at the lowest levels to 0.07 at the freeboard of the bed. As expected from U_θ fields, G exhibits its maximum value almost in the central radius of the annular bed for all the levels. In contrast, the G minimum values are in the vicinity of the SFB reactor walls.

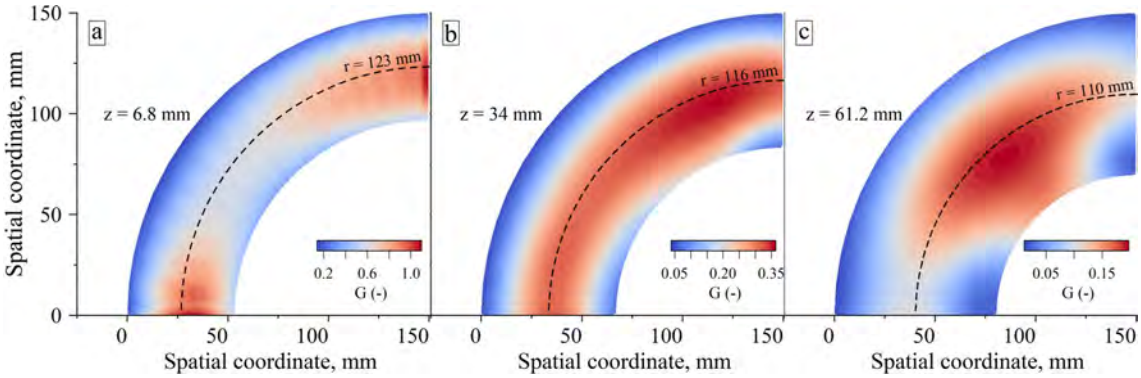

Figure 3-12 Dimensionless solids centrifugal acceleration (G) in a quarter of the SFB reactor for the air superficial velocity 2.23 m s^{-1} and particle density 1312 kg m^{-3}. Centrifugal acceleration fields correspond to three axial positions z: (a) 10%H_{bed} = 6.8 mm, (b) 50%H_{bed} = 34 mm, and (c) 90%H_{bed} = 61.2 mm. Dashed lines represent the middle line of the annular region for each height. Source: Figure created by author.

G reaches a maximum value of 1.6 at the exit of the annular distributor due to the jet velocity of the gas. Although the average G values are lower than Earth's gravitational field, the fluidization of particles in a centrifugal field reaches fluidizing gas jet stream velocities up to 67 m s^{-1}. The jet gas velocities are higher than the terminal velocity of the particle in the gravitational field, about 5.6 m s^{-1} for the 6-mm diameter plastics beads [46]. Higher gas-solid slip velocities enhance the gas-solid momentum and heat and mass transfer rates in the SFB reactor [17].

The inclined injection of the air from the bottom of the bed through trapezoidal spaces between blades promotes the azimuthal and radial mixing in the SFB reactor together with the radially outward decrease of the centrifugal acceleration. Both radially inward drag and centrifugal forces influence the bed mixing. The direct relation of these forces with the air mass flow rate in a wide flow range contributes to the use of the SFB reactor for fluidizing different particle sizes and shapes under various operating conditions.

3.3.3.2. Axial-radial plane analysis

The axial-radial plane of the bed is plotted for the solids and air hydrodynamics analysis.

3.3.3.2.1. Solids hydrodynamics

Figure 3-13 illustrates the solids profiles of four variables on the axial-radial plane of the SFB reactor: (a) the solids volume fraction α_s, and the (b) azimuthal U_θ, (c) radial U_r, and (d) axial U_z solids velocity components.

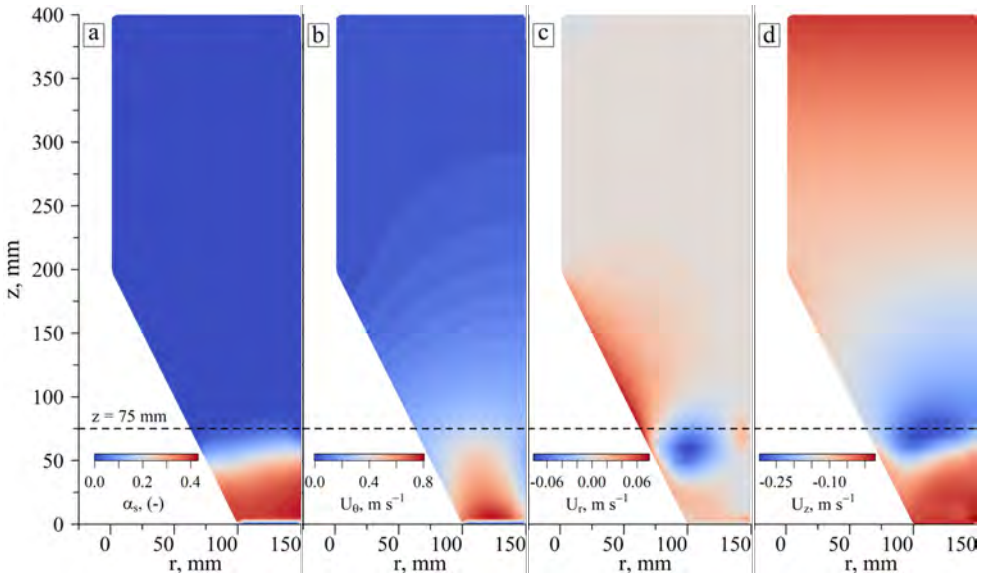

Figure 3-13 Solids hydrodynamics profiles on the axial-radial plane of the SFB reactor. (a) Solids volume fraction α_s, and (b) azimuthal U_θ, (c) radial U_r, and (d) axial U_z solids velocity components. Source: Figure created by author.

Figure 3-13a shows $\alpha_s$on the radial-axial plane of the SFB reactor exhibiting the formation of the bed of particles in the red zone at the bottom of the annular region below the axial level 75 mm. The solids volume fraction decay to zero above the level of 75 mm. α_s increases outwardly in the radial direction due to the action of the centrifugal force which entrains the particles to the outer wall of the SFB reactor and increases the bed height at the outer radius, as stated by [7], [16]. Figure 3-13a shows that α_s is approximately zero above the 75 mm level, comparable with [15]. Checking the simulated data, the actual values of α_s are in orders of magnitude of 10^{-30}. Because of this, the solids velocity values measured are not suitable indicators to describe the phenomenon related to particles motion occurring above the 75 mm level of the reactor.

Figure 3-13b exhibits that U_θ decreases when moving upwardly in the SFB reactor because of the increase of cross section area. The high values of U_θ at the bottom of the bed represent the high momentum transfer rates from the air. The inter-particle collisions and particle-wall interactions dissipates the kinetic energy of the bed which reduces U_θ in the vicinity of the walls [19], [42].

Figure 3-13c and Figure 3-13d show U_r and U_z profiles, which depict the radial mixing of the bed below the 75 mm level. The swirling effect of the bed occurs in the annular region due to axial fluidization and the gas-solid angular momentum transfer. The particles move out- and upwardly in the annular region at the exit of the distributor due to the effect of intensive centrifugal and drag forces acting at this level. Meanwhile, the particles at the top level of the bed move inwardly because the counteract of an inwardly drag force and decrease value of the centrifugal force. At the same level, the particles move downwardly because the increase of the cross-section area decreases the gas flow velocity affecting the capacity fluidization.

3.3.3.2.2. Air hydrodynamics

Figure 3-14 illustrates the air profiles of the (a) azimuthal V_θ, (b) radial V_r, and (c) axial V_z velocity components. A general overview of the profiles depicts that the axial component of the gas velocity dominates the gas flow at the levels in outlet region of the SFB reactor, i.e., above the cone. The rotational kinetic energy of the air dissipates due to gas-solid angular momentum transfer for maintain the swirling effect of the bed.

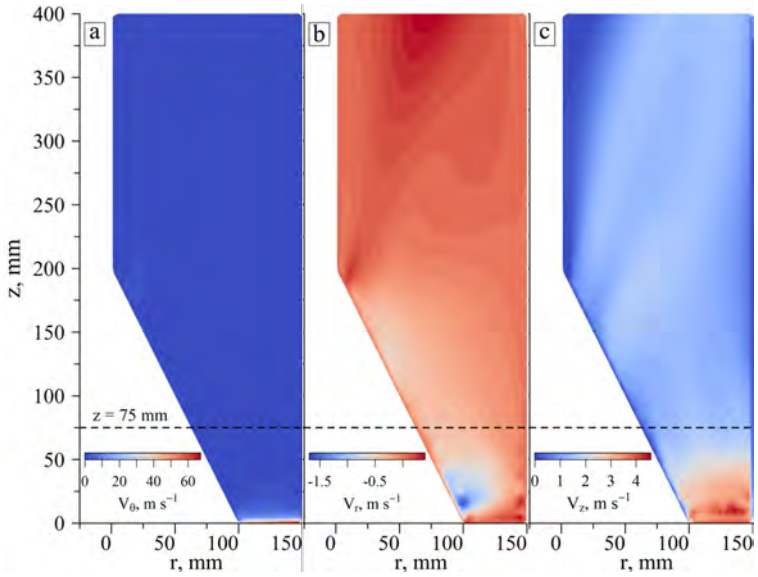

Figure 3-14 Air hydrodynamics profiles on the axial-radial plane of the SFB reactor. (a) Azimuthal V_θ, (b) radial V_r, and (c) axial V_z solids velocity components. Source: Figure created by author.

Figure 3-14a shows that V_θ maximum value is about about 67 m s^{-1} at the exit of the distributor. However, angular momentum transfer to the bed rapidly dissipates the kinetic energy almost to 90% at the mid level of the bed. Above z = 75 mm, the azimuthal velocity component approximately is zero along both the axial and radial positions which denotes that the gas totally or almost totally tranfers its rotational kinetic energy for the rotation of the bed of particles in the SFB reactor.

Figure 3-14b exhibits V_r positive values at the bottom of the annular region which indicates an outwardly directed drag force in the radial direction. The sum of the outwardly drag force and the centrifugal force entrain the particles to the outer wall of the SFB reactor increasing the bed height at outer radius. Moving upwardly, the V_r is predominantly negative generating an inwardly drag force directed to the center of the SFB reactor acting on the bed. This drag force counteracts the centrifugal force and entraines the particles to the cone wall promoting the radial mixing of the bed. Above the free area of the bed, V_r is negative and its magnitude decreases due to the increase of cross section area until it fluctuates around zero.

Figure 3-14c illustrates the distribution of U_z in the SFB reactor. The higher value of U_z is at the bottom of the bed where the major momentum transfer occurs to fluidize the bed. While the air flow approximates to the top level of the bed of particles, U_z continously decreases due to the cross section

area until the end of the annular region. The air flow continues moving upwardly until it leaves the SFB reactor.

During biomass conversion process, the particles experience reduction of size which facilitates the to estrained the particles out of the reactor using the upwardly directed gas flow. Nevertheless, decreasing of U_z limits the particle size able to entraine out of the reactor due to minimum fluidization requirements. In this case, the average U_z at the outlet region of the reactor is about 1.36 m s^{-1}.

Equation (3-22) gives the minimum fluidization velocity based on Ergun equation [46] and using Chitester et al. constants C_1 = 28.7 and C_2 = 0.0494 [47].

$$V_{\mathrm{mf}} = \left[\sqrt{C_1^2 + C_2 \frac{d_s^3 \rho_g (\rho_s - \rho_g) g}{\mu_g^2}} - C_1\right] \frac{\mu_g}{\rho_g d_s} \tag{3-22}$$

Equation (3-22) and the average U_z at the outlet region gives the maximum particle size able to fluidize. For example, a rice husk combustion process results in rice husk ash particles of approximately 2000 kg m^{-3} density [48]. The maximum particle size d_s able is 2.8 mm to achieve fluidization of the rice husk ash at the average gas velocity 1.36 m s-1.

3.4. Conclusion

This work develops a gas-solid SFB reactor CFD simulation using the Eulerian-Eulerian approach in OpenFOAM® v2106. The model validation compared the numerical and experimental average solids azimuthal velocity. The specularity coefficients combination to obtain good agreement between simulation and experiments were $\varphi_{s,p}$ = 0.125 on the pipe wall and $\varphi_{s,c}$ = 0.05 on the cone wall. These values work within a range of operating conditions with relative error lower than 5% compared to the experimental data.

The simulation results showed solid and gas phase energy dissipation along the axial direction. At all the levels, the fields of U_θ exhibited a positive gradient from the outer and inner wall to the middle line of the bed. The maximum value of U_θ = 1.37 m s^{-1} occurred at the bottom of the bed. The fields of U_r confirmed the swirling movement of the particles about the central radius of the bed with the direction change at different levels. The centrifugal acceleration showed that the bed rotated at average G values between 0.48-0.07, reducing with the axial location. The maximum value of G equals 1.6.

The gas-phase behavior was different from the solid phase. As soon as the air leaves the gas distributor, it loses around 90% of its energy, decreasing V_θ rapidly from jet stream velocity to a superficial value. V_r inward direction generates a drag force in the same direction, whose effect balances with the centrifugal force contributing to the bed mixing. The inclined injection of the air from the bottom of the bed promotes the azimuthal and radial mixing in the SFB reactor.

The SFB reactor is useful for fluidizing different particle sizes and shapes under varying operating conditions. Further research should include the analysis of gas-solid interface slip velocities to gain insights into the bed's momentum change. In addition, the analysis of the granular temperature is

essential to identify turbulent fluctuations in the bed. Some parametric studies are essential to determine the better operating and design conditions of the SFB reactor. Finally, the solids azimuthal velocity and acceleration profile study provides in-depth details about drag and frictional forces acting in the swirling direction. Before performing additional studies, efforts should focus on improving the mesh generation process to obtain a more structured grid. The new mesh would decrease the required number of cells and simulation times for solving the SFB reactor model.

Performing parametric studies to analyze the effect of design variables of the SFB reactor on its operation using CFD-based simulation eliminates the need of equipment acquisition. The design variables are easier to configure in a software-based study than in an experimental setup. The simulation results would contribute to decision making of experiment levels limits of a laboratory study of the performance of the SFB reactor and of an adequate design of the reactor.

3.5. References

[1] H. Wang *et al.*, "A review of process intensification applied to solids handling", *Chem. Eng. Process. Process Intensif.*, vol. 118, pp. 78–107, 2017, doi: https://doi.org/10.1016/j.cep.2017.04.007.
[2] V. V Kumar, V. R. Raghavan, V. Vinod Kumar, and V. R. Raghavan, "Developments in fluidized bed technology — A review", in *2011 National Postgraduate Conference*, 2011, pp. 1–10. doi: 10.1109/NatPC.2011.6136395.
[3] Torftech Group, "An executive summary". Torftech Group.
[4] Torftech Group, "Torftech Pilot Plant Facilities". Torftech Group. [Online]. Available: http://www.torftech.com/
[5] M. Paulose, "Hydrodynamic Study of Swirling Fluidized Bed and the Role of Distributor", COCHIN UNIVERSITY OF SCIENCE AND TECHNOLOGY, 2006.
[6] G. A. Wellwood, "Hydrodynamic behaviour of the Torbed® reactor operating in fine particle mode", University of Queensland, 2000.
[7] B. Sreenivasan and V. R. Raghavan, "Hydrodynamics of a swirling fluidised bed", *Chem. Eng. Process. Process Intensif.*, vol. 41, no. 2, pp. 99–106, 2002, doi: https://doi.org/10.1016/S0255-2701(00)00155-0.
[8] C. E. Dodson, "Apparatus for processing matter in a turbulent mass of particulate material", US4479920, 1984
[9] C. S. Miin, S. A. Sulaiman, V. R. Raghavan, M. R. Heikal, and M. Y. Naz, "Hydrodynamics of multi-sized particles in stable regime of a swirling bed", *Korean J. Chem. Eng.*, vol. 32, no. 11, pp. 2361–2367, 2015, doi: 10.1007/s11814-015-0151-6.
[10] M. H. M. Tawfik, M. Refaat Diab, and H. Mohmed Abdelmotalib, "An experimental investigation of wall-bed heat transfer and flow characteristics in a swirling fluidized bed reactor", *Appl. Therm. Eng.*, vol. 155, no. April, pp. 501–507, 2019, doi: 10.1016/j.applthermaleng.2019.04.022.
[11] M. F. Mohideen, B. Sreenivasan, S. A. Sulaiman, and V. R. Raghavan, "Heat transfer in a swirling fluidized bed with geldart type-D particles", *Korean J. Chem. Eng.*, vol. 29, no. 7, pp. 862–867, 2012, doi: 10.1007/s11814-011-0255-6.
[12] M. Faizal, M. S. Suzairin, M. Al-Hafiz, and V. R. Raghavan, "CFD Studies on Velocity Distribution of Air in a Swirling Fluidized Bed", *Adv. Mater. Res.*, vol. 468–471, pp. 25–29, 2012, doi: 10.4028/www.scientific.net/AMR.468-471.25.
[13] M. F. M. Batcha, M. A. H. M. Nawi, S. A. Sulaiman, and V. R. Raghavan, "Numerical investigation of airflow in a swirling fluidized bed", *Asian J. Sci. Res.*, vol. 6, no. 2, pp. 157–166, 2013, doi: 10.3923/ajsr.2013.157.166.

[14] H. Hussein, M. A. M. Nawi, M. H. M. Hazwan, D. L. J. Feng, K. M. Y. K. Ibrahim, and M. L. A. Latif, "Effect of plenum chamber design on discharge coefficient in swirling fluidized bed", *AIP Conf. Proc.*, vol. 2291, no. November, 2020, doi: 10.1063/5.0022910.
[15] K. Sirisomboon and P. Arromdee, "A computational fluid dynamics study of gas–solid distribution of Geldart Group B particles in a swirling fluidized bed", *Powder Technol.*, vol. 393, pp. 734–750, 2021, doi: 10.1016/j.powtec.2021.08.020.
[16] Q. Wu, S. Wang, K. Zhang, Y. Zhao, and Y. He, "Numerical studies of gas-solid flow behaviors and wall wear in a swirling fluidized bed", *Powder Technol.*, vol. 388, pp. 233–240, 2021, doi: 10.1016/j.powtec.2021.04.083.
[17] A. Gonzalez-Quiroga *et al.*, "Azimuthal and radial flow patterns of 1g-Geldart B-type particles in a gas-solid vortex reactor", *Powder Technol.*, vol. 354, pp. 410–422, 2019, doi: https://doi.org/10.1016/j.powtec.2019.06.015.
[18] L. A. Vandewalle, A. Gonzalez-Quiroga, P. Perreault, K. M. Van Geem, and G. B. Marin, "Process intensification in a gas-solid vortex unit: Computational fluid dynamics model based analysis and design", *Ind. Eng. Chem. Res.*, vol. 58, no. 28, pp. 12751–12765, 2019, doi: 10.1021/acs.iecr.9b01566.
[19] M. Y. Naz, S. A. Sulaiman, and M. A. Bou-Rabee, "Particle tracking velocimetry investigations on density dependent velocity vector profiles of a swirling fluidized bed", *Dry. Technol.*, vol. 35, no. 2, pp. 193–202, Jan. 2017, doi: 10.1080/07373937.2016.1166124.
[20] B. G. M. van Wachem, "Derivation, implementation, and validation of computer simulation models for gas-solid fluidized beds", Delft University of Technology, Delft, 2000.
[21] D. Gidaspow, Multiphase flow and fluidization: continuum and kinetic theory descriptions. Academic press, 1994.
[22] F. Moukalled, L. Mangani, and M. Darwish, *The Finite Volume Method in Computational Fluid Dynamics*, vol. 168. New York: Springer, 2016. doi: 10.1007/978-3-319-16874-6.
[23] C. K. K. Lun, S. B. Savage, D. J. Jeffrey, and N. Chepurniy, "Kinetic theories for granular flow: Inelastic particles in Couette flow and slightly inelastic particles in a general flowfield", *J. Fluid Mech.*, vol. 140, pp. 223–256, 1984, doi: 10.1017/S0022112084000586.
[24] J. L. Sinclair and R. Jackson, "Gas-particle flow in a vertical pipe with particle-particle interactions", *AIChE J.*, vol. 35, no. 9, pp. 1473–1486, 1989, doi: 10.1002/aic.690350908.
[25] K. Agrawal, P. N. Loezos, M. Syamlal, and S. Sundaresan, "The role of meso-scale structures in rapid gas-solid flows", *J. Fluid Mech.*, vol. 445, no. October 2001, pp. 151–181, 2001, doi: 10.1017/s0022112001005663.
[26] ANSYS Fluent, "ANSYS Fluent User' s Guide, Release 15.0". ANSYS, Inc., Canonsburg, 2013.
[27] P. C. Johnson, P. Nott, and R. Jackson, "Frictional–Collisional Equations of Motion for Particulate Flows and Their Application To Chutes", *J. Fluid Mech.*, vol. 241, no. 20, pp. 125–144, 1990, doi: 10.1017/S0022112090001380.
[28] D. O. Njobuenwu, M. Fairweather, and J. Yao, "Coupled RANS–LPT modelling of dilute, particle-laden flow in a duct with a 90° bend", *Int. J. Multiph. Flow*, vol. 50, pp. 71–88, 2013, doi: https://doi.org/10.1016/j.ijmultiphaseflow.2012.10.009.
[29] H. Norouzi and R. Khodabandehlou, "Mastering twoPhaseEulerFoam. One : Fluidized bed - How to simulate a gas-solid fluidized bed using OpenFOAM®", 2019. [Online]. Available: https://www.cemf.ir/sdm_downloads/mastering-twophaseeulerfoam-one-fluidized-bed/
[30] P. C. Johnson and R. Jackson, "Frictional-collisional constitutive relations for granular materials, with application to plane shearing", *J. Fluid Mech.*, vol. 176, pp. 67–93, 1987, doi: 10.1017/S0022112087000570.
[31] H. Zhong, X. Lan, J. Gao, Y. Zheng, and Z. Zhang, "The difference between specularity coefficient of 1 and no-slip solid phase wall boundary conditions in CFD simulation of gas–solid fluidized beds", *Powder Technol.*, vol. 286, pp. 740–743, 2015, doi: https://doi.org/10.1016/j.powtec.2015.08.055.

[32] J. Rajchenbach, "Dense, Rapid Flows of Inelastic Grains under Gravity", *Phys. Rev. Lett.*, vol. 90, no. 14, p. 4, 2003, doi: 10.1103/PhysRevLett.90.144302.
[33] A. Manni, "An introduction to twoPhaseEulerFoam with addition of an heat exchange model", 2014. [Online]. Available: http://www.tfd.chalmers.se/~hani/kurser/OS_CFD_2014/Alessandro Manni/ReportAM.pdf
[34] R. Courant, K. Friedrichs, and H. Lewy, "Über die partiellen Di erenzengleichungen der mathematischen Physik. w thF ennF, 100 (1): 32 74, 1928", *English Transl. Partial Differ. equations Math. physics. sfw tF esF hevelopF*, vol. 11, pp. 215–234, 1967.
[35] F. Scala, *Fluidized Bed Technologies for near-Zero Emission Combustion and Gasification*. Cambridge, UNITED KINGDOM: Elsevier Science & Technology, 2013. [Online]. Available: http://ebookcentral.proquest.com/lib/unorte-ebooks/detail.action?docID=1581395
[36] OpenCFD Ltd., "OpenFOAM®: User Guide", 2020. https://www.openfoam.com/documentation/user-guide/1-introduction (accessed Aug. 06, 2021).
[37] T. Xing and F. Stern, "Factors of safety for Richardson extrapolation", *J. Fluids Eng.*, vol. 132, no. 6, pp. 0614031–0640313, 2010, doi: 10.1115/1.4001771.
[38] NPARC Alliance CFD Verification and Validation, "Examining Spatial (Grid) Convergence", 2021. https://www.grc.nasa.gov/www/wind/valid/tutorial/spatconv.html (accessed Dec. 01, 2021).
[39] P. J. Roache, "Quantification of uncertainty in computational fluid dynamics", *Annu. Rev. Fluid Mech.*, vol. 29, no. 1, pp. 123–160, 1997.
[40] P. J. Roache, "Verification of Codes and Calculations", *AIAA J.*, vol. 36, no. 5, pp. 696–702, May 1998, doi: 10.2514/2.457.
[41] S. A. Sulaiman, C. S. Miin, M. Y. Naz, and V. R. Raghavan, "Particle Image Velocimetry of a Swirling Fluidized Bed at Different Blade Angles", *Chem. Eng. Technol.*, vol. 39, no. 6, pp. 1151–1160, Jun. 2016, doi: 10.1002/ceat.201500074.
[42] M. A. Javed, S. Shukrullah, M. Y. Naz, and R. A. Sarfraz, "Image velocimetry and statistical analysis of a mesh-coupled axial blade distributor for mass transfer in a swirling bed", *J. Theor. Appl. Mech.*, vol. 58, no. 3, pp. 779–790, 2020, doi: 10.15632/JTAM-PL/120806.
[43] S. Shukrullah, M. A. Javed, M. Y. Naz, Y. Khan, M. A. S. S. Alkanhal, and H. Anwar, "PIV and Statistical Analysis of a Swirling Bed Process Carried out Using a Hybrid Model of Axial Blade Distributor", *Process.* , vol. 7, no. 10, 2019, doi: 10.3390/pr7100697.
[44] M. Y. Naz, S. A. Sulaiman, S. Shukrullah, A. Ghaffar, Y. Khan, and I. Ahmad, "PIV investigations on particle velocity distribution in uniform swirling regime of fluidization", *Granul. Matter*, vol. 19, no. 2, 2017, doi: 10.1007/s10035-017-0727-4.
[45] S. R. Kulkarni *et al.*, "Computational Fluid Dynamics-Assisted Process Intensification Study for Biomass Fast Pyrolysis in a Gas–Solid Vortex Reactor", *Energy & Fuels*, vol. 32, no. 10, pp. 10169–10183, Oct. 2018, doi: 10.1021/acs.energyfuels.8b01008.
[46] W. Yang, Handbook of fluidization and fluid-particle systems. CRC press, 2003.
[47] D. C. Chitester, R. M. Kornosky, L.-S. Fan, and J. P. Danko, "Characteristics of fluidization at high pressure", *Chem. Eng. Sci.*, vol. 39, no. 2, pp. 253–261, 1984, doi: https://doi.org/10.1016/0009-2509(84)80025-1.
[48] M. Rozainee, S. P. Ngo, A. A. Salema, K. G. Tan, M. Ariffin, and Z. N. Zainura, "Effect of fluidising velocity on the combustion of rice husk in a bench-scale fluidised bed combustor for the production of amorphous rice husk ash", *Bioresour. Technol.*, vol. 99, no. 4, pp. 703–713, 2008, doi: https://doi.org/10.1016/j.biortech.2007.01.049.

4. Design of a Swirling Fluidized Bed Reactor demonstration unit for biomass conversion

Abstract

Process Intensification (PI) of gas-solid operations promotes the design of alternatives technologies to meet the current needs of the chemical industry. Centrifugal fluidized beds operates in a dense bed with higher gas-solid slip velocities, enhancing mass and heat transfer rates compared to a conventional fluidized bed. A design procedure of a Swirling Fluidized Bed (SFB) demonstration unit is proposed for biomass thermochemical conversion into energy, fuels, and other chemicals including four processes: combustion, gasification, pyrolysis and torrefaction. Theoretical and semi-experimental models, and technical procedures derived from chemical, thermodynamics and mechanical are used for dimensioning the SFB reactor. An experimental-based case study of design is conducted for comparing the design procedure results with the actual working SFB reactor for burning 80 kg h^{-1} of rice husk. Complete combustion of the rice husk requires an actual air flow rate of 536.09 kg h^{-1} producing an outlet hot gas flow rate of 617.63 kg h^{-1}. The designed SFB reactor generates a power output of 132 kW with 40% of thermal efficiency. The construction of the SFB reactor under the operating conditions requires a material with a minimum yield strength of 200 MPa. Materials selection analysis revealed that stainless steels and Ni-based alloys have the best performance for rice husk combustion. Final dimensions of the designed SFB reactor are in line with the actual setup from the experimental study. The selection of the gas driving system ensures the supply of gas flow requirements for heating, reactions and fluidization. Further works should focus on the design of a thermal insulation system for the SFB reactor through a heat transfer analysis across the reactor walls. Also, dimensioning the solids feeder would add enough information about material and energy consumptions to study the economic feasibility of a SFB reactor installation.

4.1. Introduction

The transition to a more sustainable chemical industry using alternative natural resources to produce chemicals, fuels, and by-products, e.g., electric power, leads to innovative reactor designs [1]. The implementation of process intensification (PI) strategies would achieve this objective. PI reduces equipment size by orders of magnitude; enhances heat, mass, and momentum transfer rates; and improves control combined with safer, cost-effective, and energy-efficient operation [2]. The wide use of gas-solid fluidized beds (FB) for reactive and non-reactive processes makes it an attractive option for PI application [3]. This work focuses on the design of a Swirling Fluidized Bed (SFB) reactor demonstration unit for biomass thermochemical conversion in a centrifugal field [8]–[10]. Replacing the gravitational field with a centrifugal one results in a dense fluidized bed with higher gas-solid slip velocities enhancing the interfacial transfer of heat, mass, and momentum [4]. The SFB reactor has the potential to process particles in gas-solid contact for different industries, e.g., biomass conversion in fuels, energy, or high-value chemicals [5]–[7]. The processes concerned in the design of the SFB are combustion, gasification, pyrolysis, and torrefaction of biomass because they are the most common technologies for biomass thermochemical valorization [11]–[13].

Conventional FBs, i.e., gravitational beds, present inherent limitations in gas-solid contact operations. First, the gas-solid slip velocities cannot exceed the terminal velocity of the particles in the earth's gravitational field. Further disadvantages include the width-height ratio of the bed of particles must be small enough to avoid the formation of non-uniformities and the capacity to fluidize a narrow range of particle sizes and densities [4], [14]–[16]. In the SFB reactor, the gas flow passes through inclined blades, increasing its velocity and changing its direction while the solid particles are continuously fed [17]. The current gas flow through the bed of particles fluidizes the particles and changes their angular momentum generating a centrifugal force. The combined effect of the centrifugal force and the gravitational field induces a swirling movement to the bed of particles (i.e., circumferential and helical simultaneously) [10], [18], [19]. The centrifugal field in the SFB reactor removes the restriction in gas-solid slip velocity, contributes to the rapid formation of a uniform circulating mass of particles, and increases the process efficiency. The higher velocities and better distribution of particles in the enhances the heat, mass, and momentum transfer rates between the particles and the gas flow, improving temperature control in the processing chamber [20]–[23]. The characteristics of a SFB reactor design offer a wide range of gas flow rates and processing particles of various sizes, densities, and shapes [10], [24]. Both experimental and numerical studies reveal the potential of the SFB reactor for process intensification. The SFB reactor use have been proposed in several industries: flash roasting [25], calcination [26], gas adsorption [27], food processing [28], wastes management [29], drying [30], combustion [17], [31], gasification [7], pyrolysis [32], and torrefaction [33].

Research about the SFB reactor has focused on the study of hydrodynamics, e.g., [34], [35], and thermal [36], [37] bed behaviors, to identify and derive mathematical models for predicting bed properties. Others analyze the SFB performance changing operating conditions in various applications, e.g., combustion [38], [39] and drying [40], [41]. A common aspect in these studies is the insufficient information about the selection and dimensioning of the SFB reactor design

parameters, such as the number of blades, and the blade and the vessel thickness, for the desired operation. Only two works concern the design details of the SFB reactor from the literature review. First, Paulose [42] studied the hydrodynamics of the SFB reactor for drying food and developed design models focusing on the geometry of the SFB gas distributor. Later, Venkiteswaran [43] used the models in [42] to design a demonstration unit of the SFB reactor and perform experimental works. The review reveals the knowledge gap in procedures or calculation datasheets about the mechanical design of the SFB reactor.

This work represents the next step in designing SFB reactors for biomass thermochemical conversion into energy, fuels, chemical precursors, and high-value molecules through a basic design procedure. The first section presents a detailed description of the SFB reactor demonstration unit for biomass thermochemical conversion. Then, depending on the thermochemical conversion process, the equilibrium of reactions and the steady-state mass and energy balances solve a preliminary size of the SFB reactor [12]. The minimum fluidization of the particles and fluid mechanics models, e.g., continuity equation and linear momentum balance, give the acting forces in the SFB reactor due to gas flow [44], [45]. Subsequently, a force and stress analysis in the components of the reactor gives the thickness and maximum allowable yield strength [46], [47]. The design results are summarized as design specifications in the requirements lists [48]. The material selection for building the SFB reactor follows the methodology based on Ashby's approach [49]. The procedure includes the estimation of major pressure drops across the SFB reactor. Finally, the proposed design procedure is employed to solve a case study to design a SFB reactor for rice husk combustion based on experimental data.

4.2. Swirling fluidized bed operational setting

Figure 4-1 illustrates the functioning of the SFB reactor for biomass processing. The operation starts injecting the fluidizing agent into the reactor unit at a constant flow rate, $\dot{m}_g$ (Figure 4-1a). The injection depends on the gas requirement of the operation, e.g., a blower unit draws air into the reactor for combustion and gasification, or a vapor generator or high-pressure gas system injects either water vapor or N_2, respectively, for pyrolysis [12]. The gas enters through the lateral inlet of the SFB reactor to the plenum chamber, where it is distributed and flows upwardly through the annular region between the outer cylindrical wall and the inner structure wall. The air faces the single row blades distributor whose openings with a reduced area between blades split the air flow, increasing its velocity magnitude (Figure 4-1b). The reduction of area in the distributor. The horizontal inclination of the blades changes the air flow direction resulting in an inclined flow with two main components: axial and tangential [8].

Simultaneously, a feeder delivers the biomass particles at the top of the gas distributor at a constant mass rate, $\dot{m}_s$ (Figure 4-1a). Some operations use the SFB reactor under batch operation, i.e., a fixed mass of particles rests on the top of the distributor without a continuous feed of particles to the system while the air is drawn into the reactor. Once the inclined air flow contacts the static bed of particles, the air transfers momentum to the particles to produce the fluidization of the bed (Figure 4-1c). The axial component is responsible for lifting and fluidizing the particles, while the tangential component

causes the rotation of the bed about the central axis of the SFB reactor [50]. The central cone contributes to the uniformity of particle distribution in the bed. Also, the increase of the axial section area promotes the helical movement of the particle in the bed.

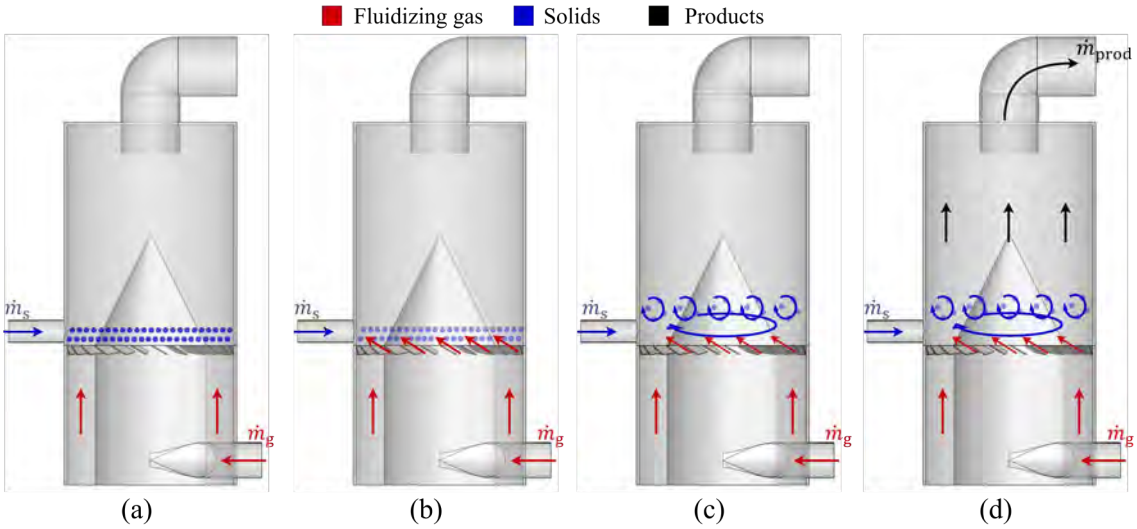

Figure 4-1 SFB reactor operational schematic diagram. (a)-(d) illustrate the steps of the SFB reactor operation. The color of the elements in the diagram represents the process streams: red represents the fluidizing gas, blue the solids, and black the products. Source: Figure created by author.

Depending on the process, an additional burner is needed to reach the desired temperature inside the reactor [17], [39]. After the biomass processing is complete, the products $\dot{m}_{\mathrm{prod}}$ flow upwardly and exits the reactor at the top outlet (Figure 4-1d). The design of the particle feeder and post-processing separation of the products using cyclones or other equipment is beyond the scope of this work.

4.2.1. Operating conditions and input requirements of biomass treatments

This section describes the thermochemical models used to determine $\dot{m}_{\mathrm{g}}$, $\dot{m}_{\mathrm{s}}$, and $\dot{m}_{\mathrm{prod}}$ of the SFB reactor.

This section deals with the sizing of four biomass treatments: combustion, gasification, pyrolysis, and torrefaction. Table 4-1 shows operating conditions and the pre-drying requirements of these processes.

Table 4-1 Operating conditions of biomass treating processes considered for the design of the SFB reactor [12].

Process	**Combustion**	**Gasification**	**Pyrolysis**	**Torrefaction**
Temperature, °C	700-1400	500-1300	300-600	200-300
Pressure, MPa	≥0.1	≥0.1	0.1-0.5	0.1
Drying	Not essential	Necessary	Necessary	Necessary

The following assumptions reduce the chemical and thermodynamics analysis of each process [12], [51]:

a. The process occurs under steady operating conditions.
b. Kinetic and potential energy changes are negligible.
c. Heat transfer between the reacting zone and the surroundings causes an energy loss through the reactor wall.
d. The reactor housing is a rigid tank and does not include rotary shafts, i.e., the net power output is zero (there is neither boundary nor shaft work).
e. Dry air is approximated as 21% oxygen and 79% nitrogen by mole numbers, i.e., each mole of oxygen in the reactions is accompanied by 0.79/0.21=3.76 moles of nitrogen.
f. The reactions are stoichiometric and thus complete.
g. Reactive and product gases are ideal gases.

4.2.1.1. Combustion

The combustion of biomass is a direct burning process used to release the chemical energy stored in biomass as heat through the oxidization of the fuel. The heat is in the form of hot gases at temperatures between 700-1400 °C. Depending on the needs, additional equipment transforms the heat into mechanical power or electricity [52]. The SFB reactor burns any type of biomass in single or co-combustion processes [11]. A high level of elutriation in the SFB reactor leads to combustion efficiencies up to 99.9% due to the intensive mass and transfer rates [53]. The preferred biomass moisture content is <50%, though it seems to not significatively affect combustion performance [39], [54], [55]. According to Basu [12], the customer must provide the following information to specify the combustion process of biomass:

a. the biomass ultimate analysis with moisture content,
b. air moisture content ω_{a},
c. either the required power output of the combustor $\dot{Q}_{\mathrm{total}}$ or the biomass feed rate $\dot{m}_{\mathrm{b}}$,
d. either the percent of excess air EA or the combustion temperature T_{comb}, and
e. the combustion pressure P_{comb}

Combustion of biomass uses air to create an oxygen-rich environment for the reaction. The assumed dry air consists of 21% oxygen and 79% nitrogen. Assuming the combustion products contain $\mathrm{CO_2}$, $\mathrm{H_2O}$, $\mathrm{SO_2}$, and $\mathrm{N_2}$, Equation (4-1) is the chemical equilibrium formula for combustion of 1 mol of biomass in dry air.

$$\mathrm{CH}_a\mathrm{O}_b\mathrm{S}_c\mathrm{N}_d + e_{\mathrm{st}}(\mathrm{O_2} + 3.76\mathrm{N_2}) \rightarrow \mathrm{CO_2} + \frac{a}{2}\mathrm{H_2O} + c\mathrm{SO_2} + \left(\frac{d}{2} + 3.76e\right)\mathrm{N_2} \qquad (4\text{-}1)$$

Where the constants a, b, c, and d in the chemical formula of the biomass depend on the wt.% of each component in the ultimate analysis in dry ash free basis, the wt.% of C, and their molecular weights as in Equation (4-2a); where $i = \mathrm{H, O, S, N}$. Equation (4-2b) calculates the value of e_{st} from the mole balance of $\mathrm{O_2}$ in the chemical reaction formula.

$$\text{constant} = \frac{\%\mathrm{wt}_i}{\%\mathrm{wt}_{\mathrm{C}}} \times \frac{\mathrm{MW}_{\mathrm{C}}}{\mathrm{MW}_i} \qquad (4\text{-}2a)$$

$$e_{\mathrm{st}} = 1 + \frac{a}{2} + c - \frac{b}{2} \tag{4-2b}$$

Therefore, Equation (4-3) gives the stoichiometric air-fuel mass ratio $\mathrm{AF_{th}}$ for the combustion of biomass in dry ash free basis.

$$\mathrm{AF_{st}} = \frac{4.76 e_{\mathrm{st}} \mathrm{MW_{air}}}{\mathrm{MW_{biomass}}} \tag{4-3}$$

Where $\mathrm{MW_{air}}$ and $\mathrm{MW_{biomass}}$ correspond to the molecular weight of the air and the biomass, respectively. $\mathrm{MW_{biomass}}$ is the molecular weight of biomass in dry ash free basis calculated from the chemical formula of the biomass and molecular weights of the species using the following relation.

$$\mathrm{MW_{biomass}} = \mathrm{MW_C} + a\mathrm{MW_H} + b\mathrm{MW_O} + c\mathrm{MW_S} + d\mathrm{MW_N}$$

The client specifies the combustor's required power output, $\dot{Q}_{total}$. Equation (4-4) denotes that the power output depends on the heat of combustion $\dot{Q}_{\mathrm{comb}}$, the heat used to vaporize the moisture content of biomass $\dot{Q}_{\mathrm{vap,biomass}}$, and the heat loss of the combustor $\dot{Q}_{\mathrm{loss}}$.

$$\dot{Q}_{\mathrm{total}} = \dot{Q}_{\mathrm{comb}} - \dot{Q}_{\mathrm{vap,b}} - \dot{Q}_{\mathrm{loss}} \tag{4-4}$$

Based on this, the designer estimates a preliminary amount of biomass feed rate into the SFB reactor with Equation (4-5):

$$\dot{m}_{\mathrm{b}} = \frac{\dot{Q}_{\mathrm{comb}}}{\mathrm{LHV_b}} \tag{4-5}$$

Where $\mathrm{LHV_b}$ is the lower heating value of the biomass, i.e., the amount of heat released after combusting 1 mole of biomass less the heat of vaporization of the water product formed in the combustion [51]. Equation (4-6) estimates the $\mathrm{LHV_b}$ on an "as-received" ("ar") basis as a function of the higher heating value of the biomass $\mathrm{HHV_b}$ on "ar" basis, and the latent heat of steam h_{fg} at the operating pressure.

$$\mathrm{LHV_b} = \mathrm{HHV_b} - h_{fg} \frac{a}{2} \frac{\mathrm{MW_{H_2O}}}{\mathrm{MW_{biomass}}} \tag{4-6}$$

Equation (4-7) is a unified correlation for $\mathrm{HHV_b}$ [12]; where C, H, S, O, N, and ASH are the % wt from the ultimate analysis of biomass on a dry basis.

$$\mathrm{HHV_b} = 349.1\mathrm{C} + 1178.3\mathrm{H} + 100.5\mathrm{S} - 103.4\mathrm{O} - 15.1\mathrm{N} - 21.1\mathrm{ASH} \tag{4-7}$$

The enthalpy of formation of the biomass is estimated from the definition of the enthalpy of combustion h_{comb}. h_{comb} is the heat released during a steady-flow combustion process after burning 1 kmol of fuel at a specified temperature and pressure. Equation (4-8a) denotes h_{comb} as the difference between the enthalpy of formation of the products H_{prod} and reactants H_{react} at a specified state of reference. The value of h_{comb} is approximated to the $\mathrm{HHV_b}$ of the biomass fuel in Equation (4-8b) [51].

$$-\mathrm{HHV_b} = h_{\mathrm{comb}} = H_{\mathrm{prod}} - H_{react} \tag{4-8a}$$

$$-\mathrm{HHV} = \sum N_{\mathrm{prod}} \bar{h}^{\circ}_{f,\mathrm{prod}} - \sum N_{\mathrm{react}} \bar{h}^{\circ}_{f,\mathrm{react}} \tag{4-8b}$$

where N_i is the number of moles, and $\bar{h}^{\circ}_{f,i}$ the enthalpy of formation of the compound i of the products and reactive from the stoichiometric formula (4-1). Then, the enthalpy of formation of the biomass $\bar{h}^{\circ}_{f,\mathrm{b}}$ is obtained with Equation (4-9). $\mathrm{N_2}$ and $\mathrm{O_2}$ related terms disappear since their enthalpy of formation is zero [51].

$$\bar{h}^{\circ}_{f,\mathrm{b}} = \mathrm{HHV} + N_{\mathrm{CO_2}} \bar{h}^{\circ}_{f,\mathrm{CO_2}} + N_{\mathrm{H_2O}} \bar{h}^{\circ}_{f,\mathrm{H_2O}} + N_{SO_2} \bar{h}^{\circ}_{f,\mathrm{SO_2}} \tag{4-9}$$

The combustion process at actual operating conditions considers burning the biomass with a moisture content ω_{b} using wet air with a moisture content ω_{da} at an excess air value of $\mathrm{EA} = \frac{\mathrm{AF_{act}}}{\mathrm{AF_{th}}} - 1$. Equation (4-10) is the equilibrium formula of combustion at the actual conditions of operation.

$$\begin{aligned} &\mathrm{CH}_a\mathrm{O}_b\mathrm{S}_c\mathrm{N}_d + e_{\mathrm{act}}(\mathrm{O_2} + 3.76\mathrm{N_2}) + f\mathrm{H_2O} \rightarrow \\ &\mathrm{CO_2} + c\mathrm{SO_2} + \left(\frac{d}{2} + 3.76e\right)\mathrm{N_2} + g\mathrm{H_2O} + h\mathrm{O_2} \end{aligned} \tag{4-10}$$

Where

$$e_{\mathrm{act}} = \frac{\mathrm{AF_{act}MW_{biomass}}}{4.76\mathrm{MW_{air}}}$$

$$f = \frac{(\omega_{\mathrm{b}} + e_{\mathrm{act}}\omega_{\mathrm{da}}\mathrm{MW_{air}})}{\mathrm{MW_{H_2O}}}$$

$$g = \frac{a}{2} + f$$

$$h = \frac{b}{2} + e_{\mathrm{act}} - c - \frac{a}{4} - 1$$

and Equation (4-11) gives the actual air mass flow rate.

$$\dot{m}_{\mathrm{act,air}} = \mathrm{AF_{act}}\dot{m}_{\mathrm{b}} \tag{4-11}$$

Equation (4-12) correspond to the estimation of the composition of the hot gas product comprising carbon dioxide, water vapor, nitrogen, oxygen, and sulfur dioxide derived from Equation (4-10). The mass fraction x_i of each component in the product gas is in kg per kg of fuel in dry ash free basis.

$$x_{\mathrm{CO_2}} = \frac{\mathrm{MW_{CO_2}}}{\mathrm{MW_{biomass}}} \tag{4-12a}$$

$$x_{\mathrm{H_2O}} = g\frac{\mathrm{MW_{H_2O}}}{\mathrm{MW_{biomass}}} \tag{4-12b}$$

$$x_{\mathrm{N_2}} = \left(\frac{d}{2} + 3.76e_{\mathrm{act}}\right)\frac{\mathrm{MW_{N_2}}}{\mathrm{MW_{biomass}}} \tag{4-12c}$$

$$x_{\mathrm{O_2}} = h\frac{\mathrm{MW_{O_2}}}{\mathrm{MW_{biomass}}} \tag{4-12d}$$

$$x_{SO_2} = c\frac{MW_{SO_2}}{MW_{biomass}} \tag{4-12e}$$

And the total mass flow rate of product gas is given by Equation (4-13).

$$\dot{m}_{prod} = \dot{m}_b(1 - ASH - \omega_b)(x_{CO_2} + x_{H_2O} + x_{N_2} + x_{O_2} + x_{SO_2}) \tag{4-13}$$

Equation (4-14) is the energy balance in the combustor used to solve the combustion temperature T_{comb} assuming complete vaporization of both the formed components and the moisture content of the biomass.

$$H_{prod} = H_{react} + H_{vap,H_2O} + H_{loss} \tag{4-14a}$$

$$\sum N_{prod}\left(\bar{h}_f^o + \bar{h}(T) - \bar{h}^o\right)_{prod} = \sum N_{react}\left(\bar{h}_f^o + \bar{h}(T) - \bar{h}^o\right)_{react} + h_{fg}\frac{\omega_b}{MW_{H_2O}} + \dot{Q}_{loss} \tag{4-14b}$$

Where $\bar{h}_f^o$ is the enthalpy of formation; and $\bar{h}(T) - \bar{h}^o$ the enthalpy at temperature T of the ideal gas measured at a reference level $\bar{h}^o$ of the products (CO_2, H_2O, N_2, O_2, and SO_2), and the reactive (biomass and wet air, composed by N_2, O_2, and H_2O).

Equation (4-15) is the Shomate equation model for estimating $\bar{h}(T) - \bar{h}^o$ of each compound [56]. Table B-1 in Appendix B.1 summarizes the constant values of the model for each compound.

$$\bar{h}(T) - \bar{h}^o = \left(AT + B\frac{T^2}{2} + C\frac{T^3}{3} + D\frac{T^4}{4} - \frac{E}{T} + F - H\right)\frac{1000}{MW_i} \tag{4-15}$$

4.2.1.2. Gasification

The gasification process consists of partial oxidation of biomass to convert it into a combustible gas mixture at high temperatures, known as syngas. The syngas is burnt directly for heat and power generation or used as a feedstock for producing chemicals [52]. Effective biomass gasification requires a controlled-oxygen environment, i.e., using an air-fuel ratio below the theoretical value for complete combustion. Therefore, the customer must provide the following information to specify the biomass gasification process [12]:

a. the biomass ultimate analysis with moisture content,
b. desired product gas composition,
c. desired heating value LHV_{prod}
d. either the required power output of the gasifier $\dot{Q}$, or the desired production gas rate $\dot{m}_{prod}$,
e. the biomass feed rate $\dot{m}_b$,
f. the gasification pressure P_{gasif}, and
g. the gasification temperature T_{gasif}.

Equation (4-16) preliminarily calculates the product volumetric flow rate $\dot{V}_{prod}$ depending on the required power output $\dot{Q}_{total}$ and the desired heating value LHV_{prod} in a volume basis.

$$\dot{V}_{\text{prod}} = \frac{\dot{Q}_{\text{total}}}{\text{LHV}_{\text{prod}}} \tag{4-16}$$

and Equation (4-17) estimates $\dot{V}_{\text{prod}}$ and LHV_{prod}.

$$\dot{V}_{\text{prod}} = \frac{\dot{m}_{\text{prod}}}{\rho_{\text{prod}}} \tag{4-17a}$$

$$\text{LHV}_{\text{prod}} = \sum y_i \text{LHV}_i \tag{4-17b}$$

Where ρ_{prod} is the product gas density. LHV_{prod} estimation is based on the model of Fanchi [57] from its composition: y_i is the mole fraction of component i, and LHV_i the heating value of component i in the product gas.

Equation (4-18) is the equilibrium model used to predict the composition of the product gas, assuming the gasification products C, H_2, CO, H_2O, CO_2, CH_4, N_2 and the reaction of the biomass with air and steam.

$$\begin{aligned}\text{CH}_a\text{O}_b\text{N}_c + e_{\text{act}}(\text{O}_2 + 3.76\text{N}_2) \rightarrow n_1\text{C} + n_2\text{H}_2 + n_3\text{CO} \\ + n_4\text{H}_2\text{O} + n_5\text{CO}_2 + n_6\text{CH}_4 + n_7\text{N}_2\end{aligned} \tag{4-18}$$

where $n_1, \ldots, n_7$ correspond to the stoichiometric coefficients of the products. Equation (4-2a) solves a, b, and c from the ultimate analysis of the biomass to obtain the chemical formula $\text{CH}_a\text{O}_b\text{N}_c$. Estimation of the e_{act} value will be described later in this section depending on the ultimate analysis and the biomass feed rate.

Equation (4-19) is the biomass feed rate $\dot{m}_{\text{b}}$ depending on the required power output $\dot{Q}_{\text{total}}$, the LHV_{b} of the biomass, and the gasifier efficiency η_{gasif}. The LHV_{b} is estimated using the Equations (4-6) and (4-7).

$$\dot{m}_{\text{b}} = \frac{\dot{Q}_{\text{total}}}{\text{LHV}_{\text{b}}\eta_{\text{gasif}}} \tag{4-19}$$

The complete combustion of 1 kmol of fuel requires $4.76e_{\text{th}}$ of air (Equation (4-2a)) when the sulfur content from the ultimate analysis of the biomass is zero. Then, the theoretical air mass flow rate is equal to

$$\dot{m}_{\text{st,air}} = 4.76e_{\text{st}} \frac{\text{MW}_{\text{air}}}{\text{MW}_{\text{biomass}}} \dot{m}_{\text{b}}$$

Equations (4-20) and (4-21) are the actual air mass flow rate requirement $\dot{m}_{\text{act,air}}$ for gasification of biomass and the e_{act} value, respectively, as functions of $\dot{m}_{\text{st,air}}$ and the equivalence ratio (ER).

$$\dot{m}_{\text{act,air}} = \dot{m}_{\text{st,air}}\text{ER} \tag{4-20}$$

$$e_{\text{act}} = e_{\text{st}}\text{ER} \tag{4-21}$$

A first-guess value suggested for determining the adequate ER value is 0.25 [12].

Using the equilibrium equation (4-18), the total number of unknown coefficients is seven. Equation (4-22) corresponds to the atomic balance of carbon, hydrogen, oxygen, and nitrogen.

$$\text{C: } n_1 + n_3 + n_5 + n_6 = 1 \tag{4-22a}$$

$$\text{H: } 2n_2 + 2n_4 + 4n_6 = a + 2d \tag{4-22b}$$

$$\text{O: } n_3 + n_4 + 2n_5 = b + 2e_{\text{act}} \tag{4-22c}$$

$$\text{N: } n_7 = c + 7.52e \tag{4-22d}$$

Considering a simplified approach to the equilibrium model of a gasifier, reactions R1, R2, R3, and R9 in Equation (4-23) take place [12].

$$\text{R1: } \mathrm{CO_2 + C \rightarrow 2CO} \tag{4-23a}$$

$$\text{R2: } \mathrm{C + H_2O \rightarrow H_2 + CO} \tag{4-23b}$$

$$\text{R3: } \mathrm{C + 2H_2 \rightarrow CH_4} \tag{4-23c}$$

$$\text{R9: } \mathrm{CO + H_2O \rightarrow CO_2 + H_2} \tag{4-23d}$$

Considering the water gas shift reaction, R9, as the subtraction of the steam gasification and Boudouard reactions, the gasification process only includes the equilibrium of reactions R1, R2, and R3. The equilibrium constants K_{e_i} derives the Equation (4-24) to solve reactions R1, R2, and R3 for a gasifier pressure, P [12]

$$K_{e_1} = \frac{y_{CO}^2 P}{y_{CO_2}} = \frac{n_3^2 P}{n_5 n_{total}} \tag{4-24a}$$

$$K_{e_2} = \frac{y_{CO} y_{H_2} P}{y_{H_2O}} = \frac{n_3 n_2 P}{n_4 n_{total}} \tag{4-24b}$$

$$K_{e_3} = \frac{y_{CH_4}}{y_{H_2}^2 P} = \frac{n_3 n_{total}}{n_4^2 P} \tag{4-24c}$$

where y_i is the mole fraction for compounds i of CO, $\mathrm{H_2}$, $\mathrm{H_2O}$, $\mathrm{CH_4}$, and $\mathrm{CO_2}$; and n_{total} is the sum of the coefficients of the products in the equilibrium equation (4-18). The equilibrium constants are functions of temperature in °C. They are calculated with regression models constructed from collected data of an AspenPlus® equilibrium reactor model set with reactions R1, R2, and R3 valid in the range of 700-1200 °C [58]. Equation (4-25) are the corresponding regression models for the equilibrium constants.

$$K_{e_1} = 1.58 \times 10^{-5} T^3 - 3.90 \times 10^{-2} T^2 + 32.1T - 8.79 \times 10^3 \tag{4-25a}$$

$$K_{e_2} = 4.44 \times 10^{-6} T^3 - 1.04 \times 10^{-2} T^2 + 8.23T - 2.18 \times 10^3 \tag{4-25b}$$

$$K_{e_3} = -2.60 \times 10^{-9} T^3 + 8.17 \times 10^{-6} T^2 - 8.56 \times 10^{-3} T + 2.99 \tag{4-25c}$$

The non-linear systems of equations encompassing Equations (4-22), (4-24), and (4-25) enable the calculation of $\mathrm{LHV_{prod}}$. The estimation of the desired heating value of the products requires an iterative process varying the ER until the calculated $\mathrm{LHV_{prod}}$ converges.

The product constants in the equilibrium formula at actual conditions give the Equation (4-26) which corresponds to the composition of the hot gas product comprising carbon dioxide, water vapor, nitrogen, oxygen, and sulfur dioxide. The mass fraction x_i of each component in the product gas is in kg per kg of fuel.

$$x_{\mathrm{C}} = n_1 \frac{\mathrm{MW_C}}{\mathrm{MW_{biomass}}} \tag{4-26a}$$

$$x_{\mathrm{H_2}} = n_2 \frac{\mathrm{MW_{H_2}}}{\mathrm{MW_{biomass}}} \tag{4-26b}$$

$$x_{\mathrm{CO}} = n_3 \frac{\mathrm{MW_{CO}}}{\mathrm{MW_{biomass}}} \tag{4-26c}$$

$$x_{\mathrm{H_2O}} = n_4 \frac{\mathrm{MW_{H_2O}}}{\mathrm{MW_{biomass}}} \tag{4-26d}$$

$$x_{\mathrm{CO_2}} = n_5 \frac{\mathrm{MW_{CO_2}}}{\mathrm{MW_{biomass}}} \tag{4-26e}$$

$$x_{\mathrm{CH_4}} = n_6 \frac{\mathrm{MW_{CH_4}}}{\mathrm{MW_{biomass}}} \tag{4-26f}$$

$$x_{\mathrm{N_2}} = n_7 \frac{\mathrm{MW_{N_2}}}{\mathrm{MW_{biomass}}} \tag{4-26g}$$

Finally, Equation (4-27) expresses the gas product flow rate of the gasification process

$$\dot{m}_{\mathrm{prod}} = \dot{m}_{\mathrm{b}}(x_{\mathrm{C}} + x_{\mathrm{H_2}} + x_{\mathrm{CO}} + x_{\mathrm{H_2O}} + x_{\mathrm{CO_2}} + x_{\mathrm{CH_4}} + x_{\mathrm{N_2}}) \tag{4-27}$$

4.2.1.3. Pyrolysis

The conversion of biomass through pyrolysis yields three products: liquid bio-oil, solid char, and pyrolysis gas. The typical pyrolysis process consists of heating the biomass without oxygen to around 500 °C. Despite the possibility of obtaining three energy products, the fast pyrolysis process maximizes bio-oil production obtaining biomass-to-oil conversion yields of up to 75% [52], [59]. The biomass heating rate is as high as 1000-10000 °C $\mathrm{s^{-1}}$, but the peak temperature must not exceed 650 °C to avoid biomass decomposition and obtain the desired bio-oil characteristics [12]. The fast pyrolysis mathematical models and their results in this section are valid only for wood biomass feedstocks.

The customer must provide the following information to specify the biomass fast pyrolysis process:

a. the biomass ultimate analysis with moisture content,
b. either the required power output from the pyrolysis process $\dot{Q}_{\mathrm{total}}$ or the biomass feed rate $\dot{m}_{\mathrm{b}}$,
c. the pyrolysis temperature T_{pyr},

d. the pyrolysis pressure P_{pyr},
e. the external heating rate B,
f. fluidizing gas type (e.g., N_2, oxygen-free combustion gases), and
g. inlet temperature of fluidizing gas and biomass, $T_{0,\mathrm{g}}$ and $T_{0,\mathrm{b}}$, respectively.

The bio-oil product volumetric flow rate $\dot{V}_{\mathrm{oil}}$ is calculated with Equation (4-28)

$$\dot{V}_{\mathrm{oil}} = \frac{\dot{Q}_{\mathrm{total}}}{\mathrm{LHV}_{\mathrm{oil}}} \tag{4-28}$$

Where $\mathrm{LHV}_{\mathrm{oil}}$ is the lower heating value of the bio-oil. Equation (4-29) gives the $\mathrm{LHV}_{\mathrm{oil}}$ which is the total energy content released after burning off the bio-oil products from pyrolysis in air $\mathrm{HHV}_{\mathrm{oil}}$ minus the energy required to vaporize the fraction of the formed water $x_{\mathrm{H_2O}}$ [60].

$$\mathrm{LHV}_{\mathrm{oil}} = \mathrm{HHV}_{\mathrm{oil}} - h_{\mathrm{fg,H_2O@25°C}} x_{\mathrm{H_2O}} \tag{4-29}$$

Equation (4-30) is the IGT (Institute of Gas Technology) formula for estimating $\mathrm{HHV}_{\mathrm{oil}}$ from the proximate and ultimate analysis of the liquid products on a dry basis [60].

$$\mathrm{HHV}_{\mathrm{oil}} = 341\mathrm{C} + 1323\mathrm{H} + 68\mathrm{S} - 15.3\mathrm{ASH} - 120(\mathrm{O} + \mathrm{N}) \tag{4-30}$$

A solver routine developed by [61] gives the yields and composition of bio-oil based on the fast-pyrolysis experimental results from [62]. This routine uses the ultimate analysis of the wood biomass on a dry basis to close the atomic balance with the water and ash content in the char product. The ultimate analysis on a dry basis of the bio-oil is the result of the routine with carbon (C), hydrogen (H), and oxygen (O) in kg per kg of bio-oil.

The solver routine also obtains the conversion rate of the biomass into bio-oil X, which solves the biomass feed flow rate using Equation (4-31).

$$\dot{m}_b = \frac{\dot{V}_{\mathrm{oil}} \rho_{\mathrm{oil}}}{X} \tag{4-31}$$

The fluidizing gas flow rate $\dot{m}_{\mathrm{g}}$ depends on the heat requirement for pyrolysis $\dot{Q}_{\mathrm{total}}$ as a function of the difference between the temperature of pyrolysis T_{pyr} and inlet temperature of the fluidizing gas using Equation (4-32).

$$\dot{m}_{\mathrm{g}} = \frac{\dot{Q}_{\mathrm{total}}}{c_{p,\mathrm{g}}(T_{\mathrm{pyr}} - T_{0,g})} \tag{4-32}$$

Where $c_{p,\mathrm{g}}$ is the specific heat capacity of the fluidizing gas.

Pyrolysis is an endothermic reaction, i.e., requires a heat supply to induce the process. When the process occurs in the SFB reactor, the fluidizing gas transfers heat directly to the biomass. Equation (4-33a) denotes the heat requirement for the reaction, which comprises the heat to increase the biomass temperature to the temperature at which pyrolysis occurs and the heat for the endothermic pyrolysis [63]. A drying process removes the moisture content from the biomass ω_{b} before the actual

pyrolysis (Equation (4-33b)). Equation (4-33c) corresponds to the total heat requirement for the pyrolysis of biomass $\dot{Q}_{\text{total}}$.

$$\dot{Q}_{\text{pyr}} = \dot{m}_{\text{b}}(1-\omega_{\text{b}})\left[c_{p,\text{b}}\left(T_{\text{pyr}}-T_{0,\text{b}}\right)+\Delta H_r\right] \quad (4\text{-}33a)$$

$$\dot{Q}_{\text{dry}} = \dot{m}_{\text{b}}\omega_{\text{b}}\left[c_{p,\text{H}_2\text{O}}\left(100-T_{0,\text{b}}\right)+h_{\text{fg,H}_2\text{O}}\right] \quad (4\text{-}33b)$$

$$\dot{Q}_{\text{total}} = \dot{Q}_{\text{pyr}} + \dot{Q}_{\text{dry}} + \dot{Q}_{\text{loss}} \quad (4\text{-}33c)$$

Where $c_{p,b}$ is the specific heat capacity of the biomass, ΔH_r the reaction heat, $c_{p,\text{H}_2\text{O}}$ the specific heat capacity of the water, and $h_{\text{fg,H}_2\text{O}}$ the vaporization enthalpy of water at the operating pressure P.

Equation (4-34) estimates the specific heat capacity for typical wood biomass in kJ kg^{-1} K^{-1} [12]

$$C_{p,\text{b}} = 0.00614T + 0.84916 \quad (4\text{-}34)$$

Equation (4-35) is a derived model from [63] to estimate ΔH_r as a function of the external heating rate (B), the experimental action rate constant of the biomass (k), and the bio-oil fraction of conversion (X) during pyrolysis obtained from the solver routine [62].

$$\Delta H_r \leq -c_{p,\text{b}}\text{Bln}\,(1-X)/(0.5kX) \quad (4\text{-}35)$$

The value of B should exceed 4.81 °C s^{-1}, and k is a function of temperature and the biomass properties as expressed in Equation (4-36)

$$k = A\exp\left(-\frac{E_a}{RT}\right) \quad (4\text{-}36)$$

Where A_{rh} is the pre-exponential factor of the Arrhenius Equation, E_a the activation energy of the biomass, R the universal gas constant, and T. Table 4-2 summarizes values of these variables for different wood biomass [63].

Table 4-2 pre-exponential factor of the Arrhenius Equation A and the activation energy E_a for different wood biomass [63].

Sample	A_{rh}, s^{-1}	E_a, kJ kmol^{-1}
Oak	2.47×10^{6}	106.5
Hardwood	1.48×10^{6}	89.52
Gum tree	3.64×10^{4}	69.1
Forest wood	2.4×10^{4}	95.4
Beech	2.4×10^{4}	95.4

4.2.1.4. Torrefaction

Torrefaction of biomass is a thermochemical process that occurs in an inert or limited oxygen environment to obtain a solid product with high-intensive mass and energy yield. The heating process of the biomass is slow until it increases the temperature to a specified range. Then, the temperature is

maintained for a prolonged period to reach a near complete degradation of hemicellulose in the biomass [12].

The customer must provide the following information to specify the torrefaction of biomass [12]:

a. the biomass ultimate analysis with moisture content,
b. required solid products flow rate $\dot{m}_{\mathrm{prod}}$,
c. torrefaction temperature, T_{torr}
d. desired mass yield as dry ash-free $\mathrm{MY_{daf}}$,
e. expected moisture ω_{prod} and ash $\mathrm{ASH_{prod}}$ fractions of the product, and
f. fluidizing gas type (e.g., N_2, oxygen-free combustion gases).

Equation (4-37) gives the raw biomass feed flow rate to meet the capacity of the torrefier and the desired mass yield

$$\dot{m}_{\mathrm{b}} = \frac{\dot{m}_t(1 - \omega_{\mathrm{prod}} - \mathrm{ASH_{prod}})}{\mathrm{MY_{daf}}(1 - \omega_{\mathrm{b}} - \mathrm{ASH_b})} \tag{4-37}$$

Equation (4-38) is the estimation of the water vapor flow rate after drying the moisture content of the biomass.

$$\dot{m}_{\mathrm{moist}} = \omega_{\mathrm{b}}\dot{m}_b \tag{4-38}$$

The mass balance in the torrefier gives Equation (4-39) to calculate the volatiles flow rate.

$$\dot{m}_{\mathrm{prod}} = \dot{m}_{\mathrm{b}} - \dot{m}_{\mathrm{prod}} - \omega_{\mathrm{b}}\dot{m}_{\mathrm{b}} \tag{4-39}$$

The heating of the biomass until the torrefaction temperature T_{torr} comprises three stages: preheat, drying of biomass, and post-drying heating. Equation (4-40) corresponds to the required heat tranfer input for each stage.

i. Preheat from inlet temperature to drying temperature

$$\dot{Q}_{\mathrm{ph}} = \dot{m}_{\mathrm{b}}\left[(1 - \omega_{\mathrm{b}})c_{p,\mathrm{b}} + \omega_{\mathrm{b}}c_{p,\mathrm{H_2O}}\right](100 - T_{0,\mathrm{b}}) \tag{4-40a}$$

ii. Evaporation of moisture in biomass

$$\dot{Q}_{\mathrm{dr}} = \dot{m}_{\mathrm{b}}\omega_{\mathrm{b}}h_{\mathrm{fg,H_2O}} \tag{4-40b}$$

iii. Post-drying heat to torrefaction temperature

$$\dot{Q}_{\mathrm{pd}} = \dot{m}_{\mathrm{b}}(1 - \omega_{\mathrm{b}})c_{p,\mathrm{b}}(T_{\mathrm{torr}} - 100) \tag{4-40b}$$

Equation (4-41) represents the sum of the three heat transfers values and the heat losses through the reactor vessel wall equivalent to the heat required to reach the torrefaction temperature

$$\dot{Q}_{\mathrm{total}} = \dot{Q}_{\mathrm{ph}} + \dot{Q}_{\mathrm{dr}} + \dot{Q}_{\mathrm{pd}} + \dot{Q}_{\mathrm{loss}} \tag{4-41}$$

Similarly, as in Equation (4-32), the mass flow rate of fluidizing gas depends on $\dot{Q}_{\text{total}}$, $c_{p,\text{g}}$, T_{torr} and the inlet temperature of the fluidizing gas $T_{0,\text{g}}$, giving Equation (4-42).

$$\dot{m}_{\text{g}} = \frac{\dot{Q}_{\text{total}}}{c_{p,\text{g}}(T_{\text{torr}} - T_{0,g})} \tag{4-42}$$

4.3. Design procedure of the swirling fluidized bed reactor

4.3.1. Minimum fluidization velocity and actual gas velocity

The functioning of any type of fluidized bed relies on the characteristic gas velocity known as the minimum fluidization velocity V_{mf}. Gas velocities below the minimum fluidization maintain the packed bed of solid static, although there is a measurement of pressure drop across the bed [44]. The gas stream supports all the bed particles at the minimum fluidization velocity, starting fluidization from the lowest to upper layers [50].

Figure 4-2 shows the gas velocity vectors before (V_{sup}) and after (V_{inj}) the gas flow passes through the distributor openings. V_{sup} is the gas velocity when the gas flows through the annular region between the inner and outer radii of the reactor, known as superficial velocity. After the gas flow passes the distributor openings, the reduced area increases the magnitude of the gas velocity to the injection velocity V_{inj}. The incompressible continuity relation in Equation (4-43) is a good approximation to relate the magnitude of V_{sup} and V_{inj}.

$$\dot{V}_{\text{msf}} = V_{\text{inj}} A_{\text{op,total}} = V_{\text{sup}} A_{\text{bed}} \tag{4-43}$$

Where $A_{\text{op,total}}$ is the total area of the distributor openings normal to the flow direction, and $A_{\text{bed}} = \pi(r_o^2 - r_i^2)$ is the annular area of the reactor, which applies for both the top and the bottom of the distributor in this design. Section 4.3.2 will describe the geometry of the distributor, including details of $A_{\text{op,total}}$ estimation.

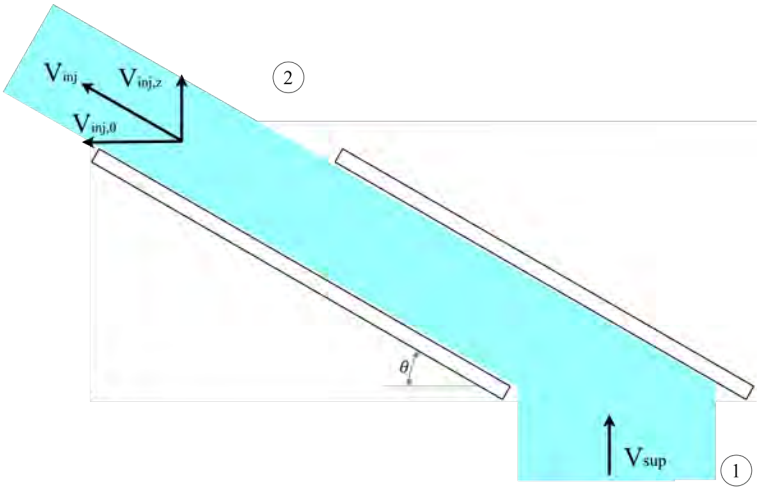

Figure 4-2 Schematic of gas flow passing through the openings of the distributor. V_{sup} is the superficial gas velocity before the distributor, and V_{inj} the injection gas velocity after passing the distributor. $V_{inj,z}$ and $V_{inj,\theta}$ are axial and azimuthal components of the injection gas velocity in the cylindrical coordinates. Source: Figure created by author.

The inclined openings change the gas flow direction, resulting in two components of V_{inj}: axial and tangential. The axial component $V_{\mathrm{inj,z}}$ is responsible for the bed fluidization, and the tangential $V_{\mathrm{inj,\theta}}$ one for the swirl motion of the bed material [34]. Equation (4-44) gives the minimum magnitude of the axial velocity which should meet the minimum fluidization velocity of the system.

$$V_{\mathrm{mf}} = V_{\mathrm{inj,z,mf}} = V_{\mathrm{inj,mf}} \sin\theta \tag{4-44}$$

Equation (4-45) is the Ergun equation as a function of the Reynolds number and Archimedes number used to solve V_{mf} [44]

$$\mathrm{Re}_{\mathrm{mf}} = \sqrt{C_1^2 + C_2 \mathrm{Ar}} - C_1 \tag{4-45}$$

Where C_1 and C_2 are constants from different studies. The modified form of the Ergun Equation from Chitester et al. [64] proposed the constant values $C_1 = 28.7$ and $C_2 = 0.0494$. The study showed that these values improved the prediction of V_{mf} from the Ergun Equation in a wider range of Ar compared to other modifications. Equation (4-46) estimates $(\mathrm{Re})_{\mathrm{mf}}$ and Ar values.

$$\mathrm{Re}_{\mathrm{mf}} = \frac{V_{\mathrm{mf}} \rho_{\mathrm{g}} d_{\mathrm{s}}}{\mu_{\mathrm{g}}} \tag{4-46a}$$

$$\mathrm{Ar} = \frac{d_{\mathrm{s}}^3 \rho_{\mathrm{g}} (\rho_{\mathrm{s}} - \rho_{\mathrm{g}}) \mathrm{g}}{\mu_{\mathrm{g}}^2} \tag{4-46b}$$

For a particle with a diameter d_{s} and density ρ_{s}, and fluidizing gas with a density ρ_{g} and dynamic viscosity μ_{g}.

Solving V_{mf} from Equations (4-45) and (4-46) results in Equation (4-47).

$$V_{\mathrm{mf}} = \left[\sqrt{C_1^2 + C_2 \frac{d_{\mathrm{s}}^3 \rho_{\mathrm{g}} (\rho_{\mathrm{s}} - \rho_{\mathrm{g}}) \mathrm{g}}{\mu_{\mathrm{g}}^2}} - C_1 \right] \frac{\mu_{\mathrm{g}}}{\rho_{\mathrm{g}} d_{\mathrm{s}}} \tag{4-47}$$

During the operation of the SFB reactor, increasing the magnitudes of the velocity components affects the contribution to the fluidization and swirl of the bed, resulting in different bed regimes [50]. The desired operation regime is the swirling regime which ensures the swirl flow motion of the bed. Kumar and Murthy [65] found that the minimum swirling velocity V_{msf} is about 1.2-3.3 times the minimum fluidization velocity of the system. Equation (4-48) is a first guess of V_{msf}.

$$V_{\mathrm{msf}} \cong 2.25\, V_{\mathrm{mf}} \tag{4-48}$$

Equation (4-49) gives the injection velocity after the blades for minimum swirling fluidization based on Equation (4-44).

$$V_{\mathrm{inj,msf}} = \frac{V_{\mathrm{msf}}}{\sin\theta} \tag{4-49}$$

Equation (4-50) relates the magnitudes of the minimum swirling superficial $V_{\mathrm{sup,msf}}$ and injection $V_{\mathrm{inj,msf}}$ gas velocities using the same assumptions as in Equation (4-43).

$$\dot{V}_{\mathrm{msf}} = V_{\mathrm{inj,msf}} A_{\mathrm{op,total}} = V_{\mathrm{sup,msf}} A_{\mathrm{bed}} \tag{4-50}$$

Using Equations (4-49) and (4-50) to solve $V_{\mathrm{sup,msf}}$ gives Equation (4-51).

$$V_{\mathrm{sup,msf}} = \frac{V_{\mathrm{msf}}}{\sin\theta} \frac{A_{\mathrm{op,total}}}{A_{\mathrm{bed}}} \tag{4-51}$$

Equation (4-52) represents the ratio between the distributor openings area and the annular section, known as the percentage area of opening %op.

$$\%\mathrm{op} = \frac{A_{\mathrm{op,total}}}{A_{\mathrm{bed}}} \times 100 \tag{4-52}$$

and solves Equation (4-51) into Equation (4-53)

$$V_{\mathrm{sup,msf}} = \frac{V_{\mathrm{msf}}}{\sin\theta} \%\mathrm{op} \tag{4-53}$$

The actual operation of the SFB reactor with a distributor design of %op and the actual superficial gas velocity should meet the Equation (4-54).

$$V_{\mathrm{sup,act}} \geq V_{\mathrm{sup,msf}} \tag{4-54a}$$

$$V_{\mathrm{sup,act}} \geq \frac{V_{\mathrm{msf}}}{\sin\theta} \frac{\%\mathrm{op}}{100} \tag{4-54b}$$

The calculated gas flow rate $\dot{m}_{\mathrm{g}}$ from Section 4.2.1 and the gas density ρ_{g} solve the actual volumetric gas flow rate

$$\dot{V}_{\mathrm{g,act}} = \frac{\dot{m}_{\mathrm{g}}}{\rho_{\mathrm{g}}}$$

Equation (4-55) gives $V_{\mathrm{sup,act}}$ as a function of $\dot{m}_{\mathrm{g}}$ from the definition of the volumetric gas flow rate.

$$V_{\mathrm{sup,act}} = \frac{\dot{m}_{\mathrm{g}}}{\rho_{\mathrm{g}} A_{\mathrm{bed}}} \tag{4-55}$$

Using Equations (4-54a) and (4-55) solves Equation (4-56) for estimation the maximum A_{bed} required to ensure the fluidization and swirl flow of the bed with the actual operating conditions to treat biomass in the SFB reactor.

$$A_{\mathrm{bed}} \leq \frac{\dot{m}_{\mathrm{g}} \sin\theta}{V_{\mathrm{msf}} \rho} \frac{100}{\%\mathrm{op}} \tag{4-56}$$

The information received from the customer about the SFB reactor desired size or the available space for the installation is relevant for selecting A_{bed}.

4.3.2. Dimensioning of the swirling fluidized bed reactor

4.3.2.1. Housing

Figure 4-3 Figure 4-3shows the global dimensions of the SFB reactor housing for the compact and expanded type reactors. The available space for the installation of the SFB reactor limits the height (H_{vessel}) and the outer radius (r_{o} for compact type and r_{c} for expanded type) of the reactor. The customer must provide the constraints about space to the designer for the adequate sizing of the reactor.

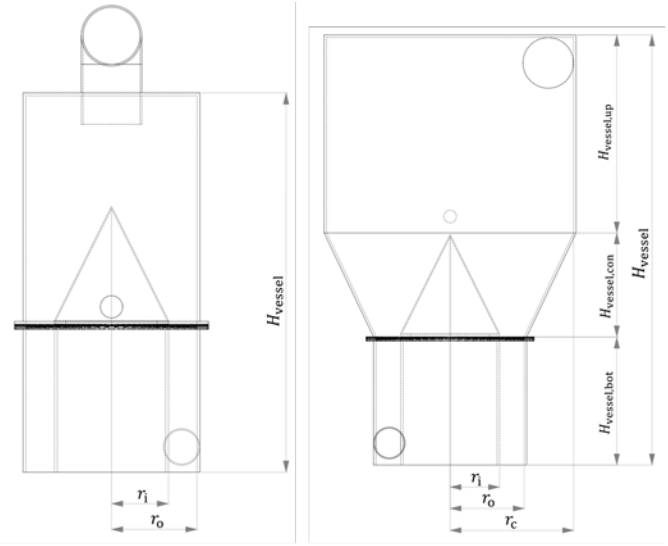

Figure 4-3 Global dimensions of the (a) compact and (b) expanded SFB reactors. Source: Figure created by author.

In the case of the expanded SFB reactor, H_{vessel} comprises three sections: the cylindrical bottom $H_{\text{vessel,bot}}$, the conical center $H_{\text{vessel,con}}$, and the cylindrical upper $H_{\text{vessel,up}}$. The inner radius r_{i} will depend on the desired annular area A_{bed} in Equation (4-56) for achieving the actual gas flow rate at the expected gas velocity.

Table 4-3 compares the compact and expanded SFB reactor according to the 1g-Geldart's group of particles. The designer should compare the characteristics of the particle of interest and decide which type of reactor is adequate for the application.

Table 4-3 Compact and expanded SFB reactor operating constraints for selection purposes.

	Compact	**Expanded**
Feedstock 1g-Geldart's group	D	A, B, and C
Particle size	Size from 25 mm to a few microns	Size from 150 to 5 μm
Particle shape	Spherical, cylindrical, plate-like, shredded, or other shapes	Spherical, cylindrical, plate-like, shredded, or other shapes
Typical solid's residence time	0.1-120 s	5-10 min

4.3.2.2. Single row blades type distributor

This section describes the geometrical analysis of the single row blade type distributor used in the SFB reactor [42]. Figure 4-4 shows a schematic of the distributor, which comprises a circumferential array of static inclined blades, two support rings (inner and outer), and a central cone above the blades array. Figure 4-5a illustrates the design of the blades, which is a truncated sector of a circle and overlapped to form an annular region between the distributor inner (r_{i}) and outer (r_{o}) radii. Blade length corresponds to $L = r_{\mathrm{o}} - r_{\mathrm{i}}$. The blade angle ($\phi = \gamma + \beta$) covers the arc of circle of the blade. Figure 4-5b illustrates the overlapped blades, angle α is the separation between adjacent blades between their top edges on the horizontal plane and depends on the number of blades N_{blade}. Angles β and γ are the free length and overlapping length, respectively.

Figure 4-5c shows the front view of the opening between blades trapezoidal-shaped, and its area depends on the horizontal blade inclination angle θ, width between blades y, and blade thickness t. Equation (4-57) denotes the distance between the points a and c in Figure 4-5c, which are the top edges of two adjacent blades, as a function of the radial position $r\epsilon[r_{\mathrm{i}}, r_{\mathrm{o}}]$.

$$ac(r) = r\sqrt{2\,(1-\cos\alpha)} \tag{4-57}$$

Equations (4-58) and (4-59) give the width between blades and angle between blades

$$y(r) = r\sqrt{2\,(1-\cos\alpha)}\sin\theta - t \tag{4-58}$$

$$\alpha = \frac{360°}{N_{\mathrm{blade}}} \tag{4-59}$$

The angle β is a function of the angle between blades α according to Equation (4-60)

$$\beta = \cos^{-1}[1-\cos^2(1-\cos\alpha)] \tag{4-60}$$

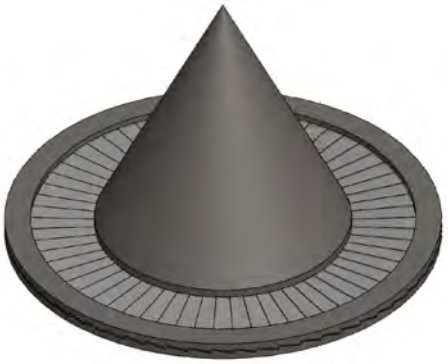

Figure 4-4 Schematic of a single row blade distributor. Source: Figure created by author.

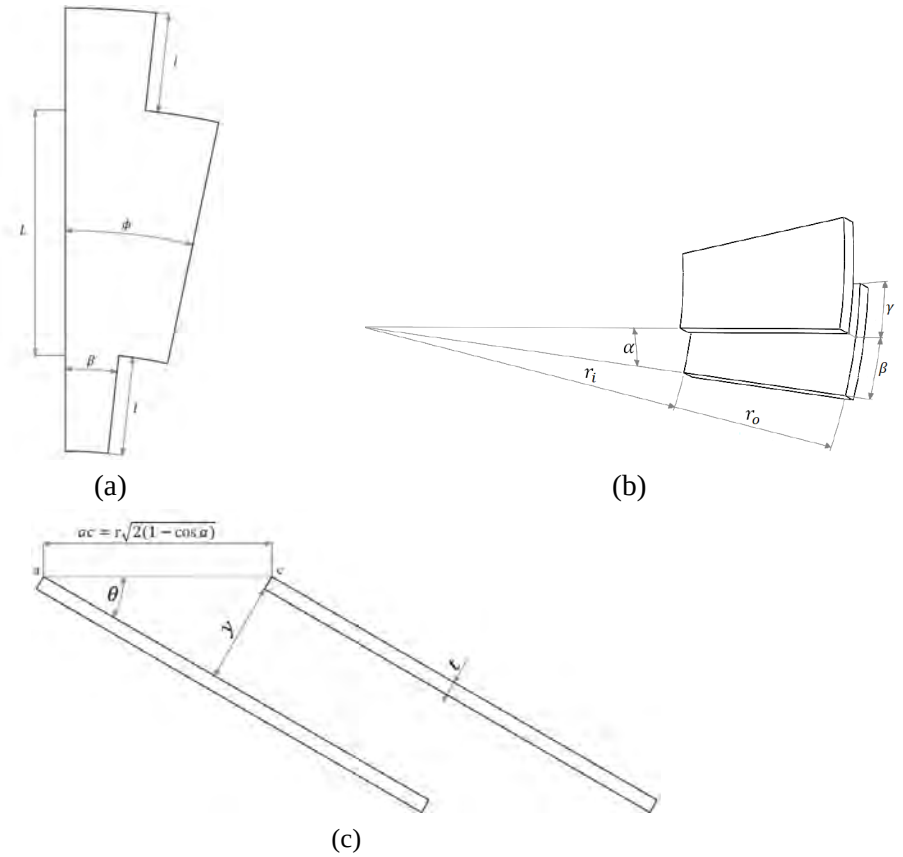

Figure 4-5 Geometrical specifications of the blades' arrangement. The top view of one blade (a) illustrates the main angles and lengths. The top (b) and front (c) views show the separation and overlapping dimensions in the distributor. Source: Adapted from [42].

Equations (4-61) to (4-64) give the annular bed area A_{bed}, the opening area between two adjacent blades $A_{\text{op,blade}}$ normal to θ, the total opening area of the distributor $A_{\text{op,total}}$, and the percentage area of opening %op.

$$A_{\text{bed}} = \pi\left(r_{\text{o}}^2 - r_{\text{i}}^2\right) \tag{4-61}$$

$$A_{\text{op,blade}} = \frac{y_{\text{o}} - y_{\text{i}}}{2}(r_{\text{o}} - r_{\text{i}}) \tag{4-62}$$

$$A_{\text{op,total}} = A_{\text{op,blade}}\, N_{\text{blade}} \tag{4-63}$$

$$\%\text{op} = \frac{A_{\text{op,total}}}{A_{\text{bed}}} \times 100 \tag{4-64}$$

An essential aspect of the distributor design process is the possible interference between blades nearby the inner ring because of the trapezoidal shape of the openings. Equation (4-65) calculates the minimum allowed inner radius before interference between blades $r_{\text{i,min}}$ as a function of blade thickness t, the horizontal blade inclination angle θ, and number of blades N_{blade}.

$$r_{\mathrm{i,min}} = \frac{t}{\sin\theta\sqrt{2\left(1-\cos\frac{360°}{N_{\mathrm{blade}}}\right)}} \tag{4-65}$$

Table B-2 in Appendix B.2 presents some values of $r_{\mathrm{i,min}}$ for different combinations of t and θ and a fixed value of $N_{\mathrm{blade}} = 60$.

4.3.3. Load and stress analysis

This section describes the mathematical models related to the load analysis and mechanical design through stress estimation in the components.

4.3.3.1. Single row blades type distributor

4.3.3.1.1. External forces and moments and free body diagram

The distributor design procedure assumes the following operating conditions:

- The gas flows upwardly from the bottom of the reactor at a constant rate $\dot{m}_{\mathrm{g,total}}$, and
- the mass of the bed of particles m_{bed} rests on the blades.

Figure 4-6 illustrates the forces acting on the blades of the distributor. The bed weight W_{bed} and the force acting on the blades due to gas flow F_{flow} are assumed as uniform distributed loads at the free length of the blades to simplify the model.

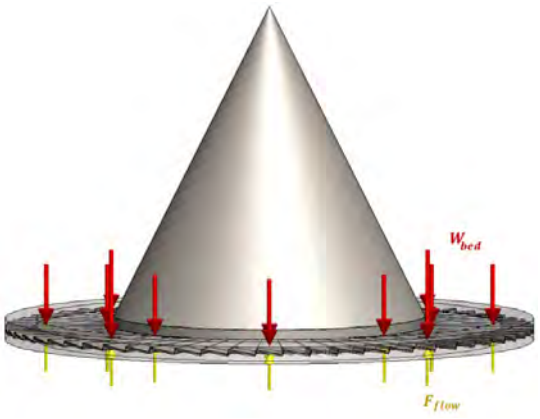

Figure 4-6 Annular single row blades distributor scheme. W_{bed} is the bed weight and F_{flow} the force acting on the blades due to gas flow. Source: Figure created by author.

Equation (4-66) gives the gas mass flow rate in the reactor starting from the gas volumetric flow rate $\dot{V}_{\mathrm{g}}$, and the gas density ρ_{g}.

$$\dot{m}_{\mathrm{total}} = \dot{V}\rho_{\mathrm{g}} \tag{4-66}$$

Equations (4-67) and (4-68) calculate the reacting force due to gas flow on each blade $F_{\mathrm{R,blade}}$ and the gas flow rate through each opening $\dot{m}_{\mathrm{blade}}$ as functions of the number of blades N.

$$F_{\mathrm{blade}} = \frac{F_{\mathrm{flow}}}{N_{\mathrm{blade}}} \tag{4-67}$$

$$\dot{m}_{\text{blade}} = \frac{\dot{m}_{\text{total}}}{N_{\text{blade}}} \tag{4-68}$$

The linear momentum balance of the system is in Equation (4-69) [66]. The term on the right side of Equation (4-69a) is the change of linear momentum of the system equal to the sum of all forces acting on the system material considered a free body. In Equation (4-69b), the first term on the left side corresponds to the rate of change of linear momentum within the control volume, and the second term is the net flux of linear momentum between the outlet and inlet control surfaces.

$$\frac{d}{dt}(mV)_{\text{syst}} = \sum F \tag{4-69a}$$

$$\sum F = \frac{d}{dt}\left(\int_{\text{CV}} V\rho d^{\circ}\text{V}\right) + \int_{\text{CS}} V\rho(V \cdot \text{n})dA \tag{4-69b}$$

Figure 4-7 illustrates the control volume (CV) cutting through the inlet and exit of the jet and the adjacent blade. The blade friction is internally self-canceling since there is no cut along the blade-jet interface. The weight of fluid and blade within the CV are neglected.

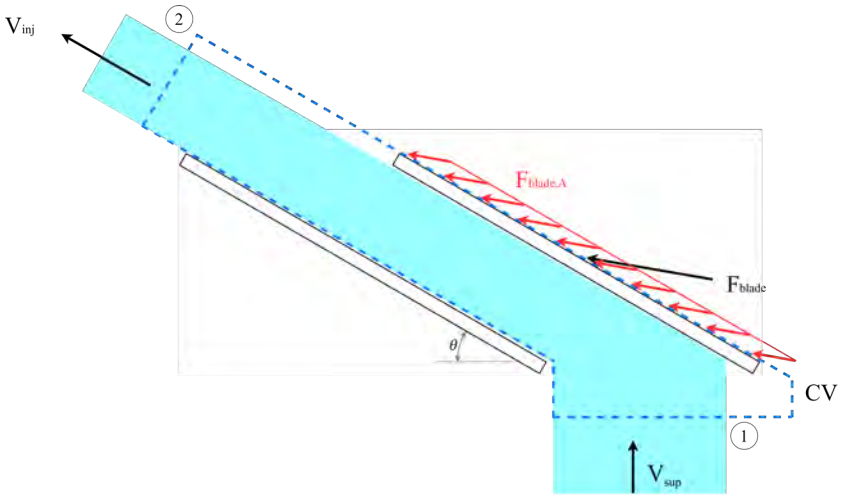

Figure 4-7 Free body diagram of the control volume CV, comprising the gas flow passing through the opening between two adjacent blades, and the net applied force on a fixed inclined blade due to gas flow F_{blade}. Source: Figure created by author.

The dot product in Equation (4-69b) for a one-dimensional cross-section, V and ρ are uniform over the area, and the integrated result is

$$\int_{\text{CS}} V\rho(V \cdot \text{n})dA = V(\rho V_n A) = \pm\dot{m}V$$

The final term is positive for outlet flux and negative for inlet flux. The proposed model has a one-dimensional inlet and outlet, and the system is operating under a steady state. Solving Equation (4-69a) with these assumptions gives Equation (4-70)

$$\sum F = \sum (\dot{m}_i V_i)_{\text{out}} - \sum (\dot{m}_i V_i)_{\text{in}} \tag{4-70}$$

The right-side term is equal to

$$\sum F = \vec{F}_{\text{blade}} + \vec{F}_{\text{Press,1}} + \vec{F}_{\text{Press,2}}$$

The mass balance of the CV in Figure 4-7 between states 1 and 2 yields

$$\dot{m}_1 = \dot{m}_2 = \dot{m}_{\text{blade}}$$

With these, Equation (4-71) is obtained

$$\vec{F}_{\text{blade}} + \vec{F}_{\text{Press,1}} + \vec{F}_{\text{Press,2}} = \dot{m}_{\text{blade}}(\vec{V}_{\text{inj}} - \vec{V}_{\text{sup}}) \tag{4-71}$$

Where the magnitude of $\vec{F}_{\text{Press,1}} + \vec{F}_{\text{Press,2}}$ is equal to the product between the pressure drop across the distributor ΔP_{dist} and the normal area of the opening $A_{\text{op,blade}}$. Due to the low value of $A_{\text{op,blade}} \ll 1$ the product is minimal compared to the linear momentum at the distributor outlet

$$\Delta P_{\text{dist}} A_{\text{orifice}} \ll \dot{m} V_{\text{inj}}$$
$$\rightarrow \Delta P_{\text{dist}} A_{\text{orifice}} \approx 0$$

Considering this assumption and the forces acting on the system results in Equation (4-72), which solves the vector of the reacting force due to gas flow on each blade.

$$\vec{F}_{\text{blade}} = \dot{m}_{\text{blade}}(\vec{V}_{\text{inj}} - \vec{V}_{\text{sup}}) \tag{4-72}$$

Figure 4-8 illustrates the vector diagram for the force and momentum change of the proposed model. Equation (4-73) denotes the rectangular components of F_{blade}.

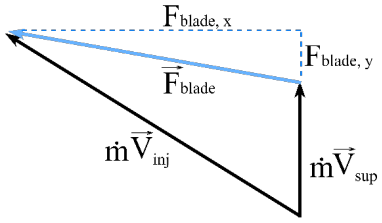

Figure 4-8 Vector diagram for solving the linear momentum change and the net force on the blade. Source: Figure created by author.

$$F_{\text{blade,y}} = \dot{m}_{\text{blade}}(V_{\text{inj}} \sin\theta - V_{\text{sup}}) \tag{4-73a}$$

$$F_{\text{blade,z}} = \dot{m}_{\text{blade}} V_{\text{inj}} \cos\theta \tag{4-73b}$$

$\vec{V}_{\text{sup}}$ and $\vec{V}_{\text{inj}}$ are the vectors of the gas superficial velocity at the distributor inlet and the injection velocity at the distributor outlet, respectively. The relation between these values depends on Equation (4-43).

$$\dot{V} = V_{\text{sup}} A_{\text{bed}} = V_{\text{inj}} A_{\text{op,total}}$$

Figure 4-9a shows the distributed loads acting on the blade due to the bed weight W_{bed} and the effect of gas flow F_{blade}. To ease the analysis of the blade, an axis rotation is made to avoid the use of force components during the mathematical analysis (Figure 4-9b). Equations (4-74) and (4-75) determine the distributed load due to bed weight and the y′ and z′ axis component. An analogous form is used in Equation (4-76) to determine the rectangular components of F_{blade}, i.e., $F_{\mathrm{blade,y'}}$ and $F_{\mathrm{blade,z'}}$.

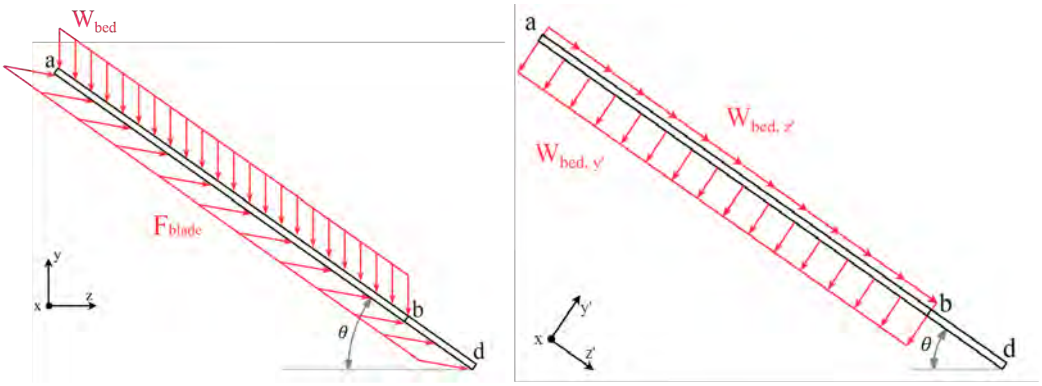

(a) (b)

Figure 4-9 (a) Acting forces on one blade due to bed weight W_{bed} and the effect of gas flow F_{blade}, and (b) rotation of coordinate axis $xy'z'$ with the conversion of bed weight to the new rectangular components $W_{bed,z'}$ and $W_{bed,y'}$. Source: Figure created by author.

$$W_{\mathrm{bed}} = \frac{m_{\mathrm{bed}}\mathrm{g}}{\pi\left(r_o^2 - r_i^2\right)} \tag{4-74}$$

$$W_{\mathrm{bed,y'}} = W_{\mathrm{bed}}\, cos\,\theta \tag{4-75a}$$

$$W_{\mathrm{bed,z'}} = W_{\mathrm{bed}}\, sin\,\theta \tag{4-75b}$$

$$F_{\mathrm{blade,y'}} = F_{\mathrm{blade,y}}\, cos\,\theta - F_{\mathrm{blade,z}} \sin\theta \tag{4-76a}$$

$$F_{\mathrm{blade,z'}} = F_{\mathrm{blade,y}} \sin\theta + F_{\mathrm{blade,z}} \cos\theta \tag{4-76b}$$

The blade model is simplified to a beam supported at both ends and subjected to the uniform loadings W_{bed} and F_{blade}. Figure 4-10 illustrates the 3D free body diagram of the blade. The diagram includes the components of the distributed loads due to bed weight $W_{\mathrm{bed,y'}}$ and $W_{\mathrm{bed,z'}}$, the effect of the gas flow on the blade $F_{\mathrm{blade,y'}}$ and $F_{\mathrm{blade,z'}}$, and the support reacting forces $R_{1,\mathrm{x}}$, $R_{1,\mathrm{y'}}$, $R_{1,\mathrm{z'}}$, $R_{2,\mathrm{x}}$, $R_{2,\mathrm{y'}}$, $R_{2,\mathrm{z'}}$ and reacting moments $M_{\mathrm{R_1}}$, $M_{\mathrm{R_2}}$.

Figure 4-11 models the beam as a 2D body where only acting forces and momentums on the x y′ plane are considered. $w_{\mathrm{bed,res,y',1}}$, $w_{\mathrm{bed,res,y',2}}$ and $F_{\mathrm{blade,res,y'}}$ included in the free body diagram are the resultant forces of the distributed loads.

The bed weight distributed load is assumed as uniform on the blade area. Due to the truncated circle section, the area increases when moving outwardly on the radial axis. This generates a linearly distributed load of the bed weight with a trapezoidal shape with the lower value $w_{\mathrm{bed,y',l}}$ at the inner radius r_{i} and the higher value $w_{\mathrm{bed,y',h}}$ at the outer radius r_{o}. The centroid of the bed weight

distributed load $\bar{x}_{w_{bed}}$ depends on the blade length and the extremes of the distributed load. For the reacting force on the blade, a linear uniform distributed load was assumed $F_{\mathrm{blade,L,y'}}$. The following relations enable the calculation of these variables.

$$w_{\mathrm{bed,y',h}} = \frac{W_{\mathrm{bed,y'}}}{N_{\mathrm{blade}}}(2\pi r_{\mathrm{o}})$$

$$w_{\mathrm{bed,y',l}} = \frac{W_{\mathrm{bed,y'}}}{N_{\mathrm{blade}}}(2\pi r_{\mathrm{i}})$$

$$w_{\mathrm{bed,res,y'}} = w_{\mathrm{bed,res,y',1}} + w_{\mathrm{bed,res,y',2}} = \frac{1}{2}\left(w_{\mathrm{bed,y',h}} + w_{\mathrm{bed,y',l}}\right)L$$

$$\bar{x}_{w_{\mathrm{bed}}} = \frac{2}{3}L\left(\frac{w_{\mathrm{bed,y',h}} + \frac{1}{2}w_{\mathrm{bed,y',l}}}{w_{\mathrm{bed,y',h}} + w_{\mathrm{bed,y',l}}}\right)$$

$$F_{\mathrm{blade,L,y'}} = F_{\mathrm{blade,y'}}\frac{r_{\mathrm{o}} + r_{\mathrm{i}}}{2}$$

$$F_{\mathrm{blade,res,y'}} = F_{\mathrm{blade,L,y'}}L$$

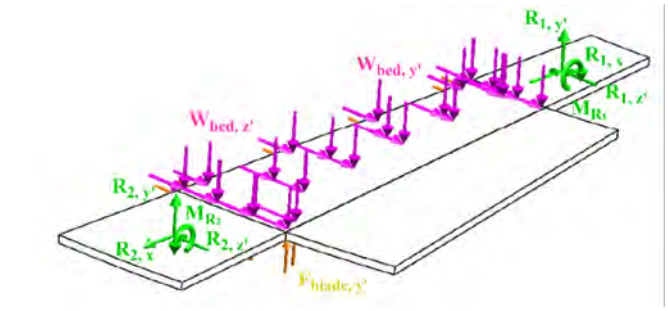

(a)

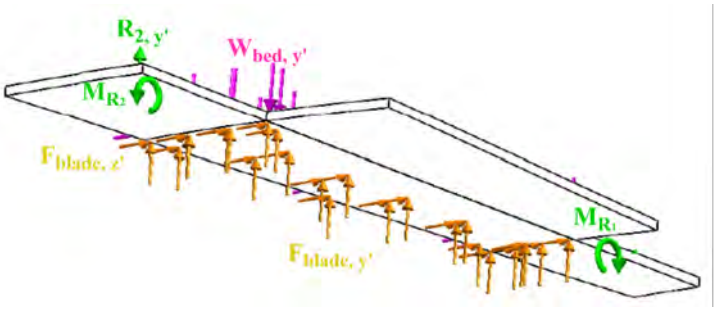

(b)

Figure 4-10 3D Free body diagram of one blade comprising: bed weight $W_{bed,y'}$ and $W_{bed,z'}$, the effect of the gas flow on the blade $F_{blade,y'}$ and $F_{blade,z'}$, and the support reacting forces $R_{1,x}$, $R_{1,y'}$, $R_{1,z'}$, $R_{2,x}$, $R_{2,y'}$, $R_{2,z'}$ and reacting moments M_{R_1}, M_{R_2}. (a) Upper view, and (b) bottom view. Source: Figure created by author.

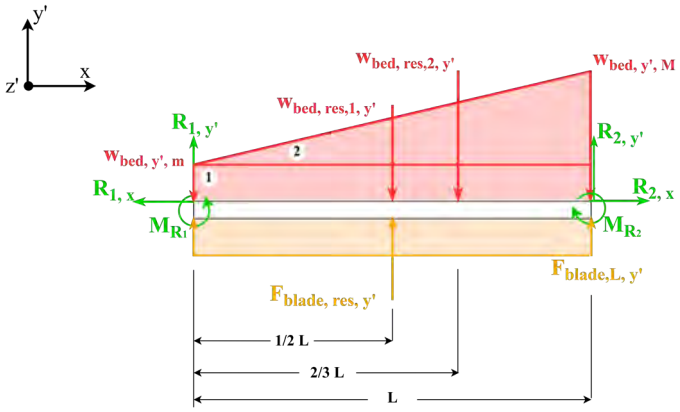

Figure 4-11 2D free body diagram of one blade. The blade is assumed as a beam supported at both ends. Source: Figure created by author.

The first Newton's law applies since the system is static, i.e., in equilibrium. Equations (4-77) to (4-79) are the equations of equilibrium in two dimensions obtained for the external forces acting in direction of x and y′ axes, and the moments of the external forces acting about the centroid $\bar{x}_{w_{\mathrm{bed}}}$.

$$\uparrow^{+} \sum F_{\mathrm{y}}: R_{1,y'} + R_{2,y'} + F_{\mathrm{blade,res,y'}} - w_{\mathrm{bed,res,y'}} = 0 \tag{4-77}$$

$$\rightarrow^{+} \sum F_{\mathrm{x}}: R_{1,\mathrm{x}} - R_{2,\mathrm{x}} = 0 \tag{4-78}$$

$$\circlearrowleft^{+} \sum M_{Z'\bar{\mathrm{x}}_{w_{bed}}}: M_{R_1} - M_{R_2} - R_{1,y'}\bar{\mathrm{x}}_{w_{\mathrm{bed}}} + R_{2,y'}\left(L - \bar{\mathrm{x}}_{w_{bed}}\right) - F_{\mathrm{blade,res,y'}}\left(\bar{\mathrm{x}}_{w_{\mathrm{bed}}} - \frac{1}{2}L\right) = 0 \tag{4-79}$$

4.3.3.1.2. Internal forces and moments

The internal loads, i.e., shearing force $V(\mathrm{x})$ and bending moment $M(\mathrm{x})$, are required in the beam model to proceed with the blade design. Figure 4-12 shows the free body diagram of the portion of the blade at a distance x. Derived Equations (4-80) and (4-81) from the free-body diagram calculate the internal shearing force $V(\mathrm{x})$ and internal bending moment $M(\mathrm{x})$.

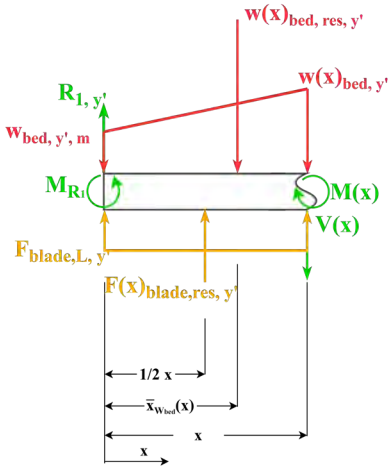

Figure 4-12 Free body diagram of a section of the blade. Source: Figure created by author.

$$V(\mathrm{x}) = R_{1,y'} - w(\mathrm{x})_{\mathrm{bed,res},y'} + F_{\mathrm{blade,L},y'}\mathrm{x} \tag{4-80}$$

$$M(\mathrm{x}) = M_{R_1} + R_{1,y'}\bar{\mathrm{x}}(\mathrm{x})_{w_{\mathrm{bed}}} - w(x)_{\mathrm{bed,res},y'}\left(\mathrm{x} - \bar{\mathrm{x}}(\mathrm{x})_{w_{\mathrm{bed}}}\right) + F_{\mathrm{blade,L},y'}\frac{\mathrm{x}^2}{2} \tag{4-81}$$

4.3.3.1.3. Statically indeterminate analysis

The previous analysis demonstrates that the unknown reactions, $R_{1,y'}$, $R_{2,y'}$ y M_{R_1} and M_{R_2}, exceed the available number of equilibrium equations (Equations (4-77) to (4-79)). The blade is assumed as a statically indeterminate element to solve the external reactions on the blade and requires the application of a load-displacement relationship, i.e., the moment differential equation

$$\frac{d^2\upsilon}{d\mathrm{x}^2} = \frac{M(\mathrm{x})}{EI(\mathrm{x})}$$

Where υ is the deflection or elastic displacement of the blade on the x-axis, $M(\mathrm{x})$ is the internal bending moment in the blade stated in Equation (4-81), E is the material modulus of elasticity, and $I(\mathrm{x})$ is the moment of inertia of the cross-sectional area about the neutral axis of the blade. $I(\mathrm{x})$, given by Equation xx, is a function of x due to changes in the blade cross-section.

$$I(\mathrm{x}) = \frac{1}{12}t^3(\mathrm{x} + r_{\mathrm{i}})\sqrt{2\,(1-\cos\alpha)}\cos\theta$$

Solving the moment differential equation through separation of variables and replacing the Equation (4-81) results in Equation (4-82).

$$\left(\int \mathrm{EI}(\mathrm{x})\,d\mathrm{x}\right)\frac{d\upsilon}{d\mathrm{x}} = M_{R_1}\mathrm{x} + R_{1,y'}\frac{\mathrm{x}^2}{2} - \frac{\mathrm{x}^4}{24L}w_{\mathrm{bed},y',\mathrm{h}} - \frac{\mathrm{x}^3}{9}w_{\mathrm{bed},y',\mathrm{l}} + F_{\mathrm{blade,L},y'}\frac{\mathrm{x}^3}{6} + C_1 \tag{4-82a}$$

$$\left(\int\int EI(\mathrm{x})\,d\mathrm{x}\,d\mathrm{x}\right)\upsilon = M_{R_1}\frac{\mathrm{x}^2}{2} + R_{1,y'}\frac{\mathrm{x}^3}{6} - \frac{\mathrm{x}^5}{120L}w_{bed,y',h} - \frac{\mathrm{x}^4}{36}w_{bed,y',l} + F_{blade,L,y'}\frac{\mathrm{x}^4}{24} + C_1\mathrm{x} + C_2 \tag{4-82b}$$

Figure 4-13 illustrates the elastic curve of the blade under the proposed operating conditions and two fixed supports at the extremes. The following boundary conditions (BC) are extracted from the elastic curve

BC_1: $\upsilon_1 = 0$ at $\mathrm{x} = 0$ $\quad$ BC_2: $\upsilon_2 = 0$ at $\mathrm{x} = L$

BC_3: $\frac{d\upsilon_1}{d\mathrm{x}} = 0$ at $\mathrm{x} = 0$ $\quad$ BC_4: $\frac{d\upsilon_2}{d\mathrm{x}} = 0$ at $\mathrm{x} = L$

Using the BC from 1 to 4 solves Equation (4-82a) for obtaining the values of M_{R_1} and $R_{1,y'}$, respectively. These variables enable to solve Equations (4-83) and (4-84) of internal shearing force and bending moment, respectively.

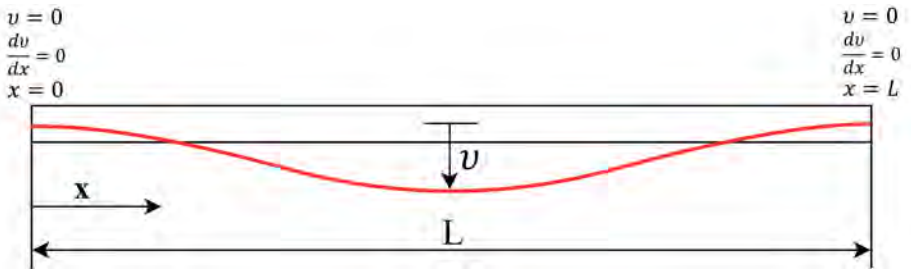

Figure 4-13 Elastic curve of one blade and its boundary conditions. The displacement and deflection are zero at both ends due to fixed supports. Source: Figure created by author.

$$R_{1,y'} = L\left(-\frac{3}{20}w_{\text{bed,y',h}} - \frac{1}{3}w_{\text{bed,y',l}} + \frac{1}{2}F_{\text{blade,L,y'}}\right) \tag{4-83}$$

$$M_{R_1} = L^2\left(-\frac{1}{30}w_{\text{bed,y',h}} - \frac{1}{18}w_{\text{bed,y',l}} + \frac{1}{12}F_{\text{blade,L,y'}}\right) \tag{4-84}$$

4.3.3.1.4. Resultant stresses and failure theory

The bending σ and shearing τ stresses in the blade are calculated using the solution of $V(\text{x})$ and $M(\text{x})$ [46]. Equations (4-85) and (4-86) calculate the maximum normal stress $\sigma_{\text{x,max}}(\text{x})$ and maximum shearing stress $\tau_{\text{xy',max}}(\text{x})$ due to internal bending moment and shearing force as functions of the position. Where $M(\text{x})$ is the resultant internal moment, c the perpendicular distance from neutral axis to a point farthest away from the neutral axis, $I(\text{x})$ the moment of inertia of the cross-sectional area about the neutral axis, $V(\text{x})$ the internal resultant shearing force, t the width of the blade's cross-sectional area, and $Q = A'\bar{y}'$ the moment of the area A' of the top portion of the blade's cross sectional area and $\bar{y}'$ is the distance from the neutral axis to the centroid of A'.

$$\sigma_{\text{x,max}}(\text{x}) = \frac{M(\text{x})c}{I(\text{x})} \tag{4-85}$$

$$\tau_{\text{xy',max}}(\text{x}) = \frac{V(\text{x})Q(\text{x})}{I(\text{x})t} \tag{4-86}$$

Based on the distortion energy theory of failure, the yielding occurs when the distortion strain energy per unit volume reaches or exceeds the distortion strain energy per unit volume for yield in simple tension or compression of the same material [47]. In this theory of failure, the criteria to predict the yield is the von Mises stress σ' compared with the yield strength S_y of the blade material as in Equation (4-87).

$$\sigma' \geq S_y \tag{4-87}$$

In the case of plane stress, the von Mises stress is calculated as

$$\sigma' = (\sigma_A^2 - \sigma_A\sigma_B + \sigma_B^2)^{1/2}$$

Using xy' components of two-dimensional stress in the blade's problem, Equation (4-88) describes the von Mises stress as

$$\sigma' = \left(\sigma_x^2 - \sigma_x\sigma_{y'} + \sigma_{y'}^2 + 3\tau_{xy'}^2\right)^{1/2} \quad (4\text{-}88)$$

Where σ_x and $\sigma_{y'}$ are the normal stresses in the respective directions, and $\tau_{xy'}$ is the shearing stress perpendicular to x-axes in the direction y'. In this case, the normal stress $\sigma_{y'} = 0$, which results in Equation (4-89).

$$\sigma' = \left(\sigma_x^2 + 3\tau_{xy'}^2\right)^{1/2} \quad (4\text{-}89)$$

Equation (4-90) corresponds to the Equation (4-89) expressed as a design equation.

$$\sigma' = \frac{S_y}{F_S} \quad (4\text{-}90)$$

Where F_S corresponds to the design safety factor and gives Equation (4-91) for estimating the minimum allowable yield strength for the selected blade's fabrication material.

$$S_{y,\text{blade}} = F_S\sigma' \quad (4\text{-}91)$$

4.3.3.2. Thin-walled vessel under internal pressure

The basic structure of the reactor is a thin-walled vessel working under internal pressure P due to process requirements. This work condition relates to the ASME Boiler and Pressure Vessel (BPV) code Section VIII [67]. The code includes the design equations to determine the stresses applied to the material and the thickness of the components. Also, Sinnott & Towler [68] summarized the mechanical design of thin-walled vessels under internal pressure.

The vessel comprises a cylindrical wall, the head, the closure, and a conical section in the case of the expanded SFB. This section details the design equations of every component of the shell.

4.3.3.2.1. Cylindrical shell wall

The cylindrical wall is subjected to two types of principal stress: hoop and longitudinal stresses [68]. Equations (4-92) and (4-93) give the hoop and longitudinal stresses, respectively, in a cylindrical vessel of an outer radius r_o and shell wall thickness t_{sw} fabricated with joints of efficiency E and subjected to the internal design pressure $P = 1.1P_{oper}$.

$$\sigma_r = \frac{\frac{2Pr_o}{t_{sw}} + 1.2P}{2E} \quad (4\text{-}92)$$

$$\sigma_L = \frac{\frac{2Pr_o}{t_{sw}} + 0.8P}{4E} \quad (4\text{-}93)$$

To select the shell material, Equation (4-94) gives the minimum yield strength allowable S_y to support the stress due to pressure depending on the design safety factor SF and the maximum between the hoop and longitudinal stress values.

$$S_{y,\text{vessel}} = F_S \max(\sigma_r, \sigma_z) \quad (4\text{-}94)$$

After estimating the required yield strength of the material, the design procedure of the other shell components uses this value to calculate the thickness of the components.

4.3.3.2.2. Heads and closures

Heads of various shapes close the ends of a cylindrical vessel. Sinnot & Towler [68] defined the principal types of heads as follows

a. Flat plates and formed flat heads; Figure 4-14.
b. Hemispherical heads; Figure 4-15a.
c. Ellipsoidal heads; Figure 4-15b.
d. Torispherical heads; Figure 4-15c

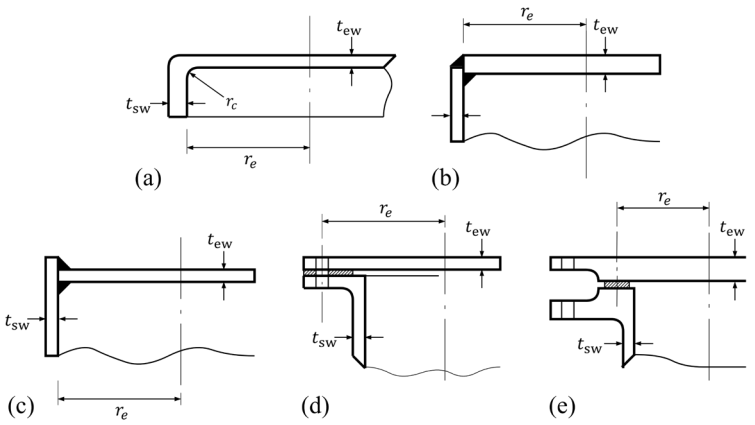

Figure 4-14 Flat ends considered in this procedure. (a) Flanged plate, (b) and (c) welded plates, and (d) and (e) bolted cover. Adapted from [68].

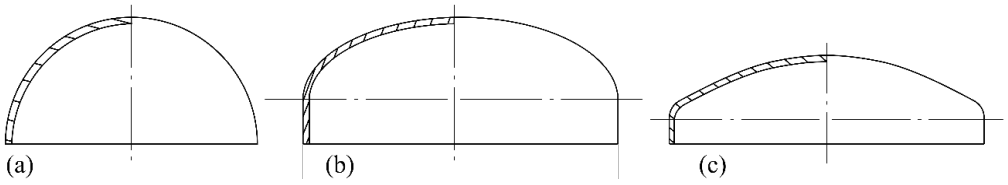

Figure 4-15 Domed ends considered in this procedure. (a) Hemispherical, (b) ellipsoidal, and (c) torispherical. Adapted from [68].

4.3.3.2.2.1. Design of flat ends

Figure 4-14 shows the four types of flat ends included in this procedure. Flat ends have a low fabrication cost, but they are not structurally efficient, requiring very thick plates for high pressures or large diameters. Equation (4-95) estimates the thickness of the flat end wall t_{ew} [68].

$$t_{\mathrm{ew}} = 2r_e\sqrt{\frac{CP}{S_y E}} \qquad (4\text{-}95)$$

Where C is a design constant, varying between flat end type, r_{e} the distance from the center to the marked point as seen in Figure 4-14, S_y the yield strength allowable of the material of the vessel (calculated in Equation (4-94)), and E the joint efficiency. Table 4-4 denotes the different flat ends type and their C value.

4.3.3.2.2.2. Design of domed ends

Figure 4-15 shows the three types of domed ends included in this procedure. Equations (4-96) to (4-98) are simplified models for estimating the thickness of the end wall t_{ew} of the different types of domed heads. These equations are suitable for the preliminary design of unpierced heads and heads with fully compensated openings or branches [68].

Hemispherical:
$$t_{\mathrm{ew}} = \frac{2Pr_{\mathrm{o}}}{4S_yE - 0.4P} \tag{4-96}$$

Ellipsoidal:
$$t_{\mathrm{ew}} = \frac{2Pr_{\mathrm{o}}}{2S_yE - 0.2P} \tag{4-97}$$

Torispherical:
$$t_{\mathrm{ew}} = \frac{0.885PR_c}{S_yE - 0.1P} \tag{4-98}$$

Where r_{o} the outer radius of the SFB reactor, S_y the yield strength allowable of the material of the vessel (calculated in Equation (4-94)), E the joint efficiency, and R_c the crown radius.

Table 4-4 Flat ends types and models to estimate the C value for each type [68].

Flat end type	Illustration	Design constant
Flanged plate	Figure 4-14a	$C = 0.17$ for $r_c < 3t_{\mathrm{ew}}$ $C = 0.1$ for $r_c \geq 3t_{\mathrm{ew}}$
Welded plate	Figure 4-14b and c	$C = 0.33\, t_{\mathrm{ew}}/t_{\mathrm{sw}}$
Bolted cover with full face gasket	Figure 4-14d	$C = 0.25$
Bolted cover with narrow face gasket	Figure 4-14e	$C = 0.3$

4.3.3.2.3. Conical section

The conical section of the SFB reactor requires the estimation of its thickness wall in case the desired configuration is an expanded bed reactor. Equation (4-99) relates the thickness required at any point on a cone to the radius. Figure 4-16 shows the main dimensions of the conical section. The shell in the transition section should be thicker than the conical or cylindrical section to reduce the stress concentration at the transition [68]. The recommended thickness to build the transition section is the estimated value from Equation (4-99) for $r_c = r_{c,\max}$.

$$t_{\mathrm{cw}} = \frac{2Pr_c}{2S_yE - P} \cdot \frac{1}{\cos\varphi} \tag{4-99}$$

Where r_c is the radius of the cone at the point, S_y the allowable yield strength of the vessel material (calculated in Equation (4-94)), E the joint efficiency, and φ half the cone apex angle.

4.3.3.2.4. Compression stress due to weight loads

The deadweight loads of the SFB reactor are the vessel shell, the single row distributor, internal and external fittings, auxiliary equipment (e.g., transmitters), insulations, and the weight of the biomass. Equation (4-100) denotes a preliminary calculation of the weight of the cylindrical vessel W_{vessel} with domed ends and uniform wall thickness [68].

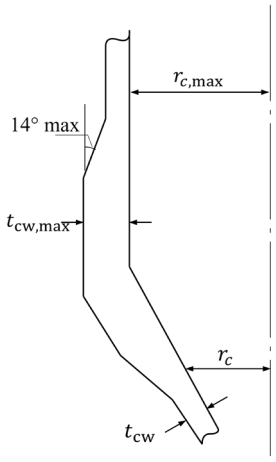

Figure 4-16 Transition of conical-cylindrical sections. Source: Adapted from [68].

$$W_{\mathrm{vessel}} = C_w \rho_m g \mathrm{V}_{\mathrm{vessel}} \tag{4-100}$$

Where C_w is a factor to account for the weight of nozzles, manways, and internal supports, among others, and is equal to 1.15 for the SFB reactor; g the gravitational acceleration; $\mathrm{V}_{\mathrm{vessel}}$ the volume of the shell of the SFB reactor vessel. Equation (4-101) estimates $\mathrm{V}_{\mathrm{vessel}}$.

$$\mathrm{V}_{\mathrm{vessel}} = \mathrm{V}_{\mathrm{cylinder}} + \mathrm{V}_{\mathrm{up\ end}} + \mathrm{V}_{\mathrm{bot\ end}} + \mathrm{V}_{\mathrm{conical}} \tag{4-101}$$

Where the $\mathrm{V}_{\mathrm{cylinder}}$ is the volume of the cylindrical walls, $\mathrm{V}_{\mathrm{up\ end}}$ and $\mathrm{V}_{\mathrm{bot\ end}}$ the volume of the upper and bottom end walls, respectively, and $\mathrm{V}_{\mathrm{conical}}$ the volume of the conical section wall which is equal to zero for the compact SFB reactor.

Then, Equation (4-102) gives the deadweight stress which is a normal compression stress in the vessel shell.

$$\sigma_w = \frac{W_{\mathrm{vessel}}}{\pi(2r_{\mathrm{o}} + t_{\mathrm{sw}})t_{\mathrm{sw}}} \tag{4-102}$$

4.3.3.2.5. Design of vessel subject to combined loads

The design of the SFB reactor requires resistance to the combined effect of both pressure and weight loads [68]. These loads cause two stress components: circumferential σ_{h} and longitudinal σ_{z}. Equations (4-103) and (4-104) calculate the two components σ_{h} and σ_{z}, respectively.

$$\sigma_{\mathrm{h}} = \sigma_{\mathrm{r}} \tag{4-103}$$

$$\sigma_{\mathrm{z}} = \sigma_L - \sigma_w \tag{4-104}$$

Where σ_r is the hoop stress due to pressurization calculated in Equation (4-92), σ_L the longitudinal stress due to pressurization calculated in Equation (4-93), σ_w the compression stress due to weight load calculated in (4-102).

Based on the maximum shear-stress theory [47], Equation (4-105) gives the maximum allowable stress intensity for the SFB reactor.

$$\sigma_{\max} = |\sigma_{\mathrm{h}} - \sigma_{\mathrm{z}}| \tag{4-105}$$

It is necessary to compare the calculated minimum yield strength $S_{y,\mathrm{vessel}}$ in Equation (4-94) and the value of $S_{y,\mathrm{comb}} = \sigma_{\max} SF$ for validating the design. If $S_{y,\mathrm{comb}}$ results to be higher than $S_{y,\mathrm{vessel}}$, then the thickness of the components needs adjustment to meet the new subjected stress.

4.3.4. Corrosion

During biomass processing through combustion, gasification, pyrolysis, or torrefaction in the SFB reactor, there is the risk of corrosion and erosion of the construction materials [68]. Ash elements (e.g., Si, K, Na, S, Cl, P, Ca, Mg, Fe) regularly generate slagging and fouling. Deposits on the surface of the reactor could occur due to intensified low temperature softening of the combinations of ash elements at high temperatures. The incorporation of Cl and alkali chlorides into the deposits increase the corrosion rate of the surface of the reactor's components. It is crucial to avoid the reactions between the metallic surface and this species to enhance the corrosion resistance of the components [13], [69]. Sulfur content in the biomass has the potential to create sulfur dioxide deposits on the surface of the components [70]. Maintaining environmental pH between 6.5 and 10 improves the corrosion resistance in steel alloys Cr-Fe-Ni [71]. In the case of pyrolysis, there is a severe risk of corrosion because the bio-oil is very acidic and contains solid metal ions (e.g., Cu, Pb, and Fe) and large amounts of water [72].

Experimental studies about corrosion resistance in biomass treatments showed that the stainless-steel alloys are the most suitable for operating under highly intensive corrosive environments. Ni-based alloys and steel chromium alloys presented good performance under corrosion. Table 4-5 shows some typical alloys used as construction material for biomass processing reactors reported in the literature.

Table 4-5 Typical alloys reported as construction material for biomass processing reactors.

Material	**Ref**
Ni-based alloy INCONEL 625	[69]
Stainless steel AISI 304	[69]
Stainless steel AISI 304L	[69], [71], [73], [74]
Stainless steel AISI 310	[69]
Stainless steel AISI 316	[72], [75]
Stainless steel AISI 316L	[74]
Stainless steel AISI 410	[76]
Stainless steel AISI 430	[74], [76]
Stainless steel TP 347H/ AISI 347	[69]
Steel 9Cr-1Mo / 50400	[76]

The ASME BPV Code Sec. VIII D.1 defines the "corrosion allowance" as an additional thickness of metal to avoid failure of the vessel for material lost due to corrosion, erosion, or scaling. Typical values of the minimum corrosion allowance are 2.00 mm for carbon and low-alloy steels with a minor

level of expected corrosion and 4.0 mm for carbon and low-alloy steels with a severe level of anticipated corrosion. If previous experience indicates that the corrosion level is almost negligible, the design does not need corrosion allowance [68].

4.3.5. Minimum wall thickness

The ASME BPV Code section VIII D defines a minimum wall thickness to ensure that any vessel is sufficiently rigid to support its weight and incidental loads. Table 4-6 shows the minimum wall thickness values, including the corrosion allowance, as a function of the vessel diameter [68]. Therefore, after determining the wall thickness in Section 4.3.3.2, the designer should compare it with the minimum wall thickness from Table 4-6 and select the higher value.

Table 4-6 Minimum wall thickness required to ensure the stiffness of the SFB reactor structure to support its own weight and incidental load [68].

Vessel diameter, m	Minimum thickness, mm
1.0	5
1.0 - 2.0	7
2.0 - 2.5	9
2.5 - 3.0	10
3.0 - 3.5	12

4.3.6. Requirements list of design specifications

Table B-3 in Appendix B.3 is a template of the requirements list of a unit of the SFB reactor. After sizing the desired biomass treating process and estimating the dimensions and allowable yield strengths, the designer should fill this template with the specifications.

The requirements list comprises the design specifications and goals of the SFB reactor under the required circumstances to meet. The list classifies the requirements as demands (D) or wishes (W) [48]. Demands are the design requirements that must be met, while whishes should be considered in the design.

4.3.7. Materials selection

The procedure to select the material of the SFB components is the software-based methodology proposed by Ashby [49]. The components consist of the gas distributor and the vessel. These are the main components due to their importance for the adequate and safe performance of the SFB reactor. Granta's design CES EduPack software is the tool to perform the material selection. CES software provides a complete materials database for comparing properties from the design requirements and constraints.

The first step of the process is defining the components' objective function. Then, the design requirements filter the materials that do not satisfy the minimum criteria to meet the functions. Later, the selection is optimized using the index of the material. The reference levels correspond to the index of the typical materials reported in reactors for treating biomass.

Table 4-7 comprises the design requirements for selecting the material of the component, i.e., the function, the constraints of design, the optimization objectives, and the free variables. The most critical component of the SFB reactor is the thin-wall pressure vessel because of the safety requirements of the operation. The component function is defined as a pressure vessel at a high temperature. The specified constraints are the yield strength of the material S_y and the maximum service temperature $T_{\max}$ of the pressure vessel material. Then, selecting a material to perform the function requires the use of the index of the material. The selection maximizes the mechanical properties (yield-before-break) and corrosion resistance of the material. A material is preferable if both cost and energy consumption for its production have low values.

Table 4-7 Design requirements for selecting the material for building a SFB reactor for biomass thermochemical conversion.

Function	Pressure vessel at high temperature
Constrains	Yield strength, S_y Maximum service temperature, $T_{\max}$
Objective	Maximize safety using the yield-before-break criterion, M_1 Maximize the corrosion resistance index, M_2
Free variables	Low cost Low energy consumption for production Choice of material

Table 4-8 shows the selected indexes to optimize the objectives: yield-before-break and corrosion resistance index (IC). Yield-before-break index measures the material resistance to general yield at a pressure still too low to cause any crack propagation [49]. Antunes & Oliveira [69] proposed the IC to select the best candidates for working under harsh corrosive environments. IC indicates how the chemical composition of the material reduces the potential of the working environment to cause corrosion on the surfaces of the material.

Table 4-8 Selected indexed to optimize the objectives of the materials required to build a SFB reactor for biomass thermochemical conversion.

Objective	Index	Model	Eq.	Ref
Maximize	Yield-before-break	$M_{i_1} = \frac{K_{1_c}}{\sigma_y}$	(T4-8.1)	[49]
Maximize	Corrosion resistance index	$M_{i_2} = \%\text{Ni} + \%\text{Cr} + 5.0(\%\text{Nb} + \%\text{Ta} + \%\text{Ti}) + \%\text{W} + \%\text{Mo}$	(T4-8.2)	[69]

Table 4-9 shows the index values of the construction materials reported for reactors used in biomass processing applications extracted from CES EduPack software [77]. These indexes are the reference

point to optimize the objectives of the design. The lowest values of M_1 and M_2 in Table 4-9 are the limits to optimize the objectives of the material selection. M_1 lower limit is 0.123, corresponding to the stainless steel (SS) AISI 410 lowest value. M_2 lower limit is 9 corresponding to the steel 9Cr-1Mo lowest value.

Table 4-9 Index values of the typical contruction material for reactors in biomass processing applications reported in the literature. The data is extracted from [77].

Material	M_1	M_2
Ni-based alloy INCONEL 625	0.455-0.556	106-117
Stainless steel AISI 304	0.196-0.314	26.7-30.3
Stainless steel AISI 304L	0.193-0.332	26.8-31.2
Stainless steel AISI 310	0.225-0.354	43.7-47.3
Stainless steel AISI 316	0.198-0.327	29.2-33.8
Stainless steel AISI 316L	0.194-0.373	29.2-33.8
Stainless steel AISI 410	0.123-0.39	11.5-13.5
Stainless steel AISI 430	0.206-0.573	16-18
Stainless steel TP 347H/ AISI 347	0.207-0.305	28.6-34.9
Steel 9Cr-1Mo / 50400	0.306-0.381	9-11

Since the typical reported constructive materials are metals for biomass treatment processes, the selection starts by including only metals to screen the constraints and objectives. Figure 4-17 is the property chart of yield strength vs. maximum service temperature for metallic materials.

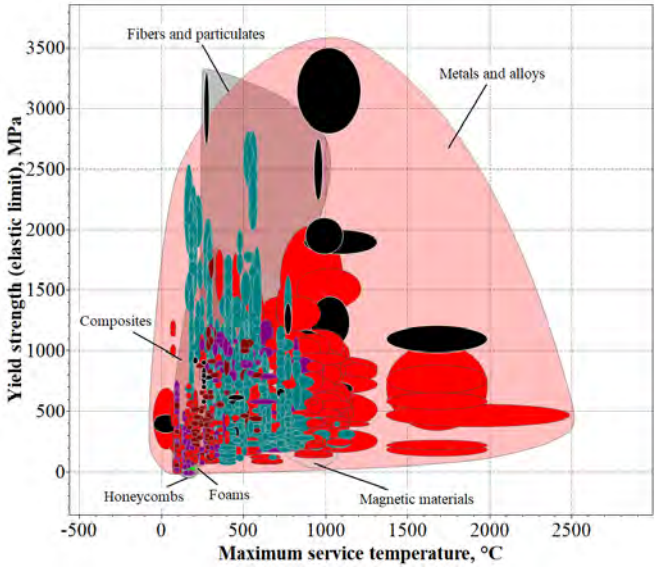

Figure 4-17 Yield strength S_y vs. maximum service temperature T_{max} for metallic materials. Source: Chart extracted from CES Edupack [77].

4.3.8. Instrumentation

Figure 4-18 illustrates the process and instrumentation diagram of the SFB reactor demonstration unit with air as fluidizing gas. The inlet filter (1) retains dust and dirt from the environment or the gas source from getting into the system. The gas transport driving system, represented as a blower (2), draws the fluidizing gas into the system, which splits into a flow control valve (3) and a turbine flowmeter (4), which works simultaneously as a flow transmitter (FT). The mass flow controller ensures that the gas flow is sufficient to fluidize the particles in the reactor based on the flow requirements of the process calculated in Section 4.3.1. Once the gas enters the SFB reactor (5), it flows upwardly and faces the single row inclined blades distributor, which changes its direction and fluidizes the bed of particles. The measurements from the pressure transmitters PT1, PT2, and PT3 are used to calculate the pressure drops across the distributor ($\Delta P_{\text{distr}} = P_1 - P_2$) and the bed ($\Delta P_{\text{bed}} = P_2 - P_3$). The temperature transmitter (TT) registers the operating temperature of the process inside the SFB reactor. A data acquisition system (DAQ) device (6) receives the signals from the electronic transmitters for later software processing, which prints out the information on a display. After treating the particles, the gas flow drags upwardly the solids and liquids products out of the reactor. A cyclone unit (7) separates condensates and solids of the gas stream. Some processes would require gas recycling for correct operation; valve (8) controls the recycle flow rate of the system.

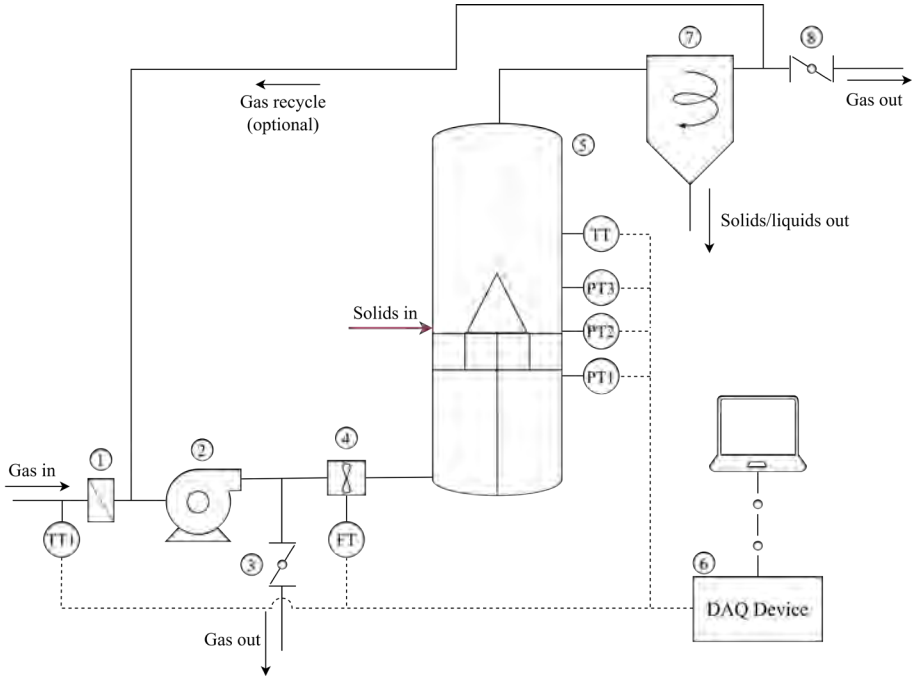

Figure 4-18 Process and Instrumentation diagram of a SFB reactor. Source: Figure created by author.

4.3.9. Pressure-drops and gas driving system selection

4.3.9.1. Pressure-drop across the distributor

Wellwood [78] proposed a semi-empirical model to predict the pressure drop across the distributor ΔP_{distr} based on the power-law. Equation (4-106) calculates ΔP_{distr} as a function of the injection gas velocity V_{inj}, the gas density ρ_{g}, and the discharge coefficient of the orifice C_D.

$$\Delta P_{\text{distr}} \cong \frac{\rho_{\text{g}} {V_{\text{inj}}}^2}{2C_D^2} \tag{4-106}$$

Equation (4-107) gives C_D depending on the coefficient C [45]. Appendix B.4 details the procedure to obtain the value of the coefficient C.

$$C_D = C\sqrt{1-\left(\frac{\%\text{op}}{100}\right)^2} \tag{4-107}$$

4.3.9.2. Pressure-drop across the bed

Kaewklum et al. [50] proposed a model for estimating the pressure drop across the bed at the minimum superficial gas velocity $\Delta P_{(\text{mf,distr})}$. The maximum pressure drop across the bed occurs at the minimum fluidization state. Equation (4-108) gives $\Delta P_{(\text{mf,distr})}$

$$\Delta P_{(\text{mf,bed})} = 3.43 V_{\text{sup,mf}}^{0.33}\left(\frac{h_{\text{bed}}}{2r_{\text{o}}}\right)^{1.02} \tag{4-108}$$

Where $V_{\text{sup,mf}}$ is the superficial gas velocity at the minimum fluidization state, h_{bed} the static bed height, and r_{o} the outer radius of the SFB reactor.

4.3.9.3. Pressure-drop across the flowmeter

The manufacturer of the flowmeter should provide the information to estimate the pressure drop across the flowmeter $\Delta P_{\text{flowmeter}}$. This value depends on the flow passing through the instrument and varies with the flowmeter model.

4.3.9.4. Pressure-drop across the cyclones

Sinnot & Towler [68] proposed a procedure for sizing cyclones depending on the performance required. This procedure includes Equation (4-109) to estimate the pressure drop across the cyclones $\Delta P_{\text{cyclone}}$

$$\Delta P_{\text{cyclone}} = \frac{\rho_{\text{g}}}{203}\left\{V_1^2\left[1+2\phi^2\left(\frac{2r_t}{r_e}-1\right)\right]+2V_2^2\right\} \tag{4-109}$$

Where ρ_{g} is the gas density, V_1 the inlet duct velocity, V_2 the exit duct velocity, r_t the radius of a circle to which the centerline of the inlet is tangential, r_e the radius of exit pipe, ϕ a factor calculated from [68].

4.3.9.5. Major pressure-drop and driving system

Equation (4-110) denotes the major pressure drop of the SFB reactor ΔP_{SFB} as the sum of the pressure-drops across the distributor, the bed at the minimum fluidization state, the flowmeter, and the cyclones.

$$\Delta P_{\text{SFB}} = \Delta P_{\text{distr}} + \Delta P_{(\text{mf,bed})} + \Delta P_{\text{flowmeter}} + \Delta P_{\text{cyclone}} \tag{4-110}$$

The driving system of the SFB reactor must provide sufficient energy $\dot{W}_{\text{flow}} = \dot{m}_{\text{g}} g H_{\text{blower}}$ to transport the required gas flow rate $\dot{m}_{\text{g}}$ calculated in Section 4.2.1 (or the volumetric gas flow rate $\dot{V}_{\text{g,act}}$) and rise enough the pressure head to overcome the pressure drop of the SFB reactor ΔP_{SFB}.

Depending on the biomass treatment, the possible gas driving system is a blower for combustion and gasification, a pressurized N2 reservoir, or a steam generator with a compressor for pyrolysis and torrefaction.

4.3.10. Particles feeder selection

The SFB reactor operation requires a solids feeder to supply the biomass particles. Table 4-10 summarizes the primary operating characteristics of four types of conveyors. Depending on the biomass characteristics and the operational requirements, the designer should select an adequate conveyor.

Table 4-10 Primary operating characteristics of four type of converyors for particles feeding in the SFB reactor.

Conveyor type	**Belt**	**Chain-type**	**Screw**	**Pneumatic**
Maximum capacity, kg s^{-1}	5556	333	556	111
Maximum transport distance, m	35000	250	200	2500
Abrasion resistance	Moderate	Extreme	Moderate	Moderate
Dusty material handling	Yes	Yes	Yes	Yes
Particle size allowable, mm	0.07 - 180	0.07 - 180	0.07 - 180	3 - 180
Wet material handling	Yes	Yes	Yes	No
Reference	[79]	[80], [81]	[80]–[82]	[83], [84]

4.4. Design of a swirling fluidized bed reactor demonstration unit for rice husk combustion

This section comprises a case study designing a SFB reactor for rice husk combustion using the proposed design procedure in Section 4.3. First, the case study starts with the operating conditions and chemical equilibrium equations for estimating the gas and biomass flow rates. Then, the load and stress analysis determine the constructive material selection of the SFB and the thickness of components. The major pressure drop estimation leads to the selection of the gas transport driving system. Finally, the results will be compared with an actual functioning SFB reactor to identify improvement opportunities and the added value of the proposed design procedure.

4.4.1. Experimental setup

Kuprianov et al. [39] run rice husk combustion experiments at a fuel feed rate of 80 kg h^{-1} and with excess air of 40%. Figure 4-19 is the schematic diagram of the expanded SFB reactor used for the experiment. The combustor included a start-up burner, a cyclone, a fuel screw feeder, and a blower. The air mass flow rate required for combustion enters at the bottom (primary air, PA) and the tangential inlet of the burner (secondary air, SA). The ratio SA/PA used for the design of the SFB reactor is 0.40. Some global dimensions of the SFB reactor are in Figure 4-19. The thickness of the

steel sheet was 4.5 mm with an internal refractory cover of 50 mm thick. The single row blades distributor in the combustor had an arrangement of eleven blades inclined at an angle of 14° to the horizontal. The inner and outer diameters of the distributor were 0.1 m and 0.25 m, respectively.

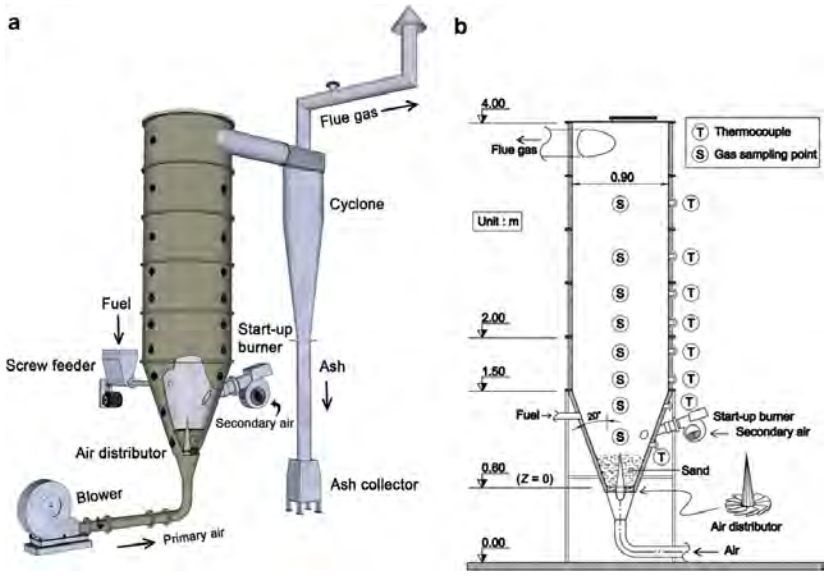

Figure 4-19 Experimental setup of the SFB reactor used for rice husk combustion. Figure extracted study from [39].

Table 4-11 shows the ultimate analysis of a sample of rice husk burned in the experiment [39]. The rice husk particles had dimensions of 2 mm wide, 0.5 mm thick, and 10 mm long. Typical particle density of the rice husk is between 400-600 kg m^{-3} [85]–[87], thus the selected particle density to solve the case study is 500 kg m^{-3}.

Table 4-11 Ultimate analysis of a sample of rice husk used in this case study. Data extracted from [39].

Element	C	H	O	N	S	M	ASH
Ultimate analysis "ar" (wt.%)	40.5	4.07	28.69	0.31	0.03	8.4	18
Ultimate analysis dry basis (wt.%)	44.21	4.44	0.34	0.03	31.32	19.65	9.17

The rice husk combustion temperature of the experiment ranged from 900 to 970°C.

The basic design procedure is applied to the presented case of rice husk combustion using this information.

4.4.2. Equilibrium and thermodynamics of the rice husk combustion

The equations defined in Section 4.2.1.1 solve the combustion of rice husk. Table 4-12 shows the solution of the equilibrium constants for the stoichiometric combustion of rice husk with dry air.

The equilibrium formula results as follows

$$CH_{1.20}O_{0.53}S_{2.77\times10^{-4}}N_{6.56\times10^{-3}} + 1.03(O_2 + 3.76N_2) \rightarrow CO_2 + 0.60H_2O + 2.77\times10^{-4}SO_2 + 3.89N_2$$

The stoichiometric air-fuel ratio and the air inlet flow rate correspond to data in Table 4-13

Table 4-12 Stoichiometric constants obtained from the molar balances of each component from the stoichiometric formula.

Stoichiometric constant	a	b	c	d	e_{st}	$\mathrm{MW}_{\mathrm{biomass}}$, kg kmol^{-1}
Value	1.20	0.53	2.77×10^{-4}	6.56×10^{-3}	1.03	21.83

Table 4-13 Results of the stoichiometric air-fuel ratio and inlet flow rate due to combustion of 80 kg h^{-1} of rice husk.

Variable	**Value**
Stoichiometric air	
$\mathrm{AF}_{\mathrm{st}}$, kg dry air kg^{-1} dry fuel	5.23
$\dot{m}_{\mathrm{da}}$, kg h^{-1}	382.92

Table 4-14 shows the solution of stoichiometric constants for actual conditions of operation of the combustion.

Table 4-14 Stoichiometric constants obtained from the molar balances of each component at actual conditions of operations of combustion of 80 kg h^{-1} of rice husk.

Stoichiometric constant	a	b	c	d	e_{act}	f	g	h
Value	1.20	0.53	2.77×10^{-4}	6.56×10^{-3}	1.45	0.47	1.07	0.41

The actual air-fuel ratio, the actual air mass flow rate, the composition of the hot product gas, and the hot product gas flow rate result from the constants in Table 4-15.

Table 4-15 Results of actual air-fuel ratio, air and hot product gas flow rates, and composition of the hot product gas due to combustion of 80 kg h^{-1} of rice husk.

Stream	**Actual air**		**Hot product gas**					
Variable	**$\mathrm{AF}_{\mathrm{act}}$, kg kg^{-1} dry fuel**	**$\dot{m}_{\mathrm{air,act}}$, kg h^{-1}**	**$\dot{m}_{\mathrm{prod}}$, kg h^{-1}**	**x_i, kg kg^{-1} mix**				
				CO_2	H_2O	N_2	O_2	SO_2
Value	9.10	536.09	617.63	2.02	0.88	6.99	0.61	8.14×10^{-4}

The actual equilibrium equation of the rice husk combustion is

$$\mathrm{CH_{1.12}O_{0.53}S_{2.77\times10^{-4}}N_{6.56\times10^{-2}}} + 1.45(\mathrm{O_2} + 3.76\mathrm{N_2}) + 0.47\mathrm{H_2O} \rightarrow \mathrm{CO_2} + 2.77\times10^{-4}\mathrm{SO_2} + 5.44\mathrm{N_2} + 1.07\mathrm{H_2O} + 0.41\mathrm{O_2}$$

Table 4-16 contains the estimated heating values and the enthalpy of formation of the rice husk using the theoretical equilibrium combustion reaction and ultimate analysis of the rice husk on a dry basis from Table 4-11.

Table 4-16 Higher and lower heating values, and enthalpy of formation of the rice husk.

HHV	LHV	$\bar{h}_f^o$	Units
15586.2	14800.0	-3455.1	kJ kg^{-1} "ar"
340234.9	323072.8	-102474.7	kJ $kmol^{-1}$

Table 4-17 summarizes the heat of combustion, the heat of vaporization, the heat loss, the power output of the SFB reactor, the enthalpy of the products, and the enthalpy of reactive. The energy balance of the SBF reactor and these values enable us to solve for the average combustion temperature reported in [39], 935 °C. Though the reported combustion efficiency surpasses 98%, the thermal efficiency of the SFB reactor is approximately 40%, according to the energy balance. The addition of thermal insulation designed from the heat transfer analysis through the reactor walls would improve the thermal performance of the SFB reactor.

The minimum fluidization state and the pressure drops require the use of actual air $\dot{m}_{\mathrm{act,air}}$ and the hot product gas $\dot{m}_{\mathrm{prod}}$ flow rates

Table 4-17 Results of the heat of combustion, the heat of vaporization, the heat loss, the power output of the SFB reactor, the enthalpy of the products, and the enthalpy of reactive due to combustion of 80 kg h^{-1} of rice husk at 935°C.

Heat flow	$\dot{Q}_i$, kW	Products	H_i, kW	Reactive	H_i, kW
Combustion	328.89	CO_2	-261.18	Rice husk	-108.36
Vaporization	-4.04	H_2O	-165.16		
Loss	-192.93	SO_2	-0.05		
		O_2	9.31		
		N_2	115.79		
Power output	**131.92**	**Total products**	**-301.29**	**Total reactive**	**-108.36**

4.4.3. Minimum fluidization velocity

Table 4-18 comprises the calculated data to define the minimum fluidization state of rice husk particles after solving the equations of Section 4.3.1. The results show that the actual superficial velocity is higher than the minimum swirling superficial velocity, as expected to maintain the swirling regime of the bed. Likewise, the maximum allowable annular area is higher than the actual area, as expected to meet the air mass flow rate to fluidize the bed.

4.4.4. Dimensions of the swirling fluidized bed reactor for rice husk combustion

4.4.4.1. Global dimensions

Kuprianov et al. [39] used an expanded SFB reactor in the rice husk combustion process. Rice husk physical properties (size and density) the equivalent particle diameter is equal to 2.6 mm. The equivalent particle size and particle density categorize the rice husk as a particle from 1g-Geldart's D group, though these properties are close to the B group. Table 4-3 denotes that the deciding factor between a compact and an expanded SFB reactor is the rice husk ash (RHA) physical properties, i.e., particle size and density. Burning rice husk in a fluidized bed produces ash with a mean particle size of 20 μm and particle density of about 2000 kg m^{-3}, i.e., RHA particle is in the A-C group from the

1g-Geldart's classification [88], [89]. Therefore, according to Table 4-3, the reactor type needed to ensure the fluidization of both the rice husk and the ash is the expanded SFB reactor.

Table 4-19 summarizes the global dimensions of the SFB reactor extracted from Figure 4-19.

Table 4-18 Results of air superficial and injection velocities for minimum fluidization, minimum swirling fluidization, and at actual conditions to achieve combustion of 80 kg h^{-1} of rice husk.

Variable	Name	Value
Ar	Archimedes number	186025
Re_{mf}	Reynolds number	71.36
$V_{mf} = V_{inj,z,mf}$, m s^{-1}	Minimum fluidization velocity, axial component of injection velocity for minimum fluidization	0.62
$V_{msf} = V_{inj,z,msf}$, m s^{-1}	Minimum swirling velocity, Axial component of injection velocity for minimum swirling	1.39
$V_{sup,mf}$, m s^{-1}	Superficial minimum fluidization velocity	0.56
$V_{sup,msf}$, m s^{-1}	Superficial minimum swirling velocity	1.25
$\dot{V}_{air,act}$, m^3 h^{-1}	Actual volumetric flow rate	404.07
$V_{sup,act}$, m s^{-1}	Actual superficial velocity	2.72
$V_{inj,act}$, m s^{-1}	Actual injection velocity	12.47
$A_{bed,max,allow}$, m^2	Maximum area of the annular section to ensure swirling regime for a fixed air inlet flow rate	9.93×10-2

Table 4-19 Global dimension of the SFB reactor for combustion of 80 kg h^{-1} of rice husk.

Dimension	r_c	r_o	r_i	$H_{vessel,bot}$	$H_{vessel,con}$	$H_{vessel,up}$
Length, m	0.45	0.125	0.05	0.0	0.9	2.5

4.4.4.2. Single row blades distributor

Table 4-20 comprises the results of the geometrical models from Section 4.3.2.2 to determine the principal dimensions of the single row blades distributor with 11 blades and 14° of blade horizontal inclination based on the experimental set up of [39].

4.4.5. Load and stress subject to the swirling fluidized bed reactor during rice husk combustion

This section depicts the results of Section 4.3.3 to estimate loads and stresses in the blades of the gas distributor and the pressure vessel.

4.4.5.1. Single row blade distributor

4.4.5.1.1. External forces and moments

The bed voidage and the static bed height determine the mass of particles in the bed required to calculate the distributor's external loads during rice husk combustion. The assumed bed voidage for rice husk is ε_{vdg}=0.85 [89], and static bed height is h_{bed}=0.3 m [39]. Table 4-21 summarizes the solution of the external forces on the blade assumed as a statically indeterminate beam.

Table 4-20 Dimensions of the single row blades distributor for combustion of 80 kg h^{-1} of rice husk.

Variable	Value
L_{blade}, mm	75
t_{blade}, mm	1
N_{blade}	11
θ, °	14
α, °	32.73
$ac(r_{\text{i}})$, m	2.82×10^{-2}
$y(r_{\text{i}})$, m	5.82×10^{-3}
$ac(r_{\text{o}})$, m	7.04×10^{-2}
$y(r_{\text{o}})$, m	1.60×10^{-2}
β, °	31.73
$A_{\text{op,blade}}$, m^2	8.20×10^{-4}
$A_{\text{op,total}}$, m^2	9.02×10^{-3}
A_{bed}, m^2	4.12×10^{-2}
%op	21.86

Table 4-21 Results of external forces on the blade assumed as a statically indeterminate beam due to combustion of 80 kg h^{-1} of rice husk.

Reacting force on each blade		Bed weight		Support reactions	
$\dot{m}_{\text{g,blade}}$, kg s^{-1}	1.08×10^{-2}	ε_{vdg}	0.85	M_{R_1}, N m	-4.68×10^{-3}
$F_{\text{blade,y}}$, N	4.50×10^{-3}	$m_{\text{total,particles}}$, kg	0.91	$R_{1,y'}$, N	-0.39
$F_{\text{blade,z}}$, N	0.12	W_{bed}, N m^{-2}	216.11		
$F_{\text{blade,y}'}$, N	-2.39×10^{-2}	$W_{\text{bed,y}'}$, N m^{-2}	209.69		
$F_{\text{blade,z}'}$, N	0.11	$W_{\text{bed,z}'}$, N m^{-2}	52.28		
$F_{\text{blade,L,y}'}$, N	-1.87×10^{-3}	$w_{\text{bed,y}',\text{h}}$, N m^{-1}	14.97		
$F_{\text{blade,res,y}'}$, N	-1.40×10^{-4}	$w_{\text{bed,y}',\text{l}}$, N m^{-1}	5.99		
		$w_{\text{bed,res,y}'}$, N	0.79		
		$\bar{\text{x}}_{w_{\text{bed}}}$, m	4.29×10^{-2}		

Table 4-22 presents the solution at different positions of the internal shear force and the bending moment in the blade. The critical load point is in the outer radius of the blade or x = 7.50×10^{-2} m. Then, the maximum stress condition occurs in this position.

Table 4-22 Change of internal shear force and bending moment in the blade at different positions.

x, m ×10^{-2}	0	0.94	1.88	2.81	3.75	4.69	5.63	6.56	7.5
$\boldsymbol{V(x)}$**, N**	-5.18	-6.31	-7.43	-8.55	-9.68	-10.80	-11.92	-13.04	-14.17
$\boldsymbol{M(x)}$**, N m**	-4.7×10^{-3}	-3.4×10^{-2}	-7.3×10^{-2}	-0.12	-0.17	-0.24	-0.31	-0.38	-0.47

4.4.5.1.2. Allowable stresses in the blades

The allowable stress solution in the blades with 1 mm thickness and 14° of horizontal inclination using equations from Section 4.3.3.1.4. Table 4-23 contains the stress values for different positions in the blade. The highest value of the tensile yield strength for the blade material is $S_{y,\text{blade}}$=90.15 MPa.

Table 4-23 Change of stress values in the blade at different positions. The allowable stress of the construction material of the blade should be at least 90 MPa.

x, m ×10^{-2}	0	0.94	1.88	2.81	3.75	4.69	5.63	6.56	7.5
$\boldsymbol{\sigma_{x,max}(x)}$**, MPa**	0.25	1.70	3.31	5.05	6.86	8.73	10.64	12.59	14.55
$\boldsymbol{\tau_{xy',max}(x)}$**, MPa**	3.89	5.14	6.45	7.82	9.24	10.68	12.16	13.66	15.18
$\boldsymbol{\sigma'}$**, MPa**	6.74	9.06	11.66	14.46	17.41	20.46	23.60	26.80	30.05
$\boldsymbol{S_{y,blade}}$**, MPa**	20.22	27.17	34.97	43.38	52.22	61.38	70.79	80.39	90.15

4.4.5.2. Vessel under internal pressure

Table 4-24 shows the thickness of vessel components and the allowable yield strength. Since the experimental setup states that the lateral wall of the shell has a uniform thickness [39], the highest value between t_{sw} and t_{cw} is the actual thickness of the SFB reactor. Then, the SFB reactor manufacturing will include a lateral wall of 3 mm thick with 2 mm of corrosion allowance, i.e., 5 mm of thickness wall. Compared to [39], the designed wall is 0.5 mm thicker but does not include the refractory cover, which increases the corrosion resistance of the reactor. This change would make the SFB reactor lighter and easier to transport.

Three types of ends were considered to design the head of the SFB reactor: flat welded plate, hemispherical domed, and flat bolted. The best options for the head are the hemispherical end and the flat bolted. In the case of the hemispherical end, increasing the thickness to 5 mm, i.e., equal to the vessel wall thickness, supports the stress in the wall without mechanical failure. The flat bolted thickness is technical and commercially feasible to manufacture. The first estimation of the closure wall thickness results in a flat welded plate with a practical thickness.

The combined loads analysis resulted in a minimum allowable stress of the construction material of the vessel $S_y \geq$186 MPa.

4.4.6. Requirements list of the swirling fluidized bed reactor for rice husk combustion

Table 4-25 establishes the design specifications of the SFB reactor for combustion of rice husk based on the operating conditions, dimensioning, and stress analysis. The selected yield strength value of

the material S_y to build SFB reactor is the highest between $S_{y,\text{blade}}$ and $S_{y,\text{vessel}}$, i.e., 186 MPa and rounded up to 200 MPa. The unified value of S_y simplifies the materials selection and fabrication of the SFB reaction. The maximum service temperature $T_{\max}$ is the upper limit of the reported experimental data [39], i.e., 970 °C.

Table 4-24 Stress components and thickness values of the components of the vessel subjected to internal pressure. The thickness value of 3 mm is adequate to construct all the components of the vessel. The minimum allowable yield strength of the construction material of the vessel should be at least 186 MPa.

Thin-shell pressure vessel	
P, MPa	0.33
Cylindrical wall	
t_{sw}, m	3×10^{-3}
E	0.8
σ_{r}, MPa	62.12
σ_L, MPa	31.02
Conical section wall	
t_{cw}, mm	1.00
Head	
E	1
Flat end up welded plate	
$t_{\text{ew,up}}$, m	0.20
Hemispherical	
$t_{\text{ew,up}}$, m	4.0×10^{-4}
Flat end up bolted	
$t_{\text{ew,up}}$, m	1.9×10^{-2}
Closure	
Flat end bottom welded plate	
$t_{\text{ew,bot}}$, m	1.4×10^{-2}
Weight load	
W_{vessel}, N	1594.43
σ_w, MPa	2.03
Combined load	
σ_{h}, MPa	62.12
σ_{z}, MPa	29.00
σ_{SST}, MPa	33.13
$S_{y,\text{comb}}$, MPa	99.40
$S_{y,\text{vessel}}$, MPa	186.37

Table 4-25 List of design specifications of the SFB reactor for combustion of 80 kg h^{-1} of rice husk.

Design specifications				
Concept	**Propose**	**D/W**	**Requirements**	**Goal**
Function	E	D	Resists pressurization	P_{oper} = 0.3 MPa
	E	D	Resists shearing and bending loads	m_{bed} = 0.91 kg
	E	D	Supports high temperature	T = 935 °C
	E	D	Fluidizes solid particles	$\dot{m}_{total}$ = 80 kg h-1 d_s = 1.3 mm ρ_s = 500 kg m-3
Dimensions	C	W	Outer radius	r_o = 0.125 m r_c = 0.45 m
	E	D	Wall thickness (including corrosion allowance)	t_{sw} = 5 mm
	C	W	Gas distributor	%op = 22% N_{blade} = 11 t_{blade} = 1 mm θ = 14°
Material	C	D	Resistance to combined loadings without exceeding the yield strength limit	$S_y \geq$ 200 MPa
	E	D	Resistance to corrosion wear	Allowable corrosion = 2 mm
	E	D	Resistance to high temperature	$T_{max} \geq$ 970 °C
Safety	E	D	Follows safety standards to build pressure vessels	ASME code section VIII
	E	D	Follows explosion-proof safety standards	ISO 6184-1:1985
Signs	C	D	Pressure measuring	Pressure transmitter
	C	D	Flow measuring	Flowmeter transmitter
	C	D	Temperature measuring	Temperature transmitter
Cost	C	W	Cost per kilo	Low
	C	W	Energy to produce material	Lower than common materials

4.4.7. Constructive material of the swirling fluidized bed reactor

Table 4-26 shows the design requirements for selecting the construction material of the SFB reactor considering the temperature for rice husk combustion.

Table 4-26 Design requirement for selecting the construction material of the SFB reactor for combustion of 80 kg h^{-1} of rice husk.

Function	Pressure vessel at high temperature
Constrains	$S_y \geq 200$ MPa $T_{\max} \geq 970$ °C
Objective	$M_1 \geq 0.123$ $M_2 \geq 9$
Free variables	Low cost Low energy for production Choice of material

The constraints specify that the yield strength (S_y) and the maximum service temperature ($T_{\max}$) of the pressure vessel material must be at least 200 MPa and 970 °C, respectively. The first screening stage passes only the materials that satisfy the constraints. Figure 4-20 shows the materials which pass the first screening stage. The 134 possible candidates are metals and alloys, and some magnetic materials.

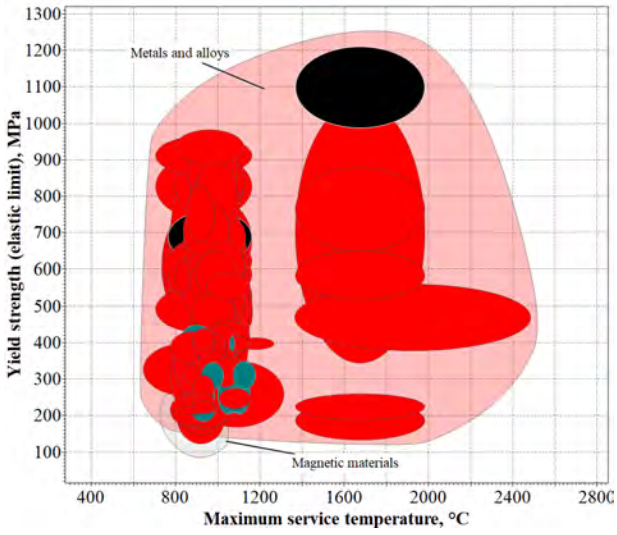

Figure 4-20 Yield strength S_y vs. maximum service temperature T_{max} after the first screening step using the constraints $S_y \geq 200$ MPa and $T_{max} \geq 970$°C. Source: Chart extracted from CES Edupack [77].

The following screening stage applies the objectives of the design requirements, i.e., the index of materials, thus obtaining a set of 94 candidates. Figure 4-21a illustrates the objectives screening stage maximizing the material indexes M_1 and M_2. Figure 4-21b shows the surviving materials, i.e., ferrous and non-ferrous alloys. Ferrous alloys are mainly stainless steel, and the non-ferrous alloys are Ni- and Ta-based alloys. Table 4-27 presents the materials with the best performance from every group.

The material selection is a free variable to the designer from the 87 remaining candidates. Table 4-27 presents the options with the best technical performance, while Table 4-28 the materials with the lowest energy required for production and cost

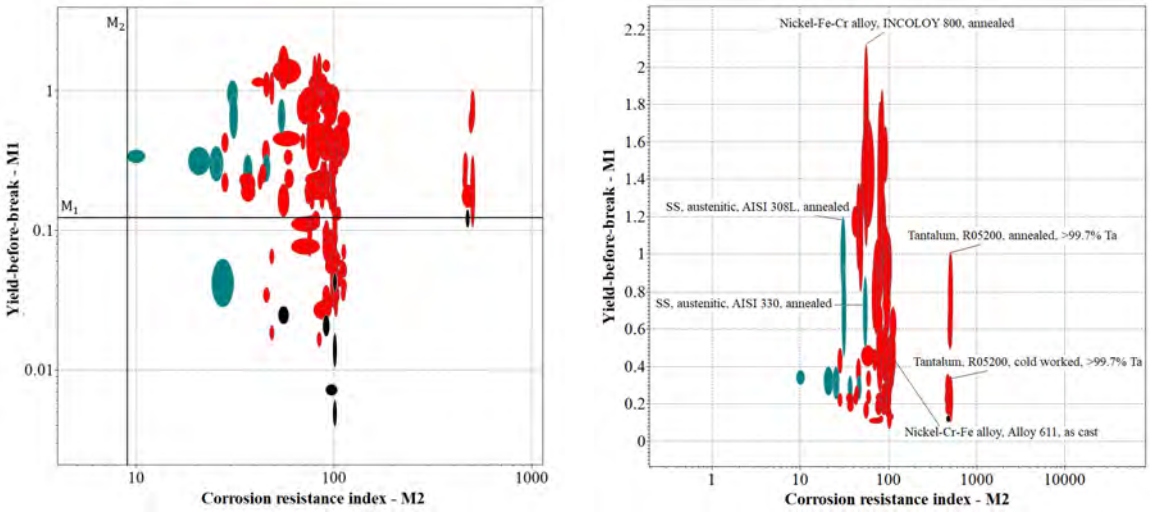

(a) (b)

Figure 4-21 Yield before break vs Corrosion resistance index (a) with the reference levels of the indexes to optimize the objectives, and (b) the surviving materials after filtering the indexes. Source: Chart extracted from CES Edupack [77].

Table 4-27 Suggested construction materials based on the best technical performance classified according to their material group.

Material group	Best performance to satisfy the objective	
	M_1	M_2
Steels	AISI 308L	AISI 330
Ni-based alloys	INCOLOY 800	Alloy 611
Ta-based alloys	R05200 annealed	R05200 cold worked

Finally, Figure 4-22 is the chart for analyzing the free variables, i.e., embodied energy for primary production vs. price per unit volume. The materials from the SS group present the lowest price per unit volume and energy consumption for primary production, followed by the Ni-based alloys. On the other hand, the Ta-based alloys have the highest values of the two free variables. The Ta-based alloys are discarded because their free variables exceed the other two groups by at least ten times the average values of the Ni-based alloys. Table 4-28 summarizes the materials from the SS and Ni-based alloys groups with the lowest energy consumption and cost.

4.4.8. Pressure-drop and blower selection

4.4.8.1. Major pressure drops

Table 4-29 comprises the pressure drops across the major contributors of the SFB reactor obtained from equations in Section 4.3.9. The detail about the pressure drops calculation of the flowmeter and the cyclone are in Appendix B.5 and B.6.

4.4.8.2. Blower selection

Table 4-30 shows the minimum required specifications of the blower to drive the SFB reactor for the combustion of 80 kg h^{-1} of rice husk.

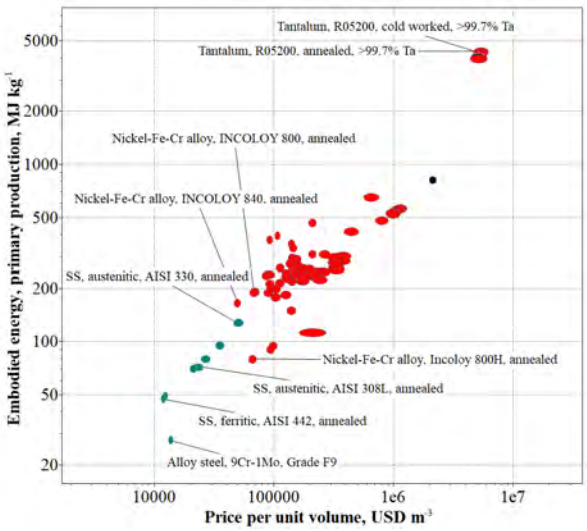

Figure 4-22 Embodied energy for primary production vs. price per unit volume of the materials obtained after screening the constraints and the objectives of the material selection methodology. Source: Chart extracted from CES Edupack [77].

Table 4-28 Suggested construction materials with the lowest energy consumption and cost.

Material group	**Best relation**	
	Energy for primary production per kg	Price per unit volume
Steels	Alloy steel 9Cr-1Mo	AISI 442
Ni-based alloys	INCOLOY 800H	INCOLOY 840

Table 4-29 Results of major pressure-drops by contributor in the SFB reactor for combustion of 80 kg h^{-1} of rice husk.

Variable	**Value**
ΔP_{distr}, kPa	7.12×10^{-2}
$\Delta P_{(\text{mf,bed})}$, kPa	3.41
$\Delta P_{\text{flowmeter}}$, kPa	8.00
$\Delta P_{\text{cyclone}}$, kPa	1.58
ΔP_{SFB}, kPa	11.07

Table 4-30 Required specifications of the blower to drive the SFB reactor for combustion of 80 kg h^{-1} of rice husk.

Variable	**Value**
$\dot{W}_{\text{flow}}$, kW	1.74
H_{blower}, m H_2O	1.13
$\dot{V}_{\text{g,act}}$, $m^3\ h^{-1}$	567

A Gardner Denver side blower channel with frequency converter model G-BH1 2BH1 900 is the selected equipment for rice husk combustion [90]. Table 4-31 summarizes the operating conditions of the selected blower based on the operation point extracted from the performance curves in Appendix B.7.

Table 4-31 Operating point conditions of the selected blower Gardner Denver G-BH1 2BH1 900 [87] for combustion of 80 kg h^{-1} of rice husk.

Variable	Value
$\dot{W}_{cons,blower}$, kW (hp)	7.6 (10)
H_{blower}, m H2O	1.13
$\dot{V}_{blower}$, m^3 h^{-1}	1050
$\dot{V}_{valve\ 3}$, m^3 h^{-1}	483
f, Hz	60
η, %	42

4.4.9. Design drawings

Appendix B.8 comprises the detailed drawings of the SFB reactor for rice husk combustion with the dimensions designed in this case study.

4.5. Conclusion

This work presents the design procedure of a SFB reactor for biomass thermochemical conversion through four different routes: combustion, gasification, pyrolysis, and torrefaction. The SFB reactor shows advantages over the conventional FBs because of the higher gas-solid slip velocities in a more uniform rotating bed with the capacity to process a wide range of particle sizes, densities, and shapes. The rotation of the bed in the SFB reactor improves the heat, mass, and momentum transfer rates between the particles and the gas flow. The proposed design procedure determines a basic design of the SFB from the operational constraints and needs of the desired biomass conversion route. The results define the internal stresses caused by the operating conditions, which gives the maximum allowable yield strength of the blades and the pressure vessel. The requirements list and the material selection specify the SFB reactor dimensions and construction materials.

The designed reactor in the case study showed good agreement with an actual unit from the literature. The SFB reactor features a combustion heat of 329 kW, which comprises 132 kW of power output, 193 kW of heat loss through the wall, and 4 kW of heat of vaporization, resulting in 40% of thermal efficiency. The estimated wall thickness is 5 mm, including corrosion allowance, while the thickness of the unit from literature was 4.5 mm. The addition of an inner refractory cover in the experiment increases the corrosion resistance of the SFB reactor, allowing a thinner structural wall. SS AISI 308 and AISI 330 are the candidates with the best performance to meet the function of the pressure vessel at high temperature, i.e., constructive material of the SFB reactor. Although to Ni-based alloys are suitable options for constructing the SFB reactor, stainless steels have a lower acquisition cost and require less energy consumption for their production.

Further works related to the design of the SFB reactor should include a heat transfer analysis across the reactor walls estimating heat losses. Using the latter value opens the opportunity of improving the thermal efficiency of the process including a thermal insulation system to reduce the heat losses. Finally, dimensioning of other subsystems, e.g., the solids feeder and cyclones, is important to determine the material and energy streams consumptions required for operating the

SFB reactor installation, contributing to possible economic feasibility studies of constructing the installation.

4.6. References

[1] R. Vooradi, M.-O. Bertran, R. Frauzem, S. B. Anne, and R. Gani, "Sustainable chemical processing and energy-carbon dioxide management: Review of challenges and opportunities", *Chem. Eng. Res. Des.*, vol. 131, pp. 440–464, 2018, doi: https://doi.org/10.1016/j.cherd.2017.12.019.
[2] A. I. Stankiewicz and J. A. Moulijn, "Process intensification: transforming chemical engineering", *Chem. Eng. Prog.*, vol. 96, no. 1, pp. 22–34, 2000.
[3] W. Zhang, "A Review of Techniques for the Process Intensification of Fluidized Bed Reactors", *Chinese J. Chem. Eng.*, vol. 17, no. 4, pp. 688–702, 2009, doi: https://doi.org/10.1016/S1004-9541(08)60264-5.
[4] H. Wang *et al.*, "A review of process intensification applied to solids handling", *Chem. Eng. Process. Process Intensif.*, vol. 118, pp. 78–107, 2017, doi: https://doi.org/10.1016/j.cep.2017.04.007.
[5] C. E. Dodson and V. I. Lakshmanan, "An innovative gas-solid torbed reactor for the recycling industries", *JOM*, vol. 50, no. 7, pp. 29–31, 1998, doi: 10.1007/s11837-998-0189-6.
[6] Torftech Group, "Energy Production from Biomass and Wastes". Torftech Group. [Online]. Available: http://www.torftech.com/
[7] Torftech Group, "Biomass Gasification Technology Presentation", no. May. Torftech Group, p. 48, 2020. [Online]. Available: https://making.com/wp-content/uploads/2021/06/20-05-21-Biomass-Gasification-Technology-Presentation.pdf
[8] C. E. Dodson, "Apparatus for processing matter in a turbulent mass of particulate material", US4479920, 1984
[9] C. E. Dodson and R. G. W. Laughlin, "Novel Thermal Treatment Capability of the TORBED ® Process Reactor Technologies", Ontario, 1998.
[10] J. Shu, V. I. Lakshmanan, and C. E. Dodson, "Hydrodynamic study of a toroidal fluidized bed reactor", *Chem. Eng. Process. Process Intensif.*, vol. 39, no. 6, pp. 499–506, 2000, doi: 10.1016/S0255-2701(00)00097-0.
[11] M. Kaltschmitt, Energy from Organic Materials (Biomass): A Volume in the Encyclopedia of Sustainability Science and Technology. Springer, 2019.
[12] P. Basu, Biomass Gasification, Pyrolysis and Torrefaction: Practical Design and Theory. 2013. doi: 10.1016/C2011-0-07564-6.
[13] J. S. Tumuluru, Biomass preprocessing and pretreatments for production of biofuels: mechanical, chemical and thermal methods. CRC Press, 2018.
[14] F. Scala, *Fluidized Bed Technologies for near-Zero Emission Combustion and Gasification*. Cambridge, UNITED KINGDOM: Elsevier Science & Technology, 2013. [Online]. Available: http://ebookcentral.proquest.com/lib/unorte-ebooks/detail.action?docID=1581395
[15] L. Theodore and D. C. Cortinhas, *Chemical Reactor Analysis and Applications for the Practicing Engineer*. New York, UNITED STATES: John Wiley & Sons, Incorporated, 2012. [Online]. Available: http://ebookcentral.proquest.com/lib/unorte-ebooks/detail.action?docID=818494
[16] V. V Kumar, V. R. Raghavan, V. Vinod Kumar, and V. R. Raghavan, "Developments in fluidized bed technology — A review", in *2011 National Postgraduate Conference*, 2011, pp. 1–10. doi: 10.1109/NatPC.2011.6136395.
[17] R. Kaewklum and V. I. Kuprianov, "Experimental studies on a novel swirling fluidized-bed combustor using an annular spiral air distributor", *Fuel*, vol. 89, no. 1, pp. 43–52, 2010, doi: https://doi.org/10.1016/j.fuel.2009.07.027.
[18] C. E. Dodson, "Particle treatment in a toroidal bed reactor", US6108935A, 2000
[19] M. F. Mohideen Batcha, "Swirling Fluidized Bed", MY164018A, 2017
[20] J. A. Kostuch and C. E. Dodson, "Furnace having Toroidal Fluid Flow Heating Zone", 2000
[21] C. Dodson, "Material processing system and method", GB2574569A, 2019
[22] C. E. Dodson, "Process for Treating a Material in a Toroidal Fluidized-Bed with Electromagnetic Radiations", WO2019145735A1, 2019

[23] C. Dodson, "Toroidal Bed Reactor", GB2558162A, 2018
[24] S. A. Sulaiman, C. S. Miin, M. Y. Naz, and V. R. Raghavan, "Particle Image Velocimetry of a Swirling Fluidized Bed at Different Blade Angles", *Chem. Eng. Technol.*, vol. 39, no. 6, pp. 1151–1160, Jun. 2016, doi: 10.1002/ceat.201500074.
[25] C. Dodson, V. Lakshmanan, R. Laughlin, and R. Sridhar, "Flash roasting of sulphide concentrates and leach residues using a TORBED reactor", *EPD Congr. 1999*, pp. 1–5, 1999, [Online]. Available: http://scholar.google.com/scholar?hl=en&btnG=Search&q=intitle:FLASH+ROASTING+OF+SULPHIDE+CONCENTRATES+AND+LEACH+RESIDUES+USING+A+TORBED+*+REACTOR#0
[26] T. Hopkins and P. Merline, "Comtor Process for Treatment of Spent Potlining", *Miner. Process. Extr. Metall. Rev.*, vol. 15, no. 1–4, pp. 247–255, 1995, doi: 10.1080/08827509508914203.
[27] J. R. McDonough, R. Law, D. A. Reay, and V. Zivkovic, "Intensified carbon capture using adsorption: Heat transfer challenges and potential solutions", *Therm. Sci. Eng. Prog.*, vol. 8, no. February, pp. 17–30, 2018, doi: 10.1016/j.tsep.2018.07.012.
[28] Planet Dryers Ltd Food Machinery Suppliers, "Torbed Hot Air Processors". Planet Dryers Ltd, 2014. [Online]. Available: www.planetdryers.co.uk
[29] Torftech Group, "An executive summary". Torftech Group.
[30] J. H. Zakaria, M. H. H. Md Zaid, M. F. Mohideen Batcha, and N. Asmuin, "Drying of sponge media using swirling fluidized bed dryer", *Appl. Mech. Mater.*, vol. 660, pp. 644–648, 2014, doi: 10.4028/www.scientific.net/AMM.660.644.
[31] M. T. Mcqueen, "Energy and High Surface Area Siliceous Ash From the Combustion of Rice Hulls", in *Proceedings of 17th FBC: 17TH International Fluidized Bed Combustion Conference*, May 2003, pp. 721–728. doi: 10.1115/FBC2003-018.
[32] W. M. Lewandowski, M. Ryms, and W. Kosakowski, "Thermal biomass conversion: A review", *Processes*, vol. 8, no. 5, 2020, doi: 10.3390/PR8050516.
[33] E. A. Christoforou and P. A. Fokaides, "Recent Advancements in Torrefaction of Solid Biomass", *Curr. Sustain. Energy Reports*, vol. 5, no. 2, pp. 163–171, 2018, doi: 10.1007/s40518-018-0110-z.
[34] B. Sreenivasan and V. R. Raghavan, "Hydrodynamics of a swirling fluidised bed", *Chem. Eng. Process. Process Intensif.*, vol. 41, no. 2, pp. 99–106, 2002, doi: https://doi.org/10.1016/S0255-2701(00)00155-0.
[35] C. S. Miin, S. A. Sulaiman, V. R. Raghavan, M. R. Heikal, and M. Y. Naz, "Hydrodynamics of multi-sized particles in stable regime of a swirling bed", *Korean J. Chem. Eng.*, vol. 32, no. 11, pp. 2361–2367, 2015, doi: 10.1007/s11814-015-0151-6.
[36] M. H. M. Tawfik, M. Refaat Diab, and H. Mohmed Abdelmotalib, "An experimental investigation of wall-bed heat transfer and flow characteristics in a swirling fluidized bed reactor", *Appl. Therm. Eng.*, vol. 155, no. April, pp. 501–507, 2019, doi: 10.1016/j.applthermaleng.2019.04.022.
[37] M. F. Mohideen, B. Sreenivasan, S. A. Sulaiman, and V. R. Raghavan, "Heat transfer in a swirling fluidized bed with geldart type-D particles", *Korean J. Chem. Eng.*, vol. 29, no. 7, pp. 862–867, 2012, doi: 10.1007/s11814-011-0255-6.
[38] P. Arromdee and V. I. Kuprianov, "A comparative study on combustion of sunflower shells in bubbling and swirling fluidized-bed combustors with a cone-shaped bed", *Chem. Eng. Process. Process Intensif.*, vol. 62, pp. 26–38, 2012, doi: 10.1016/j.cep.2012.10.002.
[39] V. I. Kuprianov, R. Kaewklum, and S. Chakritthakul, "Effects of operating conditions and fuel properties on emission performance and combustion efficiency of a swirling fluidized-bed combustor fired with a biomass fuel", *Energy*, vol. 36, no. 4, pp. 2038–2048, 2011, doi: 10.1016/j.energy.2010.05.026.
[40] J. H. Zakaria, M. H. H. M. Zaid, M. F. M. Batcha, and N. Asmuin, "Feasibility study on pliant media drying using fluidized bed dryer", *IOP Conf. Ser. Mater. Sci. Eng.*, vol. 88, no. 1, 2015, doi: 10.1088/1757-899X/88/1/012071.

[41] M. Hamdan, S. Sabudin, M. Faizal, and V. R. Raghavan, "Experimental studies on oil palm frond drying using swirling fluidized bed dryer", *AIP Conf. Proc.*, vol. 1440, no. Imat 2011, pp. 1212–1219, 2012, doi: 10.1063/1.4704339.
[42] M. Paulose, "Hydrodynamic Study of Swirling Fluidized Bed and the Role of Distributor", COCHIN UNIVERSITY OF SCIENCE AND TECHNOLOGY, 2006.
[43] V. K. Venkiteswaran, "Study of Hydrodynamic Properties of Swirling Fluidized Bed", Universiti Teknologi PETRONAS, 2014. [Online]. Available: http://utpedia.utp.edu.my/15439/
[44] W. Yang, Handbook of fluidization and fluid-particle systems. CRC press, 2003.
[45] V. L. Streeter, E. B. Wylie, and K. W. Bedford, *Fluid mechanics*, 9th ed. New York: McGraw-Hill, 2010.
[46] R. Hibbeler, *Mechanics of Materials*, 10th ed. Harlow, England: Pearson Education, 2018.
[47] J. E. Shigley, C. R. Mischke, R. G. Budnyas, and K. J. Nisbett, *Shigley's Mechanical Engineering Design*, 8th ed. McGraw-Hill, 2008.
[48] G. Pahl, W. Beitz, J. Feldhusen, and K.-H. Grote, "Engineering Design". Springer London, 2007. doi: 10.1007/978-1-84628-319-2.
[49] M. F. Ashby, *Materials selection in mechanical design*. Oxford: Elsevier Butterworth-Heinemann, 2005.
[50] R. Kaewklum, V. I. Kuprianov, and P. L. Douglas, "Hydrodynamics of air-sand flow in a conical swirling fluidized bed: A comparative study between tangential and axial air entries", *Energy Convers. Manag.*, vol. 50, no. 12, pp. 2999–3006, 2009, doi: 10.1016/j.enconman.2009.07.019.
[51] Y. A. Çengel, M. A. Boles, and M. Kanoglu, *Thermodynamics: An Engineering Approach*, 9th ed., 2021. New York: McGraw-Hill, 2019.
[52] P. McKendry, "Energy production from biomass (part 2): conversion technologies", *Bioresour. Technol.*, vol. 83, no. 1, pp. 47–54, 2002, doi: https://doi.org/10.1016/S0960-8524(01)00119-5.
[53] P. Ninduangdee, P. Arromdee, C. Se, and V. I. Kuprianov, "Effects of (Co-)Combustion Techniques and Operating Conditions on the Performance and NO Emission Reduction in a Biomass-Fueled Twin-Cyclone Fluidized-Bed Combustor", *Waste and Biomass Valorization*, vol. 11, no. 10, pp. 5375–5391, 2020, doi: 10.1007/s12649-020-01124-z.
[54] V. I. Kuprianov, R. Kaewklum, and K. Janvijitsakul, "A Study of Firing Rice Husk in a Swirling Fluidized-Bed Combustor Using Annular Spiral Air Distributor", pp. 26–31, 2008.
[55] V. I. Kuprianov, R. Kaewklum, K. Sirisomboon, P. Arromdee, and S. Chakritthakul, "Combustion and emission characteristics of a swirling fluidized-bed combustor burning moisturized rice husk", *Appl. Energy*, vol. 87, no. 9, pp. 2899–2906, 2010, doi: https://doi.org/10.1016/j.apenergy.2009.09.009.
[56] National Institute of Standards and Technology - NIST, *NIST Chemistry WebBook*. National Institute of Standards and Technology - NIST. doi: 10.18434/T4D303.
[57] J. R. Fanchi, "2 - Fluid Properties", J. R. B. T.-I. R. A. M. Fanchi, Ed. Boston: Gulf Professional Publishing, 2010, pp. 17–32. doi: https://doi.org/10.1016/B978-0-12-382088-4.00002-5.
[58] J. Haydary, Chemical Process Design and Simulation: Aspen Plus and Aspen HYSYS Applications. New Jersey: JohnWiley & Sons, Inc., 2019.
[59] A. V Bridgwater, "Review of fast pyrolysis of biomass and product upgrading", *Biomass and Bioenergy*, vol. 38, pp. 68–94, 2012, doi: https://doi.org/10.1016/j.biombioe.2011.01.048.
[60] S. Bilgen, S. Keleş, and K. Kaygusuz, "Calculation of higher and lower heating values and chemical exergy values of liquid products obtained from pyrolysis of hazelnut cupulae", *Energy*, vol. 41, no. 1, pp. 380–385, 2012, doi: https://doi.org/10.1016/j.energy.2012.03.001.
[61] AspenTech, "Biomass pyrolysis modeling", Bedford, MA, 2021. [Online]. Available: http://www.aspentech.com
[62] K. Iisa, R. J. French, K. A. Orton, A. Dutta, and J. A. Schaidle, "Production of low-oxygen bio-oil via ex situ catalytic fast pyrolysis and hydrotreating", *Fuel*, vol. 207, pp. 413–422, 2017, doi: https://doi.org/10.1016/j.fuel.2017.06.098.

[63] M. Van de Velden, J. Baeyens, A. Brems, B. Janssens, and R. Dewil, "Fundamentals, kinetics and endothermicity of the biomass pyrolysis reaction", *Renew. Energy*, vol. 35, no. 1, pp. 232–242, 2010, doi: https://doi.org/10.1016/j.renene.2009.04.019.
[64] D. C. Chitester, R. M. Kornosky, L.-S. Fan, and J. P. Danko, "Characteristics of fluidization at high pressure", *Chem. Eng. Sci.*, vol. 39, no. 2, pp. 253–261, 1984, doi: https://doi.org/10.1016/0009-2509(84)80025-1.
[65] S. Harish Kumar and D. V. R. Murthy, "Minimum superficial fluid velocity in a gas–solid swirled fluidized bed", *Chem. Eng. Process. Process Intensif.*, vol. 49, no. 10, pp. 1095–1100, 2010, doi: https://doi.org/10.1016/j.cep.2010.08.013.
[66] F. M. White, *Fluid Mechanics*, 7th ed. New York: McGraw-Hill, 2016.
[67] The American Society of Mechanical Engineers, "ASME Boiler and Pressure Vessel Code. Section VIII: Pressure Vessels Set". 2021.
[68] R. Sinnott and G. Towler, *Chemical engineering design: SI Edition*. Butterworth-Heinemann, 2019.
[69] R. A. Antunes and M. C. L. de Oliveira, "Corrosion in biomass combustion: A materials selection analysis and its interaction with corrosion mechanisms and mitigation strategies", *Corros. Sci.*, vol. 76, pp. 6–26, 2013, doi: https://doi.org/10.1016/j.corsci.2013.07.013.
[70] R. Elger, R. Norling, and R. Pettersson, "Corrosion and deposit formation on four steels exposed in the syngas section after a biomass gasifier", *Mater. Corros.*, vol. 67, no. 9, pp. 939–951, 2016, doi: 10.1002/maco.201508686.
[71] Y. Li *et al.*, "Characterization of oxide scales formed on heating equipment in supercritical water gasification process for producing hydrogen", *Int. J. Hydrogen Energy*, vol. 44, no. 56, pp. 29508–29515, 2019, doi: 10.1016/j.ijhydene.2019.01.284.
[72] H. Darmstadt, M. Garcia-Perez, A. Adnot, A. Chaala, D. Kretschmer, and C. Roy, "Corrosion of Metals by Bio-Oil Obtained by Vacuum Pyrolysis of Softwood Bark Residues. An X-ray Photoelectron Spectroscopy and Auger Electron Spectroscopy Study", *Energy & Fuels*, vol. 18, no. 5, pp. 1291–1301, Sep. 2004, doi: 10.1021/ef0340920.
[73] H. Hooshyar, J. Liske, L. G. Johansson, M. Seemann, and T. Jonsson, "Initial corrosion attack of 304L and T22 in 2 MW biomass gasifier: A microstructural investigation", *Mater. High Temp.*, vol. 32, no. 1–2, pp. 197–204, 2015, doi: 10.1179/0960340914Z.000000000101.
[74] D. W. Kirk, Z. R. Li, D. Fuleki, and P. C. Patnaik, "Materials Compatibility With Pyrolysis Biofuel". Jun. 04, 2001. doi: 10.1115/2001-GT-0006.
[75] D. Di Mondo, D. Ashok, F. Waldie, N. Schrier, M. Morrison, and M. Schlaf, "Stainless steel as a catalyst for the total deoxygenation of glycerol and levulinic acid in aqueous acidic medium", *ACS Catal.*, vol. 1, no. 4, pp. 355–364, 2011, doi: 10.1021/cs200053h.
[76] J. Jun, M. G. Frith, R. M. Connatser, J. R. Keiser, M. P. Brady, and S. Lewis, "Corrosion Susceptibility of Cr–Mo Steels and Ferritic Stainless Steels in Biomass-Derived Pyrolysis Oil Constituents", *Energy & Fuels*, vol. 34, no. 5, pp. 6220–6228, May 2020, doi: 10.1021/acs.energyfuels.9b04406.
[77] Granta Design Limited, "CES EduPack".
[78] G. A. Wellwood, "Hydrodynamic behaviour of the Torbed® reactor operating in fine particle mode", University of Queensland, 2000.
[79] Conveyor Equipment Manufacturers Association (CEMA), "Belt Conveyors for Bulk Material". 1988.
[80] M. E. Fayed and T. S. Skocir, *Mechanical conveyors: selection and operation*, 1st ed. New York: CRC Press, 1997. doi: 10.1201/9780203747902.
[81] C. R. Woodcock and J. S. Mason, *Bulk solids handling: an introduction to the practice and technology*. Springer Science & Business Media, 1988.
[82] Conveyor Equipment Manufacturers Association (CEMA), "CEMA Standard N° 350 Screw Conveyors for Bulk Materials". 2015.
[83] J. Fruchtbaum, *Bulk Materials Handling Handbook*. New York: Springer Science & Business Media, 1988. doi: 10.1007/978-1-4757-4695-2.
[84] D. Mills, *Pneumatic conveying design guide*. Elsevier, 2003.

[85] S. Steven, E. Restiawaty, and Y. Bindar, "Routes for energy and bio-silica production from rice husk: A comprehensive review and emerging prospect", Renew. Sustain. Energy Rev., vol. 149, no. June, p. 111329, 2021, doi: 10.1016/j.rser.2021.111329.
[86] S. J. Park et al., "Gasification operational characteristics of 20-tons-Per-Day rice husk fluidized-bed reactor", Renew. Energy, vol. 169, pp. 788–798, 2021, doi: https://doi.org/10.1016/j.renene.2021.01.045.
[87] C.-B. Dinh, C.-C. Liao, and S.-S. Hsiau, "Numerical study of hydrodynamics with surface heat transfer in a bubbling fluidized-bed reactor applied to fast pyrolysis of rice husk", Adv. Powder Technol., vol. 28, no. 2, pp. 419–429, 2017, doi: https://doi.org/10.1016/j.apt.2016.10.013.
[88] I. J. Fernandes et al., "Characterization of rice husk ash produced using different biomass combustion techniques for energy", Fuel, vol. 165, pp. 351–359, 2016, doi: https://doi.org/10.1016/j.fuel.2015.10.086.
[89] M. Rozainee, S. P. Ngo, A. A. Salema, K. G. Tan, M. Ariffin, and Z. N. Zainura, "Effect of fluidising velocity on the combustion of rice husk in a bench-scale fluidised bed combustor for the production of amorphous rice husk ash", Bioresour. Technol., vol. 99, no. 4, pp. 703–713, 2008, doi: https://doi.org/10.1016/j.biortech.2007.01.049.
[90] Gardner Denver, "G-BH1 e - Data sheet 2BH1 900 - Side channel blower with Frequency Converter", Bad Neustadt, 2015. [Online]. Available: https://www.gardnerdenver.com/en-in/elmorietschle/products/side-channel/compressor-g-bh1-c

5. Conclusions and perspectives

5.1. Conclusions

The objective of this work was to develop a design procedure of a Swirling Fluidized Bed (SFB) reactors for thermochemical conversion of biomass into energy, fuels, chemical precursors, and high-value molecules. The first point was to construct a systematic literature review of the history of the SFB reactor in terms of reported applications and research advancements since its invention in 1984 until the developments of 2021. The PRISMA methodology guided the screening process for selecting the suitable records related to the SFB technology which amounted to 96 published documents. A content-based analysis assessed the selected records by their objectives, and methodologies, applications, and type of particles fluidized. The review revealed that the most common reported application of the SFB reactor is for experimental purposes with the interest of identifying relationships between variables and operating parameters. Most of the studies focused on the effect of the input and operating parameters on the bed behavior in the early ages of the SFB reactor for understanding its operation. Variations of SFB reactor designs and fabrication techniques extend its capacity of processing particles from all the groups of the 1g-Geldart's classification, highlighting the fluidization of biomass. Some research advancements led to develop theoretical and semi-experimental models for estimating operating variables of the SFB reactor, such as the minimum fluidization velocity, pressure-drops across the distributor and the bed, and heat transfer coefficient. Major understanding of the SFB reactor increased the interest of different industries, where the reactor has shown a remarkable performance, e.g., biomass combustion efficiencies reaches up to 99%, and transfer rates in drying operation are higher than those in conventional fluidized beds. CFD modeling has been relevant for analyzing details in the SFB reactor operation with further opportunities for studying flow patterns in binary phase simulations. Related to the design of the SFB reactor, only one author developed geometrical models to solve three configurations of the annular gas distributor. Nevertheless, there is a lack of information about detailed dimensioning and materials selection to construct the SFB reactor. A CFD-based model of the SFB reactor and the design of the equipment for thermochemical conversion of biomass were developed in this work.

The second point was to perform a cold flow CFD-based simulation of a gas-solid SFB reactor solved in the open-source software OpenFOAM® from the Euler-Euler approach. The simulation used a SFB reactor for fluidizing 6 mm particle beads with air at a superficial velocity of 2.23 m s^{-1}. The air passed through a single row blades type gas distributor of 30 cm outer and 20 cm inner diameters with 60 blades horizontally inclined 10°. The selection of the specularity coefficients combination validated the simulation results with experimental data. The combination $\varphi_{s,p}$ = 0.125 on the pipe wall and $\varphi_{s,c}$ = 0.05 on the cone wall worked within a range of operating conditions with relative error lower than 5% compared to the experimental data. The solids flow patterns denoted that the combined effect of the centrifugal force and drag force contributed to the bed axial and radial mixing. The bed rotated at

average G values between 0.48-0.07 with a maximum value of 1.6 at the bottom. The gas flow patterns depicted that the gas lost almost 90% of its kinetic energy as soon as it left the distributor. The inclined injection of the air contributed to the particles mixing in the SFB reactor. The CFD-based simulation of a gas-solid SFB reactor proved to be a useful tool to gain insight into the gas-solid behaviors. The use of CFD would contribute to the analysis of the operation of a SFB reactor as a post-design step for decision-making before the construction and acquisition of the actual equipment.

The final step was to establish the design procedure of the SFB reactor for thermochemical conversion of biomass. The procedure coupled some theoretical and semi-experimental models, and technical information from the systematic literature review. Some chemical, thermodynamics, and mechanical models were adapted for solving the design of the SFB reactor. The design procedure included four biomass conversion routes: combustion, gasification, pyrolysis, and torrefaction. The solution of species molar balances with chemical reactions occurring at equilibrium and the steady state mass and energy balances gave the actual flow rates of biomass and fluidizing gas. Defined operating conditions solved the basic design of the blades and the pressure vessel of the SFB reactor determining the minimum allowable yield strength of the materials for supporting the loads. A list of design specification contributed to the materials selection for construction of the SFB reactor. An experimental-based case study of design of a SFB reactor was solved for combustion of 80 kg h^{-1} of rice husk. The analysis of the flow passing through the gas distributor showed that the actual air velocity surpassed minimum fluidization with the defined geometry in the experiment. The rice husk combustion in the SFB reactor featured a power output of 132 kW with a thermal efficiency of 40% due to intensive heat transfer through the walls. The minimum allowable yield strength amounted to 190 MPa, which indicated that the suitable construction materials were stainless steels and Ni-based alloys. However, SS were preferred due to lower economic cost of acquisition and less energy consumption required for their production. The estimated wall thickness of the pressure vessel was 5 mm, including corrosion allowance, is in line with the actual SFB reactor used for the experiments. The obtained results from the proposed design procedure of SFB reactors showed good agreement with an installed equipment.

This MSc thesis stated a guideline design procedure of SFB reactors for biomass thermochemical conversion to energy, fuels, chemical precursors, and high-value chemicals. The initial literature review established the state-of-the-art of the SFB reactor and recent developments expanding the understanding of the technology. From the review presented in Chapter 2 it was identified the high interest of biomass treating in the SFB reactor, and some mathematical models and technical information for contributing the design procedure. The CFD model of a gas-solid SFB reactor developed in Chapter 3 showed a more detailed analysis of bed behavior compared to experiments. The addition of CFD simulations to the design of the SFB reactor could reduce the economic cost in the acquisition and testing of prototypes. Finally, Chapter 4 proposed a design procedure of the SFB reactor applicable to four biomass conversion routes: combustion, gasification, pyrolysis, and torrefaction. The results provided a starting point for dimensioning a SFB reactor to achieve an expected production considering costumer's requirements. However, a number of challenges persist, some of which are summarized in the following section.

5.2. Future perspectives

Future woks about the SFB reactor should focus on three areas: experimentation, simulation, and design. Additional experimental studies would expand the analysis of the effect of input parameters in less reported variables, e.g., bed temperature and particle residence times. Additional experiments could determine optimum operating conditions of the SFB reactor in general cases or specific applications. A deepen understanding of the SFB reactor should lead to develop simplified models for predicting the bed behavior, which could improve future designs of the reactor.

Improving CFD-based simulation in the SFB reactor requires a mesh with more structured grid which should reduce simulation times and number of cells required to solve the model. Further hydrodynamics analysis is proposed, such as the gas-solid interface slip velocities to gain insights into the bed's momentum change and the analysis of the granular temperature to identify turbulent fluctuations in the bed. In addition, a study of the solids azimuthal velocity and acceleration profiles would provide in-depth details about drag and frictional forces acting on the bed in the swirling direction. CFD simulation studies have excluded heat and mass transfer to the models of the SFB reactor, which would provide results related to heating and reacting applications. Since there is no previous data, the studies should focus on simulating single phase heat transfer in the SFB reactor as a start point. Conducting parametric studies through CFD-based simulations of the SFB reactor would suggest the best operating and design conditions to obtain an optimum performance.

The design procedure of the SFB reactor should include a heat transfer analysis across the walls for estimating heat losses and analyzing strategies to improve the thermal efficiency of the process, e.g., the installation of a thermal insulation system. Scaling the design procedure to larger applications could include a guide to conduct an economic feasibility study of the designed SFB reactor. The feasibility study would require the estimation of all material and energy streams of the SFB reactor installation, i.e., dimensioning the subsystems, such as the solid feeder, the filtration and separation system, and optional burners or heating systems.

A. Systematic Literature Review

A.1. Articles in the ‘Only-mention’ category

Refer to the attached table A.1. in the Excel File, Appendix A.xlsx, to see the consolidated articles in the ‘Only-mention’ category.

A.2. Articles in the ‘Related records’ category

Refer to the attached table A.2. in the Excel File, Appendix A.xlsx, to see the consolidated articles in the ‘Related records’ category.

A.3. Database of the content-based analysis of the selected records

Refer to the attached table A.3. in the Excel File, Appendix A.xlsx, to see the Database to guide the content-based analysis of the systematic literature review.

B. Calculation and dimensioning of the gas-solid Swirling Fluidized Bed reactor

B.1. Shomate equation constants to estimate the enthalpy of the ideal gas at temperature *T*

Table B-1 Shomate equation constants for the formed compounds during biomass combustion [1]**.**

Compound	***T*** (K)	A	B	C	D	E	F	H
CO_2	298. - 1200.	25.00	55.19	-33.69	7.95	-0.14	-403.61	-393.52
	1200. - 6000.	58.17	2.72	-0.49	0.04	-6.45	-425.92	-393.52
H_2O	500. - 1700.	30.09	6.83	6.79	-2.53	0.08	-250.88	-241.83
	1700. - 6000.	41.96	8.62	-1.50	0.10	-11.16	-272.18	-241.83
SO_2	298. - 1200.	21.43	74.35	-57.75	16.36	0.09	-305.77	-296.84
	1200. - 6000.	57.48	1.01	-0.08	0.01	-4.05	-324.41	-296.84
O_2	100. - 700.	31.32	-20.24	57.87	-36.51	-0.01	-8.90	0.00
	700. - 2000.	30.03	8.77	-3.99	0.79	-0.74	-11.32	0.00
	2000. - 6000.	20.91	10.72	-2.02	0.15	9.25	5.34	0.00
N_2	100. - 500.	28.99	1.85	-9.65	16.64	0.00	-8.67	0.00
	500. - 2000.	19.51	19.89	-8.60	1.37	0.53	-4.94	0.00
	2000. - 6000.	35.52	1.13	-0.20	0.01	-4.55	-18.97	0.00

B.2. Minimum inner radius of the distributor to avoid interference

Table B-2 Minimum inner radius r_i values for different combinations of t and θ with 60 blades to avoid interference between the blades.

$r_{i,min}$, mm					
θ, °	10	15	20	25	30
t, mm					
0.5	2.87	1.93	1.46	1.18	1.00
0.6	3.45	2.31	1.75	1.42	1.20
0.7	4.02	2.70	2.04	1.65	1.40
0.8	4.59	3.08	2.33	1.89	1.60
0.9	5.17	3.47	2.62	2.12	1.80
1.0	5.74	3.85	2.92	2.36	1.99
1.1	6.32	4.24	3.21	2.60	2.19
1.2	6.89	4.62	3.50	2.83	2.39
1.3	7.47	5.01	3.79	3.07	2.59
1.4	8.04	5.39	4.08	3.30	2.79
1.5	8.61	5.78	4.37	3.54	2.99
1.6	9.19	6.17	4.67	3.78	3.19
1.7	9.76	6.55	4.96	4.01	3.39
1.8	10.34	6.94	5.25	4.25	3.59
1.9	10.91	7.32	5.54	4.48	3.79
2.0	11.49	7.71	5.83	4.72	3.99

B.3. List of design specifications

Table B-3 Template of a list of designs specifications of a SFB reactor for biomass thermochemical conversion.

Design specifications				
Concept	**Propose**	**D/W**	**Requirements**	**Goal**
Function	E	D	Resists pressurization	P_{oper}
	E	D	Resists shearing and bending loads	m_{bed}
	E	D	Supports high temperature	T
	E	D	Fluidizes solid particles	$\dot{m}_{\text{total}}$ d_{s} ρ_{s}
Dimensions	C	W	Outer radius	r_{o} and r_c
	E	D	Wall thickness	t_{sw}
	C	W	Gas distributor	%op N_{blade} $t_{\boldsymbol{blade}}$ θ
Material	C	D	Resistance to combined loadings without exceeding the yield strength limit	S_y
	E	D	Resistance to corrosion wear	Allowable corrosion
	E	D	Resistance to high temperature	Maximum service temperature, T_{max}
Safety	E	D	Follows safety standards to build pressure vessels	ASME code section VIII
	E	D	Follows explosion-proof safety standards	ISO 6184-1:1985
Signs	C	D	Pressure measuring	Pressure transmitter
	C	D	Flow measuring	Flowmeter transmitter
	C	D	Temperature measuring	Temperature transmitter
Cost	C	W	Cost per kilo	Low
	C	W	Energy to produce material	Lower than common materials

B.4. Determination of the drag coefficient in the openings between blades.

Figure B-1 is the Instrument Society of America (ISA) flow nozzle chart for estimating the value of the coefficient C. C is a function of the superficial Reynolds number Re_s and the orifice-to-upstream-area ratio, i.e., the percentage area of opening %op [2]. These values correspond to the calculated from Equations (B-1) and (B-2).

$$\mathrm{Re}_s = \frac{\mathrm{d}_A V_{\mathrm{sup}} \rho_{\mathrm{g}}}{\mu_{\mathrm{g}}} \tag{B-1}$$

$$\frac{A_{\mathrm{op,total}}}{A_{\mathrm{bed}}} = \frac{\%\mathrm{op}}{100} \tag{B-2}$$

Where V_{sup} is the superficial velocity of the gas, μ_{g} the dynamic viscosity of the gas, and d_{A} the equivalent hydraulic diameter of the area of the annular section A_{bed} and perimeter p_{bed} calculated as follows

$$d_{\mathrm{A}} = \frac{4A_{\mathrm{bed}}}{p_{\mathrm{bed}}} = \frac{4\pi\left(r_{\mathrm{o}}^2 - r_{\mathrm{i}}^2\right)}{2\pi(r_{\mathrm{o}} + r_{\mathrm{i}})} = \frac{2\left(r_{\mathrm{o}}^2 - r_{\mathrm{i}}^2\right)}{(r_{\mathrm{o}} + r_{\mathrm{i}})}$$

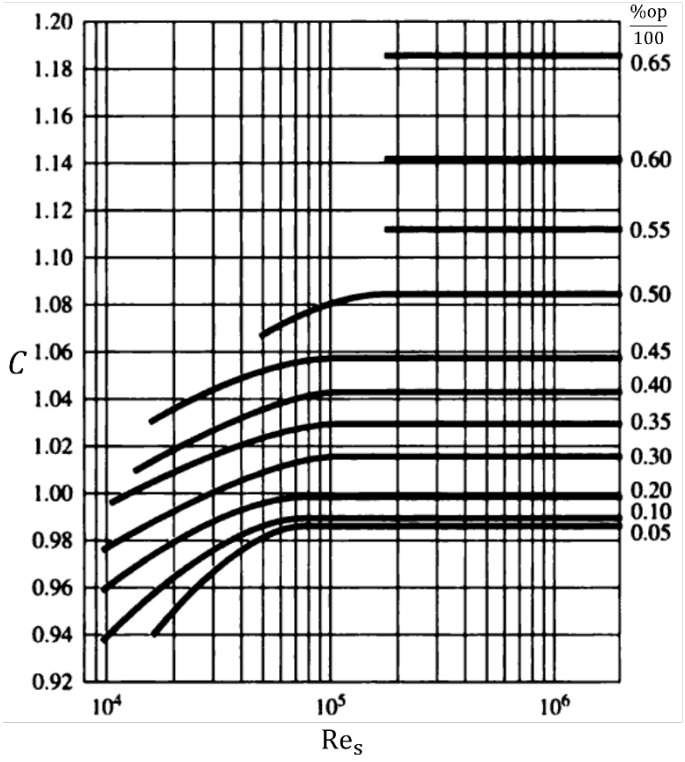

Figure B-1 ISA flow nozzle chart for estimating the discharge coefficient value. Source: Extracted and adapted from [2].

B.5. Pressure-drop through the turbine flowmeter

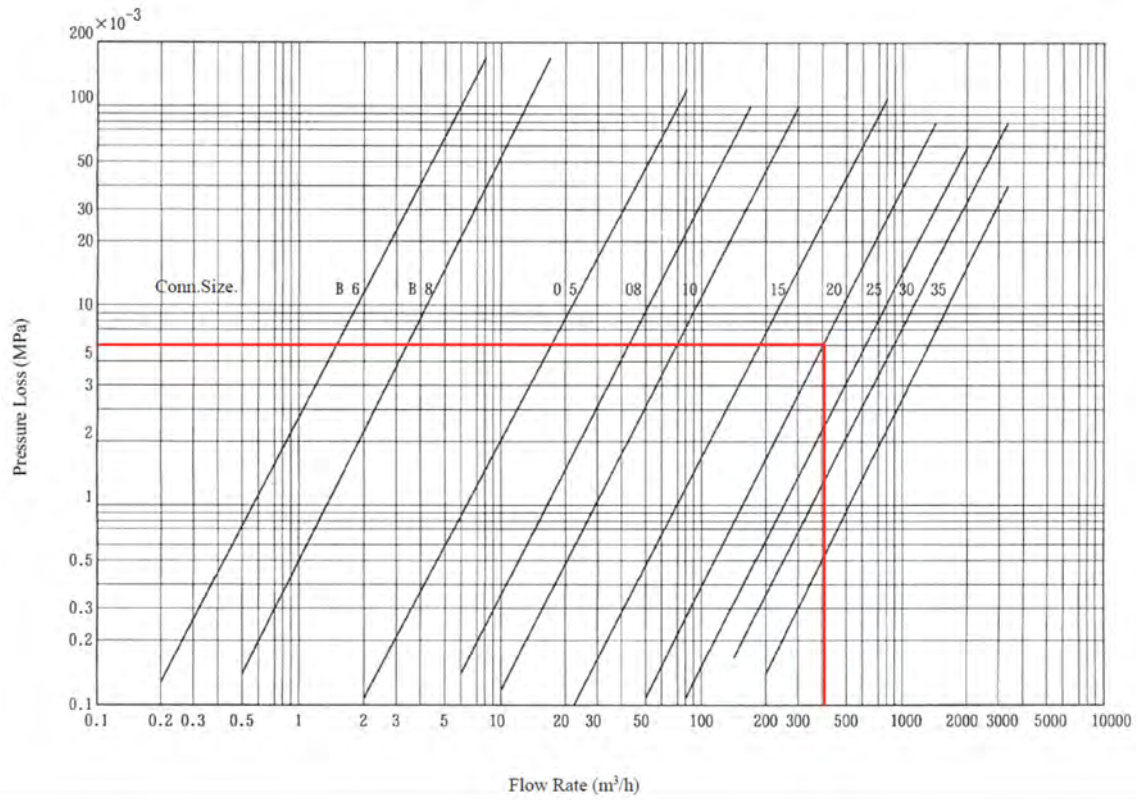

Figure B-2 Tokico turbine flowmeter model GS-F2011E-02 pressure drop characteristic curves extracted from [3]. The vertical red line is the actual operating point with 404.86 m3 h-1. The horizontal red line represents the pressure drop of the operating point for the Connection Size 20 (according to the manufacture is equal to a connection of 200 mm-diameter). The resultant pressure drop across the turbine flowmeter is about 6 kPa.

B.6. Pressure-drop across the cyclone

The estimation of the pressure-drop across the cyclone follows the recommended procedure by [4].

Sinnot & Towler [4] recommends an inlet velocity to the cyclone of 15 m s^{-1}. The flue gases volumetric flow rate is 0.22 m^3 s^{-1}. Then, the inlet area to the cyclone equals 0.01 m^2.

Assuming the distribution of the rice husk ash particles for combustion in fluidized beds as determined in the experiment of Fernandes [5], the mean particle size is lower than 5 microns. Sinnot & Towler [4] states that a high-efficiency cyclone is the optimal solution for gas-solid separation.

The pressure drop of the cyclone equals 1.58 kPa, calculated using equations and procedure from Chapter 10, Section 10.8.3 in Sinnot & Towler [4].

B.7. Blower selection from performance curves

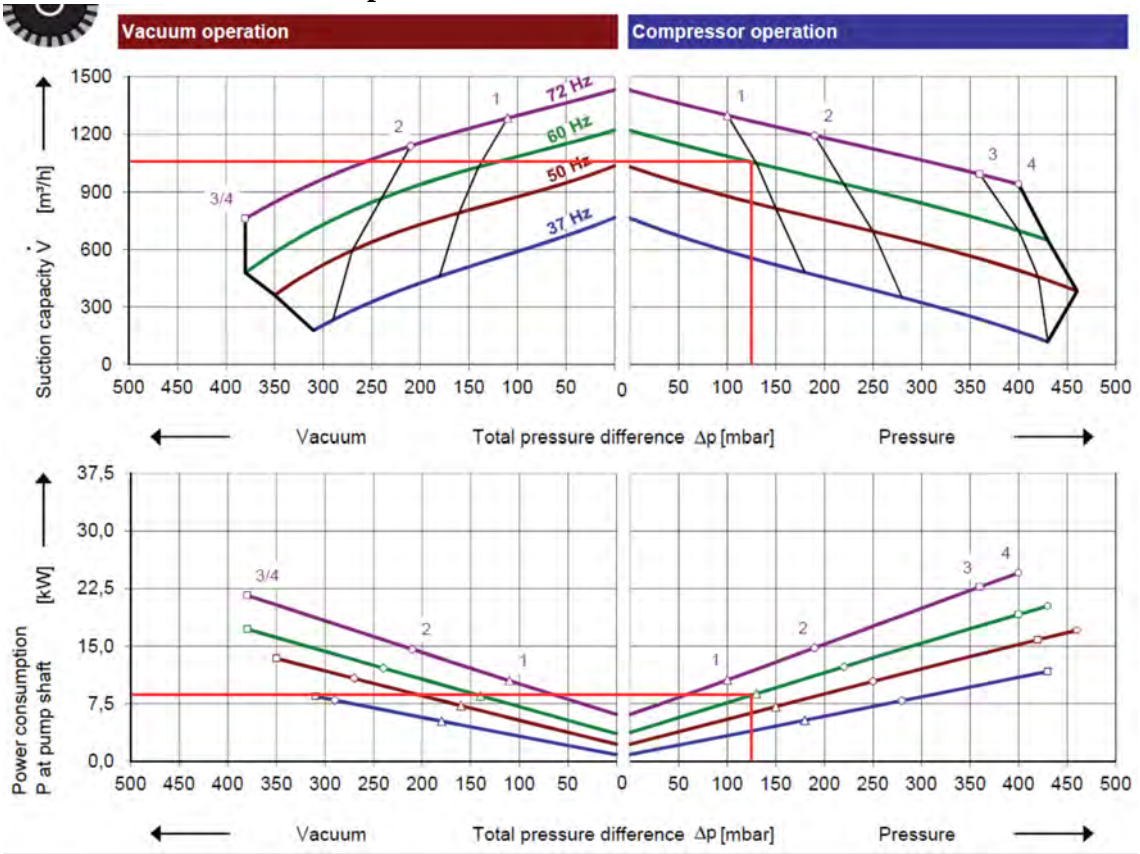

Figure B-3 Performance curves of the Gardner Denver side blower channel with frequency converter model G-BH1 2BH1 900 extracted from [6]. The operating point at the total pressure difference of 140 mbar and frequency 60 Hz. The suction capacity of the blower is around 1050 m^3 h^{-1} and the power consumption 9.1 kW at the operating point.

B.8. Design drawings of the SFB reactor for rice husk combustion

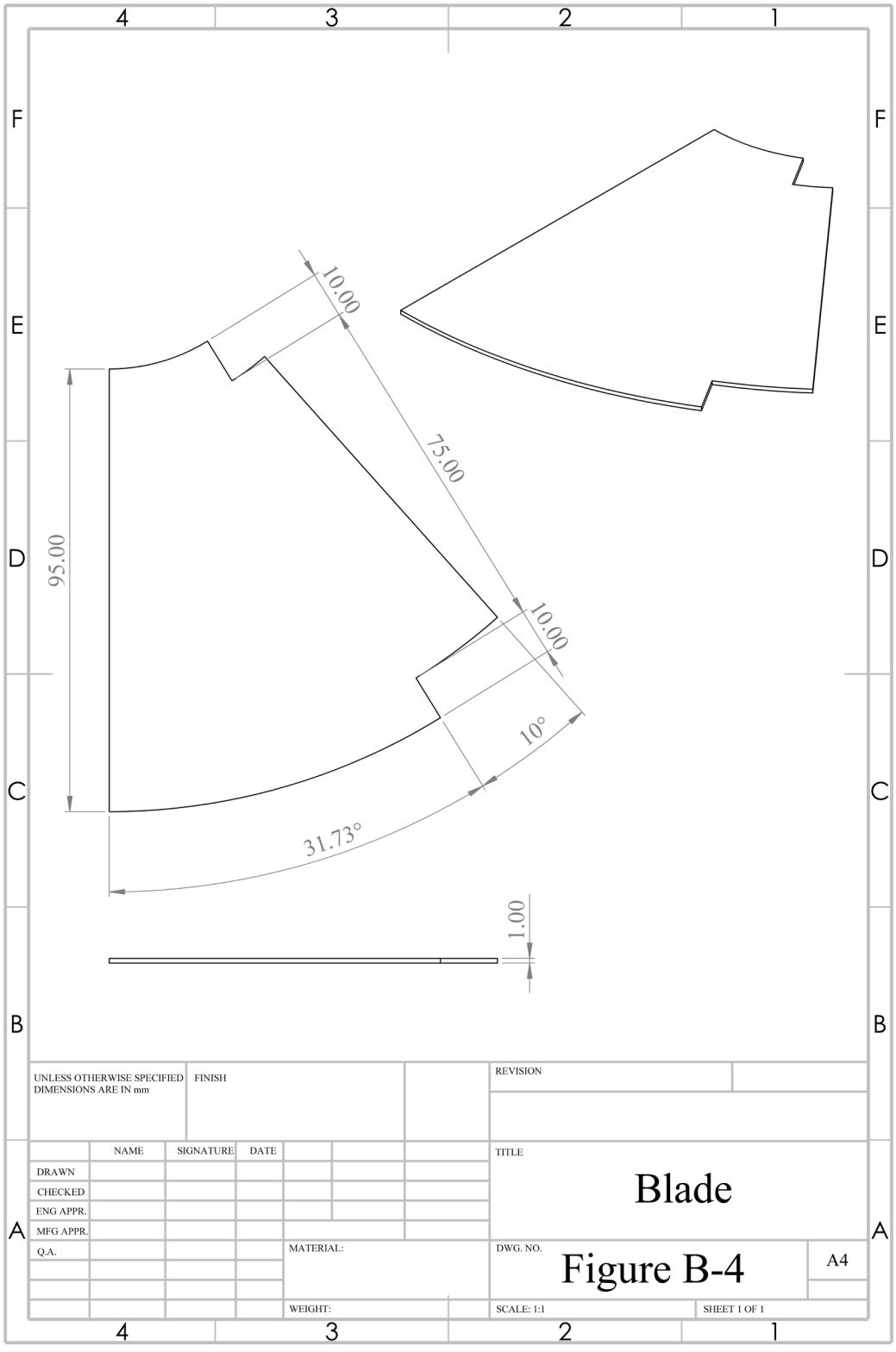

Figure B-4 Design drawing of the blade for the single row blades distributor. Source: Figure created by author.

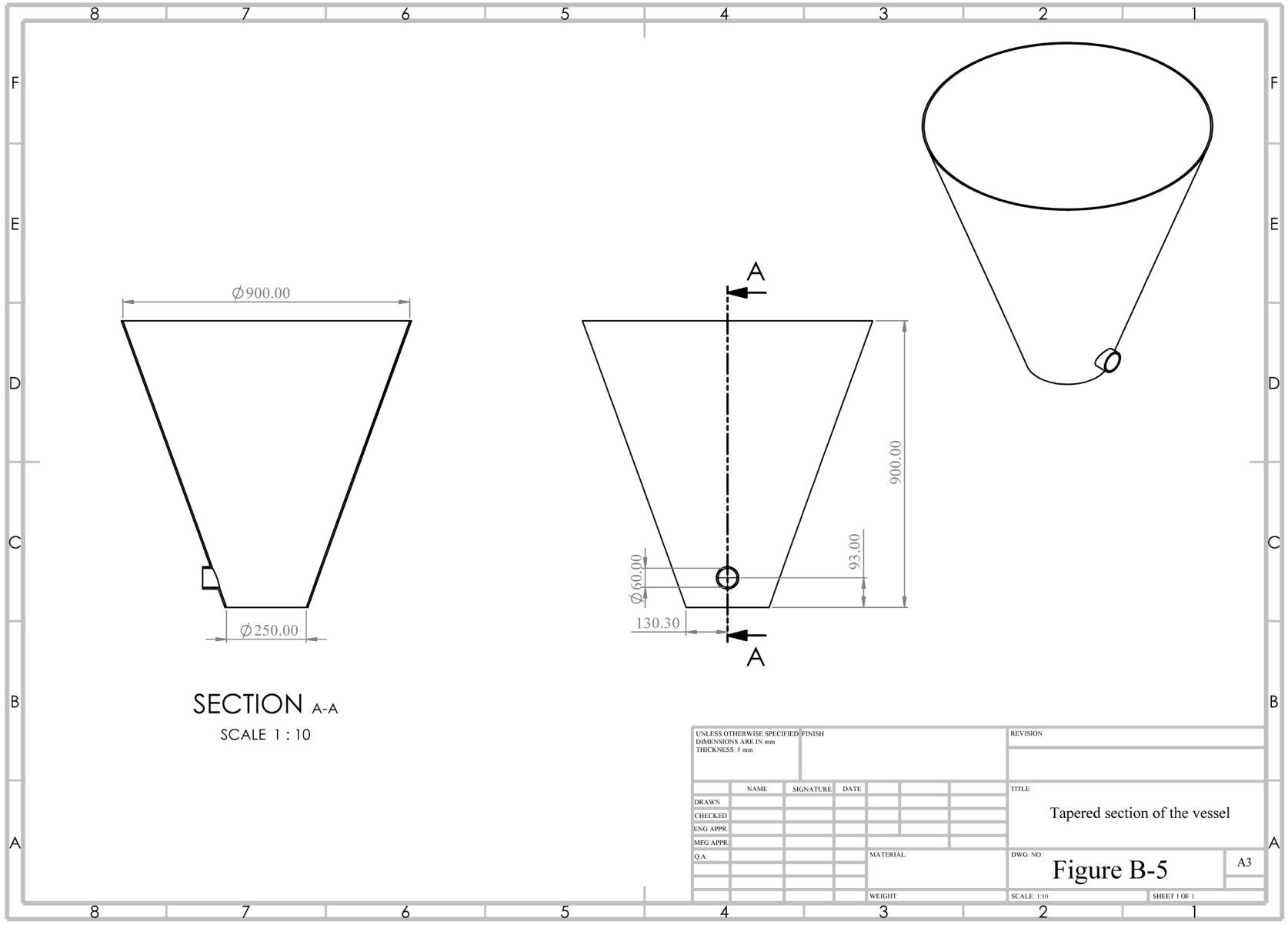

Figure B-5 Design drawing of the tapered section of the pressure vessel. Source: Figure created by author.

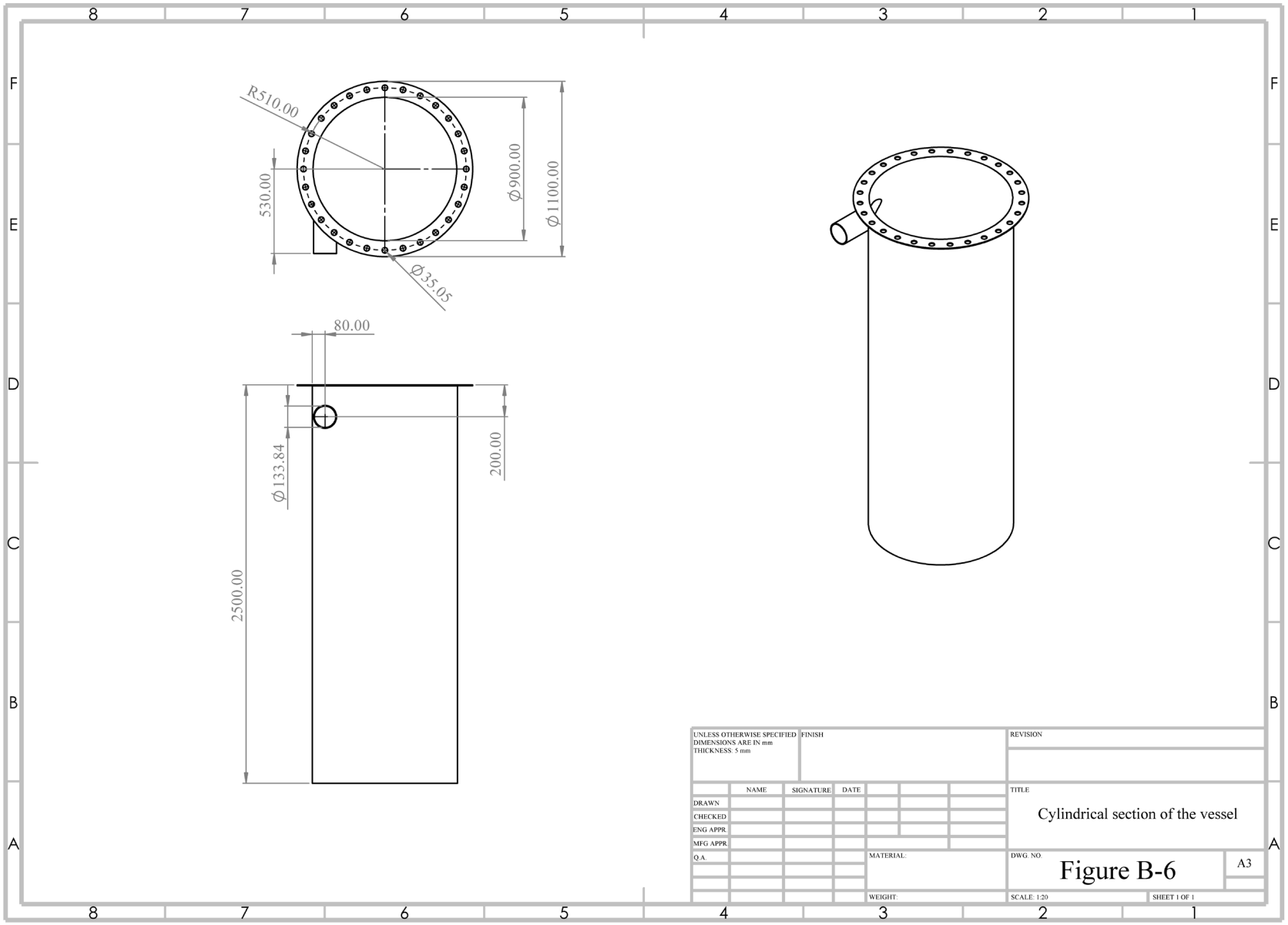

Figure B-6 Design drawing of the cylindrical section of the pressure vessel. Source: Figure created by author.

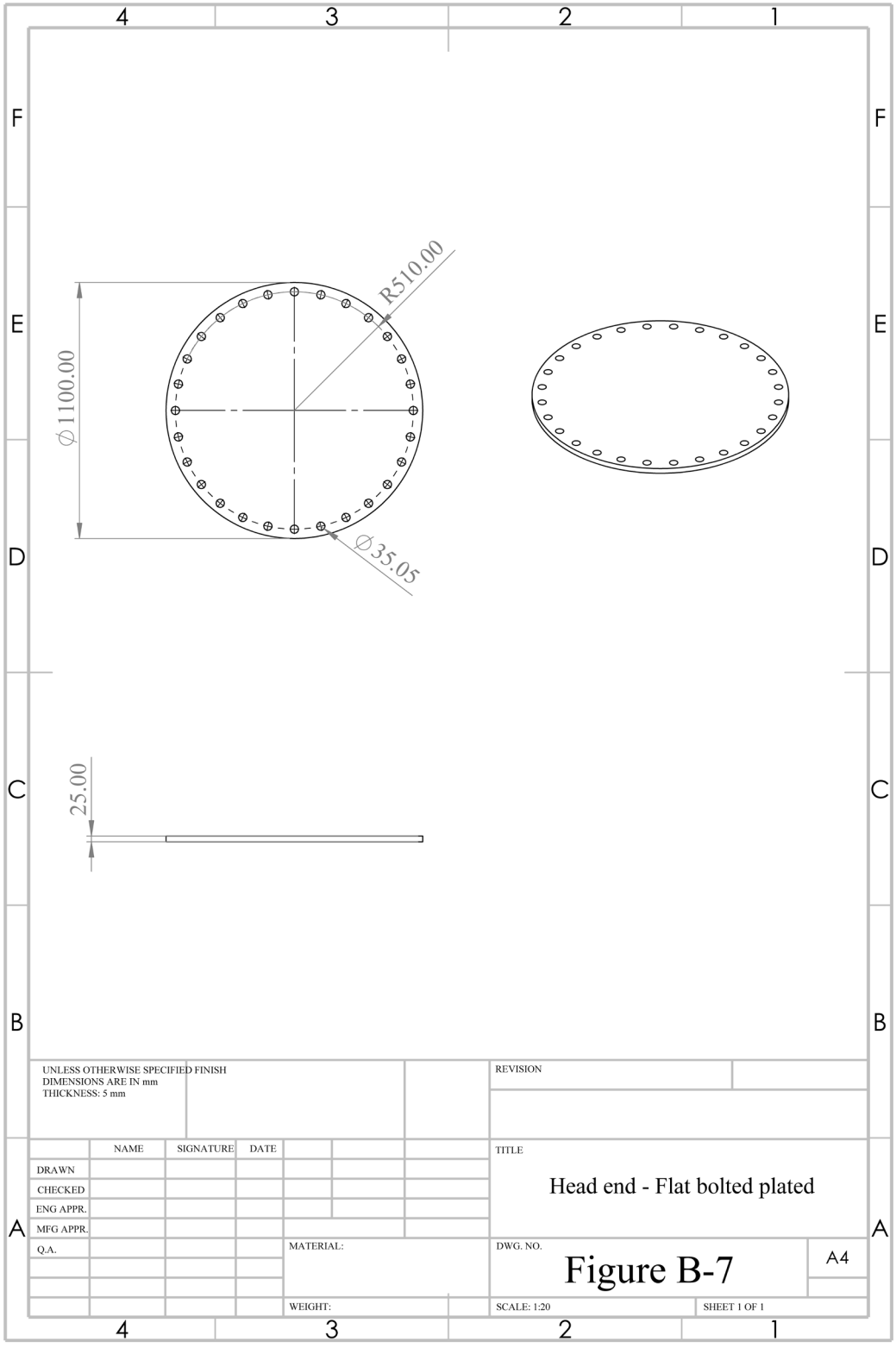

Figure B-7 Design drawing of the head flat bolted end. Source: Figure created by author.

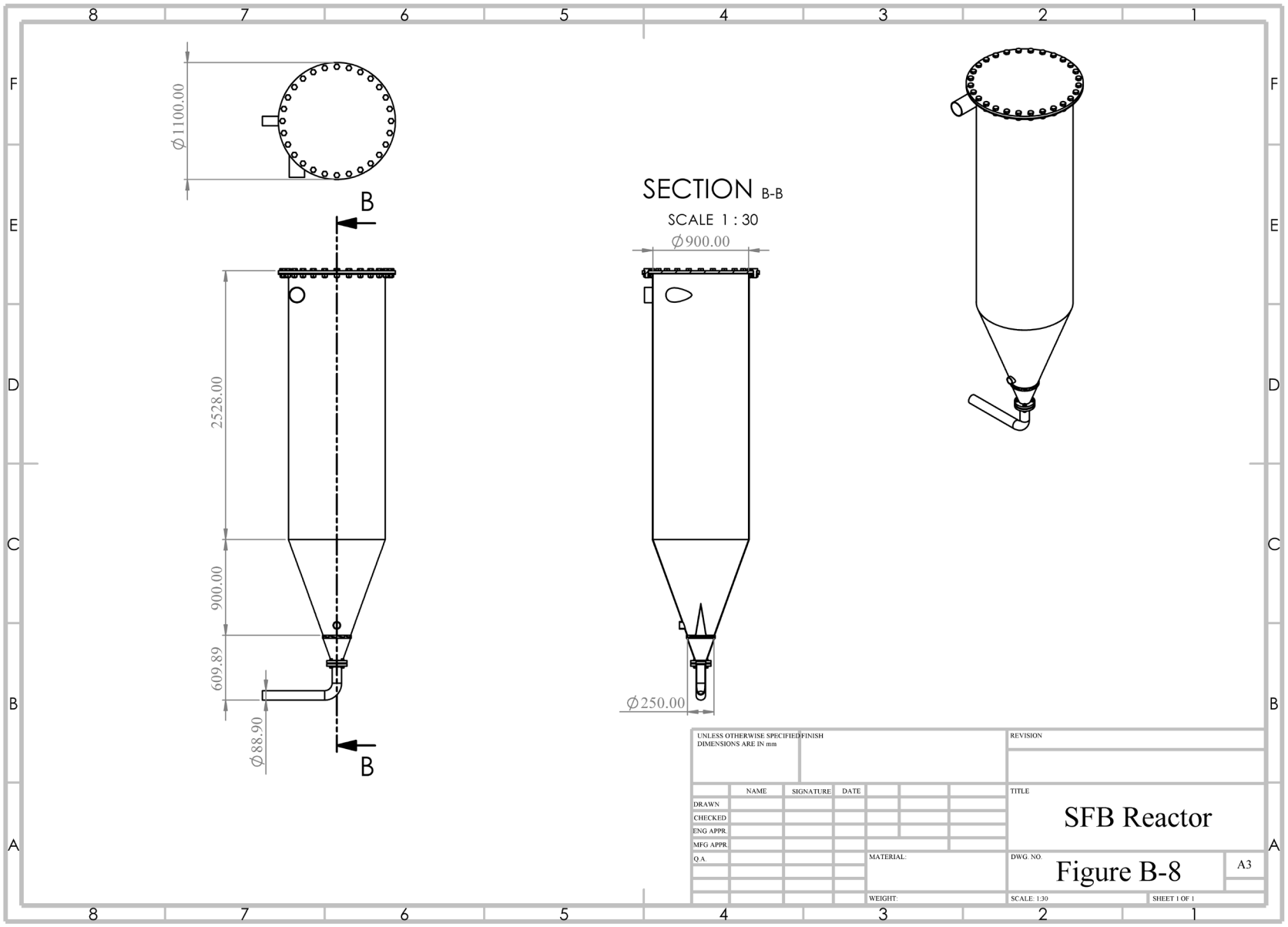

Figure B-8 Design drawing of the SFB reactor with global dimensions. Source: Figure created by author.

References

[1] National Institute of Standards and Technology - NIST, *NIST Chemistry WebBook*. National Institute of Standards and Technology - NIST. doi: 10.18434/T4D303.
[2] V. L. Streeter, E. B. Wylie, and K. W. Bedford, *Fluid mechanics*, 9th ed. New York: McGraw-Hill, 2010.
[3] Tokico System Solutions Ltd, "General Specifications Turbine Flowmeter GS-F2011E-02." Kanagawa, 2020. [Online]. Available: Tokico System Solutions Ltd
[4] R. Sinnott and G. Towler, *Chemical engineering design: SI Edition*. Butterworth-Heinemann, 2019.
[5] I. J. Fernandes *et al.*, "Characterization of rice husk ash produced using different biomass combustion techniques for energy," *Fuel*, vol. 165, pp. 351–359, 2016, doi: https://doi.org/10.1016/j.fuel.2015.10.086.
[6] Gardner Denver, "G-BH1 e - Data sheet 2BH1 900 - Side channel blower with Frequency Converter," Bad Neustadt, 2015. [Online]. Available: https://www.gardnerdenver.com/en-in/elmorietschle/products/side-channel/compressor-g-bh1-c